CABLE TENSION ESTIMATION OF CABLE-STAYED BRIDGE USING VISION-BASED MONITORING SYSTEM

by

Cevdet Enes Çukacı

B.S., Civil Engineering, Boğaziçi University, 2020

Submitted to the Institute for Graduate Studies in
Science and Engineering in partial fulfillment of
the requirements for the degree of
Master of Science

Graduate Program in Civil Engineering

Boğaziçi University

2023

Dedicated to my dear family

ACKNOWLEDGEMENTS

I am deeply grateful to my advisor, Prof. Serdar Soyöz, for his unwavering support, insightful guidance, and continuous encouragement throughout this thesis. His dedication to academic excellence and commitment to fostering my intellectual growth have been truly invaluable, significantly shaping both the direction of the thesis and my development as a researcher. Also, I extend my appreciation to thesis committee members, Prof. Çetin Yılmaz and Assoc. Prof. Barlas Özden Çağlayan, for valuable insights, constructive feedback, and dedication to ensuring the success of this thesis.

I would like to express my thanks to Mahmut Esat Partal from GDH in Turkey and Arif Erdiş for providing the data that has greatly enriched the thesis content.

I want to thank to The Scientific and Technological Research Council of Turkey (TÜBİTAK) for their financial support by the 2210-A Master's Scholarship Program.

I want to express my gratitude to the research assistants, Emre Aytulun and Cem Tura, for their assistance and contributions to the various aspects. Thank you very much to all my friends and colleagues, whose names are too many to be listed here without the fear of leaving someone out. I am truly thankful to all of you who were with me, or helped me and touched my life. Lastly, I extend my sincere appreciation to my best friend, Özlem Özdemir. Your unwavering belief, endless support, and understanding have been my rock, bringing joy and inspiration to my academic journey. Thank you for being my confidante through the challenges and triumphs.

I am deeply grateful to my family—Nalan and Yusuf Cahit, my parents, and my brother, Eren—for unwavering support. Your belief in me is my greatest motivation, and I dedicate this achievement to you. Your sacrifices and encouragement have been the cornerstone of my academic journey. Thank you for the strength and inspiration.

ABSTRACT

CABLE TENSION ESTIMATION OF CABLE-STAYED BRIDGE USING VISION-BASED MONITORING SYSTEM

In this study, it is aimed to estimate the cable tensions of the New Kömürhan Cable-stayed Bridge using a vision-based monitoring system. The number of structures where cables are used as main load carrying members is increasing with the development of material properties, analysis, and construction processes. Structural Health Monitoring (SHM) is necessary to ensure operational and structural safety and integrity. The estimation of the cable tensions is one of the most important factors in early detection of deterioration and damage. Fatigue damage caused by cyclic traffic and wind loads, corrosion due to environmental factors, and sudden earthquake loads cause a decrease in cable tensions, which affects the overall performance of the structure. In this study, cable tensions were determined using the lift-off test and the vibration response under seismic events recorded by existing acceleration sensors on the bridge. The image processing technique was developed through experiments, two of which were conducted in the laboratory and two in the field. Then, cable tensions were estimated by vision-based methods using video. In the first two methods, only 8 of 42 cables are continuously monitored; on the other hand, all cable tensions were estimated with the vision-based monitoring system and gave consistent results compared to 8 cables. In the last part of the study, Finite Element Model (FEM) of the bridge was developed and verified by comparing cable tensions obtained from FEM and measurements. Additionally, pylon and deck frequencies of verified FEM match with those obtained from vibration records.

ÖZET

GERGİN EĞİK ASKILI KÖPRÜDE GÖRÜNTÜ TABANLI İZLEME SİSTEMİ KULLANILARAK KABLO KUVVETLERİNİN HESAPLANMASI

Bu çalışmada Yeni Kömürhan Gergin Eğik Askılı Köprüsü'nün kablo kuvvetlerinin görüntü tabanlı izleme sistemi kullanılarak tahmin edilmesi amaçlanmaktadır. Malzeme özelliklerinin, analiz ve yapım süreçlerinin gelişmesiyle birlikte kabloların ana yük taşıyıcı eleman olarak kullanıldığı yapıların sayısı da artmaktadır. Operasyonel ve yapısal güvenliği ve bütünlüğü sağlamak için Yapısal Sağlık İzleme (YSİ) gereklidir. Kablo kuvvetlerinin tahmini, yıpranma ve hasarın erken tespitinde en önemli faktörlerden biridir. Çevrimsel trafik ve rüzgar yüklerinden kaynaklanan yorulma hasarları, çevresel faktörlerden kaynaklanan korozyon ve ani deprem yükleri kablo gerilimlerinde azalmaya neden olur ve bu da yapının genel performansını etkiler. Bu çalışmada, köprüdeki mevcut ivme sensörleri tarafından kaydedilen sismik olaylar altındaki titreşim tepkisi ve "kaldırma testi" kullanılarak kablo kuvvetleri belirlenmiştir. Görüntü işleme tekniği, ikisi laboratuvarda, ikisi de sahada gerçekleştirilen deneylerle geliştirildi. Daha sonra kablo kuvvetleri, video kayıtlarından görüntü tabanlı izleme sistemiyle tahmin edildi. İlk iki yöntemde 42 kablodan sadece 8'i sürekli olarak izlenmektedir. Öte yandan görüntü tabanlı izleme sistemi ile tüm kablo kuvvetleri tahmin edilmiş ve 8 kabloya kıyasla tutarlı sonuçlar vermiştir. Çalışmanın son bölümünde, sonlu eleman modelinden elde edilen kablo kuvvetleri ve ölçümler karşılaştırılarak köprünün sonlu elemanlar modeli geliştirilmiş ve doğrulanmıştır. Ek olarak, doğrulanan sonlu eleman modelinin pilon ve tabliye frekansları, titreşim kayıtlarından elde edilenlerle eşleşmektedir.

TABLE OF CONTENTS

ACKNOWLEDGEMENTS iv
ABSTRACT v
ÖZET vi
LIST OF FIGURES ix
LIST OF TABLES xxi
LIST OF SYMBOLS xxiii
LIST OF ACRONYMS/ABBREVIATIONS xxiv
1. INTRODUCTION 1
1.1. Literature Review 2
1.1.1. Cable Tension Calculation Methods 4
1.1.1.1. Direct Measurement Methods 4
1.1.1.2. Indirect Measurement Methods 8
1.2. Scope and Objectives 24
1.3. Thesis Outline 25
2. METHODOLOGY 27
2.1. Definition of Monitoring Systems 27
2.2. Definition of Earthquakes 29
2.3. Cable Tension Calculations 31
2.3.1. Lift-off Test 31
2.3.2. Vibration Test 32
2.3.3. Vision-based Monitoring System 34
3. BRIDGE DETAILS AND RESULTS 37
3.1. New Kömürhan Bridge and Description 37
3.2. Cable Tension Calculation Results 54
3.2.1. Lift-off Test Results 54
3.2.2. Cable Tension Calculation Using Existing Accelerometers 64
3.2.3. Cable Tension Calculation with Image Processing 83
3.3. Comparison of Results 107

3.4. FEM and Comparison of Dynamic Characteristic with the Model . . . 108
4. CONCLUSION 118
REFERENCES 122
APPENDIX A: Experimental Studies 134
A.1. Shaking Table Test 136
A.2. Cable Experiment 147
A.3. Vision-based Analysis of Wind Turbine 164
A.4. Lightning Rod Measurement 172

LIST OF FIGURES

Figure 2.1. Existing SHM system of New Kömürhan Bridge. 28

Figure 2.2. Bridge, station, and earthquake locations. 29

Figure 2.3. Earthquake time history of. 30

Figure 3.1. General view of New Kömürhan Bridge. 38

Figure 3.2. FEM of New Kömürhan Bridge. 39

Figure 3.3. Longitudinal section of New Kömürhan Bridge. 39

Figure 3.4. Plan view of New Kömürhan Bridge. 39

Figure 3.5. Plan view of FEM of New Kömürhan Bridge. 39

Figure 3.6. Views of the pylon of New Kömürhan Bridge. 40

Figure 3.7. Cross-section of main span of New Kömürhan Bridge. 41

Figure 3.8. Details of cross-section of main span of New Kömürhan Bridge. . . 41

Figure 3.9. FEM cross-section of main span of New Kömürhan Bridge. 42

Figure 3.10. Cross-section details: (a) section longitudinal view of pylon, (b) section 1-1, (c) section 2-2, (d) section 3-3, (e) section 4-4, (f) section 5-5. 42

Figure 3.11. Cross-section details in FEM: (a) longitudinal view of pylon, (b) section 2-2, (c) section 3-3, (d) section 4-4, (e) section 5-5. 43

Figure 3.12. Cross-section detail of the transition between the pylon and the main span. 44

Figure 3.13. Cross-section detail of the transition between the pylon and the main span in FEM. 44

Figure 3.14. Cross-section detail of support-3. 44

Figure 3.15. Cross-section detail of support-3 in FEM. 45

Figure 3.16. Cross-section detail of support-4. 45

Figure 3.17. Cross-section detail of support-4 in FEM. 46

Figure 3.18. Cross-section of transition between support-3 and 4. 46

Figure 3.19. Cross-section of transition between support-3 and 4 in FEM. . . . 46

Figure 3.20. Cross-section detail of abutment-5 in FEM. 46

Figure 3.21. Cross-section detail of abutment-5. 47

Figure 3.22. Cross-section of transition of support-4 and abutment-5. 47

Figure 3.23. Cross-section of transition between support-4 and abutment-5 in FEM. 47

Figure 3.24. Longitudinal view of the back span anchorage block. 48

Figure 3.25. Cross-section details of the back span anchorage block. 48

Figure 3.26. Plan view of the back span anchorage block. 49

Figure 3.27. Cross-section of the back span anchorage block in FEM. 49

Figure 3.28. Plan view of the back span anchorage block in FEM. 50

Figure 3.29. Cable arrangement of New Kömürhan Bridge. 50

Figure 3.30. Cable arrangement of New Kömürhan Bridge in FEM. 50

Figure 3.31. Cable arrangement plan view of New Kömürhan Bridge. 51

Figure 3.32. Lift-off test results for dataset-1. 55

Figure 3.33. Lift-off test results for dataset-2. 56

Figure 3.34. Lift-off test results for dataset-3. 57

Figure 3.35. Lift-off test results for dataset-4. 58

Figure 3.36. Lift-off test results for dataset-5. 59

Figure 3.37. Lift-off test results for dataset-6. 60

Figure 3.38. Lift-off test results for dataset-7. 61

Figure 3.39. Lift-off test results for dataset-8. 62

Figure 3.40. Vibration analysis using existing accelerometer for dataset-1. . . . 65

Figure 3.41. Vibration analysis using existing accelerometer for dataset-2. . . . 66

Figure 3.42. Vibration analysis using existing accelerometer for dataset-3. . . . 67

Figure 3.43. Vibration analysis using existing accelerometer for dataset-4. . . . 68

Figure 3.44. Vibration analysis using existing accelerometer for dataset-5. . . . 69

Figure 3.45. Vibration analysis using existing accelerometer for dataset-6. . . . 70

Figure 3.46. Vibration analysis using existing accelerometer for dataset-7. . . . 71

Figure 3.47. Vibration analysis using existing accelerometer for dataset-8. . . . 72

Figure 3.48. Positions taken the video recording. 83

Figure 3.49. Site video recording position. 84

Figure 3.50. Vision-based monitoring results for cable 221. 85

Figure 3.51. Vision-based monitoring results for cable 220. 85

Figure 3.52. Vision-based monitoring results for cable 219. 86

Figure 3.53. Vision-based monitoring results for cable 218. 86

Figure 3.54. Vision-based monitoring results for cable 217. 87

Figure 3.55. Vision-based monitoring results for cable 216. 87

Figure 3.56. Vision-based monitoring results for cable 215. 88

Figure 3.57. Vision-based monitoring results for cable 214. 88

Figure 3.58. Vision-based monitoring results for cable 213. 89

Figure 3.59. Vision-based monitoring results for cable 212. 89

Figure 3.60. Vision-based monitoring results for cable 211. 90

Figure 3.61. Vision-based monitoring results for cable 210. 90

Figure 3.62. Vision-based monitoring results for cable 209. 91

Figure 3.63. Vision-based monitoring results for cable 208. 91

Figure 3.64. Vision-based monitoring results for cable 207. 92

Figure 3.65. Vision-based monitoring results for cable 206. 92

Figure 3.66. Vision-based monitoring results for cable 205. 93

Figure 3.67. Vision-based monitoring results for cable 204. 93

Figure 3.68. Vision-based monitoring results for cable 203. 94

Figure 3.69. Vision-based monitoring results for cable 202. 94

Figure 3.70. Vision-based monitoring results for cable 201. 95

Figure 3.71. Vision-based monitoring results for cable 101. 95

Figure 3.72. Vision-based monitoring results for cable 102. 96

Figure 3.73. Vision-based monitoring results for cable 103. 96

Figure 3.74. Vision-based monitoring results for cable 104. 97

Figure 3.75. Vision-based monitoring results for cable 105. 97

Figure 3.76. Vision-based monitoring results for cable 106. 98

Figure 3.77. Vision-based monitoring results for cable 107. 98

Figure 3.78. Vision-based monitoring results for cable 108. 99

Figure 3.79. Vision-based monitoring results for cable 109. 99

Figure 3.80. Vision-based monitoring results for cable 110. 100

Figure 3.81. Vision-based monitoring results for cable 111. 100

Figure 3.82. Vision-based monitoring results for cable 112. 101

Figure 3.83. Vision-based monitoring results for cable 113. 101

Figure 3.84. Vision-based monitoring results for cable 114. 102

Figure 3.85. Vision-based monitoring results for cable 115. 102

Figure 3.86. Vision-based monitoring results for cable 116. 103

Figure 3.87. Vision-based monitoring results for cable 117. 103

Figure 3.88. Vision-based monitoring results for cable 118. 104

Figure 3.89. Vision-based monitoring results for cable 119. 104

Figure 3.90. Vision-based monitoring results for cable 120. 105

Figure 3.91. Vision-based monitoring results for cable 121. 105

Figure 3.92. Acceleration response and PSD values of top of pylon for each data set. 109

Figure 3.93. Acceleration response and PSD values of one side of deck for each data set. 110

Figure 3.94. Acceleration response and PSD values of the other side of deck for each data set. 111

Figure A.1. Experiment setup for the vision-based analysis. 139

Figure A.2. Acceleration response of each story vs. time graph of model experiment from accelerometer. 139

Figure A.3. Data set for each applied force. 140

Figure A.4. The first story response and PSD. 141

Figure A.5. The second story response and PSD. 141

Figure A.6. The third story response and PSD. 141

Figure A.7. SVD of experimental model using vision-based system. 142

Figure A.8. Mode shapes of model experiment using accelerometer. 143

Figure A.9. Displacement response of each story vs. time graph of model experiment from vision-based system. 143

Figure A.10. Data set for each applied force. 144

Figure A.11. The first story response and PSD. 144

Figure A.12. The second story response and PSD. 144

Figure A.13. The third story response and PSD. 145

Figure A.14. SVD of experimental model using vision-based system. 145

Figure A.15. Mode shapes of model experiment using vision-based system. . . . 146

Figure A.16. Comparison of mode shapes of model experiment using accelerometers and vision-based monitoring system. 147

Figure A.17. Experiment setup for the cable. 150

Figure A.18. Acceleration response of the cable for the first case. 151

Figure A.19. Data set for each applied force for the first case. 151

Figure A.20. Acceleration response of the first part for the first case. 152

Figure A.21. PSD of the cable for the first case. 152

Figure A.22. Displacement response of the cable for the first case. 153

Figure A.23. Data set for each applied force for the first case using vision-based monitoring. 153

Figure A.24. Displacement response of the first part for the first case. 154

Figure A.25. PSD of the cable for the first case. 154

Figure A.26. Acceleration response of the cable for the second case. 155

Figure A.27. Data set for each applied force for the second case. 156

Figure A.28. Acceleration response of the first part of the cable for the second case. 156

Figure A.29. PSD of the cable for the second case. 157

Figure A.30. Displacement response of the cable for the second case. 157

Figure A.31. Data set for each applied force for the second case using vision-based processing. 158

Figure A.32. Displacement response of the first part of the cable for the second case. 158

Figure A.33. PSD of the cable for the second case. 159

Figure A.34. Acceleration response of the cable for the third case. 160

Figure A.35. Data set for each applied force for the third case. 160

Figure A.36. Acceleration response of the first part for the third case. 161

Figure A.37. PSD of the cable for the third case. 161

Figure A.38. Displacement response of the cable for the third case. 162

Figure A.39. Data set for each applied force for the first case using vision-based monitoring. 162

Figure A.40. Displacement response of the first part for the third case. 163

Figure A.41. PSD of the cable for the third case. 163

Figure A.42. The photograph taken during video recording. 169

Figure A.43. Region of interest for top displacement. 170

Figure A.44. Top displacement vs. time graph. 171

Figure A.45. PSDs for operating wind turbine. 172

Figure A.46. Sensor layouts for the lightning rod. 173

Figure A.47. Acceleration response of each level. 174

Figure A.48. PSD values for each level. 175

Figure A.49. SVD values of the structure using accelerometer. 175

Figure A.50. Mode shapes of lightning rod using accelerometer. 176

Figure A.51. ROIs for top two sensor levels. 177

Figure A.52. Displacement response and PSD for top two sensor levels. 177

Figure A.53. SVD values used in obtaining mode shapes from displacement response for top two sensor levels. 178

Figure A.54. Mode shapes obtained from displacement response for top two sensor levels. 178

Figure A.55. Comparison of mode shapes from acceleration and displacement response for top two sensor levels. 179

Figure A.56. ROIs for top four sensor levels. 179

Figure A.57. Displacement response and PSD for top four sensor levels. 180

Figure A.58. SVD values used in obtaining mode shapes from displacement response for top four sensor levels. 180

Figure A.59. Mode shapes obtained from displacement response for top four sensor levels. 181

Figure A.60. Comparison of mode shapes from acceleration and displacement response for top four sensor levels. 181

Figure A.61. ROIs for top five sensor levels. 182

Figure A.62. Displacement response and PSD for top five sensor levels. 182

Figure A.63. SVD values used in obtaining mode shapes from displacement response for top five sensor levels. 183

Figure A.64. Mode shapes obtained from displacement response for top five sensor levels. 183

Figure A.65. Comparison of mode shapes from acceleration and displacement response for top four sensor levels. 184

LIST OF TABLES

Table 2.1. Earthquake numbering and details used in analysis. 30

Table 3.1. Details of the cables on the Elazig side. 52

Table 3.2. Details of the cables on the Malatya side. 53

Table 3.3. Lift-off test results summary for each strand tension. 63

Table 3.4. Lift-off test results summary for each cable. 64

Table 3.5. Natural frequencies and cable tensions for cable-221. 75

Table 3.6. Natural frequencies and cable tensions for cable-211. 76

Table 3.7. Natural frequencies and cable tensions for cable-201. 77

Table 3.8. Natural frequencies and cable tensions for cable-105. 78

Table 3.9. Natural frequencies and cable tensions for cable-111. 79

Table 3.10. Natural frequencies and cable tensions for cable-117. 80

Table 3.11. Natural frequencies and cable tensions for cable-119. 81

Table 3.12. Natural frequencies and cable tensions for cable-121. 82

Table 3.13. Average cable tension for all cables and data sets. 83

Table 3.14. All cable tensions from vision-based monitoring system. 106

Table 3.15. Comparison of cable tensions from 3 different methods. 107

Table 3.16. Top of pylon in x-direction. 112

Table 3.17. Top of pylon in y-direction. 113

Table 3.18. The first side of deck in y-direction. 114

Table 3.19. The first side of deck in z-direction. 115

Table 3.20. The second side of deck in y-direction. 116

Table 3.21. The second side of deck in z-direction. 117

Table A.1. Frequency response of each story and section by accelerometer. . . 142

Table A.2. Frequency response of each story for each section using vision-based system. 145

Table A.3. Summary of the each section for the first case. 155

Table A.4. Summary of the each section for the second case. 159

Table A.5. Summary of the each section for the third case. 164

Table A.6. The mode frequency means when effects are removed (Soyoz et al., 2020). 171

LIST OF SYMBOLS

$\partial v(x,t)$	Displacement response of the cable in the vertical direction
E	Modulus of elasticity
EI	Bending stiffness
f_n	Natural frequency of the cable with n^{th} order vibration mode
g	Gravitational acceleration
G_{yy}	Estimated version of output power spectral density
l_e	Effective length of the cable
m	Mass per unit length of the cable
n	Total number of strands in each cable
n_s	Maximum number of measured strands
S	Diagonal matrix with the scalar singular values
t	Time
T	Tension of the cable in longitudinal direction
T_i	Tension value of each strand being measured
U_j	Orthonormal matrix
w	Unit weight of the cable
x	Coordinates in the longitudinal direction of the cable

LIST OF ACRONYMS/ABBREVIATIONS

2D	Two Dimensional
3D	Three Dimensional
AFAD	Afet ve Acil Durum Yönetimi Başkanlığı (Disaster and Emergency Management Presidency of Turkey)
AVT	Ambient Vibration Test
CFT	Concurrent Flooding Technique
CMOS	Complementary Metal Oxide Semiconductor
DAF	Dynamic Amplification Factor
DAQ	Data Acquisition
DIC	Digital Image Correlation
DIP	Digital Image Processing
DOF	Degree-of-Freedom
DSLR	Digital Single-Lens Reflex
EFDD	Enhanced Frequency Domain Decomposition
EM	Elasto-magnetic
EMA	Experimental Modal Analysis
ERA	Eigensystem Realization Algorithm
FBG	Fiber Bragg Grid
FDD	Frequency Domain Decomposition
FE	Finite Element
FEM	Finite Element Model
FFT	Fast Fourier Transform
FPS	Frame per Second
FVT	Forced Vibration Test
GFRP	Glass Fiber Reinforced Polymer
GPS	Global Positioning System
GRA	General Realization Algorithm
HDPE	High Density Polyethylene

Hz	Hertz
IMU	Inertial Measurement Unit
ITF	Image Transformation Function
KLT	Kanade-Lucas-Tomasi
kN	Kilonewton
LSD	Line Segment Detector
MAC	Modal Assurance Criterion
M-ERA	Multireference Eigensystem Realization Algorithm
MS	Multi-Strand
OCM	Orientation Code Matching
OFBG	Optical Fiber Bragg Grid
OIS	Optical Image Stabilization
OMA	Operational Modal Analysis
PSD	Power Spectral Density
RGB	Red, Green, and Blue
RMSE	Root Mean Square Error
ROI	Region of Interest
SHM	Structural Health Monitoring
SI	System Identification
SRIM	System Realization using Information Matrix
SSI	Stochastic Subspace Identification
SVD	Singular Value Decomposition
UAV	Unmanned Aerial Vehicle
UCC	Unsampled Cross-Correlation
VBMS	Vision-based Monitoring System
VIS	Vision and Inertia Measurement System
WTT	Wind Turbine Test

1. INTRODUCTION

The necessity of establishing long-term Structural Health Monitoring (SHM) systems on infrastructures and large-scale bridges in order to ensure structural and operational safety has been acknowledged by the authorities. In addition to these advantages, these systems are necessary to reduce repair costs and to detect damage or deterioration before larger catastrophic collapses. They have the advantage of assessing structural reliability, integrity and durability throughout the bridge life cycle and maintaining safe bridge operation by ensuring optimum maintenance planning. The development of a long-term monitoring system on large-scale bridges poses different levels of economic and technological challenges. The selection of appropriate sensors in SHM systems is one of these challenges. In recent years, interdisciplinary studies have been carried out with different technological developments and SHM systems that will prioritize bridge maintenance and emergency repair have been investigated (Ko & Ni, 2005).

With the development of SHM technologies, long-term monitoring systems are being implemented on the structure for assessment, surveillance, and evaluation of newly built and existing bridges around the world. The general purpose of SHM systems of bridges is:

- Detecting differences in loading and response and possible deterioration/damage to the bridge at an early stage in order to ensure operational and structural safety
- Conducting structural safety assessments and obtaining real-time information immediately after extreme events and disasters
- Determining indicators for prioritizing and planning the bridge inspection, maintenance, and repair process
- Re-evaluating the impact of maintenance and repairs on the structure and monitoring the repair and reconstruction
- Developing design specifications for similar structures to be built in the future by

verifying the design parameters

- Providing sufficient data for new research in bridge engineering such as earthquake and wind resistant designs with smart material applications

It is very difficult to implement and develop an SHM system that is optimum in every respect and can achieve the above objectives. A lot of research has been conducted on this subject (Chang et al., 2003). Research on SHM also focuses on embedded and distributed sensing, data storage, communication, data management, signal processing, damage diagnosis methods and providing information on maintenance management by detecting damage to bridges (Van der Auweraer & Peeters, 2003).

Cable-stayed and suspension bridges are a type of cable-supported structure that has been widely used in recent years and is of great significance regarding scale in crossing large spans (Sun et al., 2017). Considering determining dynamic characteristic and obtaining information about the general condition of the bridges by using SHM, the number of bridges in which cables are used as the primary load carrying members is increasing rapidly worldwide with the development in materials, construction process, and analysis technologies. In cable-stayed bridges, cable tension is one of the most important factors in the evaluation of safety and structural integrity (Kim et al., 2023). The bridge deck was supported by multiple cables and this load was transmitted to the pylon. Since the tension of these cables could be adjusted, flexibility was provided in the structural design (Li & Ou, 2016). Therefore, cables play an important role in carrying the load and maintaining the integrity of the structure (Camara et al., 2014).

1.1. Literature Review

The integrity of the structure and the cable tensions should be monitored under construction and traffic loads (Zhang et al., 2021). In Cho et al. (2013)'s study, two multistranded cables of a cable-stayed bridge under construction were investigated by three different methods. Tensions were measured before, after and 5 days after all cables were tensioned. Measurements from this bridge under construction were

compared to the design tension and all three performed well with minimal difference. In Bao et al. (2017)'s study, the real-time variation of cable tensions due to traffic loads and other environmental effects was investigated. The effect of this change in cable tensions on fatigue damage was investigated. In these evaluation, time-varying cable tensions were estimated from cable vibration measurements or from special force sensors on cables. The analysis of this study was important for the maintenance and safety assessment of cable-based bridges. For bridges under service, cable tension is a primary indicator of not only the performance of the cable but also the overall integrity of the bridges. Cumulative fatigue damage from wind excitation and dynamic loads such as cyclic traffic loads could occur on these bridges under service. For this reason, it was necessary to monitor the time-varying cable tensions (Yang et al., 2016). From this point of view, a simple method had been developed for the damage detection of cables in cable-stayed bridges. In this method, variation in support reactions was used to detect and localize damage in cables. In the determination of the support reactions, the shear force in the deck elements adjacent to the supports was used. In the analytical approach, a recursive optimization damage detection technique, in which the model was updated to account for changes in cable stiffness as a result of damage, was used as the formula. To measure the efficiency of the approach, a reduced-scale bridge model was created in the laboratory and tested on it. In addition to the laboratory experiment, its performance in the numerical study was also examined (Nazarian et al., 2016). In addition to these problems, in cable-stayed bridges, the change in cable tensions may be caused by excessive vibration, corrosion of the cable anchorage or corrosion of the cable itself, creep and/or shrinkage of the reinforced concrete elements to which the cable is attached under traffic loads (Au & Si, 2012). Deterioration in the cables due to fatigue or corrosion affected the performance of the entire bridge and caused reduction in the forces of other supports and cables. In Lan et al. (2018)'s study, the effect of quantitative corrosion on fatigue life was investigated. It was found that the fatigue life of cables decreased significantly as the corrosion level of the steel wire increased, especially at low stresses. Therefore, it was important to prevent corrosion to increase service life and prevented premature fatigue problems. In another study, the simultaneous effect of fatigue loading due to cyclic loads and environmental corrosion

was investigated. It was observed that at a certain corrosion level, the fatigue resistance of the cable was insufficient, and its service life was reduced (Jiang et al., 2020). This decrease in any cable tension caused this load to be distributed to other cables. This may affect the safety of the structure. In Ma et al. (2023)'s study, scenarios in various cable damage situations were examined. Experimental results showed that the problem in a cable changed the boundary conditions of the main deck and caused a significant change in the tension of the cable and main deck. It recommended increasing the safety factor of the cables in the mid-span of the main deck. Therefore, for a safer and longer-lasting operation, measuring cable tensions regularly and monitoring of both cable tensions and cable-stayed bridges continuously were required (Yu et al., 2014). Among the various physical quantities used to evaluate the integrity of bridge structures, cable tension was the most widely used to monitor bridge condition (Kim et al., 2013). In Li et al. (2018)'s study, different parameters were examined, and cable tension ratio was extracted as a property variable. It proposed a machine learning-based evaluation method for the remaining cables using the monitored cable tension. In addition, it was found that the cable tension ratio was only related to the cable characteristics and the transverse position of the vehicle.

1.1.1. Cable Tension Calculation Methods

The methods used to determine the cable tension are generally divided into two: the direct measurement of the cable tension and the estimation of the cable tension using the natural frequencies of cables for each mode and the cable characteristic features (Zhang et al., 2021). In the direct measurement method, an adapted device is used to measure the load. The direct methods are lift-off test, fiber Bragg grid (FBG) sensor and elasto-magnetic (EM) vector.

1.1.1.1. Direct Measurement Methods. In Cho et al. (2013)'s study, measurements were made with the lift-off test used in direct measurement using a small capacity load cell, EM sensor method and vibration method on the same cable on the Hwamyung Bridge in Korean. During these measurements, the bridge was under construction.

It was in the second tensioning phase after the key segment installation. During the second tensioning, the varying tensions of the two cables were measured directly with the lift-off test. Variable responses were measured simultaneously using accelerometers and EM sensors. The aim of this study was to understand the advantages and disadvantages of real-scale structures in measurement performance. After measuring the variable responses with two methods, they were compared with the directly measured responses obtained from lift-off test.

In the lift-off test, it is a mechanical method to measure the tension on a material. In this process, a small-scale load cell, a hydraulic jack, and a displacement meter are used. It is widely used for measuring on a single cable or a group of strands. This system is generally used to measure anchored structures, post-tensioning structures and multi-strand (MS) cables. The strands at the end of a cable are fixed to the main structure and compressed into the anchorage block. Meanwhile, a load cell and hydraulic jack are placed next to the wedge. As the displacement is measured with the inserted displacement gauge, the strand is pulled slowly with increasing jacking force. With these sensors, the force-displacement graph is calculated (Zarbaf et al., 2018).

While the specified force is transferred to the cable, the jacking force of the strands coming out of the wedge is very steep. As soon as the jacking force reaches the critical force that the wedge can hold, the wedge lifts the anchorage block upwards. The strand resists this jacking force along its entire length. Although the force does not increase that much, the displacement in the strand increases more than in the previous interval. The force-displacement graph slope reduces. For this reason, the force-displacement relationship can be represented by two linear lines. The intersection of these two lines is considered the cable tension. Since the installation of each sensor are very time-consuming and application of this method are expensive process, the lift-off test for a group of strands is performed for a few randomly selected strands. When calculating the tension on MS-type cables, the average value of tension across these few strands is found and multiplied by the total number of stands. This is the general procedure of the lift-off test (Cho et al. 2013).

Although the lift-off test is a simple test, it requires a load cell, a hydraulic jack, a displacement sensor, and a data acquisition (DAQ) system to collect data from these sensors. These sensors and measuring system are very expensive to install. In addition, at least three people are needed to install the sensors on each wire, support the strands and ensure that data is received from the measurement system during the installation operations. After the cables are anchored, this workload causes this direct measurement system to be inspected only after extreme events that could damage the cables. A load cell under a consistent load has low durability. This is another obstacle to the continuous implementation of this system (Cho et al. 2013).

When the results were examined, the lift-off test results in the Ironton-Russel Bridge compared with accelerometers and the results in the Hwamyung bridge compared with EM sensors and accelerometers gave consistent results for both evaluation. That is, the lift test could be a reliable method to determine the tension in the cables of the bridges (Cho et al. 2013; Zarbaf et al., 2018).

Another method used in direct measurement is fiber Bragg grid (FBG) sensors. This method has several advantages in small size, resistance to electromagnetic noise, light weight, integration into DAQ system, and long signal transmission distance. However, it is not suitable for direct monitoring of the cable tension of completed bridges by changing the anchorage structure of the bridge. Changing the structure of the anchor cable in bridges under operation disrupts the original structure of the bridge. For this reason, an FBG sensor is often placed at the end of the anchorage parts of the cables during the bridge construction. It would not be convenient to disconnect the cables to install an FBG sensor when construction is completed (Hu et al., 2017).

In the study of Zheng et al. (2018), FBG sensors were placed to the cable by using the embedding method. The measurability and reliability of the built-in FBG method were investigated. FBGs were joined with steel wire by structural adhesive. It had been investigated whether FBGs bonded with adhesive and steel wire could be used in bridge monitoring. Loading and unloading cyclic testing and fatigue test

cable tension were conducted. The relationship with the variables between wavelength and loading was investigated. The fatigue test revealed a small decrease in wavelength at the same load level over 200 million fatigue cycles. The load-displacement and wavelength-load graphs obtained from the experimental results showed that FBGs are of such measurability and reliability that they may find more applications in monitoring of the cable tension of bridges.

The last method in direct measurement is Elasto-magnetic (EM) vectors. The basic working principle of EM sensors is the magneto-elastic phenomenon of ferromagnetic materials. The magnetic properties of these materials vary from stress and temperature. When an external magnetic field is created around the ferromagnetic material, magnetic field flux is produced inside the material. Thus, it is possible to measure the tension of the material by knowing the relationship between magnetic permeability and voltage. This relationship is derived from the calibration process. EM sensors are usually created during the manufacturing process of cables or the construction phase of the bridge. In this process, the calibration is conducted by loading and unloading the cables while recording the temperature of the cable (Cappello et al., 2018).

The magnetic permeability depends on the temperature and voltage of the ferromagnetic material. It consists of two separate solenoids with different coils around the cable. The large outer coil generates a magnetic field to magnetize the wire where the EM sensor is placed. As the current in this primary coil is removed, the voltage in the sensing coil (inner coil) is induced by the magnetic field flux density remaining in the cable with the ferromagnetic material. The induced voltage is used when calculating the magnetic permeability. Since the field values of this cable are constant, the voltage depends on the cable tension and temperature (Cho et al., 2013).

Ferromagnetic material returns to zero magnetization, not when the magnetic field is removed, but when an opposite magnetic field is applied on the same scale. The hysteresis loop can describe the magnetic property of the material, which is defined

as magnetic permeability. Magnetic permeability is the ratio of the magnetic field flux density (B) produced in the ferromagnetic material to the external magnetic field strength (H) (Cho et al., 2013). The cable tension can be calculated using these values after the calibration process.

In the study of Cappello et al. (2018), the tension of the cables in the Adige Cable-Stayed Bridge was investigated using EM sensors. A low-cost method for installing and calibrating sensors had been explored. The cables were calibrated at two different times, one in the laboratory and one in the field. In the first experiment, force-voltage and voltage-temperature values were defined. Since the bridge was in use, the calibration process during the construction process could not be carried out. The bridge's tension cables were not allowed to be unloaded for sensor installation and calibration. For this reason, a sensor was placed around part of cable identical to the cables of the bridge under investigation. Then, tension was applied. The applied force and the estimated tension from the accelerometers were compared. As a result of the experiment, it had been shown that it did not depend on the sensor placement process, except for the offset between the load and the magnetic permeability. For this reason, it was stated that on-site installation and calibration were required to determine the offset. For non-destructive calibration of cables, cable tensions were determined by vibration method. The simplicity of installation and calibration of EM sensors in existing and new structures was demonstrated. It was shown as a suitable tool for measurement with its non-destructive and non-contact properties with its service life and corrosion resistance.

As a result, in all three methods, direct methods are generally used during construction phase to monitor the cable tensions because of the continuity problems and sensor placement costs (Kim et al., 2023).

1.1.1.2. Indirect Measurement Methods. The widely used indirect measurement methods are vibration method using accelerometers, wireless sensors, laser doppler technique, and vision-based measurement methods (Kim et al., 2023).

The vibration method with contact sensors, especially accelerometers, is generally used to monitor cable tensions of existing bridges, as it provides cost-effectiveness and great convenience compared to direct methods (Fang & Wang, 2012). In the indirect method, the cable tension is not measured directly. By measuring the dynamic responses of the cable, the tension is inversely calculated using data such as the natural frequency of each vibration mode and the cable characteristics.

In the vibration method using displacement, velocity, or acceleration response, the cable is considered as a beam to take into account the bending stiffness.

In this method, the dynamic properties of the cable such as the natural frequency and mode shape of the cable are obtained from the dynamic response of the cable with the accelerometers. Since the cable sag is not large, the frequencies in each mode are calculated and divided by the mode number. A regression line is drawn using the square of this value and the square of the corresponding mode number. In this way, besides measuring error, non-uniform cable sagging and cable bending stiffness errors are eliminated.

In Kangas et al. (2006)'s study, the Ulysses S. Grant Cable-stayed Bridge (U.S. Grant Bridge) investigated to reduce stopping motion by the Federal Highway Administration. In this study, the traditional vibration method had been tried to estimate the cable tension using accelerometers. Several experiments were conducted to determine the feasibility of this method. It was assumed that cable ties and surface sheath limited cable movement. Therefore, the sheath and inner wires were directly exposed to sagging caused by gravity. While this situation was less common with shorter cables, sagging in long cables created additional contact due to mass distribution. HDPE sheath was generally used to protect the cable strands. The use of sheath ensured that the cables are resistant to corrosion. Tests were conducted on the accuracy of measuring the response of the cable over the sheath. During these tests, the effect of sensor placement, thermal effects, wind excitation levels, cable slope and length on measurement were investigated. Appropriate signal processing techniques had been developed

to obtain the cable tension. Whether the measurement taken as a result of the tests was in-plane or out-of-plane did not affect the frequency and tension. The position of the sensor on the cable ensured measurement accuracy with a difference of less than 2%. The cable response obtained from the sheath could be used to accurately estimate the cable tension. The variation in wind load was not critical in estimating the tension accurately. Also, the effect of thermal expansion and contraction was minimal. As a result, the vibration method results were less costly and more applicable than the lift-off test.

In the study of Geier et al. (2006), it was investigated that the cable tensions could be determined by vibration test as an alternative to lift-off test with hydraulic jacks. The response of the Tulln Bridge under wind and traffic loads had been investigated. It had been shown that results estimated with the relationship between tension and frequency had similar accuracy to the lift-off test results. Results could be obtained with +-10% margin of error for short cables at high cable tensions. This method had been found to be a fast and reliable method for estimating the tension. Accuracies in the +-1% range could also be achieved by paying attention to the defined natural frequencies, bending stiffness, and boundary conditions. It was possible to determine the natural frequency of the cable by using a sensor with a low signal-to-noise ratio, which was fixed close to the anchorage of the cable, that is, close to the vibration node. Thus, the vibration response of the cable could be either in-plane or out-of-plane. Only in-plane modes were affected, as the boundary conditions, free vibration length, and anchorage could vary. These should also be considered when calculating cable tension and fatigue. It was emphasized that the estimated cable tensions could be used as a basis for the evaluation and maintenance of the structure.

As previously mentioned in Cho et al. (2013)'s study, Hwamyung Bridge was investigated using lift-off method, EM sensors, and vibration method. In the vibration method, the cable tension was estimated from the dynamic response of the cable by using the boundary conditions, cable geometry, and other mechanical properties of the cable. The vibration method results were compared with other methods. Dynamic

responses of cables were obtained by using both ambient vibration test (AVT) and forced vibration test (FVT) under traffic and wind loads. The power spectral densities of both tests in the frequency domain were compared. The amplitude of the results from the FVT was higher when the frequency values were at the same point. Peaks were more distinct. In addition, errors could be eliminated by linear regression by using a large number of natural frequencies of cables. In all three methods, data were taken while the bridge was at different construction stages. After the construction process of the bridge was completed, the tension values were compared with the design values. While the lift-off test and EM sensors results were measured with a difference of 2%, the difference in the vibration method was 3.5%. This comparison showed that all three methods made good cable tension estimations. Among the three methods, the vibration method was the least costly in terms of both equipment cost and labor. In summary, there was a tradeoff between measurement accuracy and cost.

In Benedettini and Gentile (2011)'s study, two dynamic tests of a suspended bridge were conducted, and a FEM were updated as a result of these tests. The first test was conducted using conventional accelerometers. In the second test, the displacement of the cables and natural frequency was obtained using the radar vibrometer.FEMs could not be performed with sufficient margin of error for natural frequency and mode shapes due to the uncertainties of both the material and the model. For this reason, AVT and OMA were considered ideal tools to eliminate these uncertainties and determine the dynamic properties of the structure. Data from the measurement result were analyzed using data-driven Stochastic Subspace Identification (SSI) and Enhanced Frequency Domain Decomposition (EFDD). In the theoretical part of this study, a three-dimensional FEM was established and compared with the dynamic properties measured from the analysis and estimated from the model. By changing the uncertain structural parameters and boundary conditions in the model, the natural frequency values were updated according to the measured values. In addition, the cable tensions were estimated from the natural frequency using the taut string model. The results from the EFDD and SSI and the estimated values from the model were compared using the Modal Assurance Criterion (MAC). This value is between 0 and

1. A value of 1 indicates perfect correlation. When the results were examined, the frequencies in the range of 0-10 Hz for both methods were compatible. There was a significant correlation between the experimental results and the test scenarios where the boundary conditions were changed, and the model was updated according to these results.

In Sun et al. (2017)'s study, the applications of SHM for long span bridges were investigated with a specific problem focus for two cases. In the first case, SHM data was used to send an alarm in the event of ship collision and to evaluate the overall condition of a suspension bridge. Modal data were analyzed by ERA method, and it was shown that there was no specific change due to collision. In another case, the effect of the expansion joint problem on the performance of the bridge was observed by measuring the beam end displacement. In this scenario, the cumulative displacement reflected the traffic volume and damper failure, which was the optimum value for the maintenance of the expansion joints. Finally, the performance of tuned mass dampers was investigated using beam vibrations under wind load.

Golden Gate Suspension Bridge (Abdel-Ghaffar & Scanlan, 1985), Bosporus Suspension Bridge (Brownjohn et al, 1989), Deer Isle Suspension Bridge (Kumarasena et al., 1989), Quincy Bayview Cable-Stayed Bridge (Wilson & Gravelle, 1991)), Kap Shui Mun Cable-Stayed Bridge (Chang et al., 2001), Tsing Ma Suspension Bridge (Xu et al., 1997), Maysville Cable-Stayed Bridge (Cunha et al., 2001), Roebling Suspension Bridge (Ren et al., 2004), Humber Suspension Bridge (Brownjohn et al., 2010), Hakucho Suspension Bridge (Siringoringo & Fujino, 2008), Seohae Cable-Stayed Bridge (Kim & Park, 2007), and Qingzhou Cable-Stayed Bridge (Ren et al., 2005) are other bridges for which vibration analysis has been carried out using acceleration sensors.

The installation of sensors in the vibration method are more economical than other methods. However, in bridges with a large number of cables, its application may be demanding, and high labor force required. Because these sensors take time to install, and each sensor needs to be connected to the DAQ system, wireless sensors had

been developed to solve this problem and to measure cable response more efficiently. The use of these sensors provides convenience in field tests due to their flexibility of use and low installation cost (Abdulkarem et al., 2020).

In Yu et al. (2014)'s study, the Hualu Cable-Stayed Bridge was investigated according to the vibration method with wireless sensors to estimate cable tensions. The accuracy of the wireless monitoring system had been investigated with the bridge model in the laboratory and the full-scale bridge in the field. From the field test results, the design values of the reference cables and the embedded lift-off tests were compared with the wireless monitoring system. The relative error was within 0.5%. Therefore, cable tensions could be adequately predicted with the wireless measurement system. Adjustment and maintenance in wired systems was difficult and costly due to the inflexibility of the system. Thanks to the wireless monitoring system, a very convenient, fast, reliable, and stable method was offered in terms of installation and removal by avoiding cost and intensive labor, overcoming the difficulty of placing cables in long-span bridges. In addition, it provided ease of application in emergency situations that require rapid detection.

In Siringoringo et al. (2022)'s study, wireless sensors were used as a continuous seismic monitoring system of Shin-Nakagawa Bridge, which is a cable-stayed bridge with inverted Y-shaped single pylon and 530-metre single-plane steel box girder . Some insulation bearings were partially damaged in the 2011 Tohoku Earthquake. For this reason, 26 wireless sensors were installed on the piers, the main pylon, the beams, and the deck. High-speed concurrent flooding technique (CFT) was used to transfer data of wireless sensors simultaneously. The technique had contributed to the creation of a highly efficient sensor network. Seismic responses were analyzed using the monitoring system and seismic movements were considered in the structural assessment. Structural responses of 63 earthquakes were recorded in 45 months. The ground sensors were compared with the available seismograph nearby and a good correlation was obtained. This demonstrated the reliability and accuracy of the system. The modal parameters of the bridge were defined using Multireference System Realization Algorithm (M-ERA)

and System Realization using Information Matrix (SRIM) with the major earthquake data as the multi-input and multi-output time domain system identification. Also, the decoupling effect of the beam responses and the high-frequency filtering effect were observed. The aim of the study was to record and explain seismic monitoring data, to investigate the response of the structure, and to evaluate the performance of seismically isolated bearings. When examined in terms of cost, the initial installation cost for semi-permanent monitoring systems was approximately 20% of conventional sensors. This showed that wireless sensors make more sense in relatively shorter time monitoring.

In Huynh et al. (2016)'s study, Hwamyung Cable-Stayed Bridge was repeatedly exposed to typhoons. Wireless sensors collected data from decks, pylon, and cables. During the period when the monitoring system was active, two typhoons occurred one after the other. Using data from a few sensors that survived these two typhoons, the wind-induced variations of the dynamic responses of the structure under these events were investigated using the SSI method and the short-term Fourier transform. Finally, the structural performance of the bridge was evaluated under various wind loads. The changes in the dynamic properties of the bridge due to the typhoon were translated into changes in the stiffness or flexibility of the bridge. That is, the relationship between wind speed and the structural flexibility of the pylon and deck of the bridge was investigated by determining the modal properties from their static and non-stationary responses. It had been proven that as the wind speed increased, the pylon stiffness decreased. That is, there was an increase in the natural frequency.

Although wireless sensors have flexibility and low installation costs, physical access to the structure is required for installing the sensors. In addition, there may be some problems in data transfer and traffic control. Therefore, non-contact methods that do not require physical contact between the sensor and the monitored parts had been investigated. Non-contact methods help solve some of the problems in contact methods. Frequently used non-contact methods are Laser Doppler technique and vision-based measurements (Kim et al. 2023). The use of a laser Doppler vibrometer is relatively more accurate in measuring the dynamic response. However, it is less

economical than other measurement methods (Chen & Petro, 2005).

In Kim et al. (2012)'s study, the cable tensions of Incheon Bridge was measured at a distance using a portable laser vibrometer. In addition, a computer program had been developed that calculates the cable tension simultaneously with the laser vibrometer data. The accuracy and reliability of the laser vibrometer system were investigated by comparing the results with the accelerometers. Non-contact measurements using a laser vibrometer gave reliable values. The maximum discrepancy with conventional accelerometers was 5%. It had also been proven that error correction work, geometric control of cables, calibration of jacking forces and calculation of cable tension could be done using this method.

In the study of Cunha and Caetano (1999), the responses of the Vasco Da Gama Cable-Stayed Bridge were measured during dynamic tests with the laser system, avoiding direct contact with the structure. The simplicity and accuracy of this optical method compared to conventional methods was demonstrated. In this study, bridges were investigated using both experimental and numerical approaches due to the seismic risk and aerodynamic instability of the region. In terms of these behaviors, it was aimed to determine the modal parameters of the bridge and update the FEM. Firstly, AVT was carried out to determine the natural frequency and mode shapes. Afterwards, to determine the modal damping factors, a free vibration test was carried out with a 60-tonne mass that was suddenly left eccentrically on the deck. Afterwards, the cable tensions were estimated under both the ambient vibration test and the free vibration test. In addition, DAFs were investigated under different traffic loads at different speeds in different lanes. The test results revealed that the laser vibrometer method provided advantages in terms of accessibility and flexibility, and provides a high level of accuracy, especially in the determination of natural frequencies and cable tensions.

In the methods using laser Doppler vibrometer, the accuracy of the dynamic responses and dynamic properties of the cable are relatively higher. However, it is less

economical than other measurement methods (Nassif et al., 2005). Another indirect method is vision-based monitoring using digital or industrial cameras. The advantage of this method is that the dynamic response of multiple points of a structure can be measured using a single camera at the same time. In addition, low cost and simple operation are among the other advantages. It provides convenience and accessibility as measurements can be taken using a digital camcorder or digital camera and tripod when conducting outdoor testing on the vision-based monitoring system. Since these advantages can be an alternative to traditional contact sensors, many studies have been carried out in many structures (Kim et al., 2013).

In Xu et al. (2018)'s study, multi-point displacement of the Baker Cable-Stayed Bridge with a consumer-grade camera was tracked with a low-cost, contactless vision-based monitoring system. Measurements were taken from multiple points simultaneously using a wide-angle lens. It also provided easy installation and removal. Deck displacement and cable vibration were measured under pedestrian loads with a special technique. In the analysis results, the displacement of a few centimeters due to the loads was measured. The natural frequencies of the bridge deck were calculated under varying loads and cable tension were estimated. In the laboratory experiments, the acceleration data from conventional accelerometers and the displacement data from the vision-based monitoring system were converted into velocity and compared. In the vision-based monitoring system, the analysis depended on the distance between the camera and the measurement point, the size information of the measured target, the internal parameters of the camera and the dispersion of the target tracking system in the image. Camera calibration, projection and validation should be considered to eliminate the distortion due to the lens and measurement distance. In addition, camera movement during measurement, occlusion in front of the recording target and blurring from raindrops affected the measurement. The measurement is also affected by turbulence and atmospheric refraction. Meteorological quality was essential for a solid measurement. However, when compared to traditional methods, the vision-based monitoring system gave consistent and accurate results.

In Feng and Feng (2017)'s study, a vision-based monitoring system was used as a cost-effective SHM system. First of all, the developed method was applied on a simple supported beam structure in the laboratory. The results showed the high accuracy of the vision-based monitoring system with displacement measurements. Good compatibility of natural frequencies and mode shapes from a single camera with data from multiple accelerometers had been demonstrated. At the same time, the scaling factor, the relationship between measurement resolution and field of view or measurement points, and the effect of tilt angles for camera measurement were investigated. Afterwards, real-time and multi-point measurement testing using a vision-based monitoring system was carried out on the Manhattan Suspension Bridge during train passing. It was aimed to demonstrate the usefulness of displacement measurement for modal analysis and structural damage detection. In cases where the camera optical lens was not vertical, the calibration method had been applied. In addition, scaling factor was applied to convert pixel-level displacement to physical displacement and compared with the displacement sensors. It gave consistent results for low angles.

In Lee et al. (2022)'s study, a vision-based monitoring system was implemented on the Cheonsa Cable-Stayed Bridge. During the measurements, the camera movement should be parallel to the camera plane while measuring the cable displacement. This limited the points where the camera was installed for measurement. To overcome this limitation, a new vision-based displacement measurement method with side view camera had been investigated. In this method, first the camera projection matrix was estimated. Project error occurred because camera recording could be taken from different fields of view. Then, the picture coordinates of the cable in each frame were determined. Then, using these data, the results of the cable displacement in the global coordinate were obtained. Simulation-based validation testing, laboratory-scale validation testing, and field validation testing were conducted to evaluate the performance of this method. Laboratory-scale testing showed that these tests could be conducted in a physical environment. Then, it had been shown that the cable displacement could be found with the side view camera. The measurement results from the side view, with and without this method, were compared with the results from the front view. Using

the specified method reduced its discrepancy in error to very low levels.

In Feng et al. (2015)'s study, a remote non-contact vision-based monitoring sensor system for structural displacement measurement was compared with a conventional displacement sensor. A template matching algorithm, called upsampled cross-correlation (UCC), was developed using the Fourier transform. It was intended to calculate real-time displacement from recorded video images. In order to increase the sub-pixel resolution and increase the accuracy, the sampling factor was determined. Thus, structural vibrations smaller than 1 mm could be measured precisely. A laboratory test was conducted to determine the performance of the method. Low-contrast natural targets such as bolts and salmon and high-contrast artificial targets were tracked to measure displacement in the vision-based monitoring system. In the shaking table test, displacement in all floors of the frame structure was measured using four laser displacement sensors, while it was measured with a single camera in the vision-based monitoring system. A satisfactory agreement was obtained between the vision-based monitoring and laser displacement sensors results. Then, field tests were conducted on a footbridge and a railway bridge. The results from the vision-based monitoring test were compared with laser displacement sensors in both in the time and frequency domain. The advantages of vision-based monitoring system are ease of use, low cost, and ease of taking measurements from any desired point of the structure. On the other hand, problems that caused errors such as camera vibration and heat blur could be stated as disadvantages.

In the study of Kim and Kim (2013), the cable tensions of the Gwangan Suspension Bridge were tried to be estimated using digital image processing. In the vision-based system, digital images could be obtained in two dimensions using a portable digital camcorder. DIC technique and the image transform function were used to calculate subpixels and to verify geometric distortion between deformed and undeformed frames. In addition, a fixed point was determined in the photo frame without using any extra sensors to eliminate camera movement and wind effect. According to this fixed point, the movement of the camera support was also eliminated. Also, it increased

cable recognition rate. In this way, the dynamic responses of the cables and the resolution of natural frequencies could be improved. In addition, the dynamic characteristics of the cable could be estimated using only the properties of the cable without placing any targets. In order to test the accuracy of the method, the accelerometer results under ambient vibration were compared. Taking measurements using a single portable camera was more economical than other methods to obtain the dynamic response and natural frequencies of all the cables of the bridge. However, image distortion may occur in foggy and rainy weather, night measurements and scenarios where the backlight is insufficient. To overcome this situation, image filter enhancement techniques such as spatial and frequency domain image enhancement and image restoration could be used.

In the study of Kim et al. (2020), the Namhae Suspension Bridge was analyzed using a vision-based monitoring system. The natural frequencies of the cables were determined from the dynamic responses and the geometric properties of the cables and then, the cable tensions were estimated. In order to compare the accuracy of the vision-based back analysis method, AVTs were conducted on the bridge and compared with these values. It was aimed to minimize the difference between the cable tensions by comparing the natural frequencies of the FE analysis of the suspension cables with the calculated natural frequencies. It had been shown that low-order natural frequencies were useful in reliable tension estimation in the back analysis method in the vision-based system. First of all, the recorded image files were converted to JPEG files in order to calculate the variation of the cable response with time. C=5 Laplacian was applied to define the control points by determining the detailed sections of the cable sections in each frame. The first frame, which was the reference image, was determined as a control point. To adjust the region of interest (ROI) window, the window size, which is the correlation size of the square, was determined. The zero-normalized cross-correlation was used to determine the optimal match point where the displacement was located in the ROI window. In addition, subpixels were calculated using the quadratic displacement function. Cable dynamic response was found from the displacement of each frame in pixels with respect to the reference point. From this displacement plot, the power spectral densities (PSDs) were calculated, and the natural frequencies of

each cable were found. It was shown that there is less than 3% difference between the vision-based monitoring system and the accelerometers. This showed that the vision-based monitoring method was a viable and economical method.

Yan et al. (2021) study suggested using a DIC-based method for non-contact measurement of the dynamic displacement time history of cables on the Fengguang Bridge, a real arch bridge. The natural frequencies and mode shapes of the cable were determined by frequency domain decomposition (FDD) technique from the displacement time history. It was aimed to obtain the cable tensions from the cable mode shapes by using the stretched pin-pin cable model. To test the accuracy of the methodology, a laboratory-scale and site tests were conducted. With the DIC technique, the dynamic displacement was determined by tracking the surface properties on the metal blocks along the cable. Metal blocks in the laboratory test and LED lamps in the field test as artificial targets improved the measurement results. The results showed the accuracy. Yan et al. (2019) investigated the effect of the boundary conditions. It was the use of mode shapes derived from non-contact measurement system and DIC technique to determine the cable tensions with complex boundary conditions. First, ROI was determined using a high-speed video camera and computer processing system. Subpixel registration algorithms were applied to target points in ROI window to improve dynamic displacement time history. Then, FDD was used to determine the natural frequency of the cable and the associated mode shapes. To compare the accuracy of the tensions, they were compared with the accelerometer results. A relative error is calculated as 5.4%. It had been observed that the relative errors for high modes were higher than for low modes. One of the reasons for this was that the DIC technique causes uncertainty at higher modes. It had been stated that the relative error may be due to the uncertainty in determining the effective length. In the calculations, it was stated that the third-order modes were more efficient than the first and second modes in extracting the effective length of the cable.

In Feng and Feng (2018)'s study, the experiments using a vision-based monitoring system determining the dynamic properties of structures was summarized. The

advantages of this system such as ease of installation and operation, low cost and the ability to monitor any point on the structure were stated. The general working principles of the vision-based monitoring system and comparison with the different methods were summarized. In addition, different template matching techniques for target tracking, results in tracking natural and artificial targets, determination of calibration factors for converting pixel displacement from images to physical displacement and coordinate transformation techniques were summarized. Also, 2-dimensional (2D) and 3-dimensional (3D) measurements were summarized. Then, the vision-based monitoring results of laboratory experiments and field tests on buildings, wind turbines, bridges and mechanical structures were examined. Measurement errors such as heat turbidity and various noise sources and methods that could be applied to reduce these errors were discussed. Finally, determination of structural modal properties, updating of FEMs, determination of cable tensions and determination of structural damages were discussed. It had been emphasized that new studies could be carried out with multiple cameras that could work in sync to examine different parts of large-sized structures such as long span bridges, wind turbines and high-rise buildings. The vision-based monitoring systems could be used as real-time long-term SHM systems.

In Lydon et al. (2019)'s study, low-cost displacement measurement was performed with a non-contact vision-based monitoring system. By measuring displacement responses, structural changes and service behavior could be followed under live loads. Vision-based systems had advantages over traditional displacement measurement systems and Global Positioning System (GPS) systems in terms of ease of installation, accessibility to the structure, and accuracy. It also reduced personal risks at installation of sensors. A model matching based displacement algorithm had been developed by using a high resolution, durable commercial action camera and telescopic lens instead of professional cameras. The displacement performance of the vision-based monitoring system in the laboratory study was compared and verified with the the fiber optic displacement sensor results. Then, the method was tested under live loads on the Peace Bridge and the western opening of the Governors Bridge. The vision-based results were compared with the displacements calculated from accelerometers. Measurements were

taken at night and during the Halloween event under large pedestrian loads from the Peace Bridge. Poor lighting and high viewing distance were taken into account. A root mean square error (RMSE) of 0.03 mm was obtained according to field measurements. Environmental effects such as camera movement were eliminated. In addition, in the field test, a fixed building in the distance was assumed as a fixed point and camera movement was eliminated.

In Du et al. (2020)'s study, a single or multi-point vision-based monitoring system was investigated to determine cable tensions using DIC and digital image processing (DIP) measurement methods. A digital single-lens reflex (DSLR) camera was used as a recording device. DIC had the advantage of recognition accuracy and matching, while DIP offered higher processing efficiency and better dynamic response performance. Two laboratory experiments involving single point and multi-point cable tension measurement were conducted with the combination of two methods. The minimum deviation was 0.24%, while the maximum deviation was 2.69% in single point cable tension measurement. In multi-point cable measurement, the measurement deviation was 3.05. To investigate the accuracy of the method, it was compared with accelerometers and the relative deviation between the frequency domain results was calculated as 5% on the Guanhe Cable-Stayed Bridge. In addition, the natural frequencies were compared with numerical simulations. In addition to its low cost, it helped to overcome the cable installation work and difficulties in setting up the DAQ system with the high consistency.

In Ma et al. (2022)'s study, a method was developed to estimate cable tensions using an integrated vision and inertia measurement system (VIS) by determining a reference point. The movement of the VIS was also taken into account during the measurement. First, the cable displacement was estimated using a contour-based algorithm. Then, the motion of the reference point of the VIS was determined with the inertial measurement unit (IMU) sensor, and the error in the displacement measurement was corrected. Using this corrected displacement, the cable tensions was estimated by taut string theory. To test the accuracy of this method, a laboratory

test was conducted on a full-scale pedestrian bridge. It was then validated in field testing on a single pylon cable-stayed footbridge. Then, these results were compared with accelerometer measurements and the difference was less than 1.3%. There were some limitations in this study. First, it was assumed that the background of the cable is non-woven. However, this assumption may be invalid in bad weather conditions. Secondly, the smartphone was used as the VIS. However, misalignment with the IMU sensor and the optical image stabilization (OIS) system in the phone camera could cause additional errors in camera motion correction. To overcome this problem, a VIS could be developed without using any OIS system by attaching the IMU sensor to the center of gravity of the vision camera. In addition, the cable and VIS measured as the target were limited to 6 meters. It may be insufficient for large-scale bridges.

In the study of Tian et al. (2021), unmanned aerial vehicle (UAV)-based non-contact vision-based cable tension estimation was investigated. First of all, it was aimed to capture the images of the dynamic response of the cables from a certain distance. The dynamic properties of the cables were determined by analyzing the captured image. A line segment detector (LSD) was used to detect cable boundaries. A different line matching algorithm was proposed for the calculation of dynamic displacement. The fundamental frequency of the video captured by the UAV was difficult to find. The relative displacement of the cable the adjacent high frequency difference. It was useful in extracting the effect of UAV motion on cable vibration frequency and increasing the size of the Fourier spectrum. The response of an inclined cable was measured to calculate the accuracy of the proposed method in the laboratory. In addition, the method was validated in a long span Nansha Suspension Bridge. Finally, the cable responses of the UAV were compared with response accelerometers and fixed cameras. The accuracy and robustness of UAV technology was demonstrated. This method was suitable for calculating cable tension in high vibration and windless weather conditions. Also, using the IMU could be more efficient to eliminate UAV motion in future studies.

In the study of Jeon et al. (2022), it was stated that the use of vision-based monitoring systems offered advantages in many respects, but there are two main problems

with the algorithms being implemented. The first was the manual determination of the ROI, and the other was the loss of feature of the following points when using tracking algorithms. A new method was proposed to overcome these two problems. The proposed method automatically selected the ROI by establishing a neural network and aims to prevent feature loss of the selected points using a modified Kanade-Lucas-Tomasi (Uni-KLT) algorithm. Automatic ROI selection network (Cable-ROI Net) achieved 89.6% success. In addition, Uni-KLT provided a higher level of tracking of cable displacement than conventional KLT. The method was tested on the Cheonsa Cable-Stayed Bridge. It gave high accuracy in automatically determining ROI in field tests and obtaining cable response more successfully in 30 minutes of measurement. It was stated that the developed method would benefit the development of traditional methods. The cable-to-ROI network allowed to automatically select and track all pixels containing the cable. In addition, Uni-KLT proposed a system to help track pixels with similar density. That is, the displacement of the cables could be estimated accurately and automatically.

1.2. Scope and Objectives

With the development of analysis technologies, material properties, and methods in the construction process, the number of bridges in which cables are used as the primary load carrying members is increasing worldwide. The deck of the bridge is supported by multiple cables and this load is transferred to the pylon via cables. Therefore, cables play an important role in carrying and transferring the load, and maintaining structural integrity (Kim et al., 2023). Cable tension is the most important factor in analyzing the integrity and safety of the structure. Deterioration in cable tensions due to fatigue and corrosion effects due to environmental conditions causes a decrease in cable tensions, which affects the performance of the entire structure. Such problems reduce the service life of the structure. Also, the change in support reactions can be detected and localized by cable tension changes (Bao et al. 2017; Yang et al., 2016). Therefore, monitoring of time-varying cable tensions is necessary (Camara et al., 2014).

In this study, two laboratory and two field tests were performed using vision-based monitoring system. Then, New Kömürhan Cable-Stayed Bridge located between Elazığ and Malatya was examined. Cable tensions were determined by lift-off test and vibration test with accelerometers, using the eight data sets obtained from the existing SHM system on the bridge. Using these two methods, the cable tensions of only 8 of the 42 cables was obtained. Afterwards, it was aimed to estimate all cable tensions from the video recordings using a vision-based monitoring system. By using the displacement response of vision-based monitoring results, the dynamic response of the cables were calculated and cable tensions were estimated with the vibration method. It was aimed to update the FEM with the estimated cable tension. The natural frequencies of the pylon and deck in the verified FEM were compared with 8 data sets. The aim of this study is to check the accuracy and applicability of cable estimation using a vision-based monitoring system and to measure the updateability of the FEM of the structure.

1.3. Thesis Outline

This thesis consists of four chapters. In the first chapter, general information about the background of SHM of infrastructures and bridges is given. Studies in the literature related to the calculation of cable tension with direct and indirect methods as contact and non-contact are summarized. Details and necessity of cable tension calculation and real-time SHM are given. In addition, the first chapter includes the scope and objectives of this the study.

In the second chapter, the details of the current SHM system on the New Kömürhan Cable-Stayed Bridge were given. Details of earthquakes that occurred at four different times were given. In this study, analyzes were conducted using data recorded during these four earthquakes and 3 hours before. It was explained how the cable tensions were calculated using these 8 data sets. Details about lift-off test, vibration method using accelerometers and vision-based monitoring system were given. 2 Laboratory and 2 field experiments were carried out to evaluate the performance of the vision-based monitoring system.

In the third chapter, the project details of the New Kömürhan Bridge were given. Section details of the FEM and the project details of the bridge were shown. Then, lift-off test results acceleration data in x- and y-directions for eight data sets were given for 8 cables. Natural frequencies were calculated for each mode from the acceleration data. Then, the cable tensions were estimated using the vibration method. Afterwards, displacement responses using a vision-based monitoring system were found from video recordings. Then, natural frequencies were calculated for each mode. Using the vibration method, the cable tensions were estimated for each mode. Cable tensions calculated by all three methods were compared. The FEM was updated according to each cable tension obtained using the vision-based monitoring system. Then, the natural frequencies of the pylon and deck of the FEM and the eight data sets were compared.

In the fourth chapter, a brief summary of this study is given. Concluding findings in this thesis are stated. In addition, recommendations on this subject for future studies are given.

2. METHODOLOGY

New Kömürhan Cable-Stayed Bridge is monitored regularly throughout the year with the SHM system. There are GPS sensors, 2D and 3D-accelerometers, cable force sensors, strain gauges on the reinforced concrete part of the pylon and the steel part of the deck. There is also a monitoring master station where data flow is provided. The data received from these sensors were taken from the General Directorate of Highways for earthquakes that occurred at 4 different times and 3 hours before these earthquakes, with an average of twenty minutes. First of all, the tensions of eight cables was calculated by the lift-off method using force sensors. In addition, the natural frequencies of the cables were calculated using the acceleration response in x- and y-directions. Cable tensions were estimated for eight data sets from the natural frequencies. However, in both methods, the cable tension of only 8 out of 42 cables could be obtained. A vision-based monitoring system was used to estimate the cable tensions of all cables. The natural frequencies of each cable were calculated from the displacement data using the vision-based monitoring system. Cable tensions were estimated using the vibration method from these natural frequencies. The cable tensions of three methods were compared. The FEM was then updated according to these cable tensions. The natural frequency for the pylon and deck of the verified FEM were compared with the existing SHM results.

2.1. Definition of Monitoring Systems

New Kömürhan Cable-Stayed Bridge has a SHM system assessed by General Director of Highways of Turkey. The purpose of the system is the continuous monitoring of the static and dynamic parameters of the main structural components. Sensors are selected according to the monitoring specification within the appropriate accuracy and measurement ranges. A data collection unit has been designed to place the surveillance system in a suitable section for easy access to data collection. Cable force sensors monitor cable tensions at all times simultaneously. It is also used to initiate re-tensioning

in cases such as the deterioration of the balance of the bridge as a result of expansion effects and earthquakes. It has the capacity to give information about the remaining cable life. In addition, monitoring and characterizing the bridge simultaneously during earthquake and storm help in making decisions about the type of actions after these events. In addition to accelerometers, there are devices that provide deformation measurement on reinforced concrete pylon and steel deck. There are also GPS sensors to calculate the exact position of the bridge based on 3D displacements. The monitoring system on the bridge is shown in Figure 2.1.

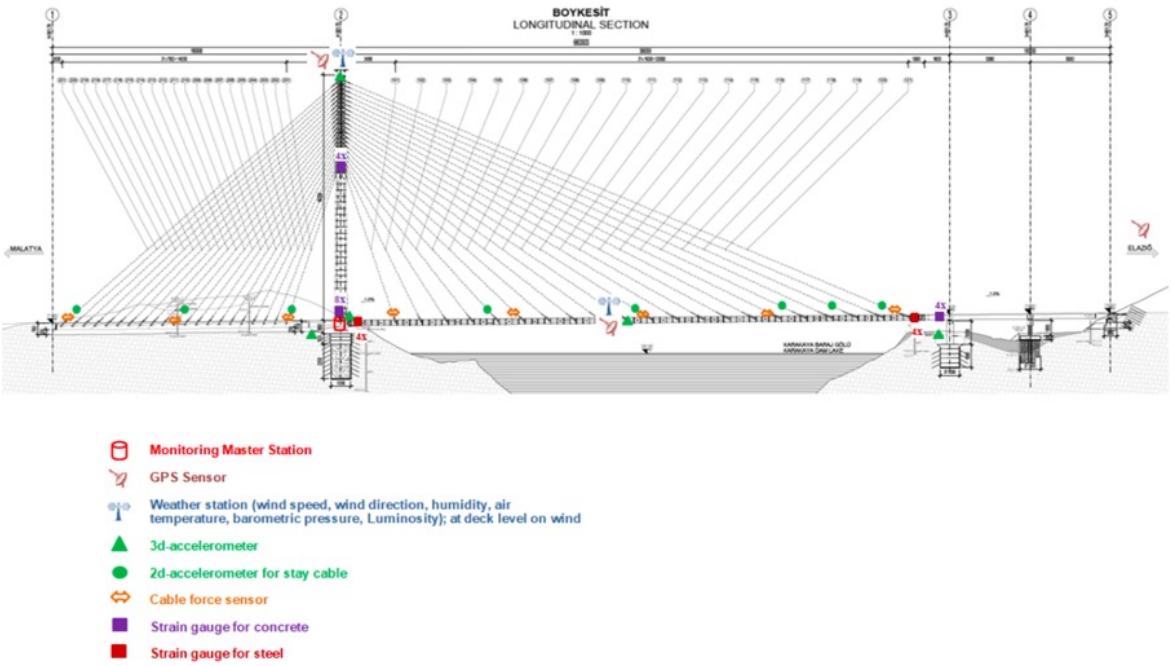


Figure 2.1. Existing SHM system of New Kömürhan Bridge.

The following accelerometers are included in the structural health monitoring system:

- 1 x 3D accelerometer on each shore
- 1 x 3D accelerometer on pylon at deck level
- 1 x 3D accelerometer on top of the pylon
- 2 x 3D accelerometers, both upstream and downstream in deck mid-span
- 8 x 2D accelerometers on selected stayed cables

Apart from accelerometers, strain sensors and GPS, there are also a wind and meteorological surveillance system to analyze the dynamic behavior of stay cables. All these sensors are designed to withstand harsh environmental conditions to avoid failures and to guarantee a long lifetime.

2.2. Definition of Earthquakes

Analysis was carried out using the force sensor and accelerometers on the bridge during earthquakes that occurred at four different times and 3 hours before the earthquakes. The location of the bridge, the epicenter of these four earthquakes and the coordinates of the station where the earthquake records were taken are shown in Figure 2.2.

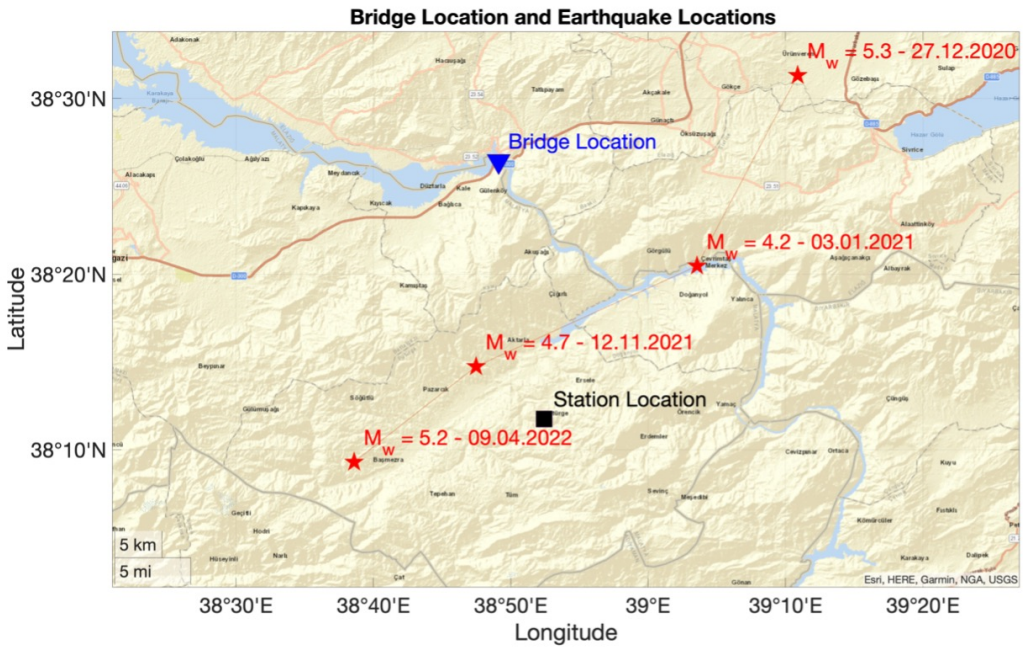


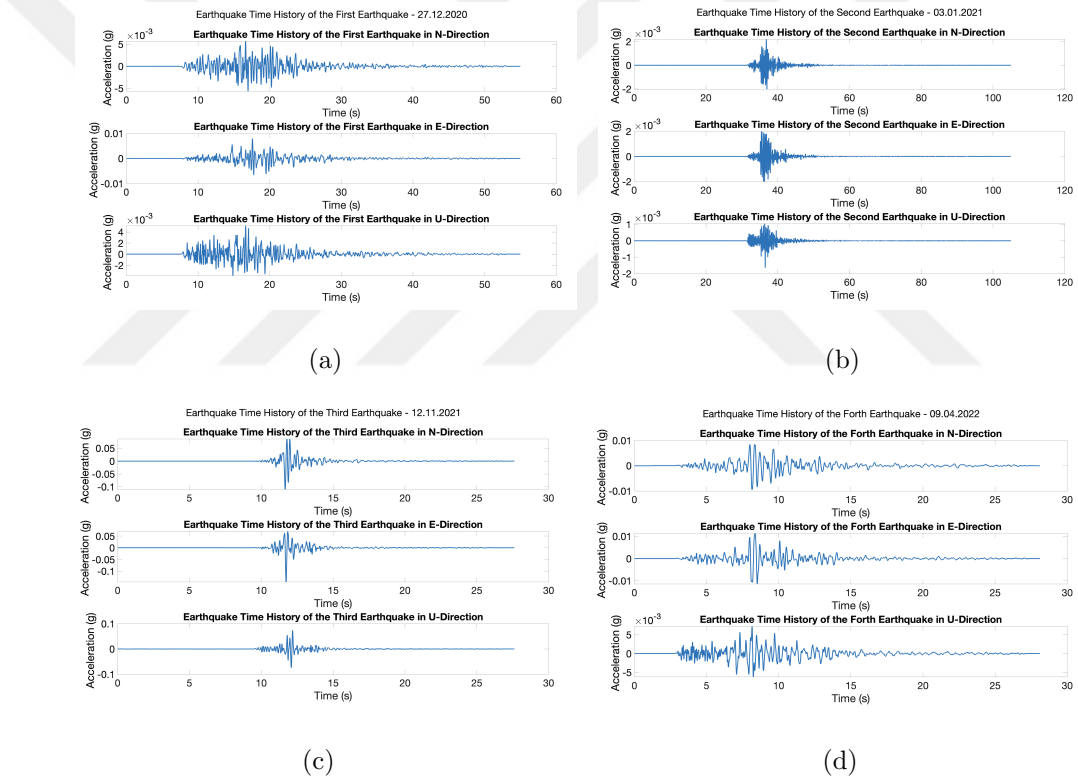
Figure 2.2. Bridge, station, and earthquake locations.

In the data received from AFAD (Disaster and Emergency Management Presidency of Turkey), the station code is "4408". The cable tensions on the bridge were calculated from these 8 data sets using the lift-off test and vibration test with accelerometers.The numbering, location, latitude and longitude, and magnitudes of earthquakes

are shown in Table 2.1.

Table 2.1. Earthquake numbering and details used in analysis.

	Date	**Mw**	**Latitude**	**Longitude**
1	27.12.2020	5.3	38.5218	39.1813
2	03.01.2021	4.2	38.3411	39.0593
3	12.11.2021	4.7	38.2458	38.7913
4	09.04.2022	5.2	38.1550	38.6433



(a) (b)

(c) (d)

Figure 2.3. Earthquake time history of (a) the first earthquake; (b) the second earthquake, (c) the third earthquake, (d) the forth earthquake.

For easier progress and understanding of the study, they will be numbered in chronological order. The acceleration graphs for station '4408' of the acceleration values of all four earthquakes in three directions are in Figure 2.3.

2.3. Cable Tension Calculations

Three different cable tension calculation methods are described below. These are lift-off test, vibration method using accelerometer and vision-based monitoring system.

2.3.1. Lift-off Test

As mentioned in the literature, the lift-off test is one of the most frequently used direct measurement methods. Lift-off testing uses a displacement sensor, a load cell, and a hydraulic jack to measure the tension of the strand inside the cable. This system is generally installed while the bridge is under construction. In this method, a load cell is placed on the strands inside the cable. The free end of the cable is pulled using a hydraulic jack (Cho et al., 2013). The pulling force obtained using the hydraulic jack is measured from the load cell. The displacement generated by the pulling force is measured using a displacement sensor. During the initial installation phase, when the pulling force of the hydraulic jack exceeds the rope tension, the wedge is lifted from the anchor block, which is fixed to the cable end (Zarbaf et al., 2018). Considering that the material property of each strand is elasto-plastic, if the displacement is in the linear range, the displacement is multiplied by the Modulus of Elasticity (E) and the tensile force is obtained. If lift occurs, the force remains constant at the point where the displacement gradient changes. This point is considered the tension of the wire. Using the force of each strand, the cable tension is calculated as

$$T = \frac{\sum_{i=1}^{n_s} T_i}{n_s} \times n. \tag{2.1}$$

In this method, the tension of a limited number of strands is measured. The n_s value in the equation represents the maximum number of measured strands. The T_i value is the tension value of each strand being measured. Using these two values, the average value of the tension of each strand is found. n is the total number of strands in the cable. To find the cable tension, the average tension is multiplied by the total number of strands (Fujiwara & Sakai, 2016).

2.3.2. Vibration Test

In stay cable bridges, as the cable is tensioned, a change in the natural frequency of each vibration mode is observed. When the applied force is known, natural frequencies of cables can be calculated from the characteristic properties of the cable (Fang & Wang, 2012). In the vibration method, the cable tension is calculated inversely by calculating the natural frequency in each vibration mode from the measured response in the cable and using the characteristics of the cable (Zui et al., 1996). Generally, when calculating the natural frequencies from the acceleration value in the frequency domain, displacement or velocity response can also be used since these will give the same results in the frequency domain. Strain sensor, acceleration sensor, laser displacement sensor and vision-based monitoring can be used to measure the cable response with displacement, velocity, and acceleration in time domain.

The vibration method emerged from a simple theory without considering the bending stiffness and the cable sag. In the later studies, they were carried out to increase the feasibility and accuracy by considering the cable sag and bending stiffness (Russell & Lardner, 1998). The least squares method is the most commonly used method for estimating the cable tension. As mentioned in the literature, the cable is considered as a beam to take into account the bending resistance of the cable. According to this assumption, the equation of motion of the cable is defined as

$$T\frac{\partial^2 \nu(x,t)}{\partial x^2} = \frac{w}{g}\frac{\partial^2 \nu(x,t)}{\partial t^2} + EI\frac{\partial^4 \nu(x,t)}{\partial x^4}. \tag{2.2}$$

In this equation, T is the tension of the cable in the longitudinal direction. $\partial v(x,t)$ indicates the displacement response of the cable in the vertical direction, x the coordinates in the longitudinal direction of the cable, and t the time. w is the unit weight of the cable and g is the gravitational acceleration. EI is the bending stiffness of the cable with respect to gravity. In theory, the bending stiffness of a real cable is assumed to vary with cable length, tension, and bending. However, according to the length of the cable, the bending stiffness of the cable is always constant (Fang & Wang, 2012). The boundary conditions at both ends of the cable as hinge boundary conditions are assumed as $v(0,t) = 0, v(l,t) = 0, v''(0,t) = 0, v''(l,t) = 0$.

Ignoring the axial vibration of the cable and assuming the boundary conditions, the equation can be written as

$$T = 4m^2_{\ell_e}\left(\frac{f_n}{n}\right)^2 - \frac{EI\pi^2}{\ell_e^2}n^2. \tag{2.3}$$

In this equation, m is its mass per unit length, and l_e is the effective length of the cable. f_n is the natural frequency of the cable with the nth order vibration mode. Cable tension can be estimated according to these variables and the bending stiffness of the cable. If the bending stiffness of the cable is supposed as small, the first part of the equation is used to estimate the cable tensions.

The vibration method is very useful as the cable tension is estimated by using each natural frequency of the cable. It can be used to correct both measurement errors and errors caused by sagging and non-linear bending stiffness of cables by using the frequency in each mode. Excluding the first mode where cable sag has the greatest effect, using the remaining natural frequencies, the average cable tension and corresponding equivalent cable bending stiffness can be calculated. Since the bending stiffness of the cable has a great influence on the vibration method, using the vibration method to estimate the tension of the short cables of suspension bridges may give incorrect results. In longer cables, the estimation of cable tensions will be more accurate, since the effect of the bending stiffness of the cables will be less (Kim et al., 2023).

The vibration method was firstly used to estimate the cable tension by using the eight acceleration responses of four earthquakes at different times from the accelerometers and the three hours before these earthquakes. By taking Fast Fourier Transform (FFT) of acceleration data, PSDs were obtained in the frequency domain. Peak values were determined and the natural frequency of the cables in each mode was found. Cable tensions were estimated using the vibration method from these natural frequencies and the characteristics of the cable.

Afterwards, the displacement response was found using the vision-based monitoring system from the video recording taken in the field. PSDs were obtained by taking the FFT of this displacement response. Peak values were determined and the natural

frequency of the cables in each mode was calculated. Using the vibration method, the cable tensions were estimated using natural frequencies and the characteristics of the cable.

Since changing the amplitude or taking derivatives/integrations in the time domain in acceleration data or displacement data does not change the location of the natural frequency peaks in the frequency domain, the natural frequency of each mode can be obtained by using acceleration or displacement response in pixel scale in both methods.

While cable tension was calculated in both accelerometer and vision-based monitoring systems, it was difficult to determine the effective vibration length in the vibration method. The uncertainty in the boundary conditions resulting from the restrictions and anchorage systems at both ends of the cables made this process even more challenging. Since the cables were anchored to both the pylon and the back span anchorage block on both sides, calculations were made assuming a fixed connection. The effects of prediction errors resulting from boundary conditions on the results and their detailed evaluation were beyond the scope of this study.

2.3.3. Vision-based Monitoring System

In the vision-based monitoring system, Nikon brand D750 model DSLR was used in 2 laboratory experiments, 2 field measurements and bridge measurements. During the recordings, the video images taken by the camera were digitized into 1920x1080 pixel images with a sampling rate of 60 frames per second (FPS). The DSLR had a Complementary Metal Oxide Semiconductor (CMOS)-type sensor. Each frame is in RGB24, which is an RGB format with 24 bits per pixel. The letters 'RGB' stand for Red, Green, and Blue. Each color channel is allocated 8 bits per pixel. The focal length of the optical lens could be adjusted to 50 mm – 200 mm with automatic or manual focusing.

The sensor has a global shutter that captures the entire image frame simultaneously. This system is the opposite of the rolling shutter system. Each image frame is recorded by scanning column by column or row by row in pixels in the rolling shutter system. The shutter system causes distortions when recording fast moving objects or objects where the vibration is important. Measurement results in rolling shutter recording need to be corrected. In addition, temporal aliasing is another important issue for vibration measurements. Considering that the natural frequency of tensioned cables in most bridge and stadium structures is below 10 Hz, a sampling rate of 50 FPS will be sufficient. This means that any frequency above 25 Hz at the sampling rate will be aliasing according to the Nyquist criterion. However, it can be said that measurements taken at 50 FPS can capture sufficient cable vibration components.

In the vision-based monitoring system, the ROI was first determined to reduce the computational load. In the first frame, this area selected from the video image was defined as the template. The template was followed in each successive image. Using the quadratic polynomial function, pixel positions were relocated, and subpixels were calculated. In this way, geometric distortion caused by deformation and displacement was corrected. In the first of the frames defined as subpixel, a row was determined in the template manually. The subpixels in this row for each frame were converted into a binary image using the intensity of light. The point where the edge point first starts for each frame was determined. The coordinate of this point was determined in each subsequent frame. This displacement was calculated in the time domain for each frame (Feng & Feng, 2017). No calibration or scale factor was applied to this displacement in pixels. The reason for this was that multiplying the displacement function by the scale factor did not change the location of the peaks in the frequency domain. For this reason, since cable natural frequencies were needed in the frequency domain to calculate the cable tensions, there is no need for an extra calculation.

PSDs were obtained by taking the FFT of this displacement function in pixels. The peak points of these values in the frequency domain represented the natural frequencies of the cable. Cable tensions were estimated using the natural frequency and

characteristic features of the cable in each mode, as specified in the vibration method.

2 laboratory and 2 field experiments were performed. The results and improvements during these experiments are given in Appendix A.

3. BRIDGE DETAILS AND RESULTS

In this section, project and cross-section details of the New Kömürhan Cable-Stayed Bridge were given. The FEM created according to the project details. Additionally, cable details were given. Afterwards, cable tensions were estimated using the lift-off test and vibration method from accelerometers from the 8 data sets. Video recording was taken from the bridge cables at a different time from these earthquakes. The natural frequencies of the cable were obtained by using video records with vision-based monitoring system. Cable tensions were estimated with the vibration method from the natural frequencies. While the tensions of 8 out of 42 cables were determined in the first two methods, the cable tensions of all cables on the bridge were estimated using the vision-based monitoring system. The FEM was updated using these cable tensions. The pylon and deck natural frequencies of verified FEM and eight data sets were compared.

3.1. New Kömürhan Bridge and Description

Since the second Kömürhan Bridge, which was built in 1986, is not suitable for the divided road geometry and does not comply with the earthquake regulations, it was decided to build the 3rd Kömürhan Bridge in 2010, which is also the subject of this study. The new bridge was placed to the south of the old bridge, considering the structure of the land, the road route and not disrupting the traffic during the construction. Also, the deck level was increased by 10 meters. It was constructed in 2021. This bridge, built at the 49th kilometer of the Malatya-Elazig highway, at the junction of the highway and the Euphrates River, is the only river crossing point of the Euphrates, together with the second bridge in this region. The bridge is located on the shortest route between Malatya and Elazig and therefore there is no alternative. Thus, the bridge is a strategically important structure in the region.

The design specifications are the general directorate of highways technical specification, Eurocode, the use of prestressed ropes as inclined suspension cables (CEB-FIP), recommendations for Cable stays (Setra, June 2002), AASHTO LRFD Bridge Design Specifications, AASHTO Guide Specifications for LRFD seismic bridge design and DLH earthquake regulation Annex-A.

It is 168.5 meters high. It is 660 meters long. The bridge consists of approaching viaduct, main span, and back span anchorage block, which are 100 meters, 380 meters, and 180 meters long, respectively. The bridge is different from the typical cable-stayed bridges in the world with its single inverted Y-shaped pylon and single span. The cylindrical and cubic compressive strength after 28 days of lean concrete is C16/20. The cylindrical and cubic compressive strength after 28 days of foundation of piers and pylon is C30/37. The cylindrical and cubic compressive strength after 28 days of pylon is C50/60.

The general view, cross-section detail of each part and, corresponding section in FEM are shown in between Figure 3.1-Figure 3.27. The section and material properties are also given below.



Figure 3.1. General view of New Kömürhan Bridge.

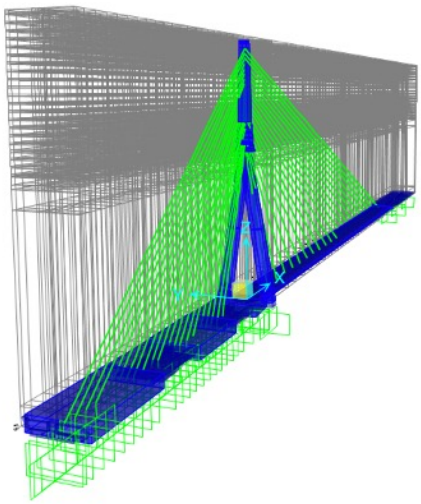


Figure 3.2. FEM of New Kömürhan Bridge.

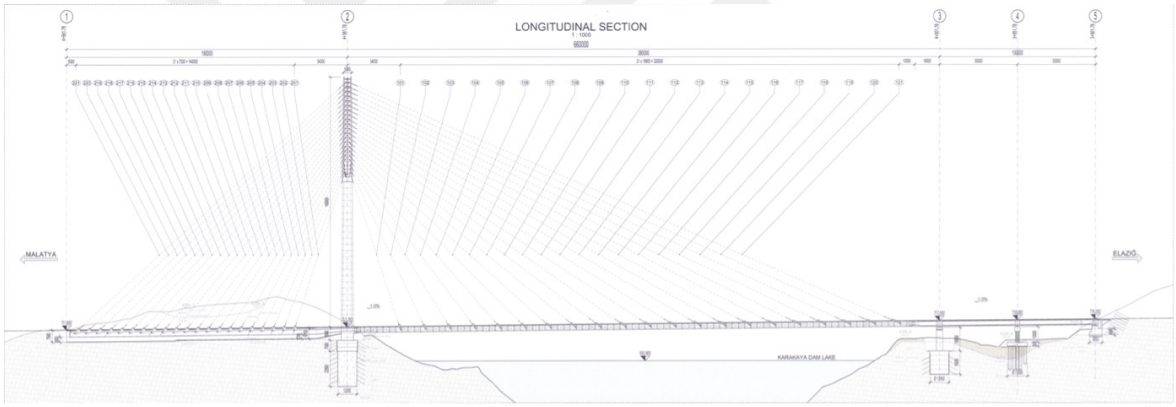


Figure 3.3. Longitudinal section of New Kömürhan Bridge.

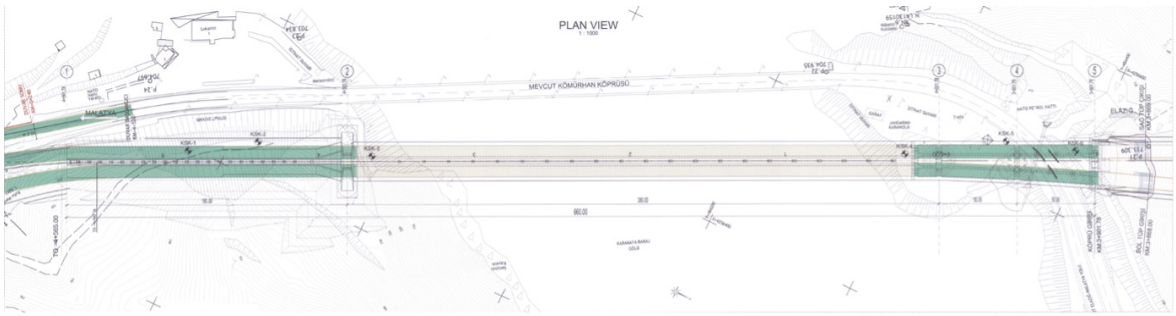


Figure 3.4. Plan view of New Kömürhan Bridge.

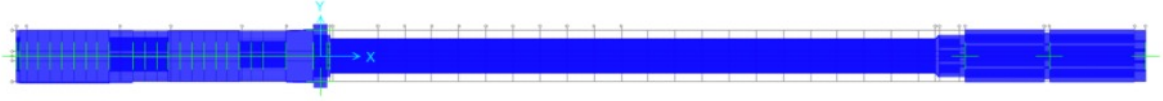
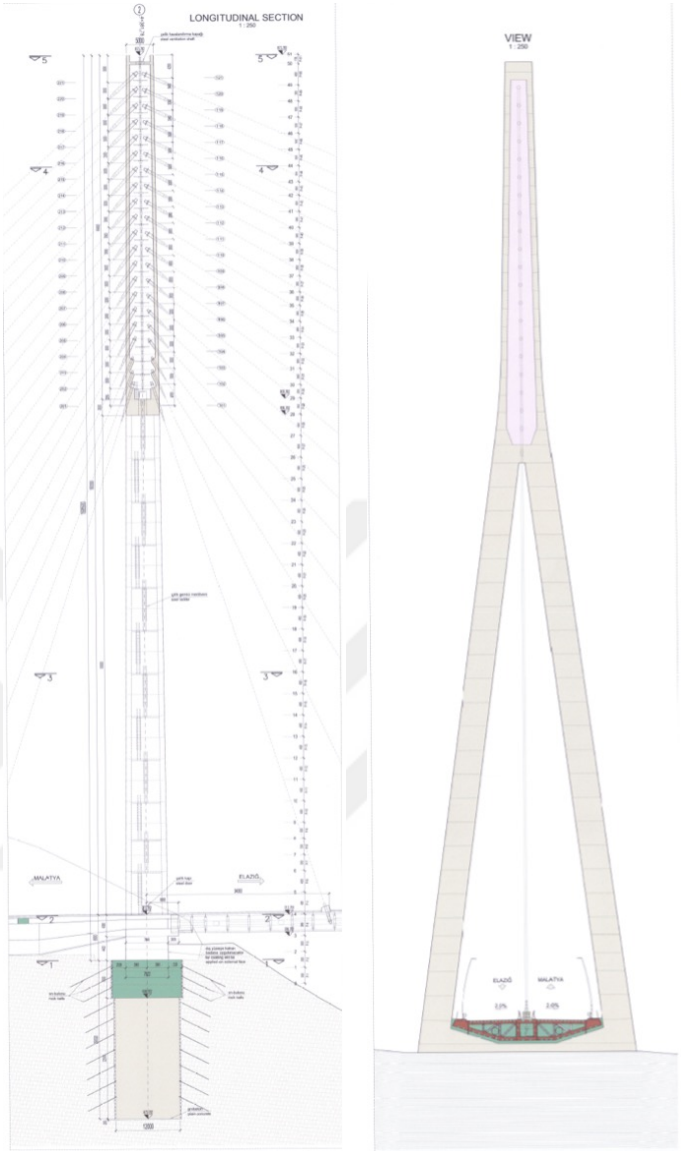


Figure 3.5. Plan view of FEM of New Kömürhan Bridge.



(a) (b)

Figure 3.6. Views of New Kömürhan Bridge: (a) Longitudinal section of the pylon, (b) view of the pylon.

21 cables are connected to the deck in the main span of the bridge in a single plane. These 21 cables, which are connected to a single pylon, are stabilized by the same number of cables anchored to the 180-meter-long back span anchorage block on the Malatya side. The cylindrical and cubic compressive strength after 28 days of back span anchorage block is C30/37.

The main span deck is orthotropic steel box girder with 2 traffic lanes in both directions in the main span. Its width is 23.9 meters. Its height is 3.6 meters. The steel grade is S355 J2 according to EN10025. The characteristic yielding strength of orthotropic steel deck is 355 MPa. Its modulus of elasticity (Young modulus) is 210 GPa. The linear thermal expansion coefficient is 12×10^{-6} $(1/^oC)$.

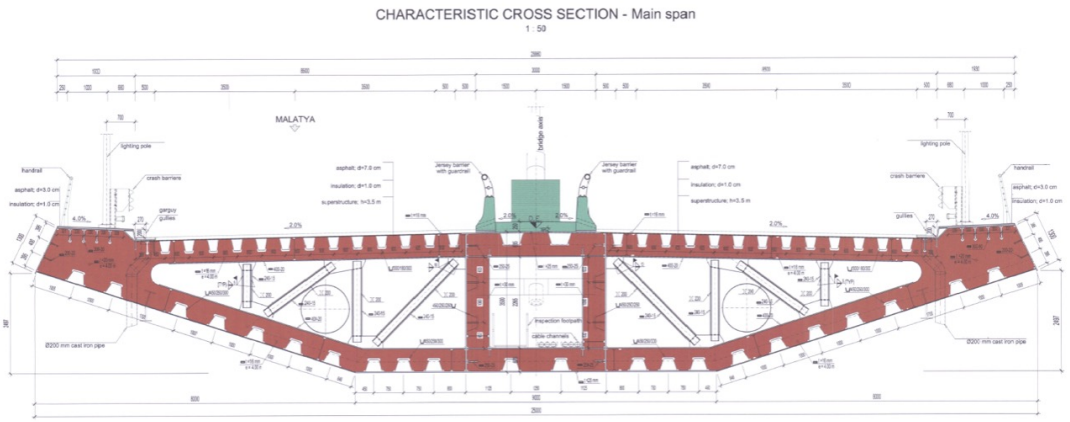


Figure 3.7. Cross-section of main span of New Kömürhan Bridge.

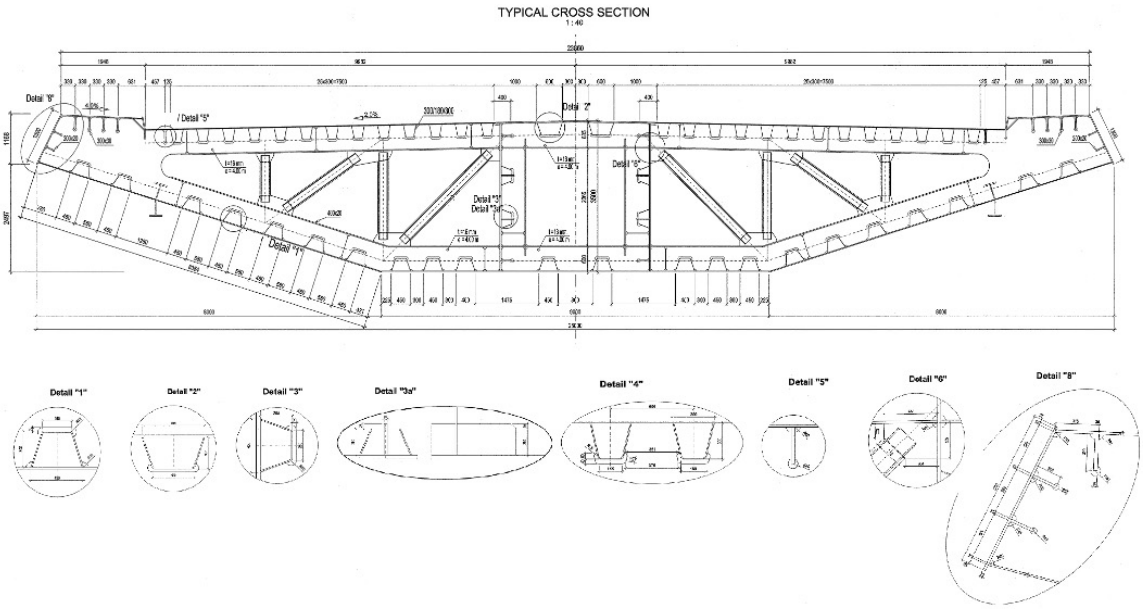


Figure 3.8. Details of cross-section of main span of New Kömürhan Bridge.

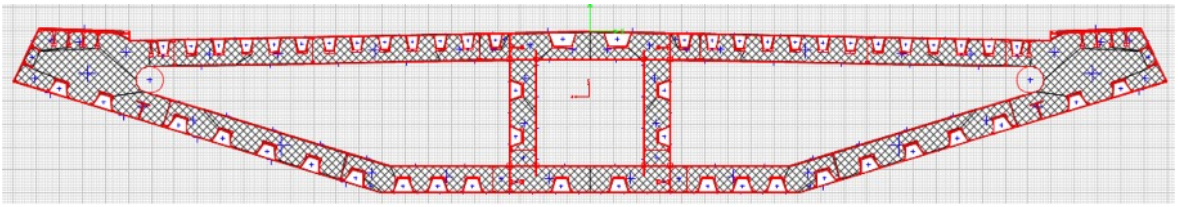


Figure 3.9. FEM cross-section of main span of New Kömürhan Bridge.

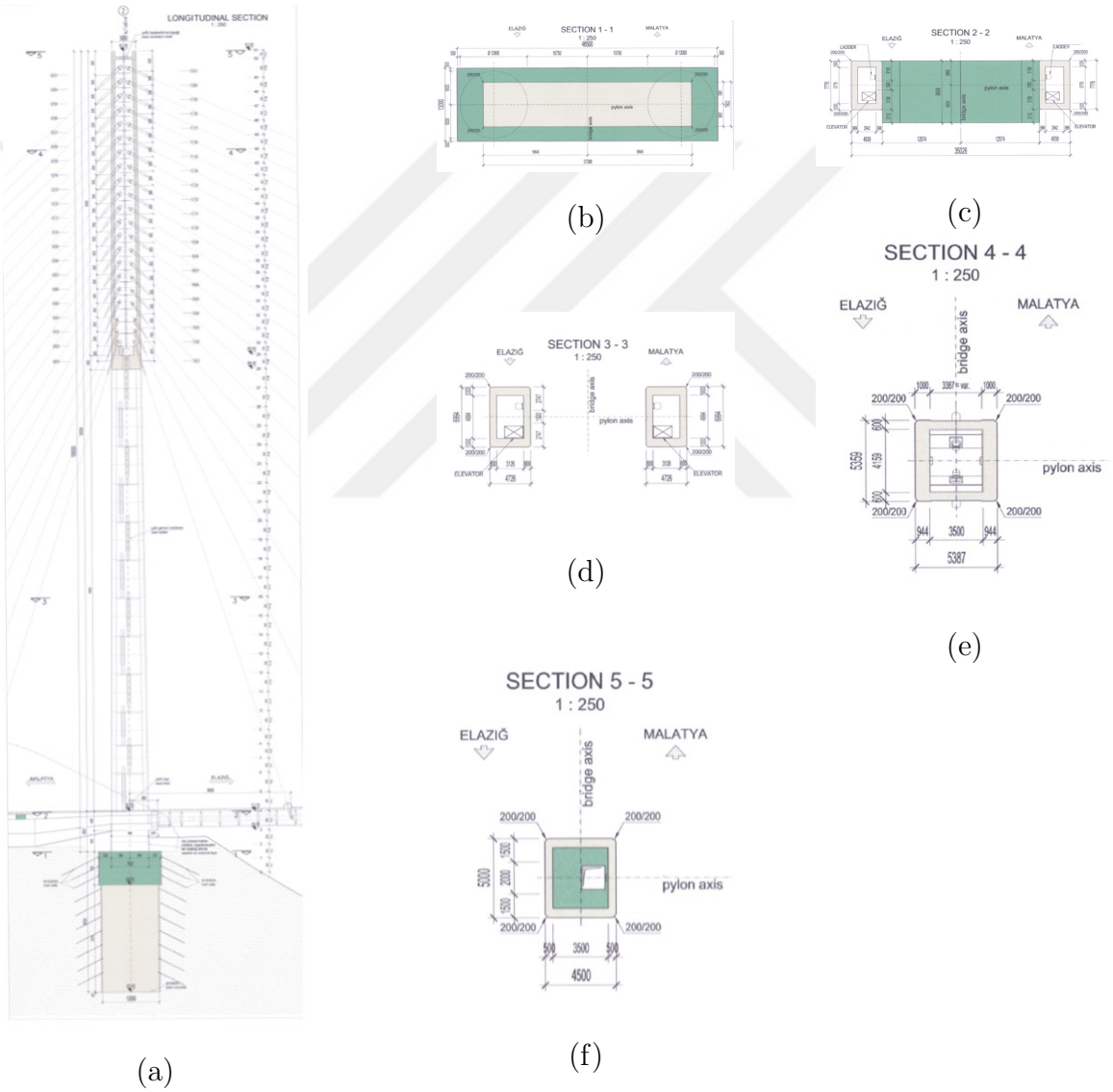


Figure 3.10. Cross-section details: (a) section longitudinal view of pylon, (b) section 1-1, (c) section 2-2, (d) section 3-3, (e) section 4-4, (f) section 5-5.

Since the bottom part is considered a fixed support in the FEM, it is not detailed. The cross-section view of the pylon and the section details at 4 different levels in FEM are shown in Figure 3.11.

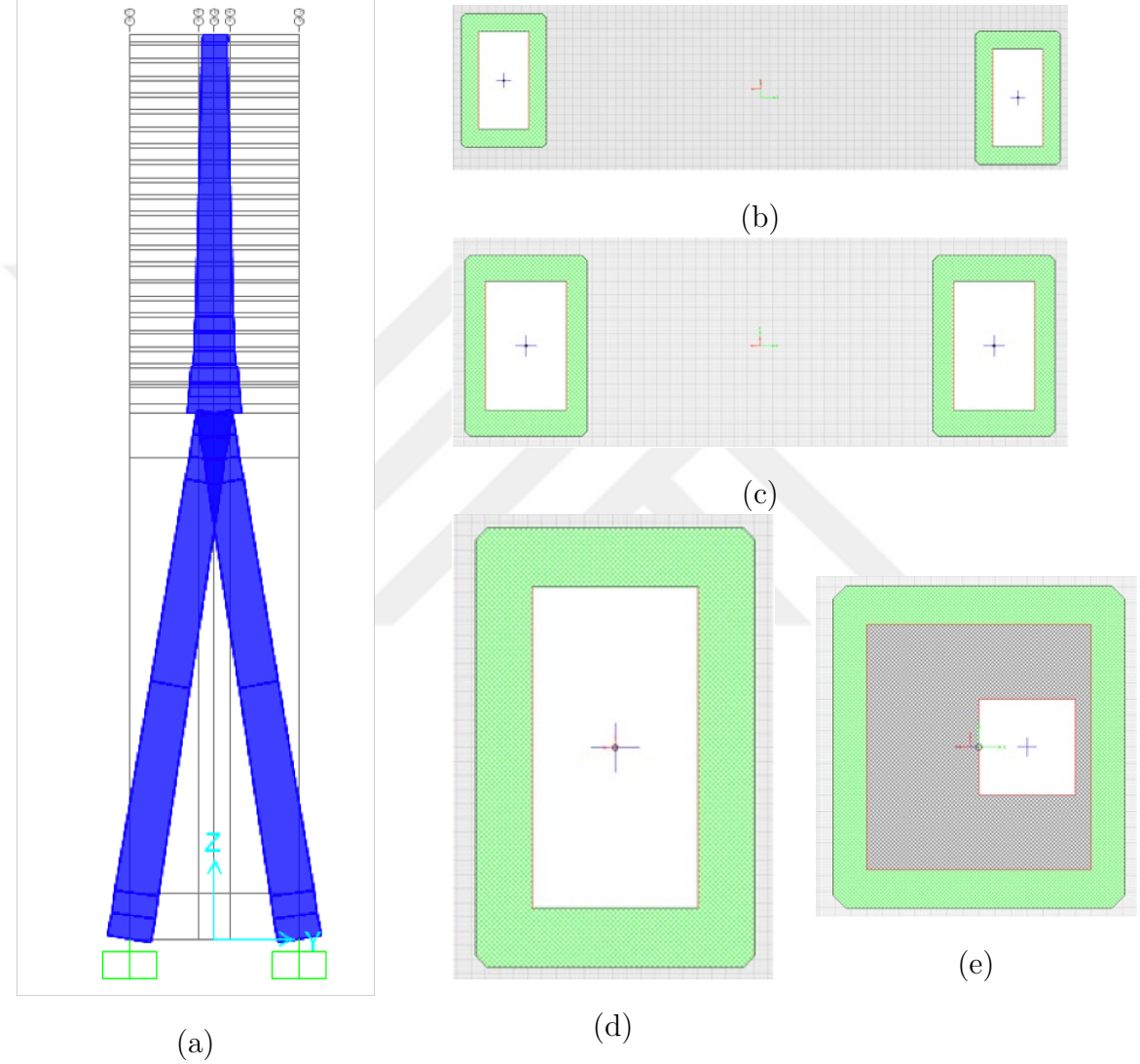


Figure 3.11. Cross-section details in FEM: (a) longitudinal view of pylon, (b) section 2-2, (c) section 3-3, (d) section 4-4, (e) section 5-5.

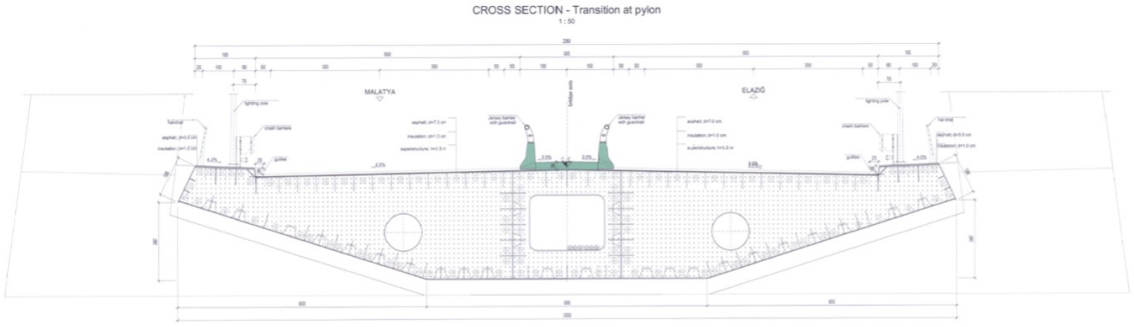


Figure 3.12. Cross-section detail of the transition between the pylon and the main span.

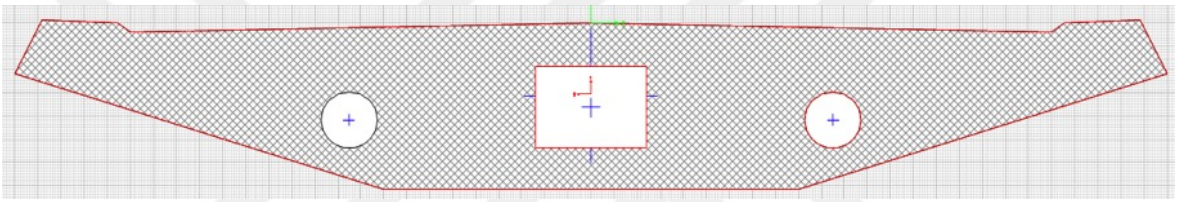


Figure 3.13. Cross-section detail of the transition between the pylon and the main span in FEM.

The supports on both sides of the main span have caisson foundations shown as Section-2 and Section-3 in the longitudinal and plan view. The cylindrical and cubic compressive strength after 28 days of caisson foundation is C30/37. The reinforced concrete section in this part is supported by a spherical bearing. Lateral movement is restricted. The detail of Section-3 is shown in Figure 3.14.

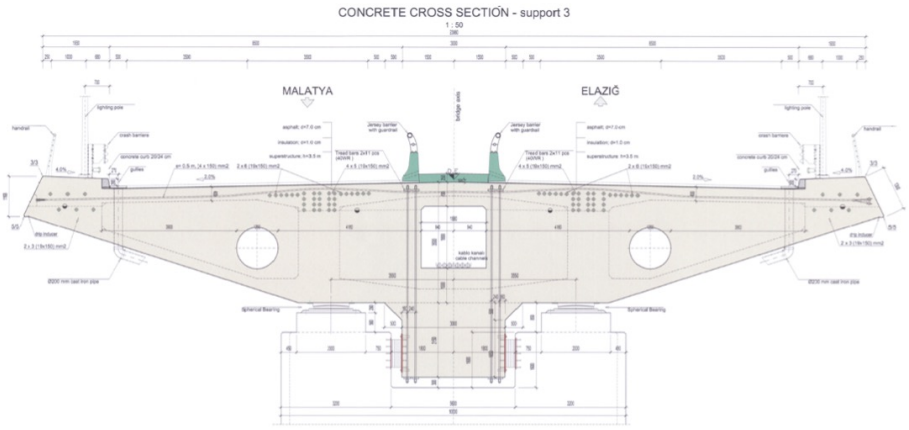


Figure 3.14. Cross-section detail of support-3.

The section above the support is modeled in SAP2000 since the lateral movement of the bottom of the support section is defined in the model to be limited.

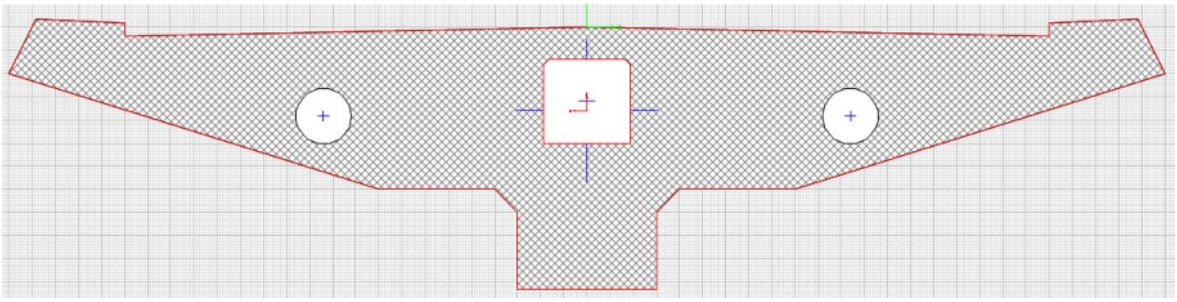


Figure 3.15. Cross-section detail of support-3 in FEM.

The support in the approaching viaduct shown as Section-4 in the longitudinal and plan view has a pile foundation. The cylindrical and cubic compressive strength after 28 days of pile foundation is C30/37. The reinforced concrete section in this part is supported by a spherical bearing. Lateral movement is not restricted.

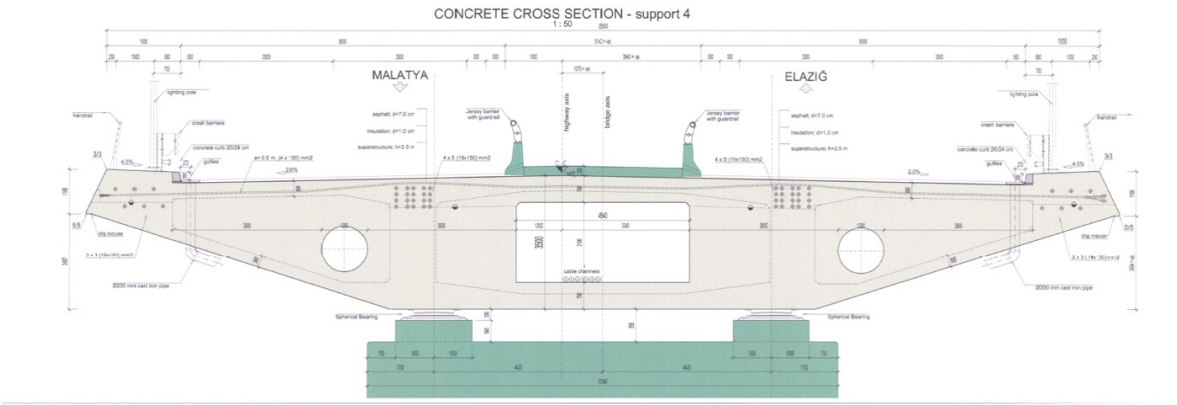


Figure 3.16. Cross-section detail of support-4.

The cross-section above the support is modeled in SAP2000 since the lateral movement of the bottom of the support section is defined in the model to be limited.

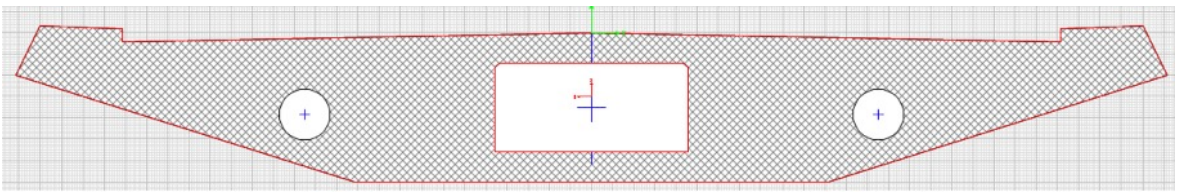


Figure 3.17. Cross-section detail of support-4 in FEM.

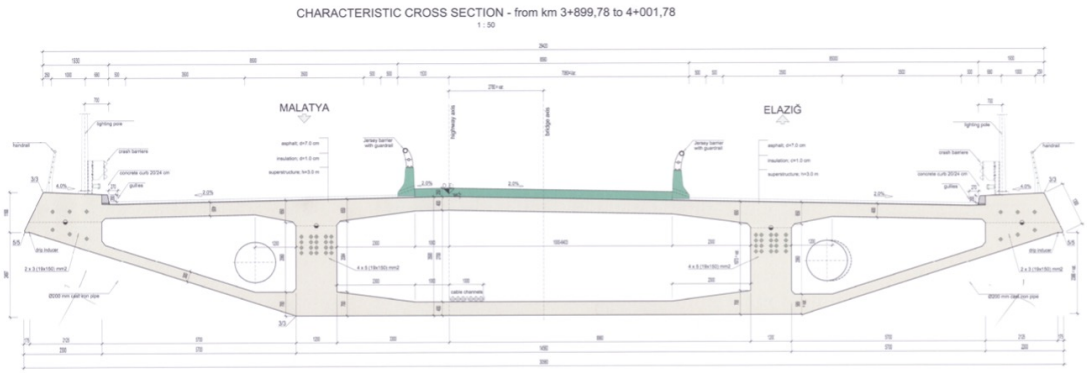


Figure 3.18. Cross-section of transition between support-3 and 4.

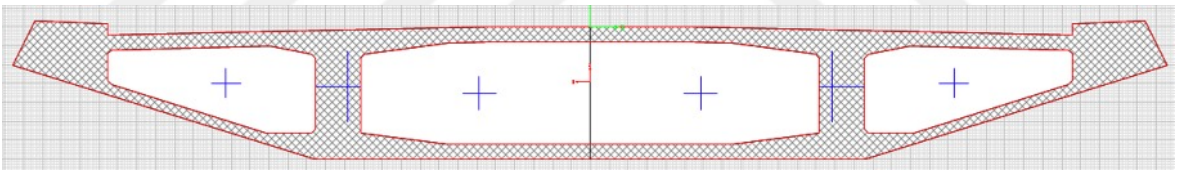


Figure 3.19. Cross-section of transition between support-3 and 4 in FEM.

The cross-section detail of Abutment-5, the first support point at the entrance of the approaching viaduct from the Elazig-side, is shown in Figure 3.21. The cylindrical and cubic compressive strength after 28 days of abutments is C30/37.

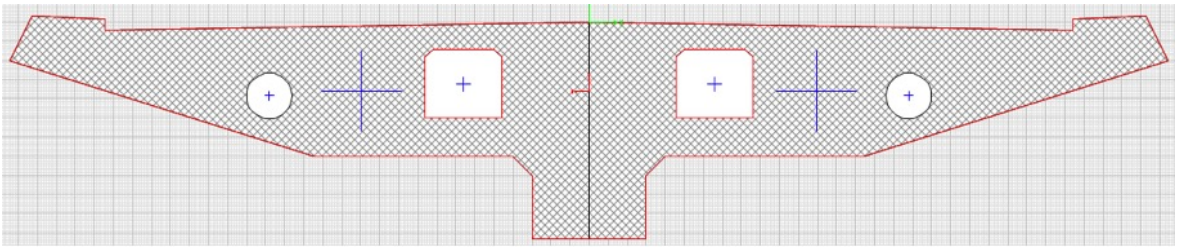


Figure 3.20. Cross-section detail of abutment-5 in FEM.

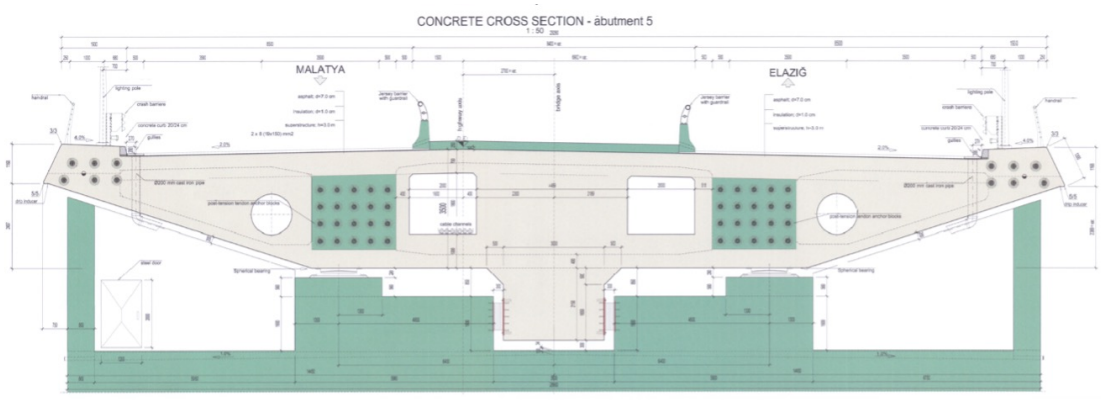


Figure 3.21. Cross-section detail of abutment-5.

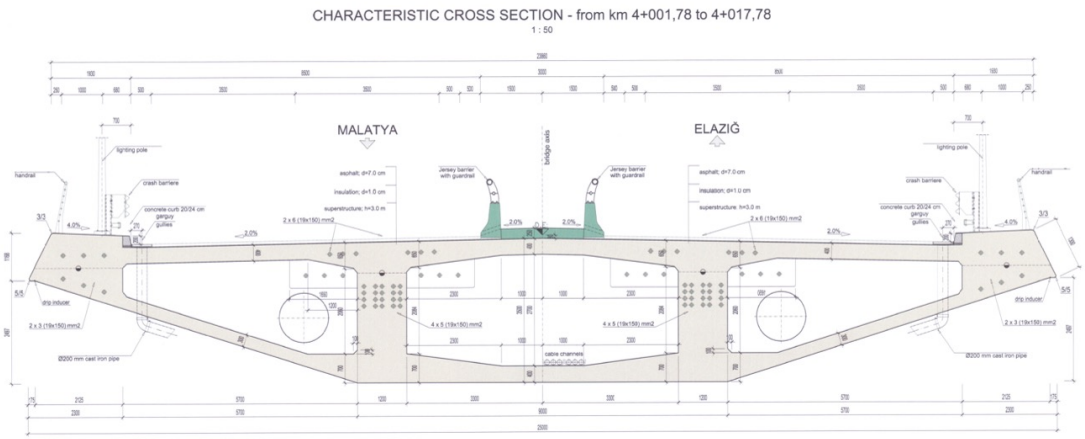


Figure 3.22. Cross-section of transition of support-4 and abutment-5.

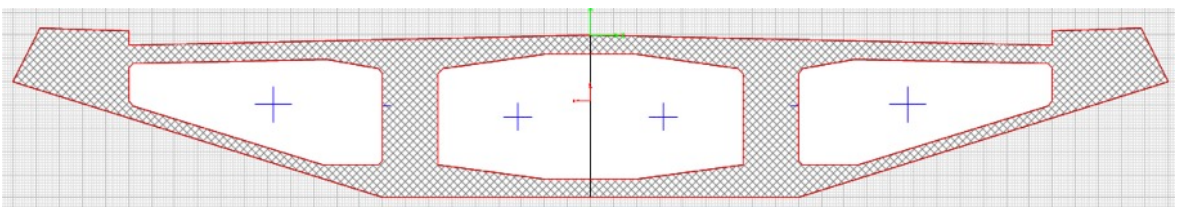


Figure 3.23. Cross-section of transition between support-4 and abutment-5 in FEM.

The back span anchorage block is in the form of an inverted T-profile. This block is built as a reinforced concrete continuous foundation. Embedded weight type continuous foundation is used in the back span anchorage block.

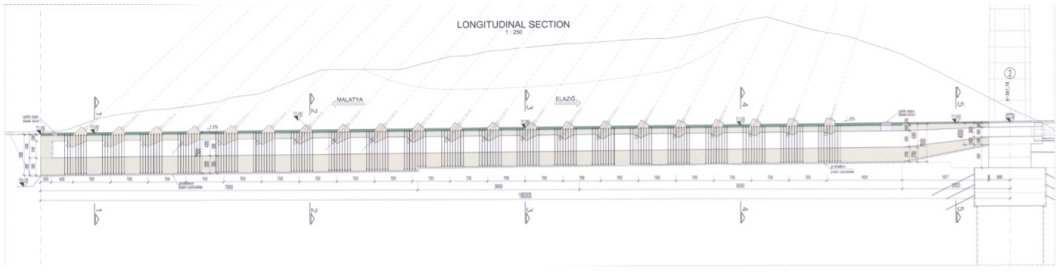
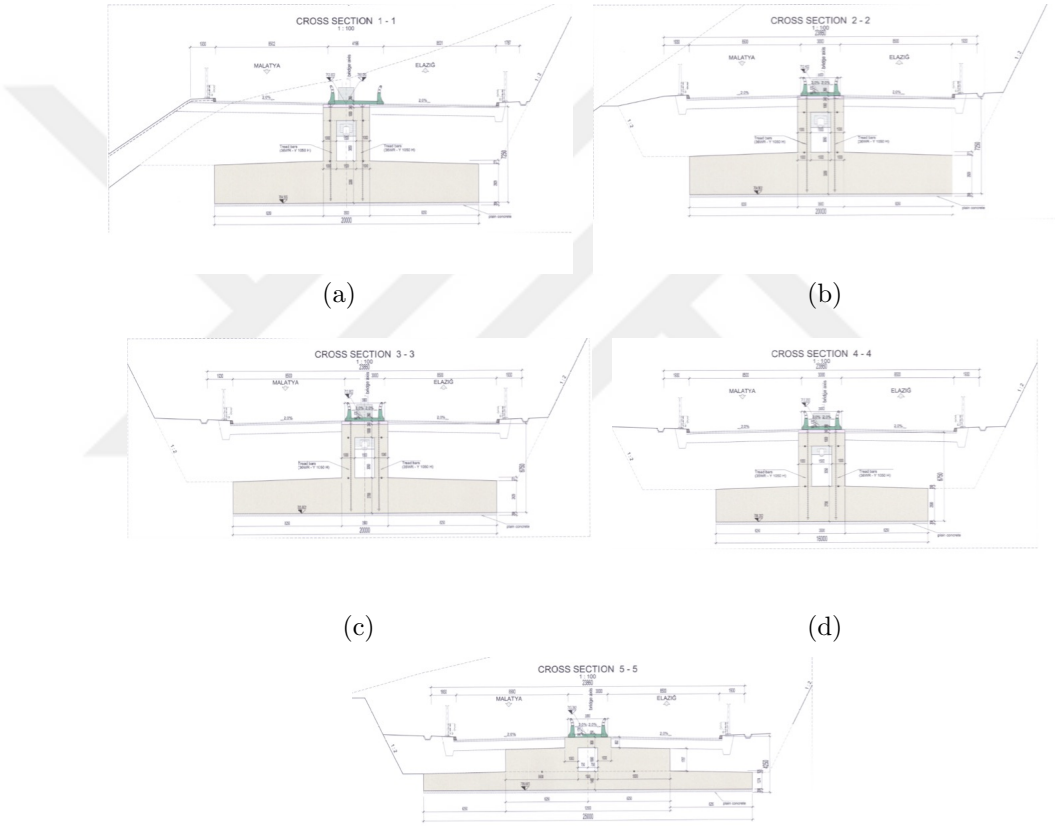


Figure 3.24. Longitudinal view of the back span anchorage block.



(a) (b)

(c) (d)

(e)

Figure 3.25. (a) Cross-section details of the back span anchorage block in cross-section 1-1, (b) cross-section 2-2, (c) cross-section 3-3, (d) cross-section 4-4, (e) cross-section 5-5.

The cross-section varies throughout the back span anchorage block. These 5 different cross-sections shown in the longitudinal view and plan view are shown in Figure 3.25.

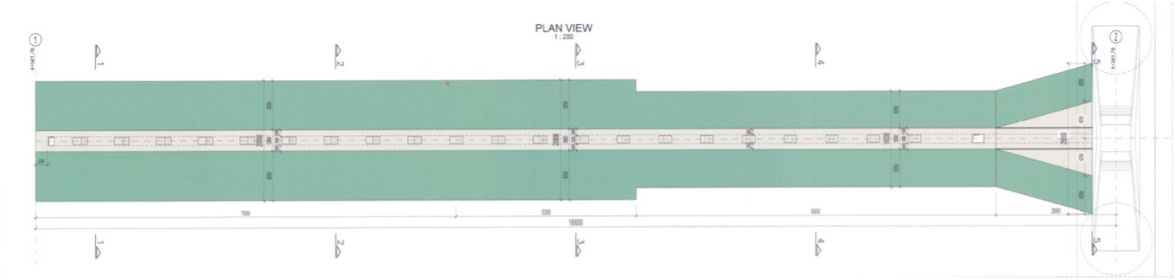
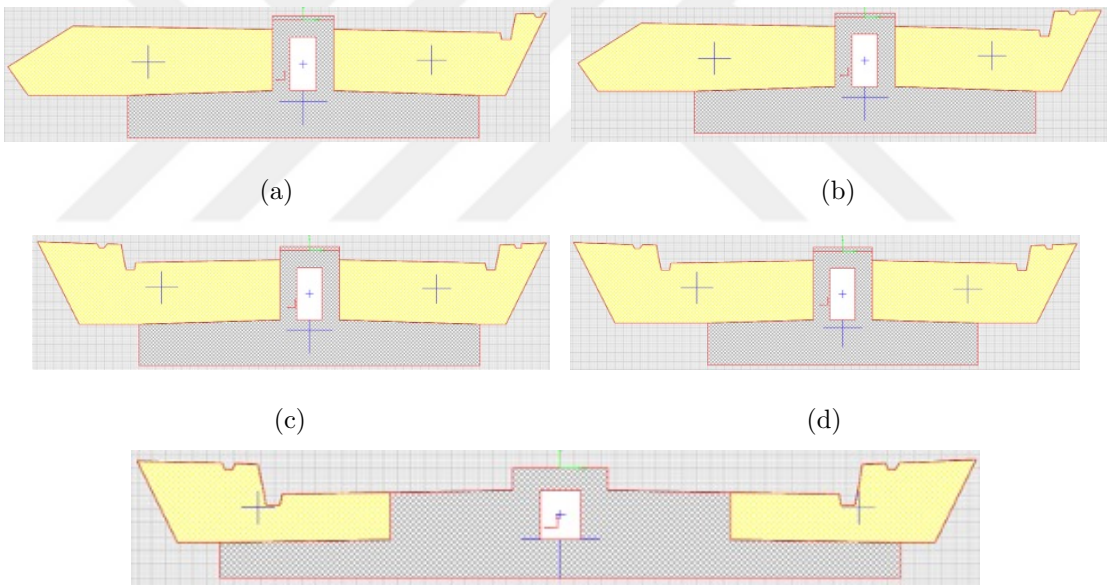


Figure 3.26. Plan view of the back span anchorage block.



(a) (b)

(c) (d)

(e)

Figure 3.27. (a) Cross-section of the back span anchorage block in cross-section 1-1 in FEM, (b) cross-section 2-2, (c) cross-section 3-3, (d) cross-section 4-4, (e) cross-section 5-5.

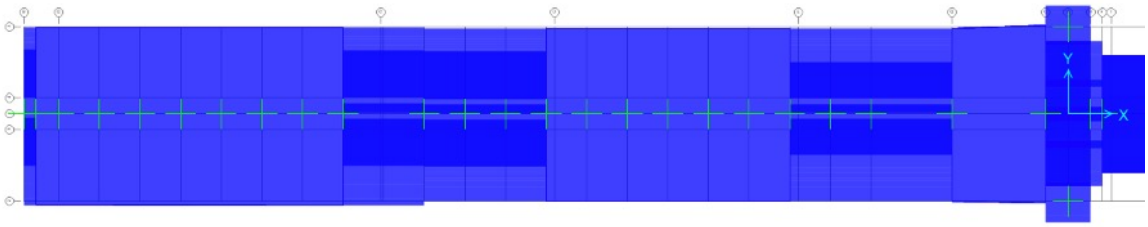


Figure 3.28. Plan view of the back span anchorage block in FEM.

Details of the approaching viaduct, main span, and back span anchorage block are given. The cable arrangement is shown in Figure 3.29.

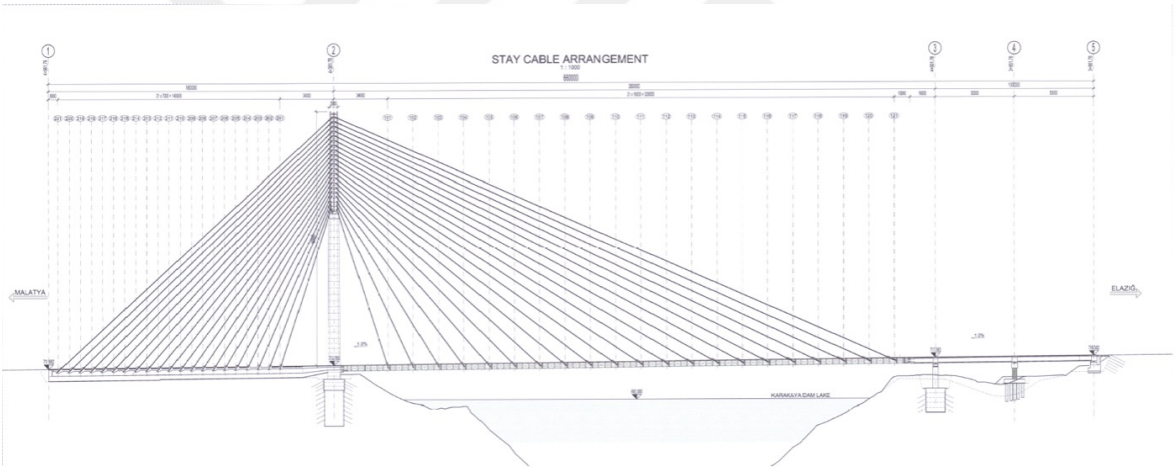


Figure 3.29. Cable arrangement of New Kömürhan Bridge.

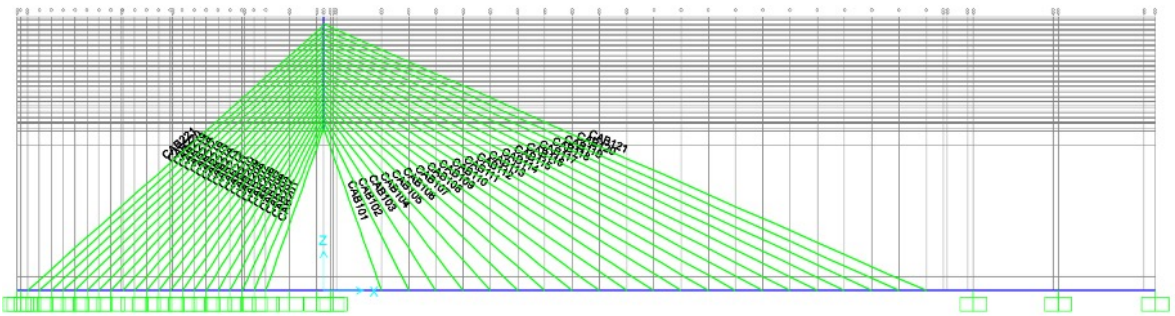


Figure 3.30. Cable arrangement of New Kömürhan Bridge in FEM.

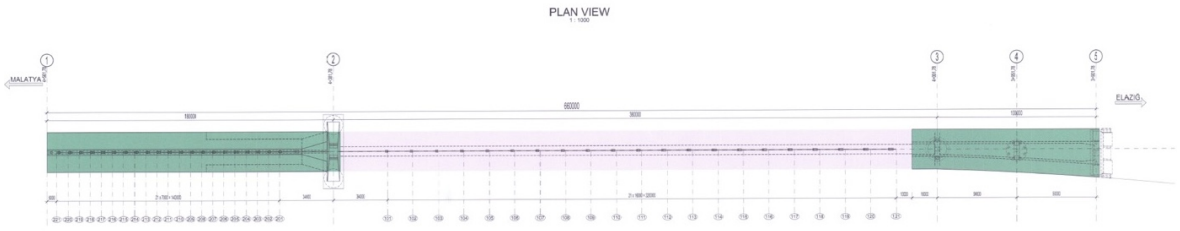


Figure 3.31. Cable arrangement plan view of New Kömürhan Bridge.

The details of the cables on the Elazig side according to their numbering in plan and longitudinal view are given in Table 3.1. In the table, the number of strands, their lengths, the angle between the main span and the cables, the mass in unit meter, the total mass and the number of internal hydraulic dampers are given according to the cable numbers. Each strand consists of 7 wires with low relaxation. Each cable is composed of strands. The material type is Grade 1860 according to EN-10138. The yield stress is 1600 MPa. The ultimate stress is 1860 MPa. The cross-sectional area of each strand is 150 mm^2. Its modulus of elasticity is 195 GPa. The strand diameter is 15.7 mm. The protection of cables and strands against corrosion is according to technical specifications. Each wire is galvanized one by one. Cables are covered with high density polyethylene (HDPE) sheath. There is wax fill between strands and sheath.

Table 3.1. Details of the cables on the Elazig side.

Cable Stay Sign	**Number of Strands**	**L (m)**	α (°)	**G (kg/m)**	**Weight (kg)**	**Internal Hydraulic Damper**
101	61	106	72.08	71.98	7630	1
102	50	115	64.74	59.00	6785	1
103	50	124	58.39	59.00	7316	1
104	55	135	53.09	64.90	8762	1
105	61	147	48.66	71.98	10581	1
106	61	162	44.95	71.98	11661	1
107	75	175	41.83	88.50	15488	1
108	75	189	39.16	88.50	16727	1
109	80	203	36.88	94.40	19163	1
110	80	218	34.91	94.40	20579	1
111	80	233	33.19	94.40	21995	1
112	80	248	31.69	94.40	23411	1
113	85	264	30.36	100.30	26479	1
114	85	279	29.18	100.30	27984	1
115	91	295	28.12	107.38	31677	1
116	91	310	27.17	107.38	33288	1
117	91	326	26.32	107.38	35006	1
118	91	341	25.54	107.38	36617	1
119	95	358	24.83	112.10	40132	1
120	100	374	24.19	118.00	44132	1
121	100	390	23.59	118.00	46020	1
				Σ	**491431**	**TOTAL 21**

The details of the cables on the Malatya side according to their numbering in plan and longitudinal view are given in Table 3.2. In the table, the number of strands, their lengths, the angle between the main span and the cables, the mass in unit meter,

the total mass and the number of internal hydraulic dampers are given according to the cable numbers.

Table 3.2. Details of the cables on the Malatya side.

Cable Stay Sign	**Number of Strands**	**L (m)**	α (°)	**G (kg/m)**	**Weight (kg)**	**Internal Hydraulic Damper**
201	61	107	72.20	71.98	7702	1
202	55	111	69.15	64.90	7204	1
203	55	117	66.36	64.90	7593	1
204	61	122	63.83	71.98	8782	1
205	75	128	61.54	88.50	11328	1
206	75	134	59.46	88.50	11859	1
207	85	140	57.57	100.30	14042	1
208	85	147	55.85	100.30	14744	1
209	91	154	54.28	107.38	16537	1
210	95	161	52.84	112.10	18048	1
211	100	167	51.52	118.00	19706	1
212	100	174	50.31	118.00	20532	1
213	109	181	49.19	128.62	23280	1
214	109	188	48.15	128.62	24181	1
215	109	195	47.19	128.62	25081	1
216	109	202	46.30	128.62	25981	1
217	115	209	45.47	135.70	28361	1
218	115	216	44.70	135.70	29311	1
219	120	223	44.98	141.60	31577	1
220	120	230	43.30	141.60	32568	1
221	120	238	42.66	141.60	33701	1
				Σ	**412117**	**TOTAL 21**
				Σ	**903548**	**TOTAL 42**

3.2. Cable Tension Calculation Results

Cable tensions were determined by lift-off test and vibration test with the 8 data sets. Using these two methods, the cable tension of only 8 of the 42 cables on the bridge was obtained. Afterwards, it was aimed to estimate all cable tensions from the videos records in the field with the vision-based monitoring system. By using the displacement response of vision-based monitoring system, the dynamic properties of the cables were calculated and the cable tensions were estimated with the vibration method.

3.2.1. Lift-off Test Results

Eight cables are monitored simultaneously with the lift-off test. Data is received from these cables at 200 Hz. Only a single strand tension is monitored in New Kömürhan Bridge. Therefore, this value was taken as an average and the cable tensions were calculated according to this value. The results of 8 data sets for each cable are plotted.

Data from 8 data sets taken from General Directorate of Highways in Turkey are shown in the figures below without any signal processing. The difference between the lowest and highest data in some sensors is large in the received data although it is low in some sensors. For this reason, average data were used instead of minimum or maximum tension both under traffic loads and during the earthquake. Some sensors contain negative or meaningless data. These values are not included in the summarized tables.

The above-mentioned problems are especially found in the first 4 data sets. It could be said that the sensors were updated or calibrated after these dates. It has been observed that the data received from the sensors moves in a lower range. For this reason, the average of these values was used.

Before the first earthquake, the average value of the each cable with the force sensor according to time is given in Figure 3.32.

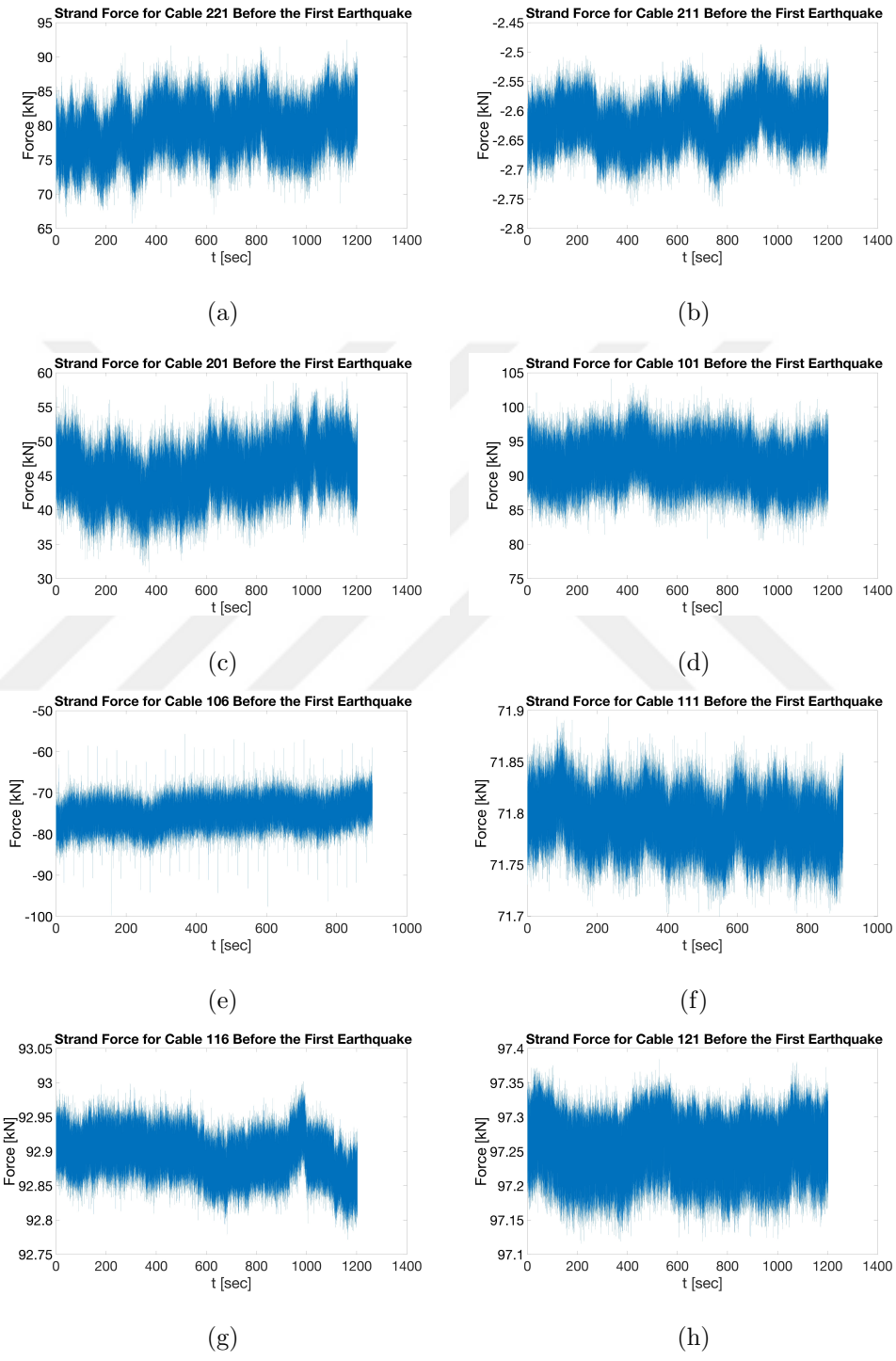


Figure 3.32. (a) Lift-off test results for dataset-1 in cable 221; (b) cable 211, (c) cable 201, (d) cable 101, (e) cable 106, (f) cable 111, (g) cable 116, (h) cable 121.

During the first earthquake, the average value of the each cable with the force sensor according to time is given in Figure 3.33.

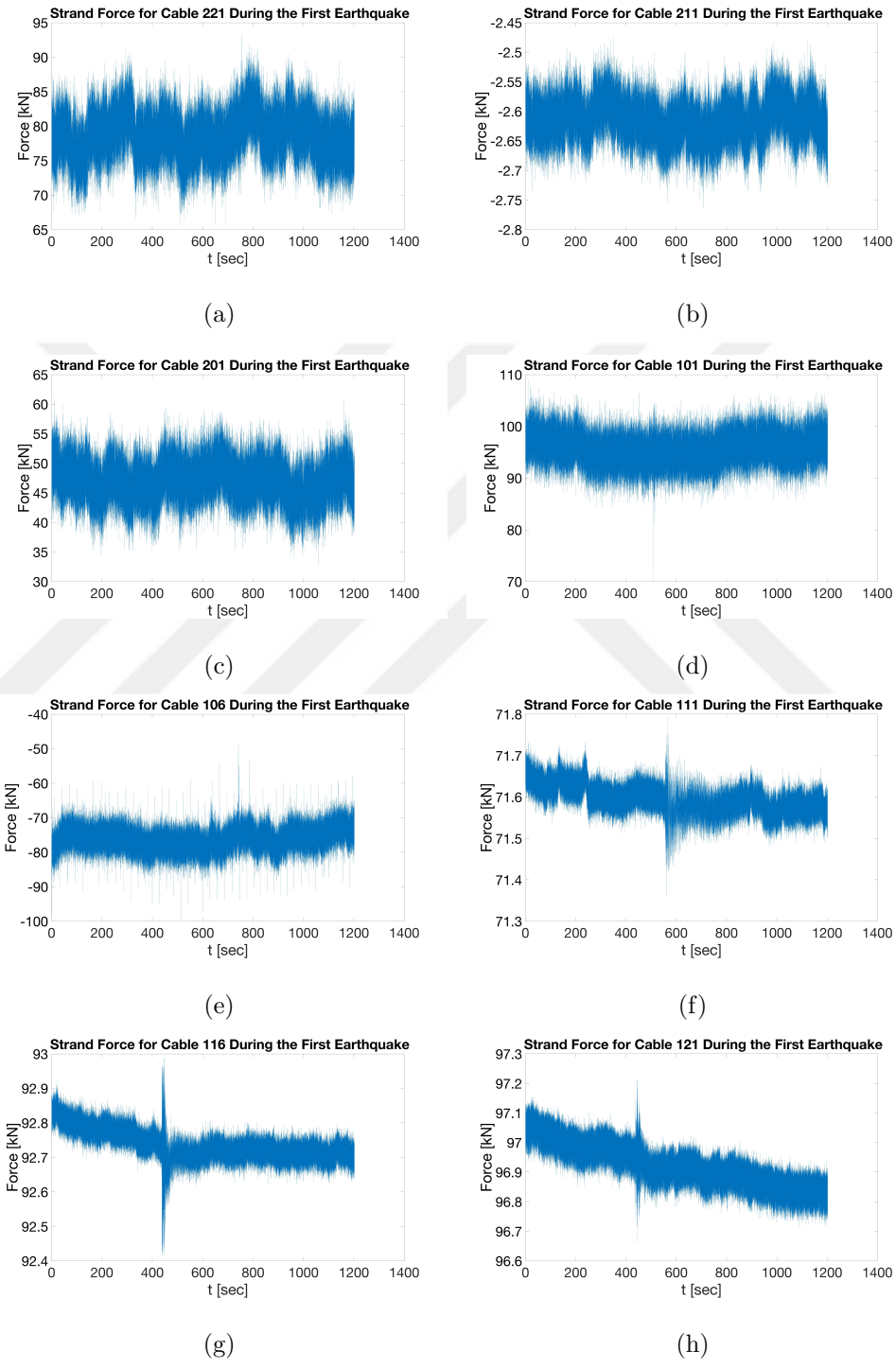


Figure 3.33. (a) Lift-off test results for dataset-2 in cable 221; (b) cable 211, (c) cable 201, (d) cable 101, (e) cable 106, (f) cable 111, (g) cable 116, (h) cable 121.

Before the second earthquake, the average value of the each cable with the force sensor according to time is given in Figure 3.34.

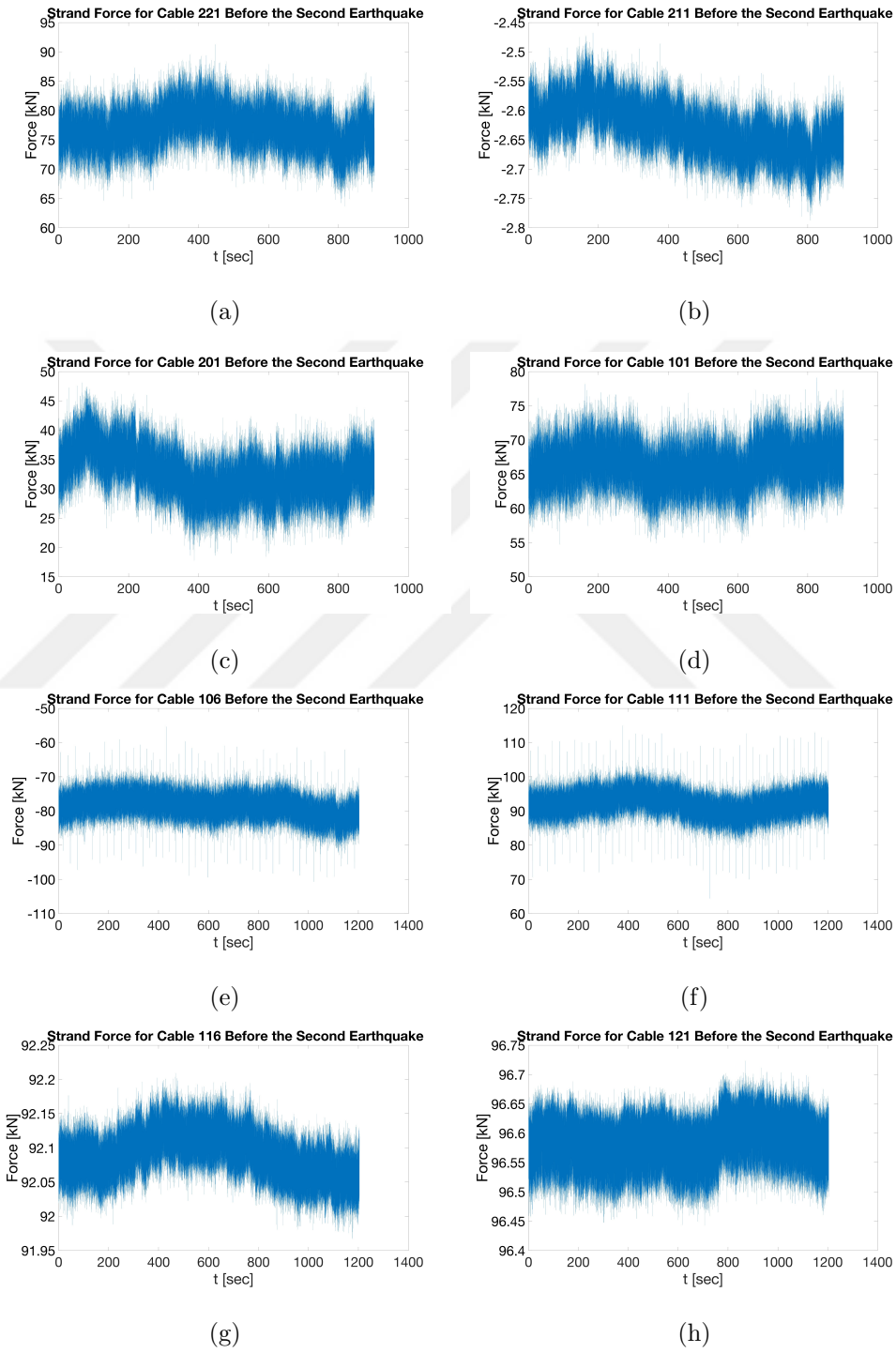


Figure 3.34. (a) Lift-off test results for dataset-3 in cable 221; (b) cable 211, (c) cable 201, (d) cable 101, (e) cable 106, (f) cable 111, (g) cable 116, (h) cable 121.

During the second earthquake, the average value of the each cable with the force sensor according to time is given in Figure 3.35.

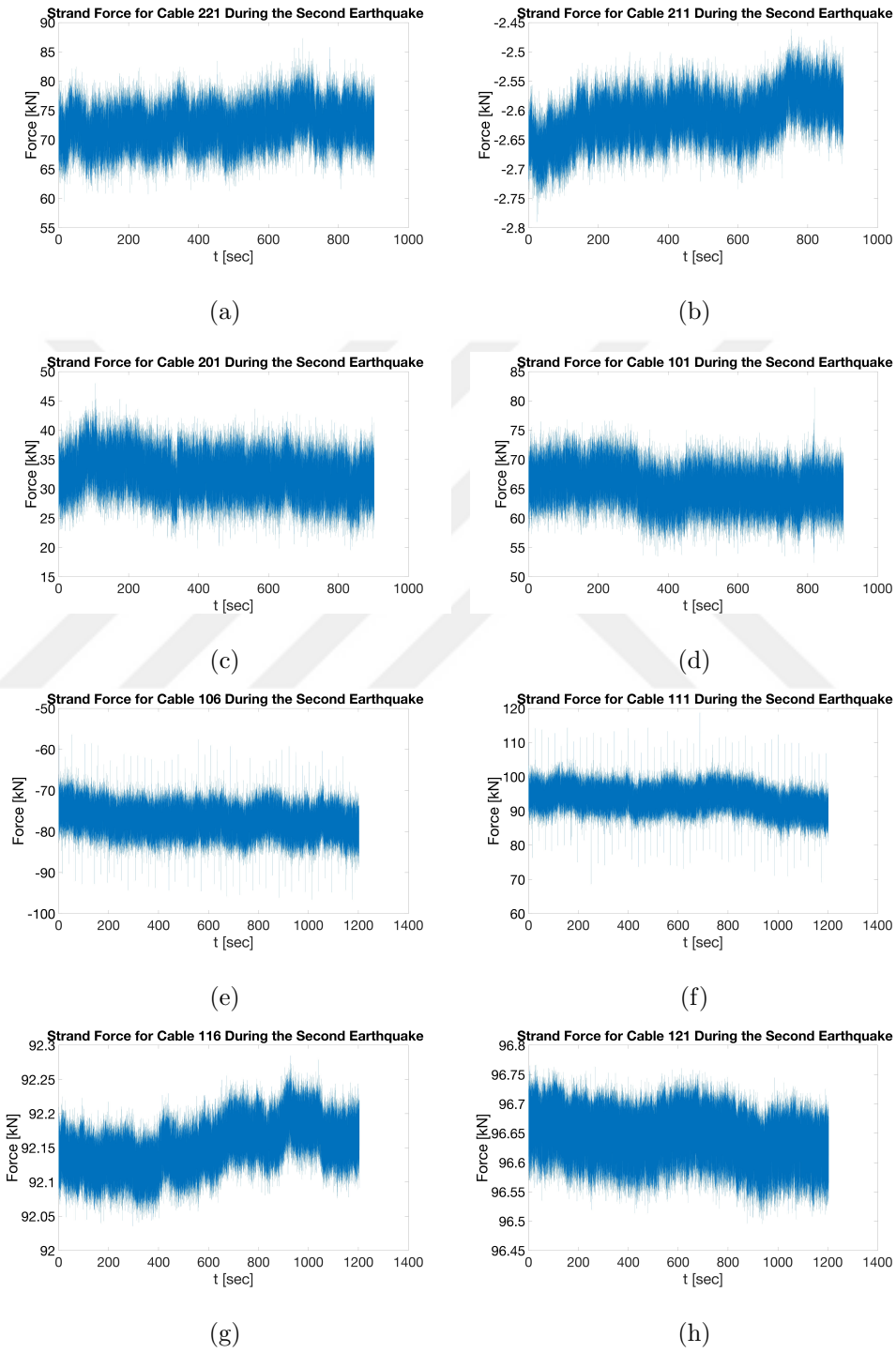


Figure 3.35. (a) Lift-off test results for dataset-4 in cable 221; (b) cable 211, (c) cable 201, (d) cable 101, (e) cable 106, (f) cable 111, (g) cable 116, (h) cable 121.

Before the third earthquake, the average value of the each cable with the force sensor according to time is given in Figure 3.36.

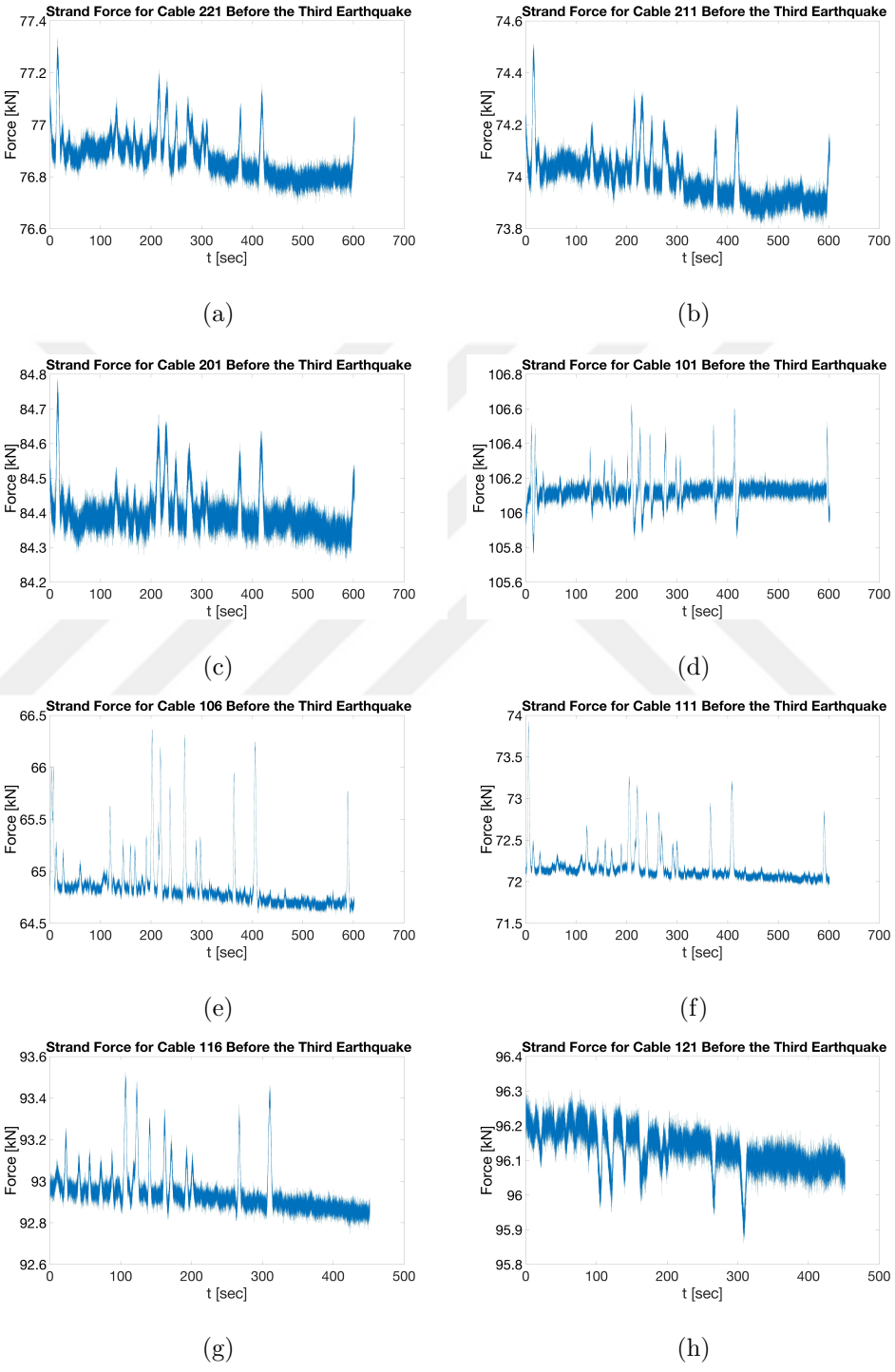


Figure 3.36. (a) Lift-off test results for dataset-5 in cable 221; (b) cable 211, (c) cable 201, (d) cable 101, (e) cable 106, (f) cable 111, (g) cable 116, (h) cable 121.

During the third earthquake, the average value of the each cable with the force sensor according to time is given in Figure 3.37.

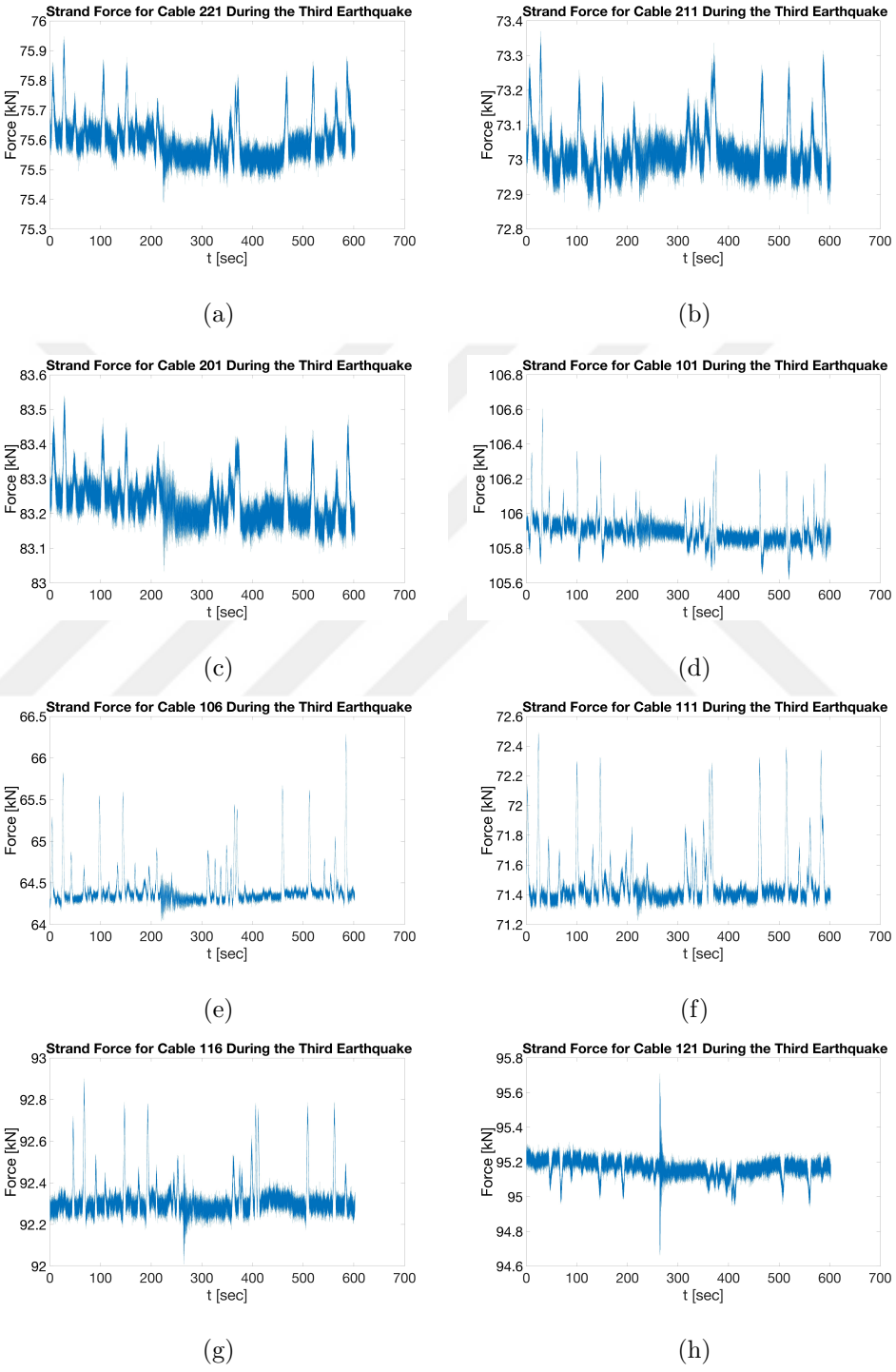


Figure 3.37. (a) Lift-off test results for dataset-6 in cable 221; (b) cable 211, (c) cable 201, (d) cable 101, (e) cable 106, (f) cable 111, (g) cable 116, (h) cable 121.

Before the forth earthquake, the average value of the each cable with the force sensor according to time is given in Figure 3.38.

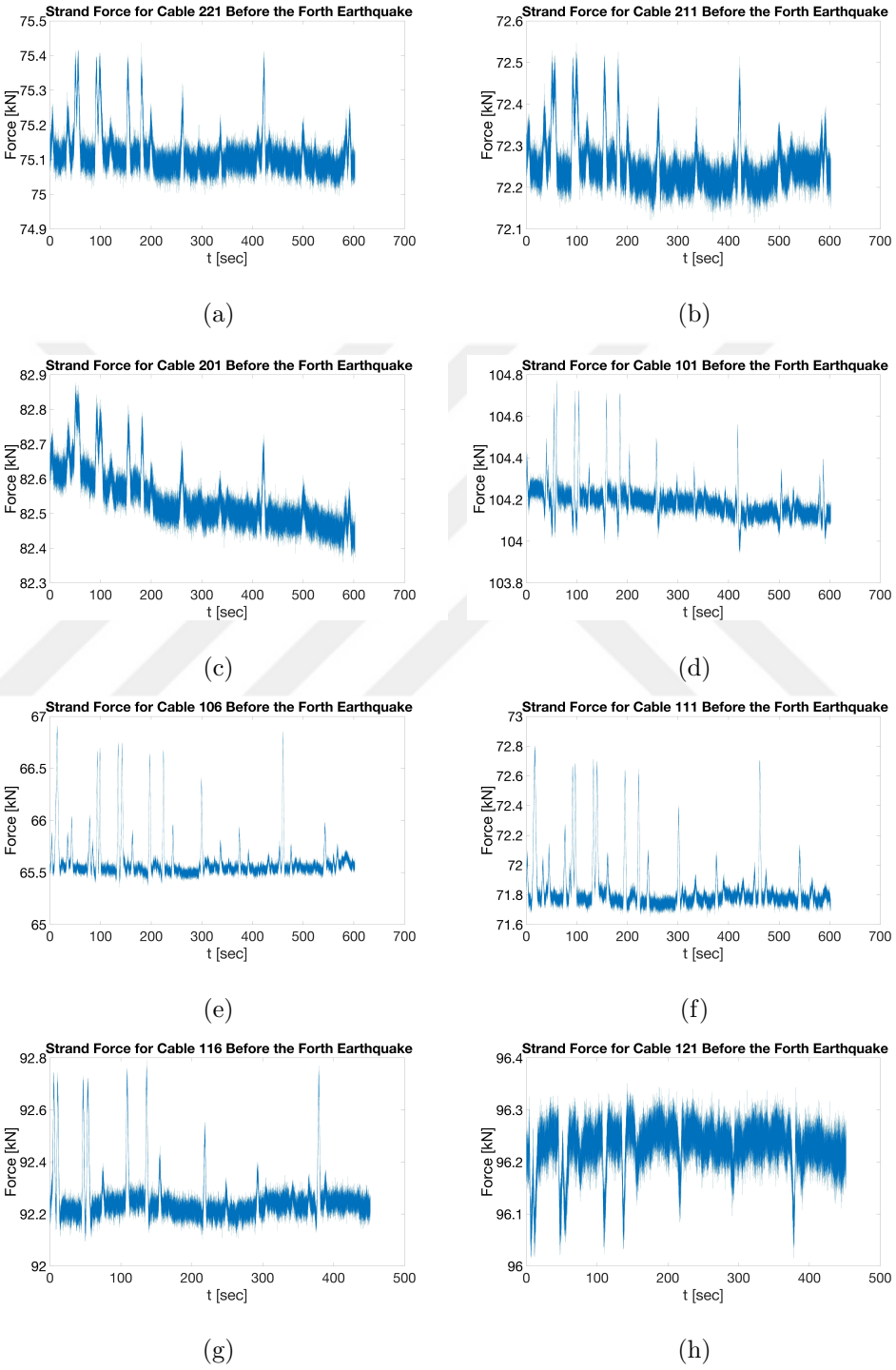


Figure 3.38. (a) Lift-off test results for dataset-7 in cable 221; (b) cable 211, (c) cable 201, (d) cable 101, (e) cable 106, (f) cable 111, (g) cable 116, (h) cable 121.

During the forth earthquake, the average value of the each cable with the force sensor according to time is given in Figure 3.39.

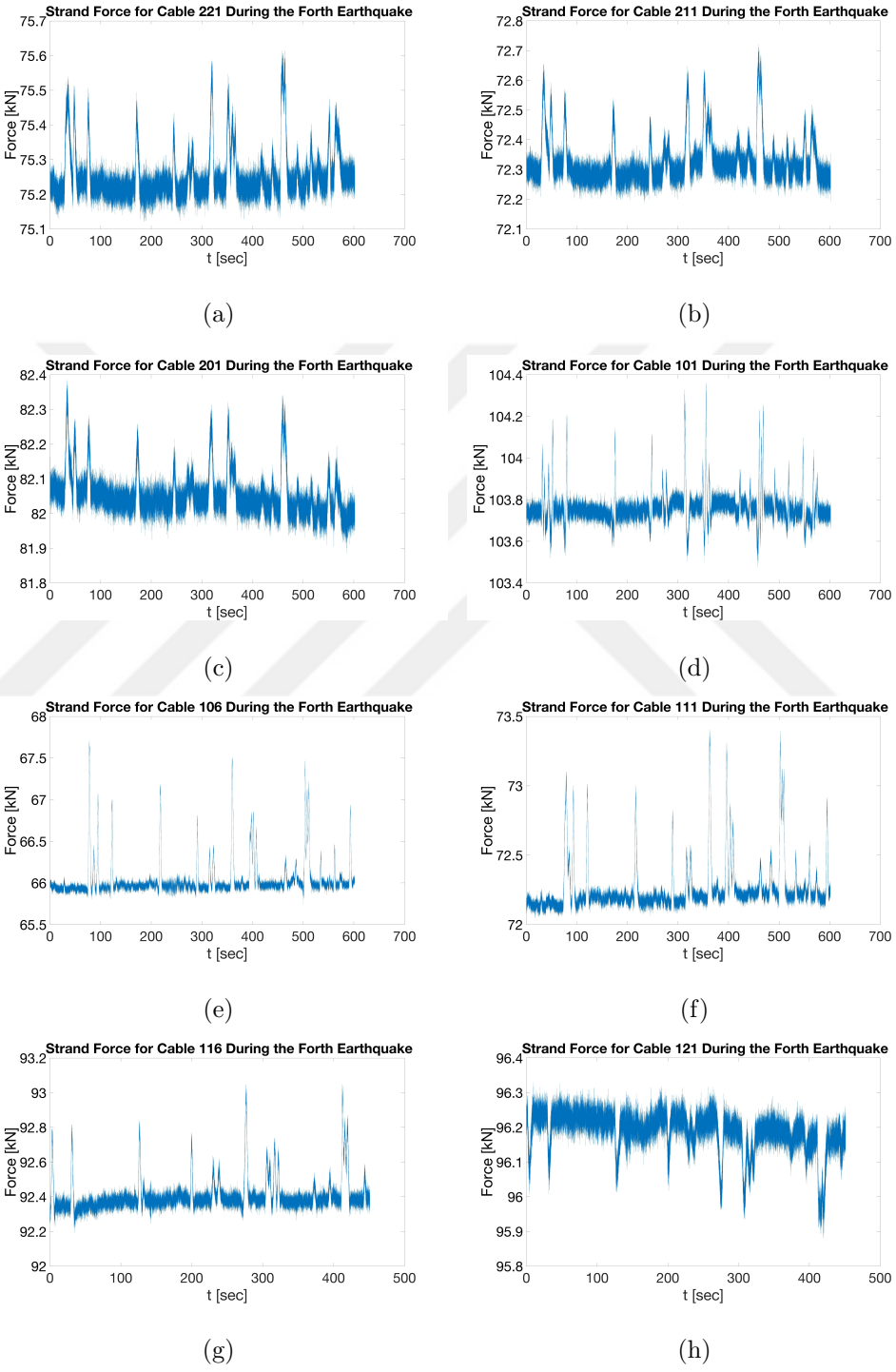


Figure 3.39. (a) Lift-off test results for dataset-8 in cable 221; (b) cable 211, (c) cable 201, (d) cable 101, (e) cable 106, (f) cable 111, (g) cable 116, (h) cable 121.

The table with the average values of the cable tensions for each strand is given in Table 3.3. Values are given in kN. The table of the cable tensions calculated by multiplying the number of strands with average tension is shown in Table 3.4.

Table 3.3. Lift-off test results summary for each strand tension.

	# **221**	# **211**	# **201**	# **101**	# **106**	# **111**	# **116**	# **121**
Before the 1st Earthquake	79.4	-	-	-	-	71.8	92.9	97.3
During the 1st Earthquake	78.6	-	-	-	-	71.6	92.7	96.9
Before the 2nd Earthquake	76.9	-	-	-	-	-	92.1	96.6
During the 2nd Earthquake	72.4	-	-	-	-	-	92.2	96.7
Before the 3rd Earthquake	76.9	74.0	84.4	106.1	64.9	72.2	92.9	96.1
During the 3rd Earthquake	75.6	73.0	83.2	105.9	64.4	71.5	92.3	95.2
Before the 4th Earthquake	75.1	72.3	82.5	104.2	65.6	71.8	92.3	96.2
During the 4th Earthquake	75.3	72.3	82.1	103.8	66.0	72.3	92.4	96.12

Since the first aim of this study is to determine the cable tensions and verify them by comparison with the other methods, the average value is taken instead of the maximum value for each dataset, although earthquake data is also available. Cable tensions are also calculated according to these values.

Table 3.4. Lift-off test results summary for each cable.

	Cable 221	**Cable 211**	**Cable 201**	**Cable 101**	**Cable 106**	**Cable 111**	**Cable 116**	**Cable 121**
Before the 1st Earthquake	9525.34	-	-	-	-	5743.30	8453.35	9726.14
During the 1st Earthquake	9436.16	-	-	-	-	5727.57	8439.01	9693.16
Before the 2nd Earthquake	9226.27	-	-	-	-	-	8380.15	9659.12
During the 2nd Earthquake	8683.71	-	-	-	-	-	8385.79	9664.98
Before the 3rd Earthquake	9225.15	7399.42	5148.26	6473.79	3956.25	5773.51	8457.79	9613.34
During the 3rd Earthquake	9071.75	7302.18	5077.26	6459.77	3929.61	5717.75	8400.81	9516.37
Before the 4th Earthquake	9014.07	7225.19	5034.93	6355.61	4001.84	5746.40	8394.88	9622.86
During the 4th Earthquake	9030.58	7232.75	5005.33	6329.48	4028.51	5780.89	8408.85	9618.80

3.2.2. Cable Tension Calculation Using Existing Accelerometers

Eight cables are monitored simultaneously with the accelerometers. Data is received from these cables at 200 Hz. There are two accelerometers on each cable in the x- and y-direction. Data taken 3 hours before and at the time of the four earthquakes for each cable are plotted.

Saturation is observed in some sensor data. The measurement limit of the sensor is estimated to be +/- 0.5g, and it is observed that it takes measurements at maximum values. The amplitude values in these graphs are very high. For this reason, there is a leakage in PSDs. For this reason, data from these sensors were not used in calculating natural frequencies. Figure 3.40(e) and Figure 3.40(h) can be shown as examples of these problems. These problems are also observed in different data sets.

Before the first earthquake, the response of the eight cables according to time and PSDs without any signal processing operation is given in Figure 3.40.

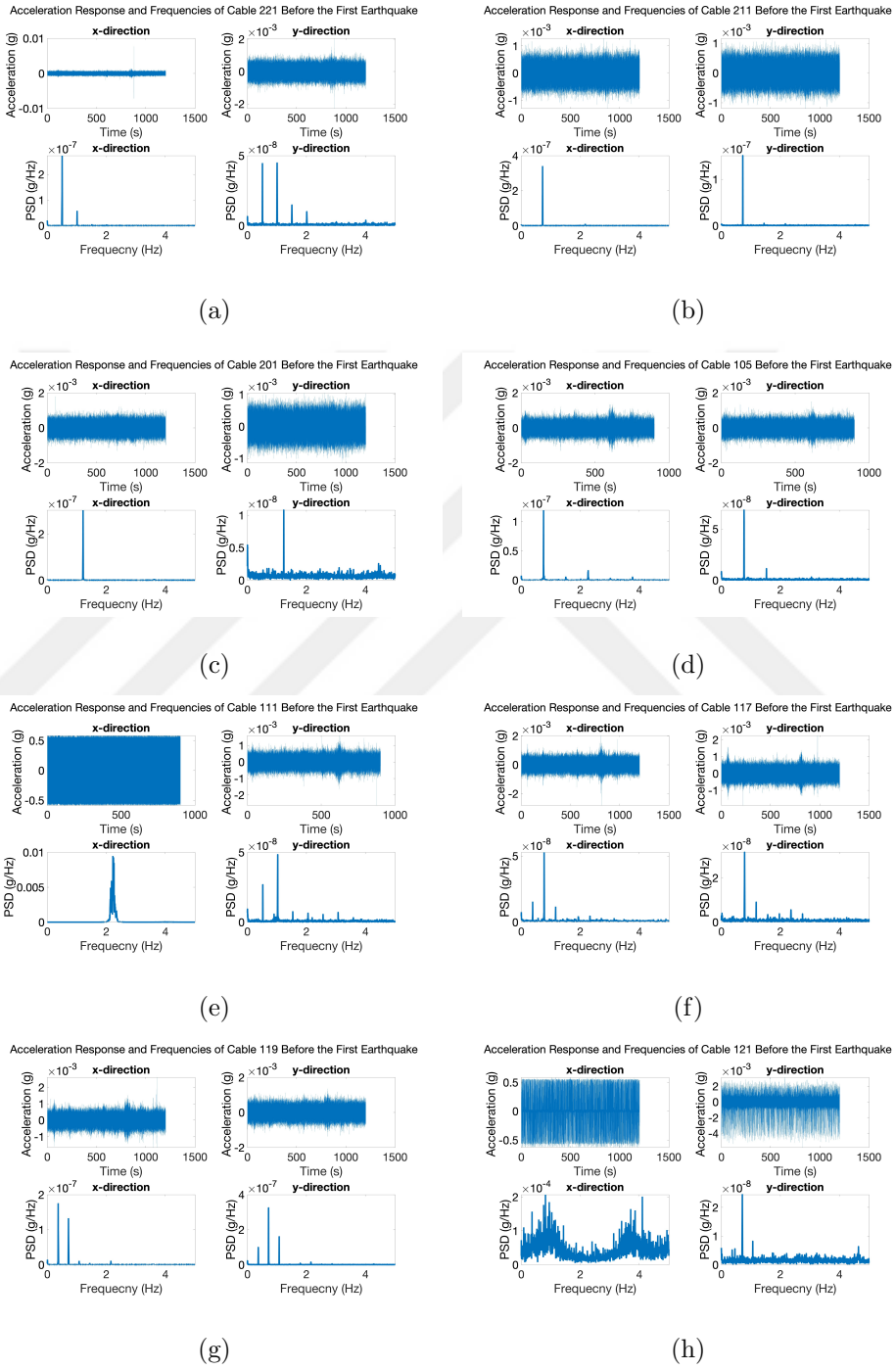


Figure 3.40. (a) Vibration analysis using existing accelerometer for dataset-1 in cable 221, (b) cable 211, (c) cable 201, (d) cable 105, (e) cable 111, (f) cable 117, (g) cable 119, (h) cable 121.

During the first earthquake, the response of the eight cables according to time and PSDs without any signal processing operation is given in Figure 3.41.

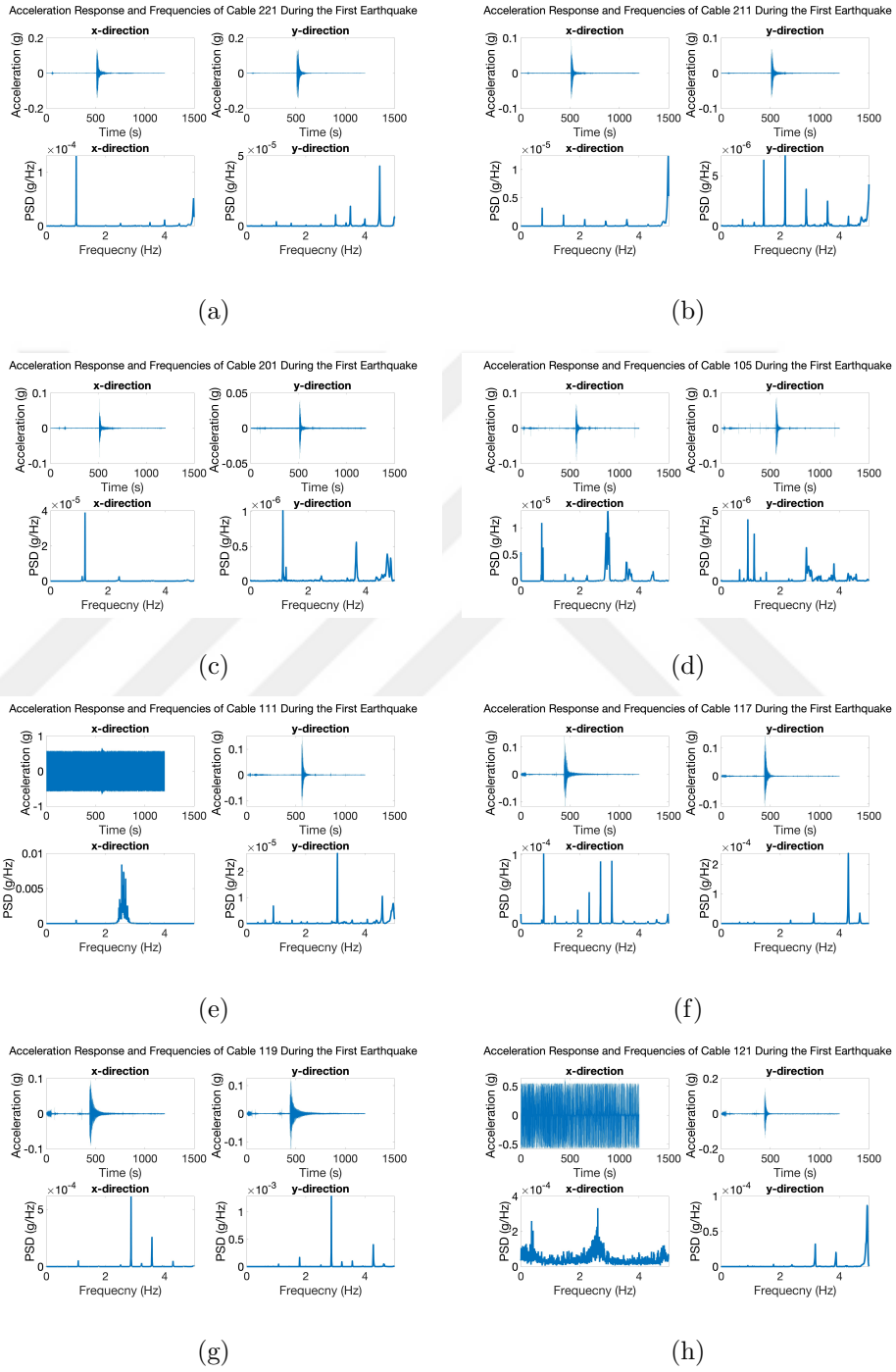


Figure 3.41. (a) Vibration analysis using existing accelerometer for dataset-2 in cable 221, (b) cable 211, (c) cable 201, (d) cable 105, (e) cable 111, (f) cable 117, (g) cable 119, (h) cable 121.

Before the second earthquake, the response of the eight cables according to time and PSDs without any signal processing operation is given in Figure 3.42.

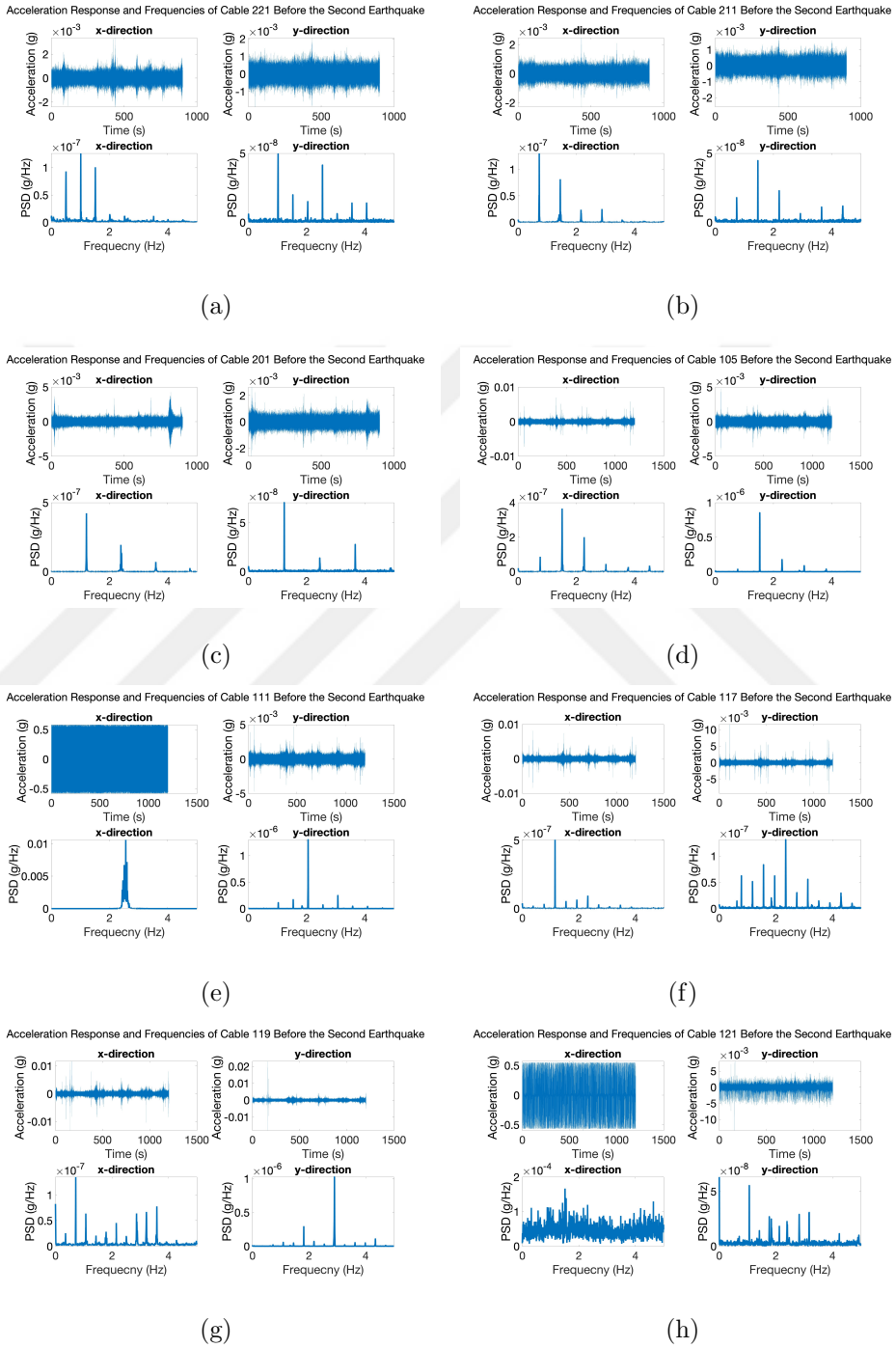


Figure 3.42. (a) Vibration analysis using existing accelerometer for dataset-3 in cable 221, (b) cable 211, (c) cable 201, (d) cable 105, (e) cable 111, (f) cable 117, (g) cable 119, (h) cable 121.

During the second earthquake, the response of the eight cables according to time and PSDs without any signal processing operation is given in Figure 3.43.

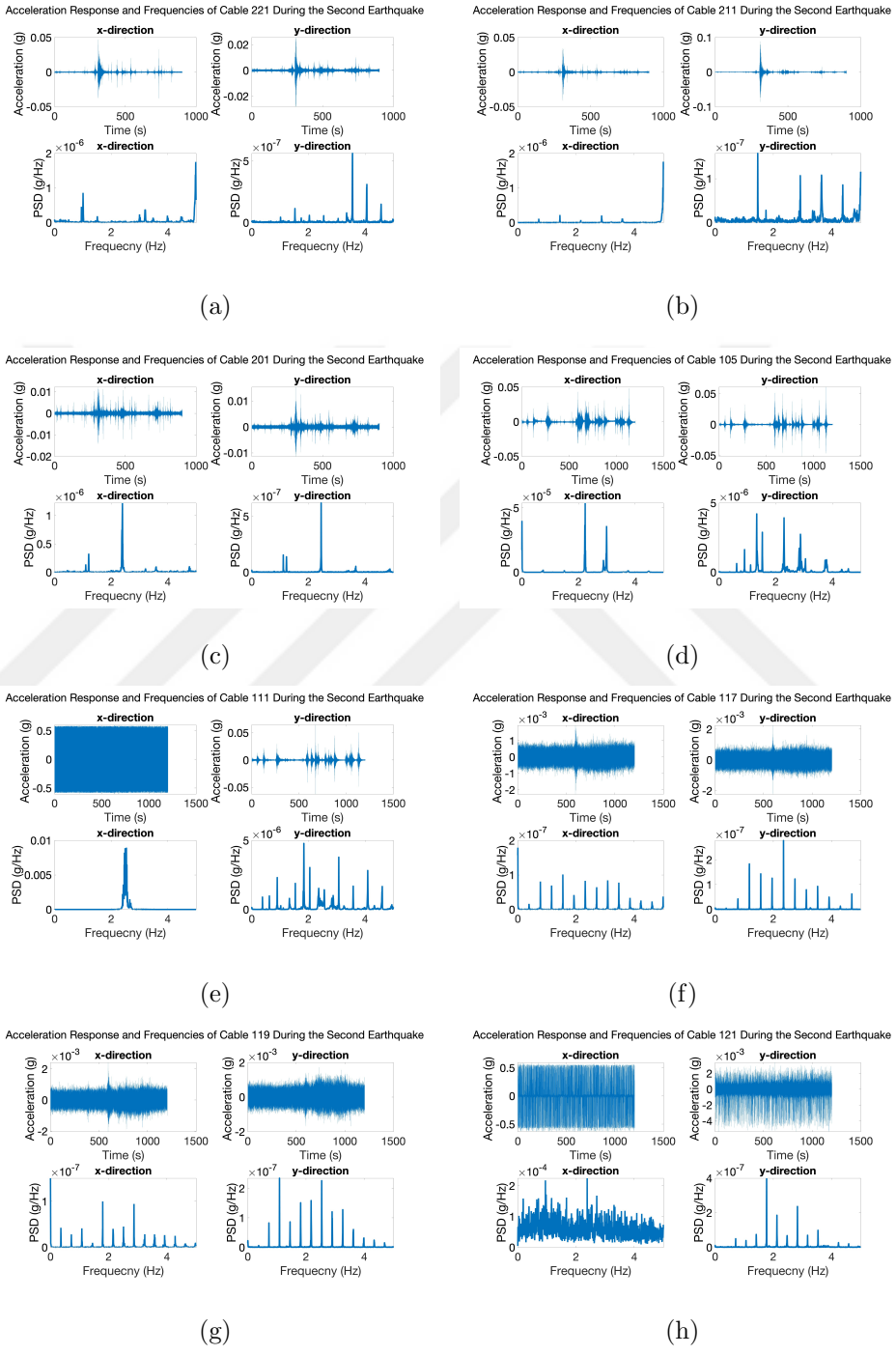


Figure 3.43. (a) Vibration analysis using existing accelerometer for dataset-4 in cable 221, (b) cable 211, (c) cable 201, (d) cable 105, (e) cable 111, (f) cable 117, (g) cable 119, (h) cable 121.

Before the third earthquake, the response of the eight cables according to time and PSDs without any signal processing operation is given in Figure 3.44.

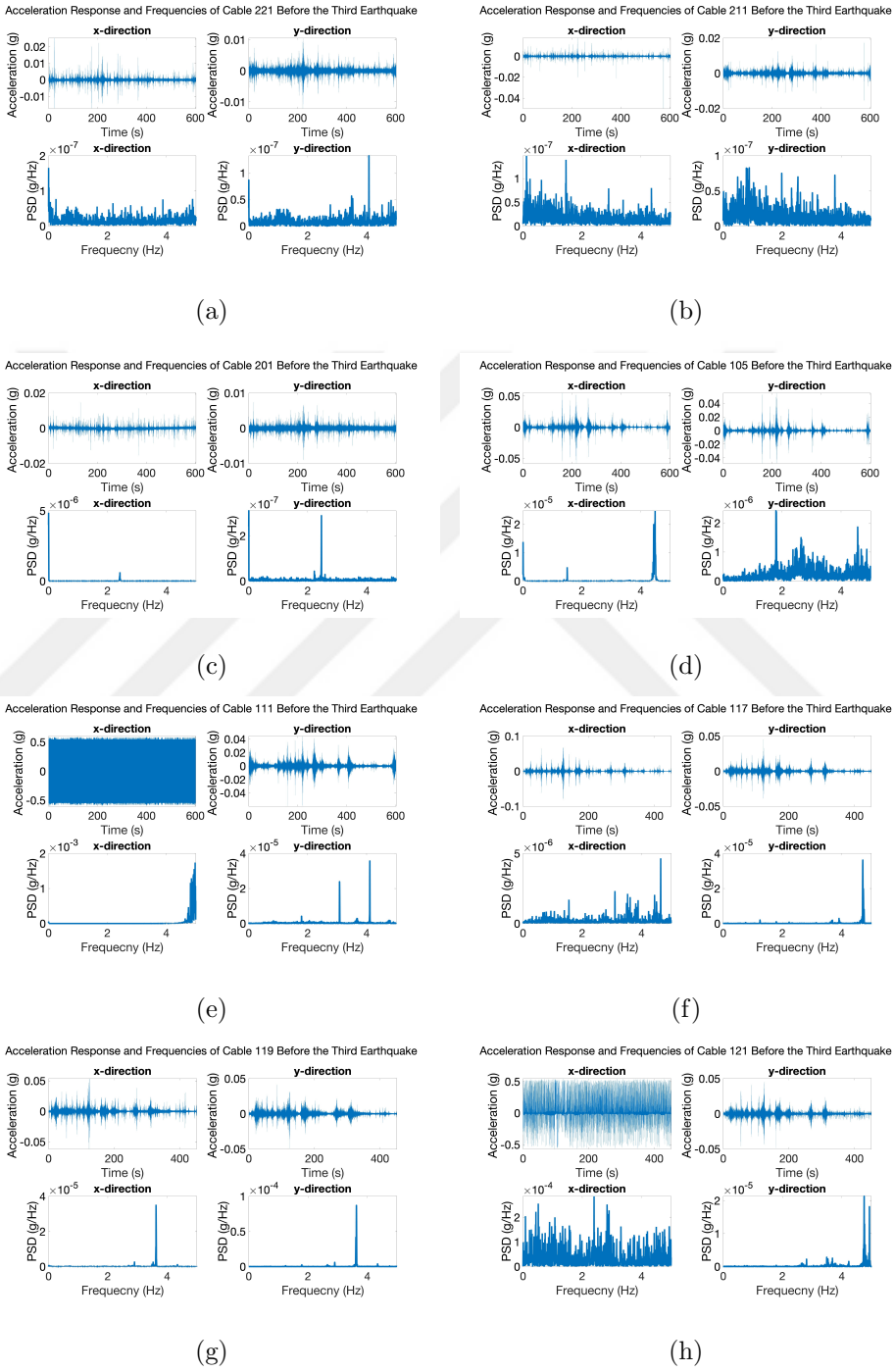


Figure 3.44. (a) Vibration analysis using existing accelerometer for dataset-5 in cable 221, (b) cable 211, (c) cable 201, (d) cable 105, (e) cable 111, (f) cable 117, (g) cable 119, (h) cable 121.

During the third earthquake, the response of the eight cables according to time and PSDs without any signal processing operation is given in Figure 3.45.

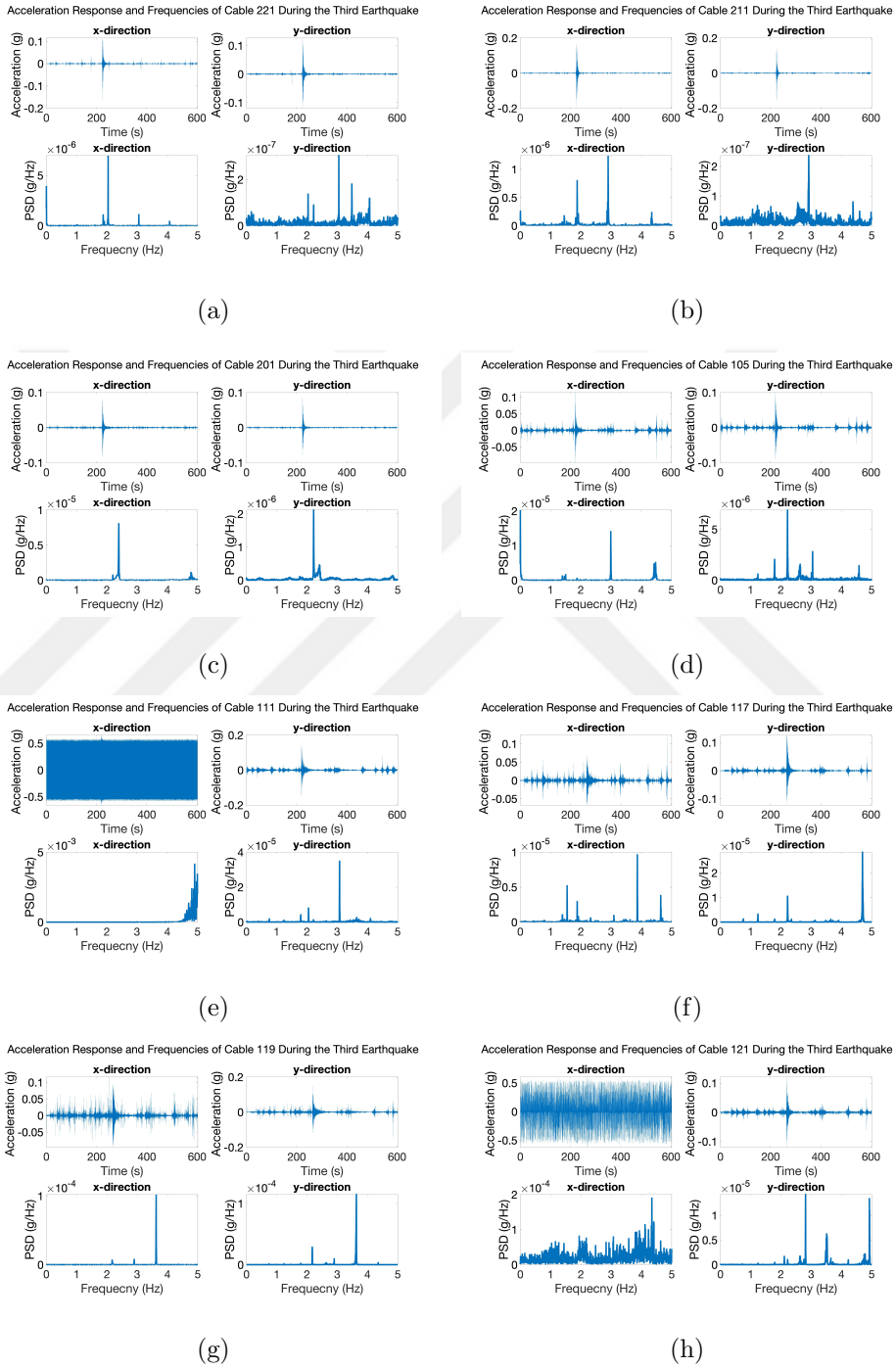


Figure 3.45. (a) Vibration analysis using existing accelerometer for dataset-6 in cable 221, (b) cable 211, (c) cable 201, (d) cable 105, (e) cable 111, (f) cable 117, (g) cable 119, (h) cable 121.

Before the forth earthquake, the response of the eight cables according to time and PSDs without any signal processing operation is given in Figure 3.46.

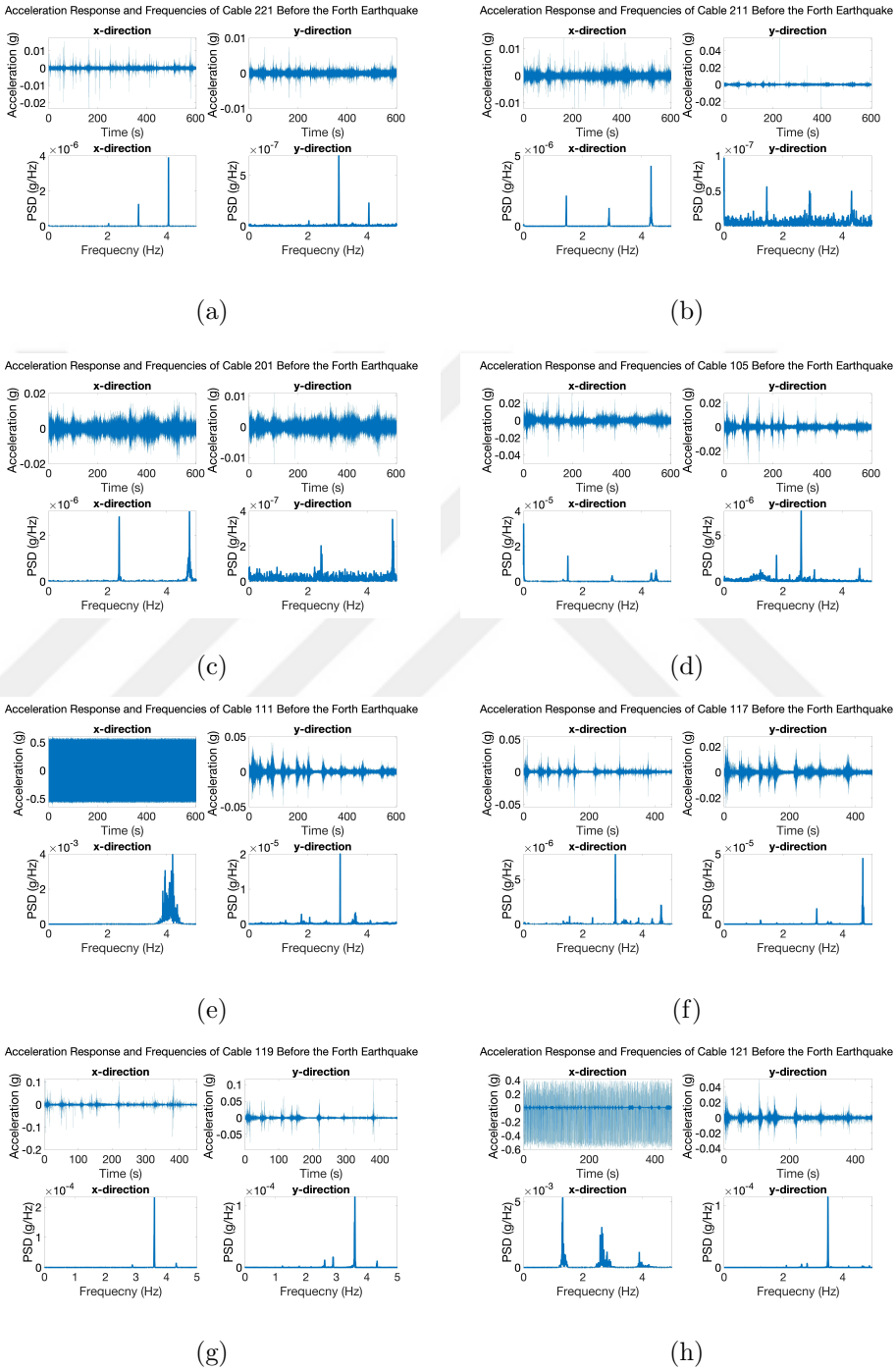


Figure 3.46. (a) Vibration analysis using existing accelerometer for dataset-7 in cable 221, (b) cable 211, (c) cable 201, (d) cable 105, (e) cable 111, (f) cable 117, (g) cable 119, (h) cable 121.

During the forth earthquake, the response of the eight cables according to time and PSDs without any signal processing operation is given in Figure 3.47.

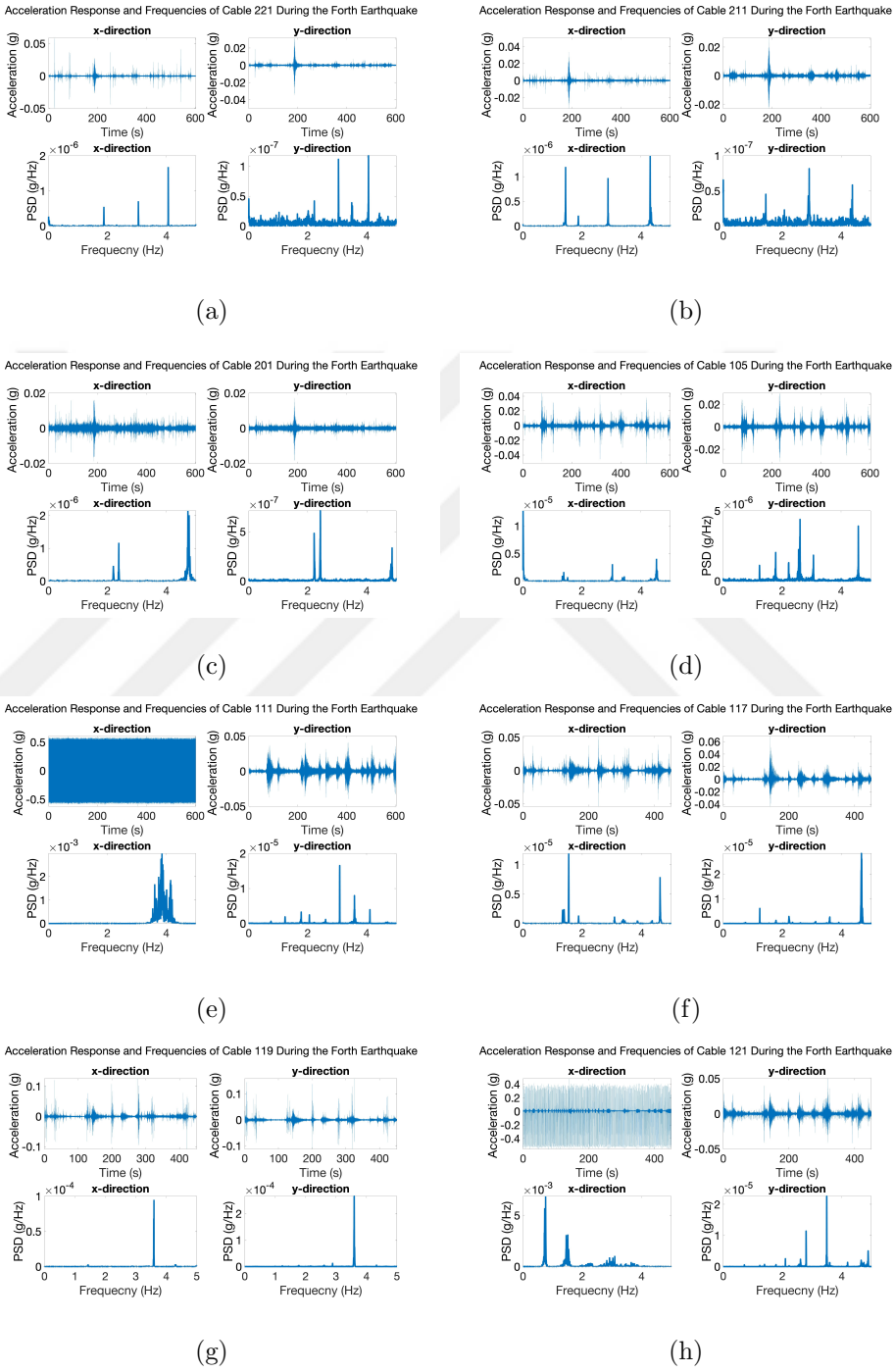


Figure 3.47. (a) Vibration analysis using existing accelerometer for dataset-8 in cable 221, (b) cable 211, (c) cable 201, (d) cable 105, (e) cable 111, (f) cable 117, (g) cable 119, (h) cable 121.

According to vibration method formula, the cable tension in each mode was estimated by using the mass of the cable in unit length, the length of the cable, the modulus of elasticity, the moment of inertia and the natural frequencies of accelerometers in the frequency domain. Cable tensions are summarized for all eight data sets in Table 3.5.

For the Cable-221, Modulus of Elasticity, E ($\mathrm{N\,m^{-2}}$), is 2×10^{11}, Moment of Inertia, I ($\mathrm{m^4}$), is 2.6×10^{-5}, mass of cable per unit length, m (kg/m), is 141.6 and length of the cable, l (m), is 238. These values are used in vibration analysis formula for Cable-221. Natural frequencies and cable tensions are summarized for Cable-221 in Table 3.5.

For the Cable-211, Modulus of Elasticity, E ($\mathrm{N\,m^{-2}}$), is 2×10^{11}, Moment of Inertia, I ($\mathrm{m^4}$), is 1.8×10^{-5}, mass of cable per unit length, m (kg/m), is 118 and length of the cable, l (m), is 167. These values are used in vibration analysis formula for Cable-211. Natural frequencies and cable tensions are summarized for Cable-211 in Table 3.6.

For the Cable-201, Modulus of Elasticity, E ($\mathrm{N\,m^{-2}}$), is 2×10^{11}, Moment of Inertia, I ($\mathrm{m^4}$), is 6.7×10^{-6}, mass of cable per unit length, m (kg/m), is 71.98 and length of the cable, l (m), is 107. These values are used in vibration analysis formula for Cable-201. Natural frequencies and cable tensions are summarized for Cable-201 in Table 3.7.

For the Cable-105, Modulus of Elasticity, E ($\mathrm{N\,m^{-2}}$), is 2×10^{11}, Moment of Inertia, I ($\mathrm{m^4}$), is 6.7×10^{-6}, mass of cable per unit length, m (kg/m), is 71.98 and length of the cable, l (m), is 147. These values are used in vibration analysis formula for Cable-105. Natural frequencies and cable tensions are summarized for Cable-105 in Table 3.8.

For the Cable-111, Modulus of Elasticity, E ($\mathrm{N\,m^{-2}}$), is 2×10^{11}, Moment of Inertia, I ($\mathrm{m^4}$), is 1.1×10^{-5}, mass of cable per unit length, m (kg/m), is 94.4 and length of the cable, l (m), is 233. These values are used in vibration analysis formula for Cable-111. Natural frequencies and cable tensions are summarized for Cable-111 in Table 3.9.

For the Cable-117, Modulus of Elasticity, E ($\mathrm{N\,m^{-2}}$), is 2×10^{11}, Moment of Inertia, I ($\mathrm{m^4}$), is 1.5×10^{-5}, mass of cable per unit length, m (kg/m), is 107.38 and length of the cable, l (m), is 326. These values are used in vibration analysis formula for Cable-117. Natural frequencies and cable tensions are summarized for Cable-117 in Table 3.10.

For the Cable-119, Modulus of Elasticity, E ($\mathrm{N\,m^{-2}}$), is 2×10^{11}, Moment of Inertia, I ($\mathrm{m^4}$), is 1.6×10^{-5}, mass of cable per unit length, m (kg/m), is 112.1 and length of the cable, l (m), is 358. These values are used in vibration analysis formula for Cable-119. Natural frequencies and cable tensions are summarized for Cable-119 in Table 3.11.

For the Cable-121, Modulus of Elasticity, E ($\mathrm{N\,m^{-2}}$), is 2×10^{11}, Moment of Inertia, I ($\mathrm{m^4}$), is 1.8×10^{-5}, mass of cable per unit length, m (kg/m), is 118 and length of the cable, l (m), is 390. These values are used in vibration analysis formula for Cable-121. Natural frequencies and cable tensions are summarized for Cable-121 in Table 3.12.

Table 3.5. Natural frequencies and cable tensions for cable-221.

Cable 221		fn						Cable Tension (kN)					
		f1 n=1	f2 n=2	f3 n=3	f4 n=4	f5 n=5	f6 n=6	1	2	3	4	5	6
Data	x-dir	0.504	1.010	1.511	2.011	2.505	3.012	8133.89	8180.61	8126.88	8096.13	8034.16	8053.98
Set-1	y-dir	0.510	1.007	1.508	2.011	-	3.012	8332.31	8131.26	8094.07	8096.13	-	8053.98
Data	x-dir	0.500	1.010	-	2.008	2.509	3.009	8035.58	8180.61	-	8071.55	8053.78	8037.61
Set-2	y-dir	0.510	1.004	1.508	2.007	2.507	3.009	8332.31	8082.06	8094.07	8061.25	8042.65	8035.95
Data	x-dir	0.504	1.010	1.511	2.008	2.521	-	8133.89	8180.61	8126.88	8071.55	8132.59	-
Set-3	y-dir	-	1.019	1.526	2.039	2.545	3.049	-	8329.71	8292.06	8319.12	8291.35	8251.83
Data	x-dir	0.500	1.007	1.511	2.014	2.509	3.003	8035.58	8131.26	8126.88	8120.75	8053.78	8004.93
Set-4	y-dir	-	1.016	1.526	2.036	2.542	3.052	-	8279.92	8292.06	8294.20	8271.37	8268.41
Data	x-dir	-	-	-	-	-	-	-	-	-	-	-	-
Set-5	y-dir	-	-	-	-	-	-	-	-	-	-	-	-
Data	x-dir	0.507	1.019	-	2.045	2.533	3.058	8232.80	8329.71	-	8369.15	8211.78	8301.63
Set-6	y-dir	0.558	-	1.535	2.039	-	3.055	10005.57	-	8391.90	8319.12	-	8285.01
Data	x-dir	0.528	-	-	2.036	-	3.059	8941.84	-	-	8294.20	-	8306.26
Set-7	y-dir	0.519	1.031	-	2.029	2.530	3.043	8634.38	8530.39	-	8244.48	8191.96	8218.66
Data	x-dir	0.467	1.038	-	2.039	-	3.049	6993.68	8631.79	-	8319.12	-	8251.83
Set-8	y-dir	-	1.028	-	2.017	-	3.043	-	8480.00	-	8145.41	-	8218.66

Table 3.6. Natural frequencies and cable tensions for cable-211.

Cable 211		fn						Cable Tension (kN)					
		f1 n=1	f2 n=2	f3 n=3	f4 n=4	f5 n=5	f6 n=6	1	2	3	4	5	6
Data	x-dir	0.723	1.447	2.167	2.744	-	-	6884.85	6881.10	6855.61	6172.85	-	-
Set-1	y-dir	0.726	1.447	2.170	2.884	-	-	6943.07	6881.10	6874.96	6822.79	-	-
Data	x-dir	0.723	1.443	2.164	2.869	3.589	4.309	6884.27	6852.09	6836.29	6750.56	6750.99	6745.08
Set-2	y-dir	0.726	1.443	2.167	2.878	3.601	4.309	6943.07	6852.09	6855.61	6793.87	6797.18	6745.08
Data	x-dir	0.723	1.447	2.161	2.881	3.574	4.324	6884.85	6881.10	6816.94	6808.32	6693.44	6793.25
Set-3	y-dir	0.735	1.465	2.197	2.927	3.656	4.385	7119.25	7056.53	7050.42	7027.06	7007.12	6987.65
Data	x-dir	0.720	1.447	2.164	2.881	3.586	4.294	6826.85	6881.10	6836.29	6808.32	6739.47	6697.07
Set-4	y-dir	-	1.465	2.194	2.927	3.656	4.385	-	7056.53	7030.76	7027.06	7007.12	6987.65
Data	x-dir	-	-	-	-	-	-	-	-	-	-	-	-
Set-5	y-dir	-	1.459	2.164	2.905	-	4.355	-	6997.84	6836.29	6924.52	-	6890.11
Data	x-dir	0.766	1.453	-	2.902	3.595	4.343	7722.41	6939.40	-	6909.95	6774.07	6851.28
Set-6	y-dir	-	-	-	2.921	-	-	-	-	-	6997.66	-	-
Data	x-dir	0.708	1.450	-	2.896	3.510	4.318	6597.36	6910.17	-	6880.85	6454.41	6773.97
Set-7	y-dir	-	1.450	2.069	2.876	-	4.306	-	6910.17	6250.56	6785.97	-	6736.48
Data	x-dir	0.690	1.442	2.203	2.887	-	4.318	6260.46	6842.50	7089.68	6837.27	-	6773.97
Set-8	y-dir	0.766	1.447	2.075	2.917	-	4.382	7722.41	6881.10	6287.60	6983.01	-	6977.84

Table 3.7. Natural frequencies and cable tensions for cable-201.

Cable 201		fn						Cable Tension (kN)					
		f1 n=1	f2 n=2	f3 n=3	f4 n=4	f5 n=5	f6 n=6	1	2	3	4	5	6
Data	x-dir	1.212	-	3.629	-	-	-	4837.51	-	4812.29	-	-	-
Set-1	y-dir	1.233	2.463	-	-	-	-	5009.62	4993.88	-	-	-	-
Data	x-dir	1.202	2.390	3.583	4.758	5.914	-	4764.62	4701.00	4691.38	4645.58	4584.20	-
Set-2	y-dir	1.230	2.460	3.674	4.868	6.097	-	4984.86	4981.50	4934.74	4863.43	4874.19	-
Data	x-dir	1.205	2.390	3.589	4.764	-	-	4788.83	4701.00	4707.43	4657.54	-	-
Set-3	y-dir	1.230	2.451	3.671	4.883	6.107	-	4984.86	4944.44	4926.51	4894.09	4888.93	-
Data	x-dir	1.205	2.399	3.589	4.767	5.887	7.166	4788.83	4737.11	4707.43	4663.55	4541.45	4661.15
Set-4	y-dir	1.227	2.451	3.674	4.880	6.003	7.288	4960.16	4944.44	4934.74	4887.95	4723.26	4822.70
Data	x-dir	-	2.423	-	-	-	-	-	4834.15	-	-	-	-
Set-5	y-dir	1.199	2.466	3.726	4.849	-	-	4740.47	5006.26	5075.37	4826.78	-	-
Data	x-dir	-	2.396	-	4.779	-	-	-	4725.06	-	4687.55	-	-
Set-6	y-dir	1.184	2.411	3.598	4.840	-	-	4620.58	4785.51	4731.51	4808.51	-	-
Data	x-dir	-	2.393	-	4.773	-	7.108	-	4713.02	-	4675.54	-	4585.36
Set-7	y-dir	-	2.441	-	4.861	-	7.315	-	4907.55	-	4851.21	-	4859.42
Data	x-dir	1.205	2.386	3.653	4.730	6.046	7.098	4788.83	4688.96	4877.39	4591.88	4791.13	4573.46
Set-8	y-dir	1.181	2.429	3.683	4.861	6.073	7.263	4596.80	4858.54	4959.40	4851.21	4835.02	4790.16

Table 3.8. Natural frequencies and cable tensions for cable-105.

Cable 105		fn						Cable Tension (kN)					
		f1 n=1	f2 n=2	f3 n=3	f4 n=4	f5 n=5	f6 n=6	1	2	3	4	5	6
Data	x-dir	0.757	1.508	2.267	3.018	3.769	-	3563.18	3532.72	3548.87	3532.76	3520.25	-
Set-1	y-dir	0.769	1.529	-	-	-	-	3679.07	3633.61	-	-	-	-
Data	x-dir	0.751	1.498	2.243	2.991	3.745	4.477	3505.93	3489.90	3472.73	3468.57	3474.61	3442.53
Set-2	y-dir	0.769	1.526	2.292	3.033	3.818	-	3679.07	3619.12	3625.81	3568.67	3612.45	-
Data	x-dir	0.757	1.511	2.267	3.018	3.787	4.517	3563.18	3547.04	3548.87	3532.76	3554.69	3504.19
Set-3	y-dir	0.772	1.529	2.295	3.058	3.815	-	3708.33	3633.61	3635.48	3626.49	3606.66	-
Data	x-dir	0.751	1.498	2.237	2.994	3.751	4.486	3505.93	3489.90	3453.84	3475.67	3485.99	3456.71
Set-4	y-dir	0.769	1.529	2.295	3.052	-	-	3679.07	3633.61	3635.48	3612.00	-	-
Data	x-dir	-	1.501	-	3.003	-	4.489	-	3504.13	-	3497.03	-	3461.45
Set-5	y-dir	-	-	-	-	-	-	-	-	-	-	-	-
Data	x-dir	-	-	2.222	-	-	-	-	-	3406.80	-	-	-
Set-6	y-dir	-	1.501	-	2.994	-	4.477	-	3504.13	-	3475.67	-	3442.53
Data	x-dir	-	1.501	2.247	3.003	-	4.492	-	3504.13	3485.27	3497.03	-	3466.19
Set-7	y-dir	-	-	2.222	3.064	-	-	-	-	3406.80	3641.01	-	-
Data	x-dir	-	1.517	-	3.037	-	4.535	-	3575.77	-	3575.87	-	3532.83
Set-8	y-dir	-	-	2.225	3.064	-	4.587	-	-	3416.18	3641.01	-	3614.62

Table 3.9. Natural frequencies and cable tensions for cable-111.

Cable 111		fn						Cable Tension (kN)					
		f1 n=1	f2 n=2	f3 n=3	f4 n=4	f5 n=5	f6 n=6	1	2	3	4	5	6
Data	x-dir	-	-	-	-	-	-	-	-	-	-	-	-
Set-1	y-dir	0.522	1.028	1.538	2.054	2.563	3.073	5582.20	5418.91	5384.81	5397.97	5378.29	5363.12
Data	x-dir	-	1.007	-	-	-	-	-	5196.08	-	-	-	-
Set-2	y-dir	0.522	1.025	1.535	2.048	2.554	3.070	5582.20	5386.80	5363.39	5365.91	5339.85	5352.45
Data	x-dir	-	-	-	-	-	-	-	-	-	-	-	-
Set-3	y-dir	-	1.025	1.538	2.051	2.560	3.073	-	5386.80	5384.81	5381.93	5365.44	5363.12
Data	x-dir	-	-	-	-	-	-	-	-	-	-	-	-
Set-4	y-dir	0.522	1.025	1.538	2.051	2.560	3.073	5582.20	5386.80	5384.81	5381.93	5365.44	5363.12
Data	x-dir	-	-	-	-	-	-	-	-	-	-	-	-
Set-5	y-dir	-	-	-	2.057	-	3.082	-	-	-	5414.03	-	5395.23
Data	x-dir	-	-	-	-	-	-	-	-	-	-	-	-
Set-6	y-dir	-	-	-	2.054	-	3.082	-	-	-	5397.97	-	5395.23
Data	x-dir	-	-	-	-	-	-	-	-	-	-	-	-
Set-7	y-dir	-	1.062	1.523	2.057	-	3.088	-	5778.55	5278.41	5414.03	-	5416.66
Data	x-dir	-	-	-	-	-	-	-	-	-	-	-	-
Set-8	y-dir	-	-	-	2.060	2.609	3.088	-	-	-	5430.17	5572.43	5416.66

Table 3.10. Natural frequencies and cable tensions for cable-117.

Cable 117		fn						Cable Tension (kN)					
		f1 n=1	f2 n=2	f3 n=3	f4 n=4	f5 n=5	f6 n=6	1	2	3	4	5	6
Data	x-dir	0.388	0.775	1.166	-	1.932	2.328	6856.60	6855.79	6890.48	-	6807.02	6865.21
Set-1	y-dir	0.409	0.787	1.181	1.572	1.965	2.359	7633.33	7073.47	7072.12	7042.89	7046.04	7046.61
Data	x-dir	-	0.772	1.160	1.544	1.926	2.313	-	6801.92	6818.53	6798.70	6764.05	6775.39
Set-2	y-dir	-	-	1.120	-	-	2.350	-	-	6359.85	-	-	6991.92
Data	x-dir	0.385	0.772	1.160	1.547	1.932	2.319	6749.03	6801.92	6818.53	6825.60	6807.02	6811.28
Set-3	y-dir	-	0.784	1.175	1.566	1.959	2.350	-	7018.73	6999.23	6988.20	7002.18	6991.92
Data	x-dir	0.385	0.775	1.163	1.547	1.929	2.316	6749.03	6855.79	6854.46	6825.60	6785.52	6793.30
Set-4	y-dir	0.381	0.784	1.178	1.569	1.959	2.350	6642.35	7018.73	7035.63	7015.48	7002.18	6991.92
Data	x-dir	-	-	-	-	-	-	-	-	-	-	-	-
Set-5	y-dir	-	0.757	1.242	-	-	2.225	-	6535.68	7822.29	-	-	6266.16
Data	x-dir	-	0.793	-	1.547	-	2.322	-	7183.57	-	6825.60	-	6829.24
Set-6	y-dir	-	0.760	1.242	-	-	2.222	-	6588.51	7822.29	-	-	6248.96
Data	x-dir	-	0.772	1.215	1.553	1.926	2.325	-	6801.92	7480.01	6879.56	6764.05	6847.21
Set-7	y-dir	-	0.757	1.230	-	-	-	-	6535.68	7669.21	-	-	-
Data	x-dir	-	-	-	1.544	1.877	-	-	-	-	6798.70	6425.03	-
Set-8	y-dir	-	0.757	1.236	1.544	-	2.219	-	6535.68	7745.50	6798.70	-	6231.79

Table 3.11. Natural frequencies and cable tensions for cable-119.

Cable 119		fn						Cable Tension (kN)					
		f1 n=1	f2 n=2	f3 n=3	f4 n=4	f5 n=5	f6 n=6	1	2	3	4	5	6
Data	x-dir	0.369	0.717	1.077	1.437	1.761	2.155	7835.92	7388.40	7408.16	7416.99	7121.50	7401.61
Set-1	y-dir	0.369	0.717	1.077	1.437	1.791	2.151	7835.92	7388.40	7408.16	7416.99	7370.72	7380.64
Data	x-dir	0.378	0.708	1.080	1.437	1.767	-	8229.29	7200.94	7450.18	7416.99	7171.05	-
Set-2	y-dir	-	0.717	1.080	1.437	1.791	-	-	7388.40	7450.18	7416.99	7370.72	-
Data	x-dir	0.357	0.717	1.074	1.434	1.791	2.151	7326.39	7388.40	7366.26	7385.53	7370.72	7380.64
Set-3	y-dir	-	0.726	1.089	1.453	1.816	2.176	-	7578.26	7577.09	7575.39	7573.21	7549.27
Data	x-dir	0.357	0.717	1.077	1.443	1.794	2.148	7326.39	7388.40	7408.16	7480.11	7395.86	7359.71
Set-4	y-dir	0.375	0.726	1.089	1.453	1.816	2.176	8097.08	7578.26	7577.09	7575.39	7573.21	7549.27
Data	x-dir	-	-	-	-	-	-	-	-	-	-	-	-
Set-5	y-dir	-	0.745	1.144	1.443	1.791	-	-	7965.24	8360.63	7480.11	7370.72	-
Data	x-dir	-	0.723	1.166	1.398	1.764	2.176	-	7514.72	8675.72	7013.03	7146.29	7549.27
Set-6	y-dir	0.375	0.745	1.144	1.453	1.794	2.176	8097.08	7965.24	8360.63	7575.39	7395.86	7549.27
Data	x-dir	-	-	-	-	-	-	-	-	-	-	-	-
Set-7	y-dir	-	-	1.230	1.447	1.782	2.170	-	-	9656.11	7511.77	7295.55	7506.95
Data	x-dir	-	-	-	1.434	1.883	2.170	-	-	-	7385.53	8143.98	7506.95
Set-8	y-dir	-	0.757	1.236	1.544	-	2.219	-	6535.68	7745.50	6798.70	-	6231.79

Table 3.12. Natural frequencies and cable tensions for cable-121.

Cable 121		fn						Cable Tension (kN)					
		f1 n=1	f2 n=2	f3 n=3	f4 n=4	f5 n=5	f6 n=6	1	2	3	4	5	6
Data	x-dir	-	-	-	-	-	-	-	-	-	-	-	-
Set-1	y-dir	0.366	0.711	1.065	1.443	1.761	2.213	9627.73	9073.61	9046.47	9345.54	8898.25	9753.94
Data	x-dir	0.366	-	-	-	-	-	9627.73	-	-	-	-	-
Set-2	y-dir	-	-	1.062	-	1.773	2.124	-	-	8994.72	-	9022.16	8988.60
Data	x-dir	-	-	-	-	-	-	-	-	-	-	-	-
Set-3	y-dir	0.375	0.708	1.062	1.419	1.770	2.124	10115.13	8995.88	8994.72	9032.01	8991.13	8988.60
Data	x-dir	-	-	-	-	-	-	-	-	-	-	-	-
Set-4	y-dir	-	0.708	1.062	1.413	1.770	2.124	-	8995.88	8994.72	8954.37	8991.13	8988.60
Data	x-dir	-	-	-	-	-	-	-	-	-	-	-	-
Set-5	y-dir	0.394	0.714	-	1.462	1.791	2.121	11126.09	9151.66	-	9584.22	9209.58	8962.78
Data	x-dir	-	-	-	-	-	-	-	-	-	-	-	-
Set-6	y-dir	-	0.717	-	1.407	1.797	2.115	-	9230.06	-	8877.19	9272.55	8911.25
Data	x-dir	-	-	-	-	-	-	-	-	-	-	-	-
Set-7	y-dir	-	0.717	-	1.398	-	2.103	-	9230.06	-	8762.05	-	8808.56
Data	x-dir	-	-	-	-	-	-	-	-	-	-	-	-
Set-8	y-dir	-	0.757	1.236	1.544	-	2.219	-	6535.68	7745.50	6798.70	-	6231.79

The average forces of the cable tensions obtained for all eight data sets in the cables with accelerometer sensors are shown in Table 3.13.

Table 3.13. Average cable tension for all cables and data sets.

	Cable 221	**Cable 211**	**Cable 201**	**Cable 105**	**Cable 111**	**Cable 117**	**Cable 119**	**Cable 121**
Before the 1st Earthquake	8121.22	6789.54	4913.32	3572.92	5420.88	7017.23	7447.78	9290.92
During the 1st Earthquake	8093.40	6817.18	4802.55	3541.76	5369.53	6758.62	7454.97	9158.30
Before the 2nd Earthquake	8212.96	6927.16	4832.63	3587.39	5376.42	6892.15	7461.01	9186.24
During the 2nd Earthquake	8170.83	6899.84	4781.06	3542.82	5410.72	6880.83	7525.74	8984.94
Before the 3rd Earthquake	-	6912.19	4896.61	3487.54	5404.63	6874.71	7794.17	9606.86
During the 3rd Earthquake	8494.07	7032.46	4726.45	3457.28	5396.60	6916.36	7712.95	9072.76
Before the 4th Earthquake	8420.27	6699.99	4765.35	3500.07	5471.91	6996.81	7992.60	8933.56
During the 4th Earthquake	8148.64	6865.58	4766.90	3559.38	5473.09	6755.90	7549.00	8943.51

3.2.3. Cable Tension Calculation with Image Processing

The displacement response in pixel scale in time domain and the PSD values in the frequency domain obtained by taking FFT of displacement response were calculated. The positions where the video recording was taken are shown in Figure 3.48.

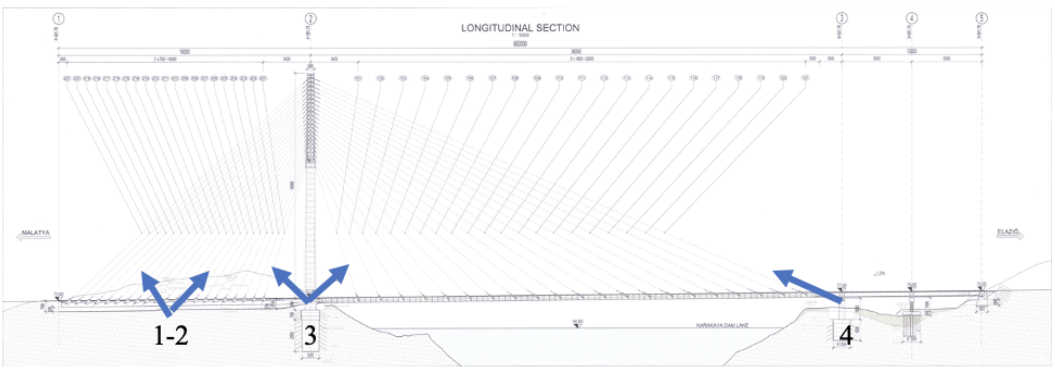


Figure 3.48. Positions taken the video recording.

Photos during the recordings in the field are shown in Figure 3.49.



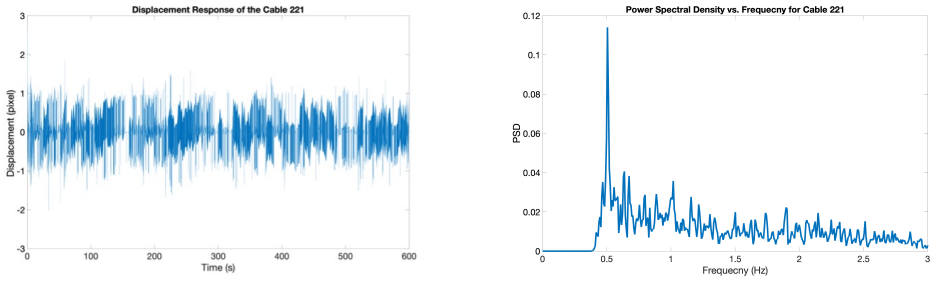
(a) (b)

(c) (d)

Figure 3.49. (a) Site video recording at position-1, (b) position-2, (c) position-3, (d) position-4.

The displacement graph obtained for Cable-221 is shown in Figure 3.50(a). In addition, high-pass filtered PSD values in the frequency domain are shown in Fig-

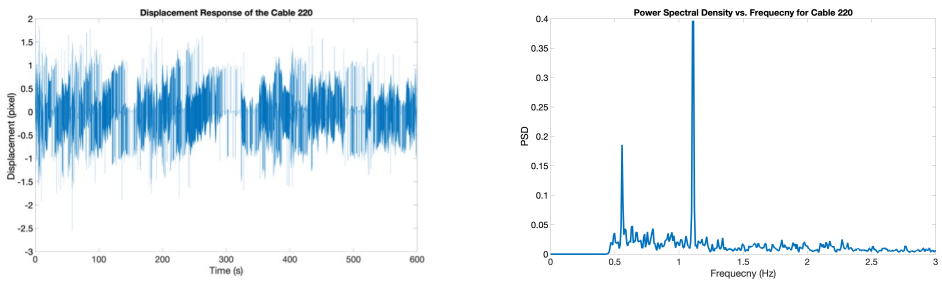
ure 3.50(b). The reason for applying a high-pass filter is that high amplitudes occur in areas close to zero. These values dominate the cable's natural frequencies, making it difficult to read.



(a) (b)

Figure 3.50. (a) Displacement response of cable 221 using vision-based monitoring, (b) PSDs and natural frequencies of cable 221.

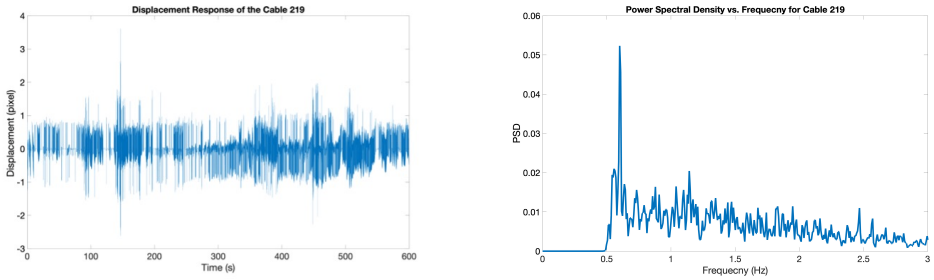
The displacement graph obtained for Cable-220 is shown in Figure 3.51(a). In addition, high-pass filtered PSD values in the frequency domain are shown in Figure 3.51(b).



(a) (b)

Figure 3.51. (a) Displacement response of cable 220 using vision-based monitoring, (b) PSDs and natural frequencies of cable 220.

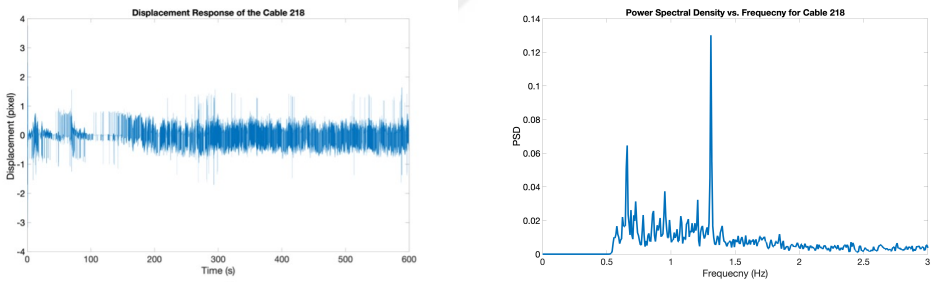
The displacement graph obtained for Cable-219 is shown in Figure 3.52(a). In addition, high-pass filtered PSD values in the frequency domain are shown in Figure 3.52(b).



(a) (b)

Figure 3.52. (a) Displacement response of cable 219 using vision-based monitoring, (b) PSDs and natural frequencies of cable 219.

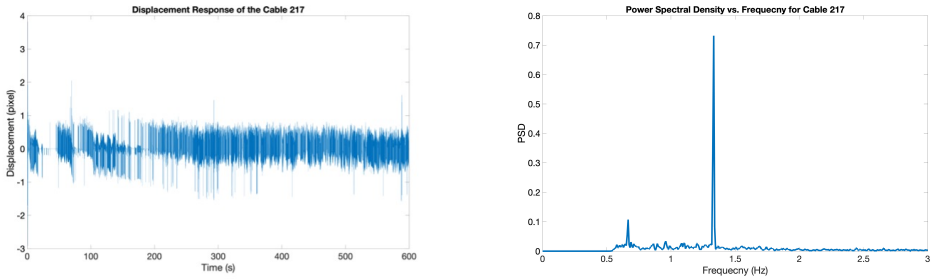
The displacement graph obtained for Cable-218 is shown in Figure 3.53(a). In addition, high-pass filtered PSD values in the frequency domain are shown in Figure 3.53(b).



(a) (b)

Figure 3.53. (a) Displacement response of cable 218 using vision-based monitoring, (b) PSDs and natural frequencies of cable 218.

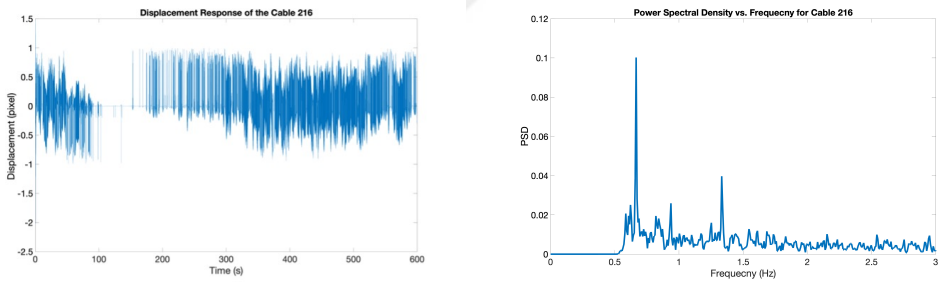
The displacement graph obtained for Cable-217 is shown in Figure 3.54(a). In addition, high-pass filtered PSD values in the frequency domain are shown in Figure 3.54(b).



(a) (b)

Figure 3.54. (a) Displacement response of cable 217 using vision-based monitoring, (b) PSDs and natural frequencies of cable 217.

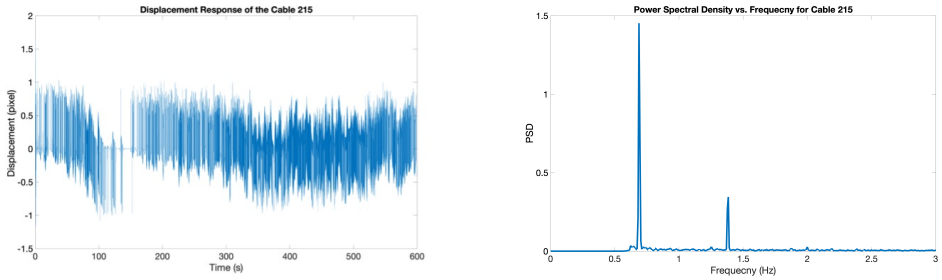
The displacement graph obtained for Cable-216 is shown in Figure 3.55(a). In addition, high-pass filtered PSD values in the frequency domain are shown in Figure 3.55(b).



(a) (b)

Figure 3.55. (a) Displacement response of cable 216 using vision-based monitoring, (b) PSDs and natural frequencies of cable 216.

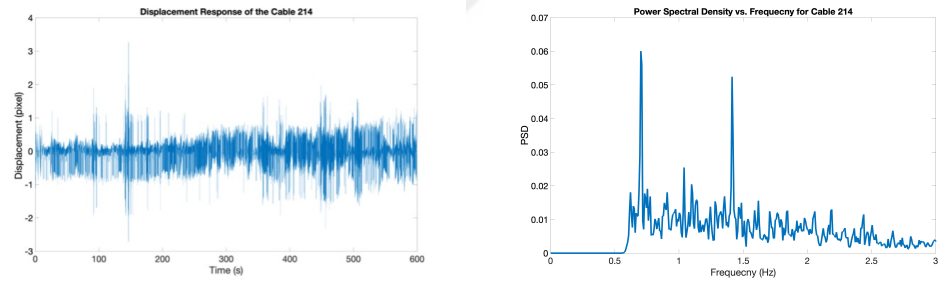
The displacement graph obtained for Cable-215 is shown in Figure 3.56(a). In addition, high-pass filtered PSD values in the frequency domain are shown in Figure 3.56(b).



(a) (b)

Figure 3.56. (a) Displacement response of cable 215 using vision-based monitoring, (b) PSDs and natural frequencies of cable 215.

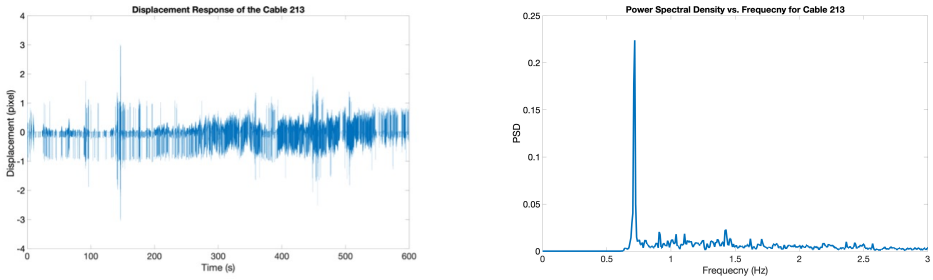
The displacement graph obtained for Cable-214 is shown in Figure 3.57(a). In addition, high-pass filtered PSD values in the frequency domain are shown in Figure 3.57(b).



(a) (b)

Figure 3.57. (a) Displacement response of cable 214 using vision-based monitoring, (b) PSDs and natural frequencies of cable 214.

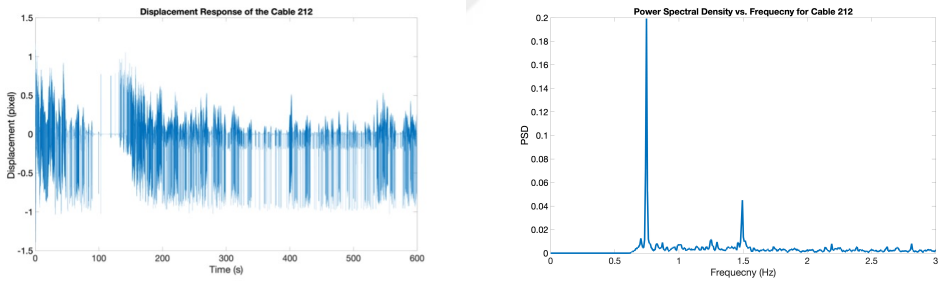
The displacement graph obtained for Cable-213 is shown in Figure 3.58(a). In addition, high-pass filtered PSD values in the frequency domain are shown in Figure 3.58(b).



(a) (b)

Figure 3.58. (a) Displacement response of cable 213 using vision-based monitoring, (b) PSDs and natural frequencies of cable 213.

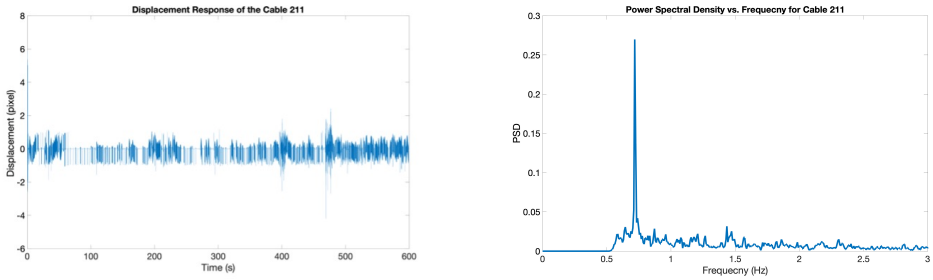
The displacement graph obtained for Cable-212 is shown in Figure 3.59(a). In addition, high-pass filtered PSD values in the frequency domain are shown in Figure 3.59(b).



(a) (b)

Figure 3.59. (a) Displacement response of cable 212 using vision-based monitoring, (b) PSDs and natural frequencies of cable 212.

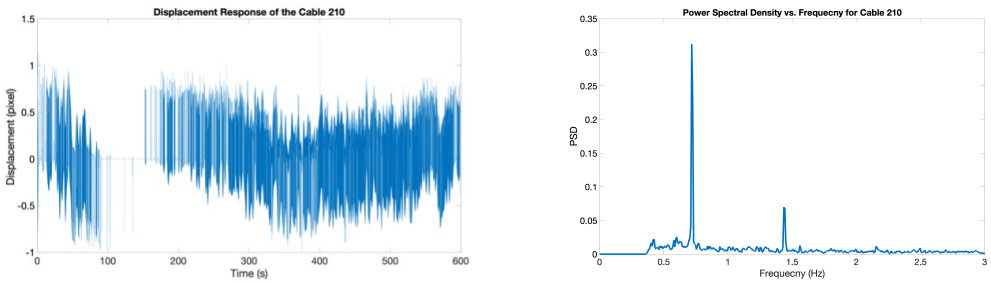
The displacement graph obtained for Cable-211 is shown in Figure 3.60(a). In addition, high-pass filtered PSD values in the frequency domain are shown in Figure 3.60(b).



(a) (b)

Figure 3.60. (a) Displacement response of cable 211 using vision-based monitoring, (b) PSDs and natural frequencies of cable 211.

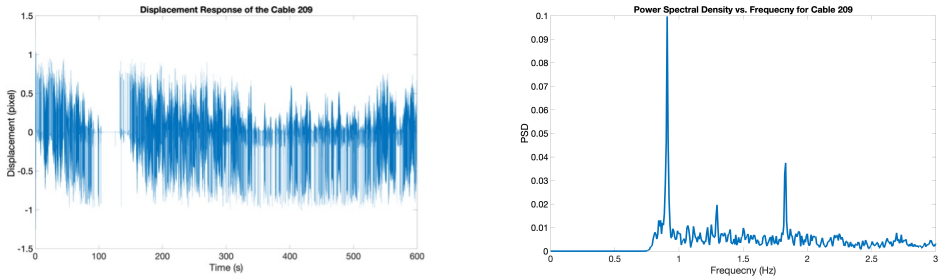
The displacement graph obtained for Cable-210 is shown in Figure 3.61(a). In addition, high-pass filtered PSD values in the frequency domain are shown in Figure 3.61(b).



(a) (b)

Figure 3.61. (a) Displacement response of cable 210 using vision-based monitoring, (b) PSDs and natural frequencies of cable 210.

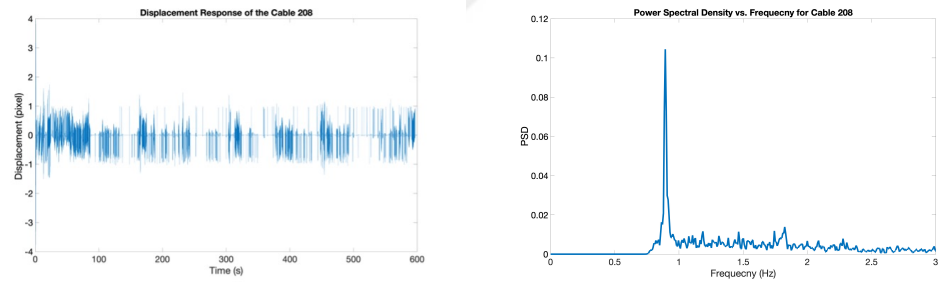
The displacement graph obtained for Cable-209 is shown in Figure 3.62(a). In addition, high-pass filtered PSD values in the frequency domain are shown in Figure 3.62(b).



(a) (b)

Figure 3.62. (a) Displacement response of cable 209 using vision-based monitoring, (b) PSDs and natural frequencies of cable 209.

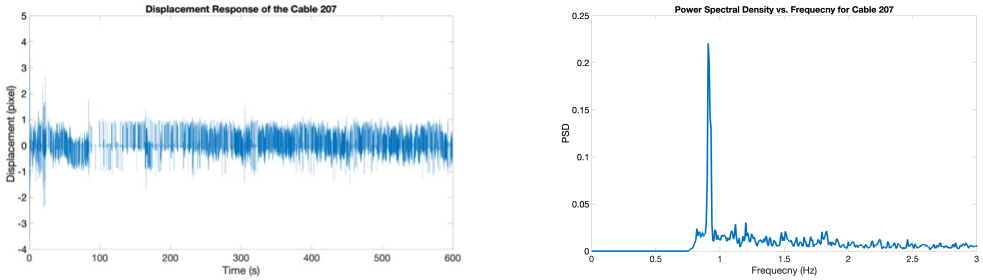
The displacement graph obtained for Cable-208 is shown in Figure 3.63(a). In addition, high-pass filtered PSD values in the frequency domain are shown in Figure 3.63(b).



(a) (b)

Figure 3.63. (a) Displacement response of cable 208 using vision-based monitoring, (b) PSDs and natural frequencies of cable 208.

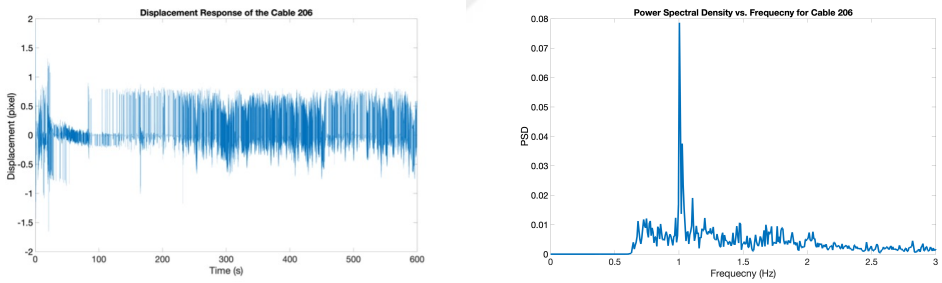
The displacement graph obtained for Cable-207 is shown in Figure 3.64(a). In addition, high-pass filtered PSD values in the frequency domain are shown in Figure 3.64(b).



(a) (b)

Figure 3.64. (a) Displacement response of cable 207 using vision-based monitoring, (b) PSDs and natural frequencies of cable 207.

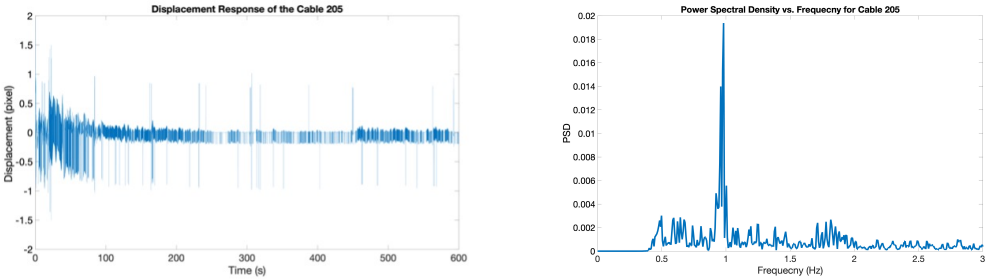
The displacement graph obtained for Cable-206 is shown in Figure 3.65(a). In addition, high-pass filtered PSD values in the frequency domain are shown in Figure 3.65(b).



(a) (b)

Figure 3.65. (a) Displacement response of cable 206 using vision-based monitoring, (b) PSDs and natural frequencies of cable 206.

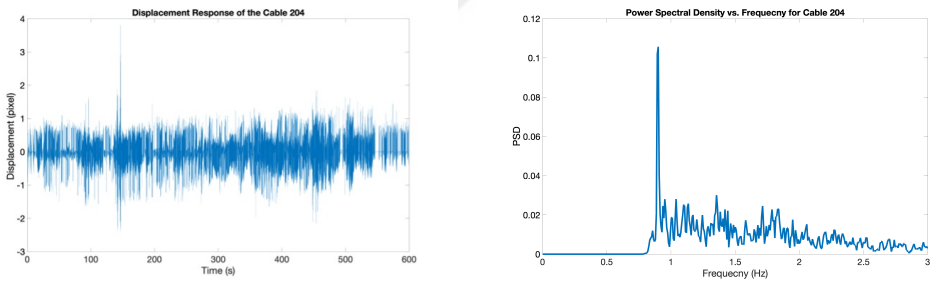
The displacement graph obtained for Cable-205 is shown in Figure 3.66(a). In addition, high-pass filtered PSD values in the frequency domain are shown in Figure 3.66(b).



(a) (b)

Figure 3.66. (a) Displacement response of cable 205 using vision-based monitoring, (b) PSDs and natural frequencies of cable 205.

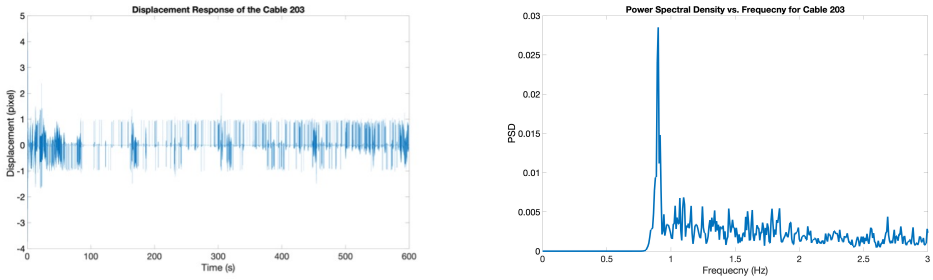
The displacement graph obtained for Cable-204 is shown in Figure 3.67(a). In addition, high-pass filtered PSD values in the frequency domain are shown in Figure 3.67(b).



(a) (b)

Figure 3.67. (a) Displacement response of cable 204 using vision-based monitoring, (b) PSDs and natural frequencies of cable 204.

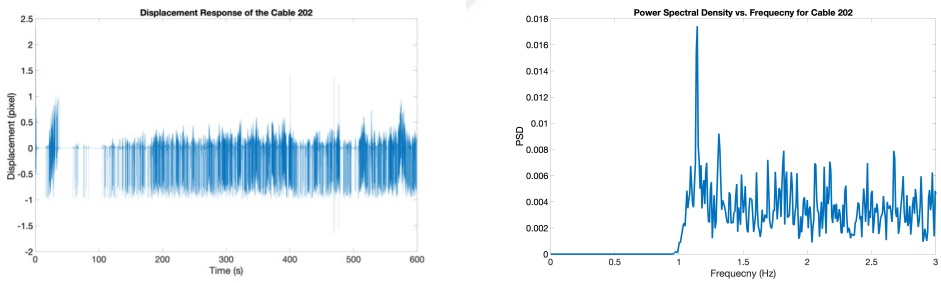
The displacement graph obtained for Cable-203 is shown in Figure 3.68(a). In addition, high-pass filtered PSD values in the frequency domain are shown in Figure 3.68(b).



(a) (b)

Figure 3.68. (a) Displacement response of cable 203 using vision-based monitoring, (b) PSDs and natural frequencies of cable 203.

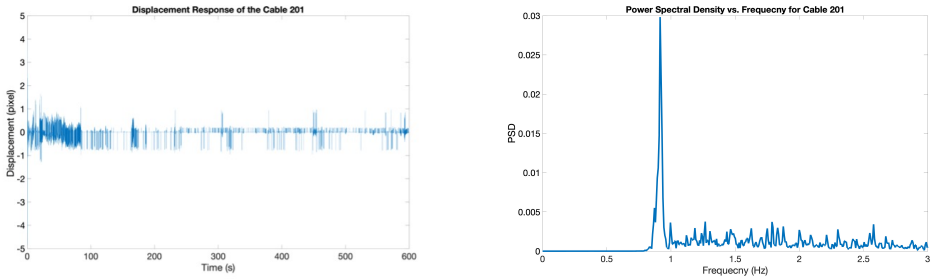
The displacement graph obtained for Cable-202 is shown in Figure 3.69(a). In addition, high-pass filtered PSD values in the frequency domain are shown in Figure 3.69(b).



(a) (b)

Figure 3.69. (a) Displacement response of cable 202 using vision-based monitoring, (b) PSDs and natural frequencies of cable 202.

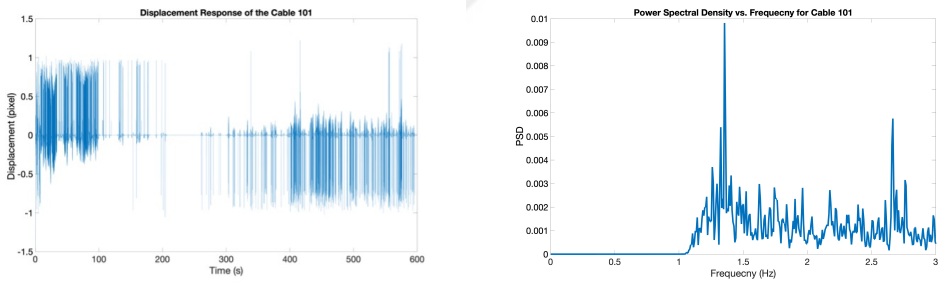
The displacement graph obtained for Cable-201 is shown in Figure 3.70(a). In addition, high-pass filtered PSD values in the frequency domain are shown in Figure 3.70(b).



(a) (b)

Figure 3.70. (a) Displacement response of cable 201 using vision-based monitoring, (b) PSDs and natural frequencies of cable 201.

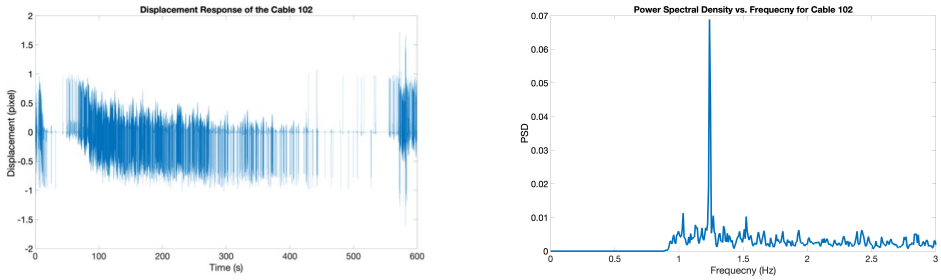
The displacement graph obtained for Cable-101 is shown in Figure 3.71(a). In addition, high-pass filtered PSD values in the frequency domain are shown in Figure 3.71(b).



(a) (b)

Figure 3.71. (a) Displacement response of cable 101 using vision-based monitoring, (b) PSDs and natural frequencies of cable 101.

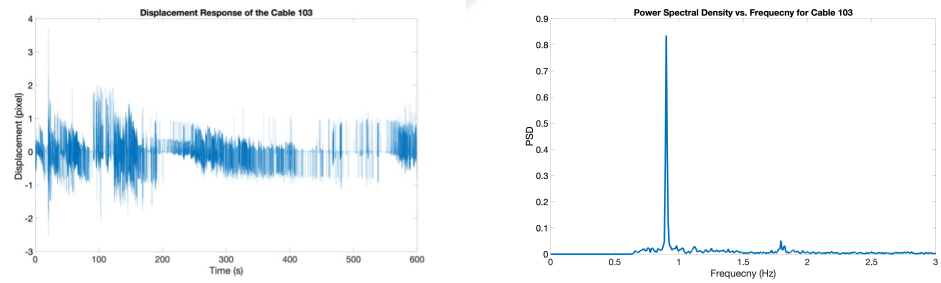
The displacement graph obtained for Cable-102 is shown in Figure 3.72(a). In addition, high-pass filtered PSD values in the frequency domain are shown in Figure 3.72(b).



(a) (b)

Figure 3.72. (a) Displacement response of cable 102 using vision-based monitoring, (b) PSDs and natural frequencies of cable 102.

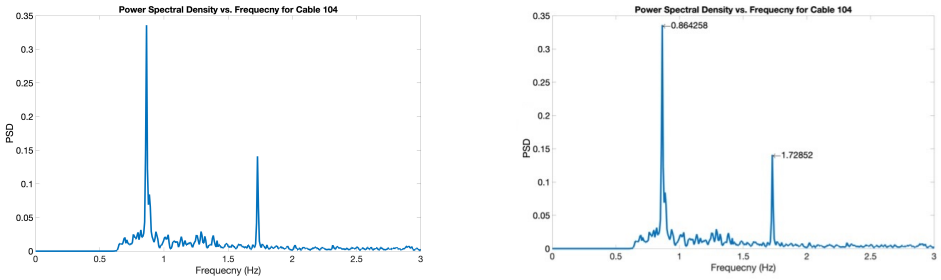
The displacement graph obtained for Cable-103 is shown in Figure 3.73(a). In addition, high-pass filtered PSD values in the frequency domain are shown in Figure 3.73(b).



(a) (b)

Figure 3.73. (a) Displacement response of cable 103 using vision-based monitoring, (b) PSDs and natural frequencies of cable 103.

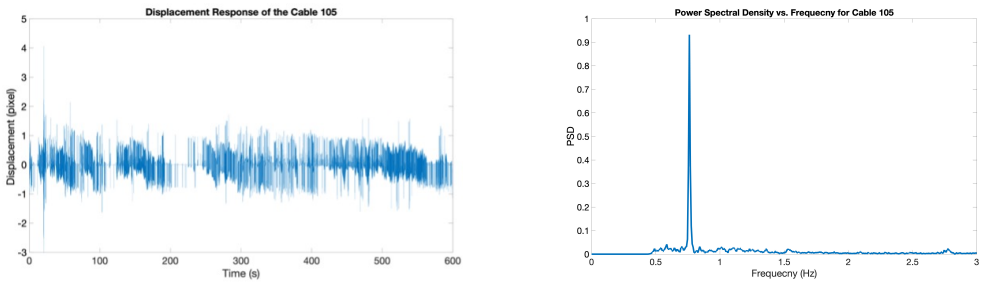
The displacement graph obtained for Cable-104 is shown in Figure 3.74(a). In addition, high-pass filtered PSD values in the frequency domain are shown in Figure 3.74(b).



(a) (b)

Figure 3.74. (a) Displacement response of cable 104 using vision-based monitoring, (b) PSDs and natural frequencies of cable 104.

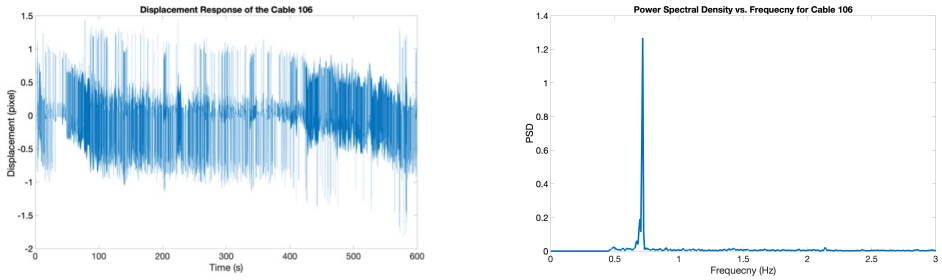
The displacement graph obtained for Cable-105 is shown in Figure 3.75(a). In addition, high-pass filtered PSD values in the frequency domain are shown in Figure 3.75(b).



(a) (b)

Figure 3.75. (a) Displacement response of cable 105 using vision-based monitoring, (b) PSDs and natural frequencies of cable 105.

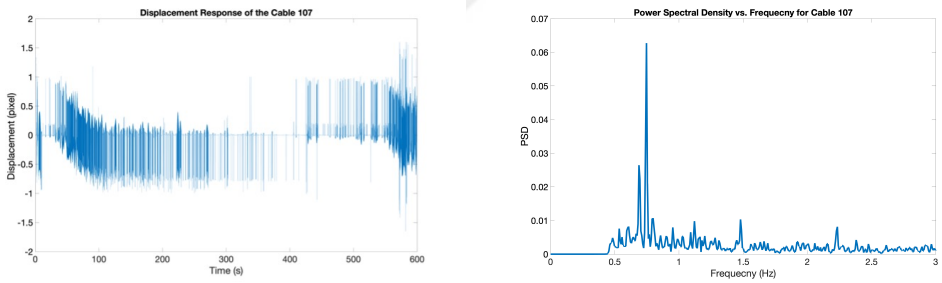
The displacement graph obtained for Cable-106 is shown in Figure 3.76(a). In addition, high-pass filtered PSD values in the frequency domain are shown in Figure 3.76(b).



(a) (b)

Figure 3.76. (a) Displacement response of cable 106 using vision-based monitoring, (b) PSDs and natural frequencies of cable 106.

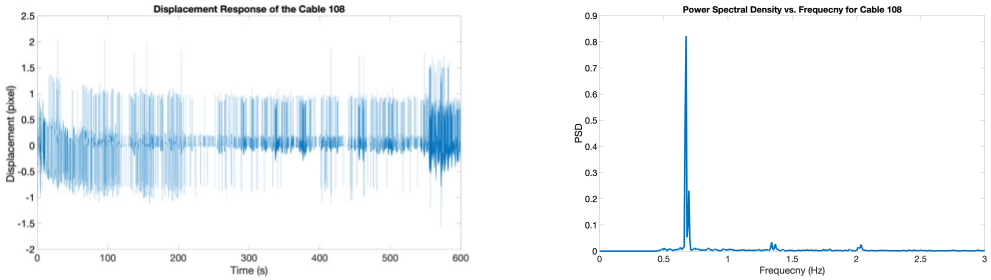
The displacement graph obtained for Cable-107 is shown in Figure 3.77(a). In addition, high-pass filtered PSD values in the frequency domain are shown in Figure 3.77(b).



(a) (b)

Figure 3.77. (a) Displacement response of cable 107 using vision-based monitoring, (b) PSDs and natural frequencies of cable 107.

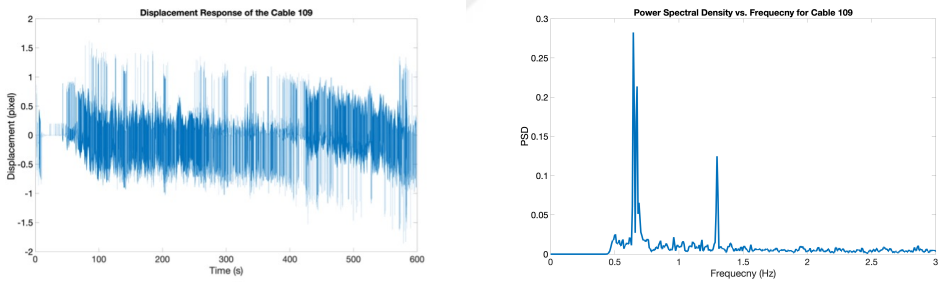
The displacement graph obtained for Cable-108 is shown in Figure 3.78(a). In addition, high-pass filtered PSD values in the frequency domain are shown in Figure 3.78(b).



(a) (b)

Figure 3.78. (a) Displacement response of cable 108 using vision-based monitoring, (b) PSDs and natural frequencies of cable 108.

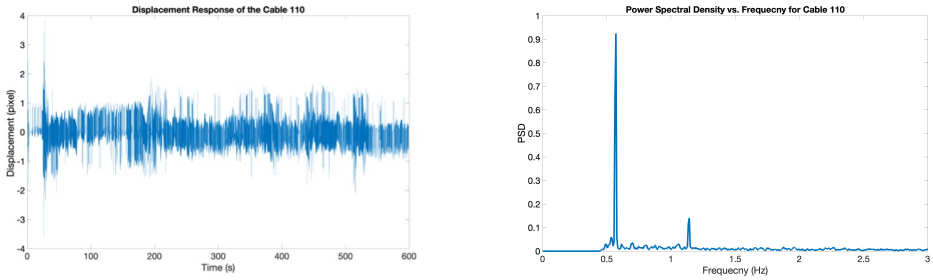
The displacement graph obtained for Cable-109 is shown in Figure 3.79(a). In addition, high-pass filtered PSD values in the frequency domain are shown in Figure 3.79(b).



(a) (b)

Figure 3.79. (a) Displacement response of cable 109 using vision-based monitoring, (b) PSDs and natural frequencies of cable 109.

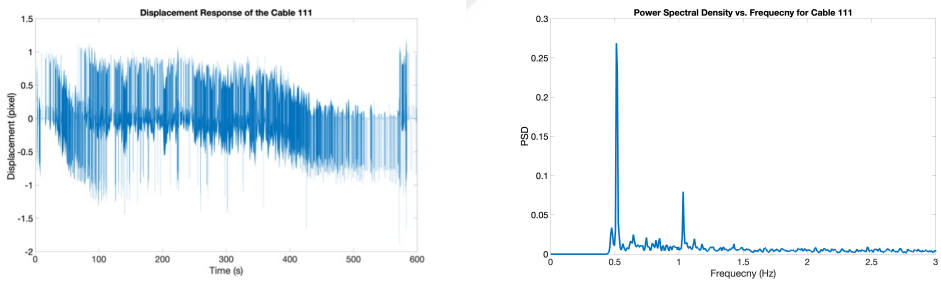
The displacement graph obtained for Cable-110 is shown in Figure 3.80(a). In addition, high-pass filtered PSD values in the frequency domain are shown in Figure 3.80(b).



(a) (b)

Figure 3.80. (a) Displacement response of cable 110 using vision-based monitoring, (b) PSDs and natural frequencies of cable 110.

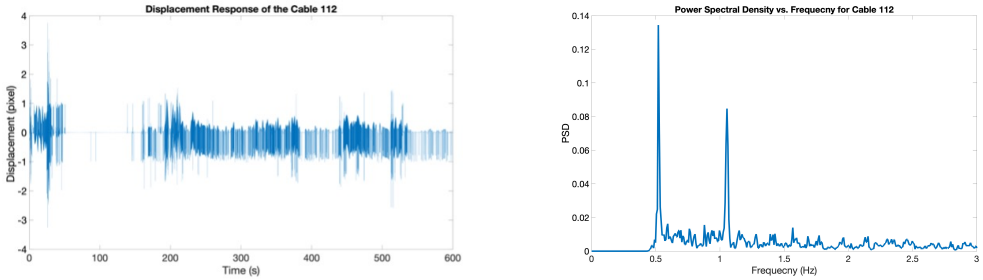
The displacement graph obtained for Cable-111 is shown in Figure 3.81(a). In addition, high-pass filtered PSD values in the frequency domain are shown in Figure 3.81(b).



(a) (b)

Figure 3.81. (a) Displacement response of cable 111 using vision-based monitoring, (b) PSDs and natural frequencies of cable 111.

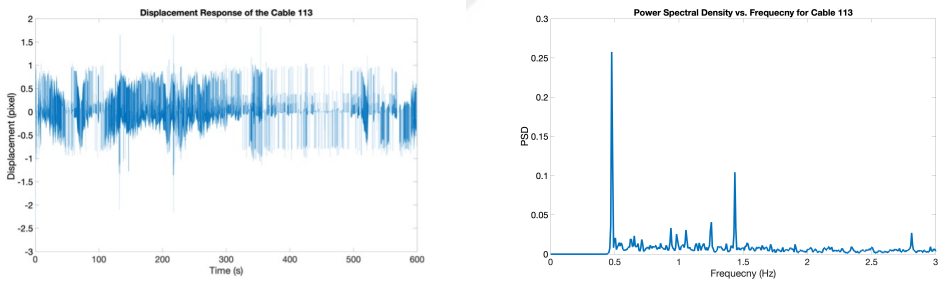
The displacement graph obtained for Cable-112 is shown in Figure 3.82(a). In addition, high-pass filtered PSD values in the frequency domain are shown in Figure 3.82(b).



(a) (b)

Figure 3.82. (a) Displacement response of cable 112 using vision-based monitoring, (b) PSDs and natural frequencies of cable 112.

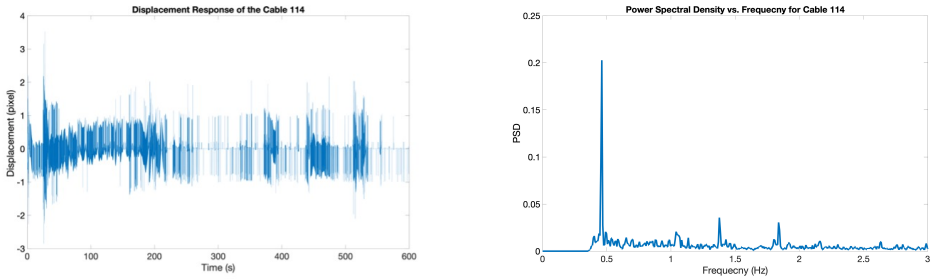
The displacement graph obtained for Cable-113 is shown in Figure 3.83(a). In addition, high-pass filtered PSD values in the frequency domain are shown in Figure 3.83(b).



(a) (b)

Figure 3.83. (a) Displacement response of cable 113 using vision-based monitoring, (b) PSDs and natural frequencies of cable 113.

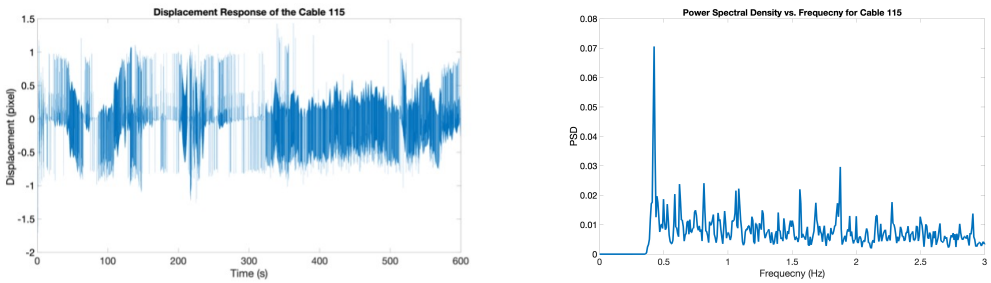
The displacement graph obtained for Cable-114 is shown in Figure 3.84(a). In addition, high-pass filtered PSD values in the frequency domain are shown in Figure 3.84(b).



(a) (b)

Figure 3.84. (a) Displacement response of cable 114 using vision-based monitoring, (b) PSDs and natural frequencies of cable 114.

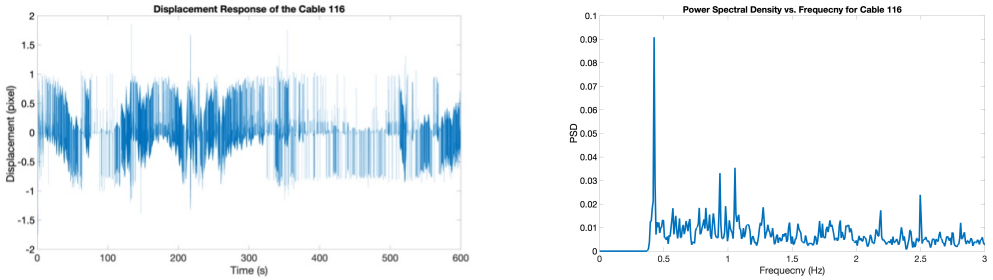
The displacement graph obtained for Cable-115 is shown in Figure 3.85(a). In addition, high-pass filtered PSD values in the frequency domain are shown in Figure 3.85(b).



(a) (b)

Figure 3.85. (a) Displacement response of cable 115 using vision-based monitoring, (b) PSDs and natural frequencies of cable 115.

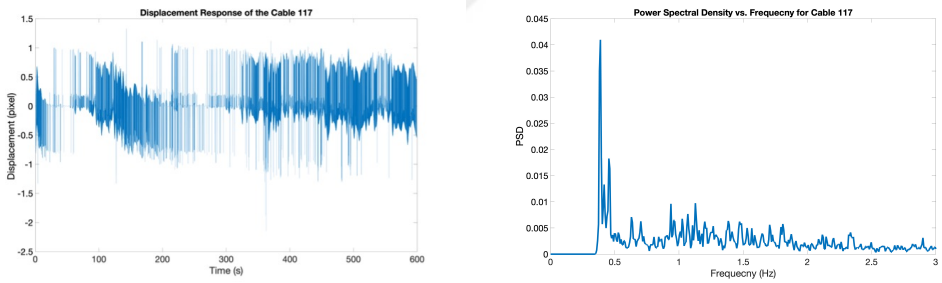
The displacement graph obtained for Cable-116 is shown in Figure 3.86(a). In addition, high-pass filtered PSD values in the frequency domain are shown in Figure 3.86(b).



(a) (b)

Figure 3.86. (a) Displacement response of cable 116 using vision-based monitoring, (b) PSDs and natural frequencies of cable 116.

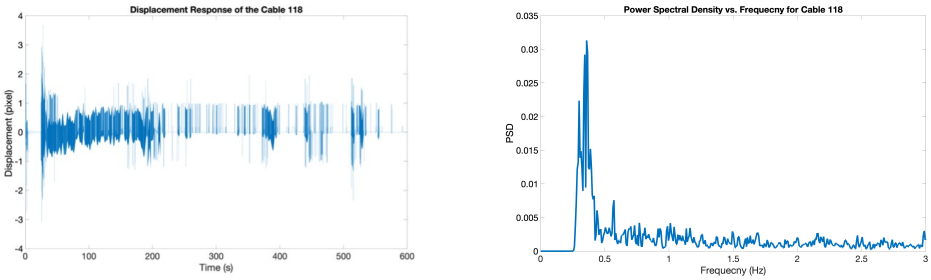
The displacement graph obtained for Cable-117 is shown in Figure 3.87(a). In addition, high-pass filtered PSD values in the frequency domain are shown in Figure 3.87(b).



(a) (b)

Figure 3.87. (a) Displacement response of cable 117 using vision-based monitoring, (b) PSDs and natural frequencies of cable 117.

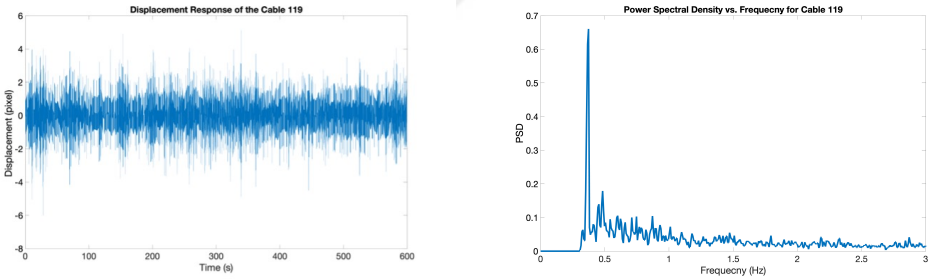
The displacement graph obtained for Cable-118 is shown in Figure 3.88(a). In addition, high-pass filtered PSD values in the frequency domain are shown in Figure 3.88(b).



(a) (b)

Figure 3.88. (a) Displacement response of cable 118 using vision-based monitoring, (b) PSDs and natural frequencies of cable 118.

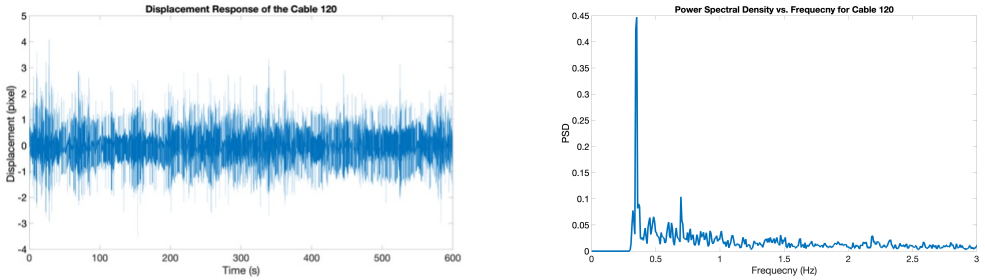
The displacement graph obtained for Cable-119 is shown in Figure 3.89(a). In addition, high-pass filtered PSD values in the frequency domain are shown in Figure 3.89(b).



(a) (b)

Figure 3.89. (a) Displacement response of cable 119 using vision-based monitoring, (b) PSDs and natural frequencies of cable 119.

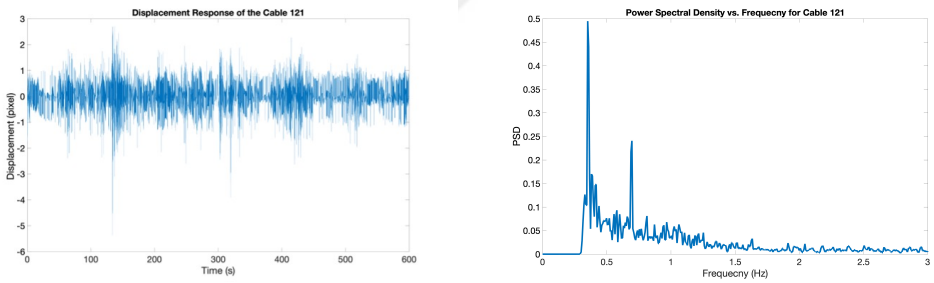
The displacement graph obtained for Cable-120 is shown in Figure 3.90(a). In addition, high-pass filtered PSD values in the frequency domain are shown in Figure 3.90(b).



(a) (b)

Figure 3.90. (a) Displacement response of cable 120 using vision-based monitoring, (b) PSDs and natural frequencies of cable 120.

The displacement graph obtained for Cable-121 is shown in Figure 3.91(a). In addition, high-pass filtered PSD values in the frequency domain are shown in Figure 3.91(b).



(a) (b)

Figure 3.91. (a) Displacement response of cable 121 using vision-based monitoring, (b) PSDs and natural frequencies of cable 121.

According to the formula obtained methodology, the cable tension in each mode was estimated by using the mass of the cable in unit length, the length of the cable, the modulus of elasticity, the moment of inertia and the natural frequencies obtained from the vision-based monitoring system in the frequency domain. Cable tensions are summarized in Table 3.14.

Table 3.14. All cable tensions from vision-based monitoring system.

	Material Prop.			fn					Cable Tension (kN)				
# No	L	m	I	f1	f2	f3	f4	f5	1	2	3	4	5
221	238	141.6	2.6E-05	0.51	1.01	-	-	-	8432.4	8190.5	-	-	-
220	230	141.6	2.6E-05	0.56	1.11	-	-	-	9282.9	9280.4	-	-	-
219	223	141.6	2.6E-05	0.60	-	-	-	-	10158.8	-	-	-	-
218	216	135.7	2.4E-05	0.66	1.31	-	-	-	11003.1	10878.4	-	-	-
217	209	135.7	2.4E-05	0.67	1.33	-	-	-	10531.6	10528.5	-	-	-
216	202	128.6	2.1E-05	0.67	1.33	-	-	-	9324.6	9321.6	-	-	-
215	195	128.6	2.1E-05	0.69	1.38	-	-	-	9271.9	9367.8	-	-	-
214	188	128.6	2.1E-05	0.70	1.41	-	-	-	8988.6	9079.0	-	-	-
213	181	128.6	2.1E-05	0.71	1.43	-	-	-	8594.0	8634.3	-	-	-
212	174	118.0	1.8E-05	0.75	1.49	-	-	-	7974.5	7970.6	-	-	-
211	167	118.0	1.8E-05	0.72	1.44	-	-	-	6780.6	6777.0	-	-	-
210	161	112.1	1.6E-05	0.72	1.44	2.16	-	-	6048.2	6013.9	6013.0	-	-
209	154	107.4	1.5E-05	0.91	1.83	-	-	-	8401.0	8499.3	-	-	-
208	147	100.3	1.3E-05	0.89	1.82	-	-	-	6920.9	7204.1	-	-	-
207	140	100.3	1.3E-05	0.91	1.83	-	-	-	6484.8	6586.0	-	-	-
206	134	88.5	1.0E-05	1.01	-	-	-	-	6492.6	-	-	-	-
205	128	88.5	1.0E-05	0.98	-	-	-	-	5585.5	-	-	-	-
204	122	72.0	6.7E-06	1.04	-	-	-	-	4648.0	-	-	-	-
203	117	64.9	5.4E-06	1.07	-	-	-	-	4100.6	-	-	-	-
202	111	64.9	5.4E-06	1.14	-	-	-	-	4174.8	-	-	-	-
201	107	72.0	6.7E-06	1.15	-	-	-	-	4372.0	-	-	-	-
101	106	72.0	6.7E-06	1.35	2.70	-	-	-	5874.4	5870.9	-	-	-
102	115	59.0	4.5E-06	1.24	-	-	-	-	4781.3	-	-	-	-
103	124	59.0	4.5E-06	0.90	1.79	-	-	-	2944.5	2918.9	-	-	-
104	135	64.9	5.4E-06	0.86	1.73	-	-	-	3533.4	3531.7	-	-	-
105	147	72.0	6.7E-06	0.76	-	-	-	-	3609.3	-	-	-	-
106	162	72.0	6.7E-06	0.72	-	-	-	-	3892.4	-	-	-	-
107	175	88.5	1.0E-05	0.75	1.48	2.33	-	-	6050.0	5930.1	6555.8	-	-
108	189	88.5	1.0E-05	0.67	1.36	2.04	-	-	5741.0	5864.8	5820.1	-	-
109	203	94.4	1.1E-05	0.64	1.30	-	-	-	6463.6	6609.8	-	-	-
110	218	94.4	1.1E-05	0.57	1.14	-	-	-	5856.3	5854.9	-	-	-
111	233	94.4	1.1E-05	0.51	1.04	-	-	-	5388.0	5541.9	-	-	-
112	248	94.4	1.1E-05	0.53	1.05	-	-	-	6458.0	6457.0	-	-	-
113	264	100.3	1.3E-05	0.48	0.94	1.44	-	2.81	6435.1	6142.6	6399.0	-	8838.4
114	279	100.3	1.3E-05	0.46	-	1.38	1.84	-	6648.9	-	6576.2	6591.5	-
115	295	107.4	1.5E-05	0.42	-	-	-	-	6744.9	-	-	-	-
116	310	107.4	1.5E-05	0.42	-	-	-	-	7448.3	-	-	-	-
117	326	107.4	1.5E-05	0.38	-	-	-	-	6621.1	-	-	-	-
118	341	107.4	1.5E-05	0.35	-	-	-	-	6172.7	-	-	-	-
119	358	112.1	1.6E-05	0.38	-	-	-	-	8335.8	-	-	-	-
120	374	118.0	1.8E-05	0.35	0.70	-	-	-	8159.7	7989.9	-	-	-
121	390	118.0	1.8E-05	0.35	0.69	-	-	-	8872.9	8506.4	-	-	-

3.3. Comparison of Results

The cable tensions obtained by all three methods are compared in Table 3.15.

Table 3.15. Comparison of cable tensions from 3 different methods.

	Cable Tension (kN)			**% error**		
Cable No	Lift-off Test	Accelerometer	Vision-based Monitoring System	Difference between lift-off and accelerometer	Difference between accelerometer and vision-based monitoring	Difference between lift-off and vision-based monitoring
221	9151.63	8237.34	8311.44	9.14	-0.74	8.40
220			9281.66			
219			10158.76			
218			10940.75			
217			10530.06			
216			9323.10			
215			9319.87			
214			9033.81			
213			8614.14			
212			7972.54			
211	7289.88	6867.99	6778.80	4.22	0.89	5.11
210			6025.07			
209			8450.11			
208			7062.48			
207			6535.41			
206			6492.61			
205			5585.51			
204			4647.97			
203			4100.60			
202			4174.80			
201	5066.45	4810.61	4372.02	2.56	4.39	6.94
101	6404.67		5872.62			5.32
102			4781.26			
103			2931.67			
104			3532.52			
105		3531.15	3609.32		-0.78	
106	3979.05		3892.40			0.87
107			6178.64			
108			5808.61			
109			6536.69			
110			5855.60			
111	5748.24	5415.47	5464.95	3.33	-0.49	2.83
112			6457.49			
113			6369.38			
114			6605.53			
115			6744.90			
116	8415.08		7448.32			9.67
117		6886.58	6621.12		2.65	
118			6172.68			
119		7617.28	8335.85		-7.19	
120			8074.82			
121	9639.35	9147.14	8689.61	4.92	4.58	9.50

3.4. FEM and Comparison of Dynamic Characteristic with the Model

It has been observed that the cable tensions obtained with the vision-based monitoring system provide measurement with sufficient accuracy. The FEM has been updated according to these cable tensions. The cable geometry was also defined accordingly. In the bridge projects, cables are defined from the points where the cables are connected to the pylon, deck and back span anchorage block. Cable geometry was edited. It was generated from the cable type with the edit lines in Edit Toolbar in SAP2000. The shape was found by specifying a tension we input at an I-end. Then, the cable tensions obtained from the vision-based monitoring system were defined as "TARGET" load on the cables. Load pattern was defined as "TARGET" with the type of other in SAP2000. Self-weight multiplier was selected as 0. This defined load pattern was assigned to the cables as Target Force. Then, the load case was defined with the Target load pattern. Static-nonlinear load case type was selected. Defined target load and dead load were added with the scale factor as 1. For the target force iteration, maximum iteration per stage was selected as 50. In addition to the target load case, modal load case was updated. The stiffness to use was selected as stiffness at end of nonlinear case using the target load.

Since the pylon and deck natural frequencies of the updated FEM with the cable tensions and the natural frequencies of 8 data sets gave consistent results, the model was verified. In the existing SHM system, there are three-dimensional accelerometers at the top of the pylon and on both sides of the deck. X is the direction of traffic flow, Y is the direction of the river flow, and Z is the direction of gravity. For this reason, natural frequencies are not expected to appear in the X direction on the deck and in the Z direction on the pylon. The data obtained from these accelerometers for each data set and the PSD values obtained by taking FFT are shown in Figure 3.92, Figure 3.93, and Figure 3.94.

For the top of the pylon:

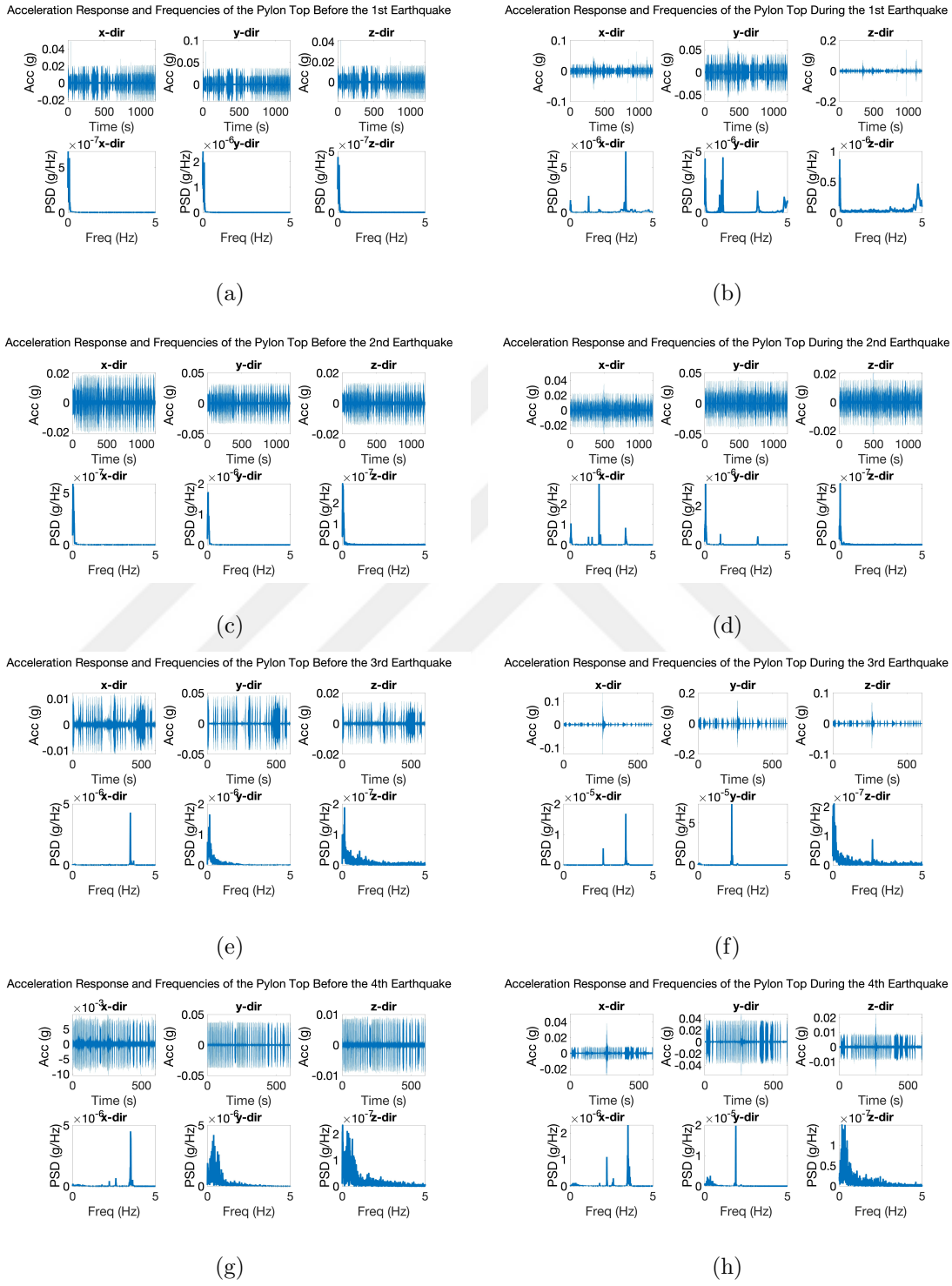


Figure 3.92. (a) Acceleration response and PSD values of top of pylon for data set-1, (b) data set-2, (c) data set-3, (d) data set-4, (e) data set-5, (f) data set-6, (g) data set-7, (h) data set-8.

For the one side of the deck:

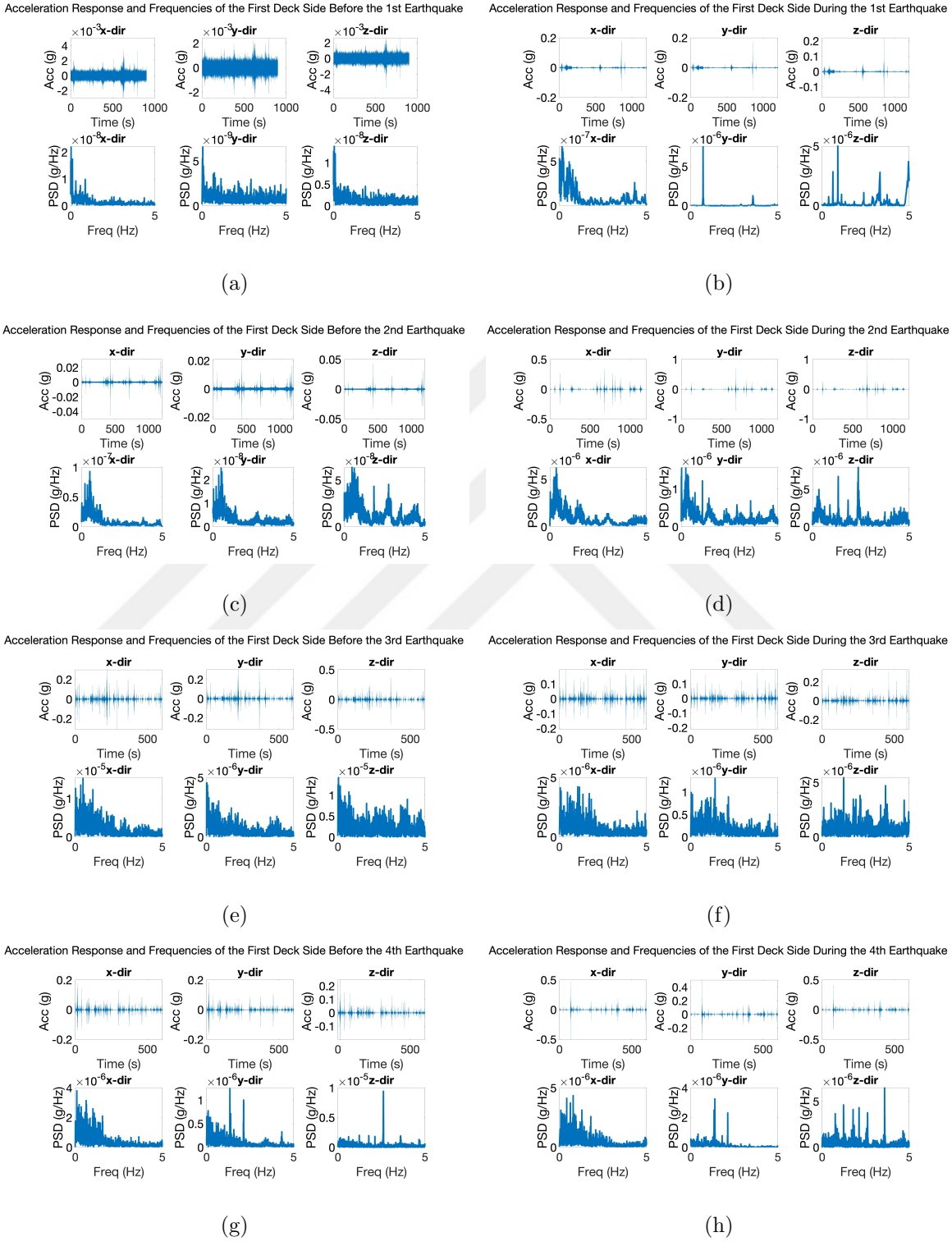


Figure 3.93. (a) Acceleration response and PSD values of one side of deck for data set-1, (b) data set-2, (c) data set-3, (d) data set-4, (e) data set-5, (f) data set-6, (g) data set-7, (h) data set-8.

For the other side of the deck:

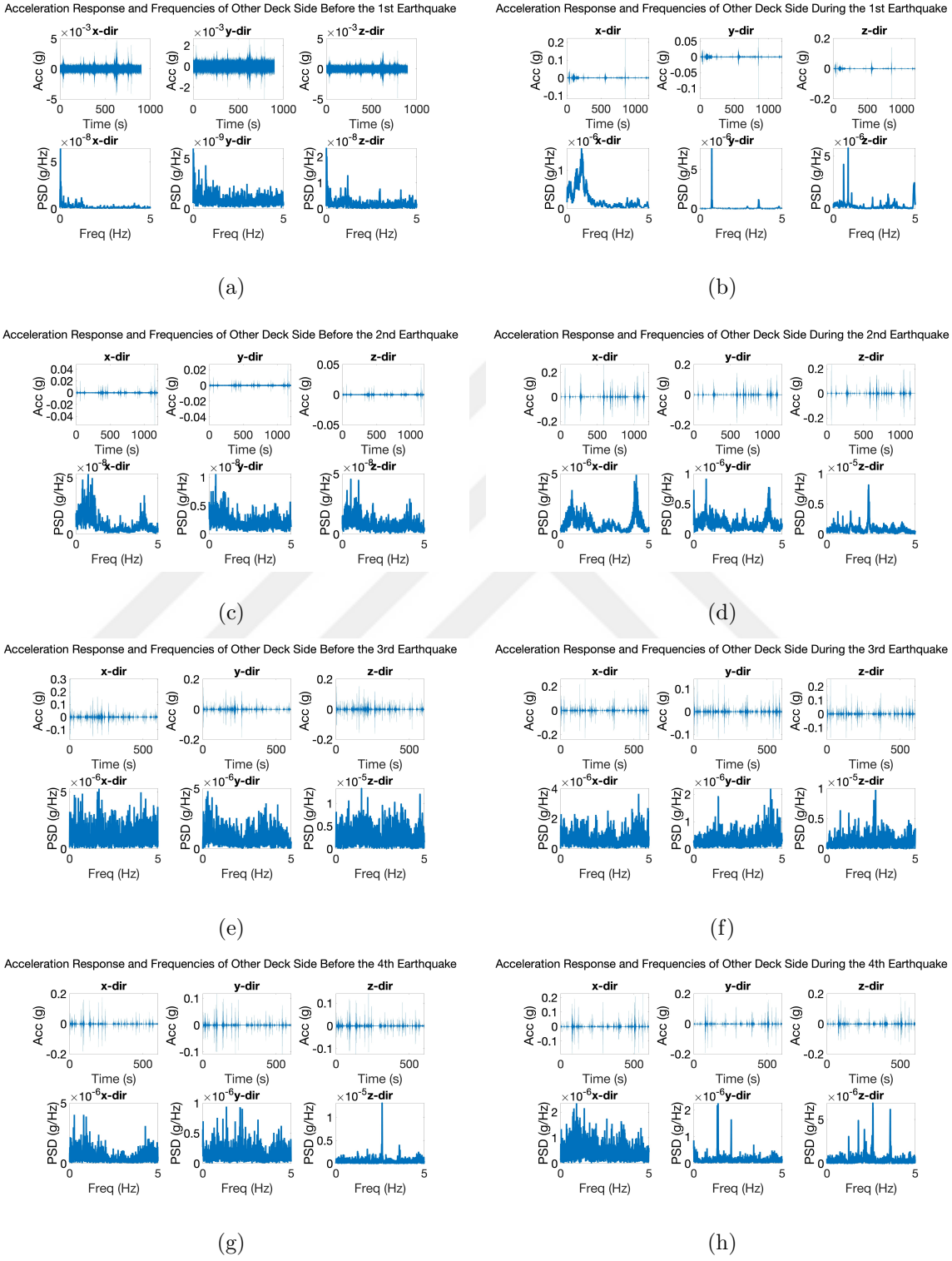


Figure 3.94. (a) Acceleration response and PSD values of the other side of deck for data set-1, (b) data set-2, (c) data set-3, (d) data set-4, (e) data set-5, (f) data set-6, (g) data set-7, (h) data set-8.

The natural frequencies of the top of the pylon in x-direction according to eight data set and verified FEM is shown in Table 3.16.

Table 3.16. Top of pylon in x-direction.

Top of Pylon in x-direction								
	fn							
	1	2	3	4	5	6	7	8
Before the 1st Earthquake	0.375	-	-	-	-	-	-	-
During the 1st Earthquake	0.381	-	0.903	1.120	1.746	1.819	2.707	3.363
Before the 2nd Earthquake	0.360	-	0.906	-	-	1.841	2.435	3.354
During the 2nd Earthquake	0.378	-	0.900	1.114	1.749	1.840	3.351	-
Before the 3rd Earthquake	0.342	-	0.931	1.120	1.794	2.225	2.377	3.491
During the 3rd Earthquake	0.302	0.760	-	1.105	1.358	1.797	2.222	3.485
Before the 4th Earthquake	0.381	0.717	-	1.129	1.324	1.776	2.219	2.615
During the 4th Earthquake	-	-	0.888	1.110	1.308	1.782	2.218	2.609
Obtained from Verified SAP2000 Model	0.393	0.658	0.929	1.064	1.567	-	2.527	4.540

The natural frequencies of the top of the pylon in y-direction according to eight data set and verified FEM is shown in Table 3.17.

Table 3.17. Top of pylon in y-direction.

Top of Pylon in y-direction								
	fn							
	1	2	3	4	5	6	7	8
Before the 1st Earthquake	0.937	-	-	-	-	-	-	-
During the 1st Earthquake	0.897	-	3.195	-	-	-	-	-
Before the 2nd Earthquake	0.937	1.337	-	-	-	-	-	-
During the 2nd Earthquake	0.949	-	3.210	-	-	-	-	-
Before the 3rd Earthquake	0.931	-	-	-	-	-	-	-
During the 3rd Earthquake	0.891	1.880	-	-	-	-	-	-
Before the 4th Earthquake	0.845	1.639	3.177	-	-	-	-	-
During the 4th Earthquake	0.897	1.880	3.076	-	-	-	-	-
Obtained from Verified SAP2000 Model	0.693	1.667	3.278	3.410	-	-	-	-

The natural frequencies of the one side of the deck in y-direction according to eight data set and verified FEM is shown in Table 3.18.

Table 3.18. The first side of deck in y-direction.

The First Side of Deck in y-direction								
	fn							
	1	2	3	4	5	6	7	8
Before the 1st Earthquake	0.735	1.129	2.155	2.914	-	-	-	-
During the 1st Earthquake	0.708	1.767	2.881	3.571	-	-	-	-
Before the 2nd Earthquake	0.726	1.389	2.783	3.320	-	-	-	-
During the 2nd Earthquake	0.714	1.099	1.434	2.341	2.884	3.592	-	-
Before the 3rd Earthquake	0.693	1.422	1.807	2.228	2.924	4.041	-	-
During the 3rd Earthquake	0.629	1.398	2.164	3.488	4.529	-	-	-
Before the 4th Earthquake	0.671	1.343	2.127	3.384	4.324	-	-	-
During the 4th Earthquake	0.876	1.386	1.804	2.124	2.878	-	-	-
Obtained from Verified SAP2000 Model	0.856	2.291	4.334	-	-	-	-	-

The natural frequencies of the one side of the deck in z-direction according to eight data set and verified FEM is shown in Table 3.19.

Table 3.19. The first side of deck in z-direction.

The First Side of Deck in z-direction								
	fn							
	1	2	3	4	5	6	7	8
Before the 1st Earthquake	0.418	0.671	0.864	1.209	1.901	2.225	2.683	-
During the 1st Earthquake	0.378	0.626	0.903	1.331	1.849	2.396	2.890	3.732
Before the 2nd Earthquake	0.366	0.620	0.836	1.126	1.840	2.750	3.534	-
During the 2nd Earthquake	0.330	0.623	0.900	1.331	1.840	2.365	2.875	3.748
Before the 3rd Earthquake	0.403	0.635	0.891	1.126	1.648	2.142	2.664	3.607
During the 3rd Earthquake	0.418	0.732	0.946	1.242	1.797	2.182	2.643	3.644
Before the 4th Earthquake	0.348	0.616	0.861	1.230	1.776	2.127	2.615	3.607
During the 4th Earthquake	0.366	0.757	1.233	1.782	2.124	2.612	3.589	4.645
Obtained from Verified SAP2000 Model	0.393	0.658	0.929	1.523	2.161	2.908	3.757	4.698

The natural frequencies of the other side of the deck in y-direction according to eight data set and verified FEM is shown in Table 3.20.

Table 3.20. The second side of deck in y-direction.

The Second Side of Deck in y-direction								
	fn							
	1	2	3	4	5	6	7	8
Before the 1st Earthquake	0.699	1.108	-	2.255	2.982	4.285	-	-
During the 1st Earthquake	0.708	1.166	-	2.887	3.568	-	-	-
Before the 2nd Earthquake	0.732	1.166	1.718	2.197	2.646	3.375	4.010	-
During the 2nd Earthquake	0.705	1.254	1.712	2.454	2.881	3.357	4.245	-
Before the 3rd Earthquake	0.766	1.340	1.917	2.185	2.890	3.170	3.583	
During the 3rd Earthquake	0.784	1.389	1.938	2.109	2.399	2.878	3.653	4.355
Before the 4th Earthquake	0.824	1.340	1.837	2.115	2.420	2.930	3.218	4.446
During the 4th Earthquake	0.754	1.379	1.703	2.124	2.631	-	3.397	-
Obtained from Verified SAP2000 Model	0.856	2.291	4.334	-	-	-	-	-

The natural frequencies of the other side of the deck in z-direction according to eight data set and verified FEM is shown in Table 3.21.

Table 3.21. The second side of deck in z-direction.

The Second Side of Deck in z-direction								
	fn							
	1	2	3	4	5	6	7	8
Before the 1st Earthquake	0.388	-	0.803	1.190	1.859	2.280	2.972	-
During the 1st Earthquake	0.381	0.626	0.903	1.120	1.849	2.396	2.881	3.339
Before the 2nd Earthquake	0.516	-	0.989	1.501	1.871	2.374	2.811	3.940
During the 2nd Earthquake	0.378	0.623	0.900	1.346	1.840	2.362	3.220	3.751
Before the 3rd Earthquake	0.330	0.726	0.992	1.450	1.801	2.634	3.024	3.696
During the 3rd Earthquake	0.452	0.760	0.909	1.242	1.596	1.794	2.258	2.759
Before the 4th Earthquake	0.409	0.781	0.925	1.227	1.468	1.779	2.179	2.615
During the 4th Earthquake	0.357	0.745	-	1.233	1.468	1.782	2.124	2.603
Obtained from Verified SAP2000 Model	0.393	0.658	0.929	1.523	2.161	2.908	3.757	4.698

4. CONCLUSION

Considering civil infrastructures, including buildings and bridges, as these structures are built and used, they begin to deteriorate, especially due to their material properties. Maintaining safe and reliable infrastructures in daily use is important for the welfare of the society. It is important and necessary to determine the integrity of the structures. Determining the structural dynamic characteristics of civil infrastructures and determining the damage levels through changes in them using SHM systems is a frequently used method in the world. In cable-supported bridges, the bridge deck located in the main span is supported by cables and this force on the cables is transferred to the pylon. Cable tension is one of the most important factors in examining and analyzing the overall safety and integrity of the structure. Evaluating all cable tensions is important to detect any damage to the structure. Fatigue caused by traffic, wind, temperature change and earthquake loads, and corrosion due to environmental effects cause a decrease in cable tension and affect the overall performance of the structure. Such problems cause the service life of the structure to shorten. Therefore, it is necessary to determine and monitor cable tensions changing over time.

Considering traditional and generally used methods, a separate sensor must be used for each cable to monitor all cables in cable-stayed bridges. Since the sensors must remain on the cable for long-term monitoring and the lifespan of these sensors exposed to vibration is short, they need to be maintained and replaced when necessary. Monitoring all cables using traditional methods is difficult in terms of economics and manpower. Therefore, a method is needed to determine and estimate the dynamic properties of cables without placing sensors. For this reason, in recent years, many studies have been carried out on determining the dynamic properties of cables using vision-based monitoring systems with the digital or industrial cameras.

Therefore, in this study, a vision-based monitoring system was used to determine the dynamic properties of New Kömürhan Cable-stayed Bridge, located between Elazig

and Malatya, using image processing technique, considering ease of use and economic efficiency. In the earthquakes that occurred at four different times and three hours before these earthquakes, cable tensions were determined by lift-off test and estimated by vibration test with accelerometers from existing SHM system. Using these two methods, the cable tension of only 8 of the 42 cables on the bridge was obtained.

Video recording was taken in the field to estimate the tensions of all cables on the bridge and to prove the effectiveness of the vision-based monitoring system at different time from these 4 earthquakes. 2 laboratory and 2 field experiments were conducted to evaluate the performance of vision-based monitoring system. During all these experiments and bridge measurements, an easily accessible, consumer grade DSLR was used.

In the first experiment, initial studies with the vision-based monitoring system were carried out on a 3-story building model at Boğaziçi University, North Campus, Structures Laboratory. Accelerometers were placed on each floor. Floor displacements were measured simultaneously with a single DSLR in pixel scale by applying external force. The response accelerometers and the vision-based monitoring system were compared in the frequency domain. The natural frequencies and mode shapes of the structure gave consistent results. In the second experiment, the cable experiment was conducted from a distance in the laboratory. Cable tensions were estimated using the vibration method with taut string theory, using the natural frequencies in each mode. The response of accelerometers and the vision-based monitoring system gave consistent results in the frequency domain. With experiments in the laboratory, subpixel estimation performed using the quadratic polynomial function, thus preventing geometric distortion caused by the lens.

In experiments performed in the laboratory, the light intensity could be adjusted with a white background. Two different experiments were conducted to assess the performance of the outside experiments. In the wind turbine experiment at Boğaziçi University Sarıtepe Campus, since the blades were active phase, its natural frequency

in a single direction was obtained. It provided consistent results with the study of Soyoz et al. (2020). In lightning rod measurements, short-term measurements taken from 3 different distances and accelerometers gave consistent results when compared in the frequency domain in terms of natural frequencies and mode shapes. However, there is a tradeoff between recording distance and measurement performance.

With the developed method, the dynamic behavior of 42 cables was obtained with recordings taken from 4 different measurement points. To reduce the computational load during the analyses, the ROI window was used and the tracked point within the ROI window was determined manually. Instead of tracking a specific pixel, the movement of the edge was measured at the subpixel scale by using the difference between the light intensity between the edge of the cable and the background. Since natural frequencies in the frequency domain would be used in the analysis results, camera calibration, projection and scale factor calculation were not performed to obtain the displacement in mm. Cable tensions were estimated using the dynamic properties of the cable and the characteristic features of the cables. These cable tensions were compared with the cable tensions obtained from 8 data sets. In the existing SHM system, the difference between the lift-off test and vibration method with accelerometers is below 9 % for the average of the eight data set. The difference between the vibration method using vision-based monitoring system and the lift-off test is less than 10 %. The difference between cable tensions estimated by vibration method using accelerometers and the vision-based monitoring system is less than 5 %. The reason for this is that the video recordings were taken approximately 2 years after the data sets. During this period, 2 major earthquakes and aftershocks occurred in the region. These ground movements may have affected the performance of the structure. Nevertheless, it can be said that the vision-based monitoring system provides consistent results. That is, the vision-based monitoring system can be used to estimate the cable tensions.

The tensions of all cables on the bridge were estimated by video recordings from four different points on the bridge. According to these cable tensions, the FEM, which was previously created in accordance with the bridge projects, was updated. The

natural frequencies of the deck and pylon of verified FEM without changing the material properties were compared with the natural frequencies of eight data sets. The accuracy of the natural frequencies in the x-direction of the pylon and the z-direction of the deck, where the movement can be observed more clearly, and the frequencies of verified model is high.

The advantage of this method is that the dynamic response of multiple points of a structure can be measured using a single camera simultaneously using a wide-angle lens instead of using multiple sensors. Additionally, cable installation work, setting up the DAQ system and labor problems may arise in measurements taken using accelerometers. In addition, low cost and simple operation are among the other advantages. It provides convenience and accessibility as measurements can be taken using a digital camcorder or digital camera and tripod when conducting outdoor testing on the vision-based monitoring system. It provides easy installation and removal. Since these advantages can be an alternative to traditional contact sensors, studies have been carried out on this system in many structures.

However, there was a tradeoff between measurement accuracy and cost. Problems that caused errors such as camera vibration and heat blur could be stated as disadvantages. Image distortion may occur in foggy and rainy weather, night measurements and scenarios where the backlight is insufficient.

REFERENCES

Abdel-Ghaffar, A.M. and R.H. Scanlan, 1985, "Ambient Vibration Studies of Golden Gate Bridge: I. Suspended Structure", *Journal of Engineering Mechanics*, Vol. 111, No. 4, pp. 463-482.

Abdulkarem, M., K. Samsudin, F.Z. Rokhani, and M.F. A Rasid, 2020, "Wireless Sensor Network for Structural Health Monitoring: A Contemporary Review of Technologies, Challenges, and Future Direction", *Structural Health Monitoring*, Vol. 19, No. 3, pp. 693-735.

Amezquita-Sanchez, J.P., M. Valtierra-Rodriguez, and H. Adeli, 2018, "Wireless Smart Sensors for Monitoring the Health Condition of Civil Infrastructure", *Scientia Iranica*, Vol. 25, pp. 2913–2925.

Au, F. T. and X.T. Si, 2012, "Time-Dependent Effects on Dynamic Properties of Cable-Stayed Bridges", *Structural Engineering and Mechanics*, Vol. 41, No. 1, pp. 139-155.

Bao, Y., Z. Shi, J.L. Beck, H. Li, and T.Y. Hou, 2017, "Identification of Time-varying Cable Tension Forces Based on Adaptive Sparse Time-frequency Analysis of Cable Vibrations", *Structural Control and Health Monitoring*, Vol. 24, No. 3, pp. 1889-1902.

Benedettini F. and C. Gentile, 2011, "Operational Modal Testing and FE Model Tuning of a Cable-stayed Bridge", *Engineering Structures*, Vol. 33, No. 6, pp. 2063–2073.

Bridge Project, 2012, New Kömürhan Bridge prepared by Yüksel Project Inc., Wiecon Co., Doğus and Gülsan Co., Ankara, Turkey

Brincker, R., L. Zhang, and P. Andersen, 2001, "Modal Identification of Output-Only Systems Using Frequency Domain Decomposition", *Smart Materials and Structures*, Vol. 10, No. 3, pp. 441-558.

Brownjohn, J.M.W., A.A. Dumanoglu, R.T. Severn, and A. Blakeborough, 1989, "Ambient Vibration Survey of the Bosporus Suspension Bridge", *Earthquake Engineering & Structural Dynamics*, Vol. 18, No. 2, pp. 263-283.

Brownjohn, J.M.W., F. Magalhaes, E. Caetano, and A. Cunha, 2010, "Ambient Vibration Re-Testing and Operational Modal Analysis of the Humber Bridge", *Engineering Structures*, Vol. 32, No. 8, pp. 2003-2018.

Caetano, E., Œ. Cunha, C. Moutinho, and F. Magalhães, 2010b, "Studies for Controlling Human-Induced Vibration of The Pedro E Inês Footbridge, Portugal. Part 2: Implementation of Tuned Mass Dampers", *Engineering Structures*, Vol. 32, No. 4, pp. 1082-1091.

Caetano, E., Œ. Cunha, F. Magalhães, and C. Moutinho, 2010a, "Studies for Controlling Human-induced Vibration of the Pedro E Inês Footbridge, Portugal. Part 1: Assessment of Dynamic Behaviour", *Engineering Structures*, Vol. 32, No. 4, pp. 1069-1081.

Camara, A., M.A. Astiz, and A.J. Ye, 2014, "Fundamental Mode Estimation for Modern Cable-stayed Bridges Considering the Tower Flexibility", *Journal of Bridge Engineering*, Vol. 19, No. 6, pp. 4014-4026.

Cappello, C., D. Zonta, H. Ait Laasri, B. Glisic, and M. Wang, 2018, "Calibration of Elasto-Magnetic Sensors on In-Service Cable-Stayed Bridges for Stress Monitoring", *Sensors*, Vol. 18, No. 2, pp. 466-482.

Casas J.R., 1994 "A Combined Method for Measuring Cable Forces: The Cable-Stayed Alamillo Bridge, Spain", *Structural Engineering International,* Vol. 4, No. 4, pp. 235-240.

Chan, T.H., D.B. Ashebo, H.Y. Tam, Y. Yu, T.F. Chan, P.C. Lee, and E. Perez Gracia, 2009, "Vertical displacement measurements for bridges using optical fiber sensors and CCD cameras—a preliminary study", *Structural Health Monitoring*, Vol. *8, No.* 3, pp. 243-249.

Chang, C.C., T.Y.P. Chang, and Q.W. Zhang, 2001, "Ambient Vibration of Long-span Cable-stayed Bridge", *Journal of Bridge Engineering*, Vol. 6, No. 1, pp. 46-53.

Chang, P.C., A. Flatau, and S.C. Liu, 2003, "Health Monitoring of Civil Infrastructure", *Structural Health Monitoring*, Vol. 2, No. 3, pp. 257-267.

Chen S.E. and S. Petro, 2005, "Nondestructive Bridge Cable Tension Assessment Using Laser Vibrometry", *Experimental Techniques,* Vol. 29, No. 2, pp. 29–32.

Cho, S., J. Yim, S.W. Shin, H.J Jung, C.B. Yun, and M.L. Wang, 2013, "Comparative Field Study of Cable Tension Measurement for a Cable-stayed Bridge", *Journal of Bridge Engineering*, Vol. 18, No. 8, pp. 748-757.

Choi, A.J. and J.H. Han, 2018, "Frequency-Based Damage Detection in Cantilever Beam Using Vision-Based Monitoring System with Motion Magnification Technique", *Journal of Intelligent Material Systems and Structures*, Vol. 29, No. 20, pp. 3923-3936.

Cunha, A. and E. Caetano, 1999, "Dynamic Measurements on Stay Cables of cable-stayed Bridges Using an Interferometry Laser System", *Experimental Techniques,* Vol. 23, pp. 38-43.

Cunha, A., E. Caetano, and R. Delgado, 2001, "Dynamic Tests on Large Cable-stayed Bridge", *Journal of Bridge Engineering*, Vol. 6, No. 1, pp. 54-62.

Disaster And Emergency Management Presidency, https://en.afad.gov.tr/, accessed on June 27, 2023

Du, W., D. Lei, P. Bai, F. Zhu, and Z. Huang, 2020, "Dynamic Measurement of Stay-Cable Force Using Digital Image Techniques", *Measurement,* Vol. 151, pp. 1072-1111.

Duan, Y.F., R. Zhang, Y. Zhao, S.W. Or, K.Q. Fan, and Z.F. Tang, 2011, "Smart Elasto-Magneto-Electric (EME) Sensors for Stress Monitoring of Steel Structures in Railway Infrastructures", *Journal of Zhejiang University-SCIENCE A*, Vol. 12, No. 2, pp. 895-901.

Fallis, M.C., 1997, "Hanging Shapes of Nonuniform Cables", *American Journal of Physics*, Vol. 65, No. 2, pp. 117-122.

Fang, Z. and J.Q. Wang, 2012, "Practical Formula for Cable Tension Estimation by Vibration Method", *Journal of Bridge Engineering*, Vol. 17, No. 1, pp. 161-164.

Feng, D. and M.Q. Feng, 2016, "Vision-based Multipoint Displacement Measurement for Structural Health Monitoring", *Structural Control and Health Monitoring*, Vol. 23, No. 5, pp. 876-890.

Feng, D. and M.Q. Feng, 2017, "Experimental Validation of Cost-effective Vision-based Structural Health Monitoring", *Mechanical Systems and Signal Processing*, Vol. 88, pp. 199-211.

Feng, D. and M.Q. Feng, 2018, "Computer Vision for SHM of Civil Infrastructure: from Dynamic Response Measurement to Damage Detection–A Review", *Engineering Structures*, Vol. 156, pp. 105-117.

Feng, D., M.Q. Feng, E. Ozer, and Y. Fukuda, 2015, "A Vision-based Sensor for Noncontact Structural Displacement Measurement", *Sensors*, Vol. 15, No. 7, pp. 16557-16575.

Fleming, J.F., 1979, "Nonlinear Static Analysis of Cable-stayed Bridge Structures", *Computers & Structures*, Vol. 10, No. 4, pp. 621-635.

Freire, A. M.S., J.H.O. Negrao, and A.V. Lopes, 2006, "Geometrical Nonlinearities on The Static Analysis of Highly Flexible Steel Cable-stayed Bridges", *Computers & Structures*, Vol. 84, No. 31-32, pp. 2128-2140.

Fujiwara, Y., and T. Sakai, 2016, "A Study of a Lift-off Test Method for Ground Anchors", *Journal of JSCE*, Vol. 4, No. 1, pp. 106-117.

Geier, R., G. De Roeck, and R. Flesch, 2006, "Accurate Cable Force Determination Using Ambient Vibration Measurements", *Structure and Infrastructure Engineering*, Vol. 2, No. 1, pp. 43-52.

Gomez-Cabrera, A. and P.J. Escamilla-Ambrosio, 2022, "Review of Machine-learning Techniques Applied to Structural Health Monitoring Systems for Building and Bridge Structures", *Applied Sciences*, Vol. 12, No. 21, pp. 10754-10794.

Hu, D., Y. Guo, X. Chen, and C. Zhang, 2017, "Cable Force Health Monitoring of Tongwamen Bridge Based on Fiber Bragg Grating", *Applied Sciences,* Vol. 7, No. 4, pp. 384-395.

Hu, W.H., S. Thöns, R.G. Rohrmann, S. Said, and W. Rücker, 2015, "Vibration-based Structural Health Monitoring of a Wind Turbine System. Part I: Resonance phenomenon", *Engineering Structures*, Vol. 89, pp. 260-272.

Huynh, T.C., J.H. Park, and J.T. Kim, 2016, "Structural Identification of Cable-stayed Bridge Under Back-to-back Typhoons by Wireless Vibration Monitoring", *Measurement,* Vol. 88, pp. 385-401.

Jeon, G., Kim, S., Ahn, S., Kim, H. K., and Yoon, H., 2022, "Vision-based automatic cable displacement measurement using Cable-ROI Net and Uni-KLT.", *Structural Control and Health Monitoring*, Vol. 29, No. 8, pp. 2977-2992.

Ji, Y.F. and C.C. Chang, 2008, "Nontarget Image-based Technique for Small Cable Vibration Measurement", *Journal of Bridge Engineering*, Vol. 13, No. 1, pp. 34-42.

Jiang, C., C. Wu, C.S. Cai, X. Jiang, and W. Xiong, 2020, "Corrosion Fatigue Analysis of Stay Cables Under Combined Loads of Random Traffic and Wind", *Engineering Structures*, Vol. 206, pp. 1101-1133.

Kaloop, M.R., 2012, "Bridge Safety Monitoring Based-GPS Technique: Case Study Zhujiang Huangpu Bridge", *Smart Structures and Systems*, Vol. 9, No. 6, pp 473-487.

Kangas, S., A. Helmicki, V. Hunt, R. Sexton, and J. Swanson, 2012, "Cable-stayed Bridges: Case Atudy for Ambient Vibration-based Cable Tension Estimation", *Journal of Bridge Engineering*, Vol. 17, No. 6, pp. 839-846.

Kim, B.H. and T. Park, 2007, "Estimation of Cable Tension Force Using the Frequency-Based System Identification Method", *Journal of Sound and Vibration*, Vol. 304, No. 3-5, pp. 660-676.

Kim, C.H., B.W. Jo, and J.T. Jun 2012, "Application of Laser Vibrometer to the Measurement and Control of Cable Tensile Forces in Cable-Stayed Bridges", *International Journal of Distributed Sensor Networks*, Vol. 8, No. 10, pp. 810-831.

Kim, J.T., K.D. Nguyen, and T.C. Huynh, 2013, "Wireless Health Monitoring of Stay Cable Ssing Piezoelectric Strain Response and Smart Skin Technique '', *Smart Structural Systems*, Vol. 12, No. 3-4, pp. 381-397.

Kim, S. W., D.U. Park, J.S. Kim, and J.B. Park, 2023, "Estimating Tension of a Prestressed Concrete Cable-stayed Bridge Under Construction and Traffic Use Conditions Using a Vision-based System", *Structures,* Vol. 47, pp. 299-312.

Kim, S.W. and N.S. Kim, 2011, "Multi-point Displacement Response Measurement of Civil Infrastructures Using Digital Image Processing", *Procedia Engineering*, Vol. 14, pp. 195-203.

Kim, S.W. and N.S. Kim, 2013, "Dynamic Characteristics of Suspension Bridge Hanger Cables Using Digital Image Processing", *Ndt & E International*, Vol. 59, pp. 25-33.

Kim, S.W., B.G. Jeon, N.S. Kim, and J.C. Park, 2013, "Vision-Based Monitoring System for Evaluating Cable Tensile Forces on A Cable-Stayed Bridge", *Structural Health Monitoring*, Vol. 12, No. 5-6, pp. 440-456.

Kim, S.W., J.H. Cheung, J.B. Park, and S.O. Na, 2020, "Image-based Back Analysis for Tension Estimation of Suspension Bridge Hanger Cables", *Structural Control and Health Monitoring,* Vol. 27, No. 4, pp. 2508-2521.

Ko, J.M. and Y.Q. Ni, 2005, "Technology Developments in Structural Health Monitoring of Large-scale Bridges", *Engineering Structures*, Vol. 27, No. 12, pp. 1715-1725.

Kumarasena, T., R.H. Scanlan, and G.R. Morris, 1989, "Deer Isle bridge: Field and Computed Vibrations", *Journal of Structural Engineering*, Vol. 115, No. 9, pp. 2313-2328.

Lan, C., Y. Xu, C. Liu, H. Li, and B.F. Spencer Jr, 2018, "Fatigue Life Prediction for Parallel-wire Stay Cables Considering Corrosion Effects", *International Journal of Fatigue*, Vol. 114, pp. 81-91.

Lee, G., S. Kim, S. Ahn, H.K. Kim, and H. Yoon, 2022, "Vision-based Cable Displacement Measurement Using Side View Video", *Sensors*, Vol. 22, No.3, pp. 962-974.

Lee, J.J. and M. Shinozuka, 2006a, "A Vision-Based System for Remote Sensing of Bridge Displacement", *Ndt & E International*, Vol. 39, No. 5, pp. 425-431.

Lee, J.J. and M. Shinozuka, 2006b, "Real-Time Displacement Measurement of a Flexible Bridge Using Digital Image Processing Techniques", *Experimental Mechanics*, Vol. *46*, pp. 105-114.

Li, H. and J. Ou, 2016, "The State of the Art in Structural Health Monitoring of Cable-Stayed Bridges", *Journal of Civil Structural Health Monitoring*, Vol. 6, pp. 43-67.

Li, S., S. Wei, Y. Bao, and H. Li, 2018, "Condition Assessment of Cables by Pattern Recognition of Vehicle-induced Cable Tension Ratio", *Engineering Structures*, Vol. 155, pp. 1-15.

Liao, W.H., D.H. Wang, and S.L. Huang, 2001, "Wireless Monitoring of Cable Tension of Cable-stayed Bridges Using PVDF Piezoelectric Films", *Journal of Intelligent Material Systems and Structures*, Vol. 12, No. 5, pp. 331-339.

Lydon, D., M. Lydon, S. Taylor, J.M. Del Rincon, D. Hester, and J.Brownjohn, 2019, "Development and Field Testing of a Vision-based Displacement System Using a Low Cost Wireless Action Camera", *Mechanical Systems and Signal Processing*, Vol. 121, pp. 343-358.

Ma, Y., A. Peng, L. Wang, L. Dai, and J. Zhang, 2023, "Structural Performance Degradation of Cable-stayed Bridges Subjected to Cable Damage: Model Test and Theoretical Prediction", *Structure and Infrastructure Engineering*, Vol. 19, No. 9, pp. 1173-1189.

Ma, Z., J. Choi, and H. Sohn, 2022, "Noncontact Cable Tension Force Estimation Using an Integrated Vision and Inertial Measurement System", *Measurement*, Vol. 199, pp. 1115-1132.

Nassif H.H., M. Gindy, and J. Davis, 2005, "Comparison of laser Dropper Vibrometer with Contact Sensors for Monitoring Bridge Deflection and Vibration", *Ndt & E International*, Vol. 38, pp. 213–218.

Nazarian, E., F. Ansari, and H. Azari, 2016, "Recursive Optimization Method for Monitoring of Tension Loss in Cables of Cable-Stayed Bridges", *Journal of Intelligent Material Systems and Structur*es, Vol. 27, No. 15, pp. 2091-2101.

Nickitopoulou, A., K. Protopsalti, and S. Stiros, 2006, "Monitoring Dynamic and Quasi-Static Deformations of Large Flexible Engineering Structures with Gps: Accuracy, Limitations and Promises", *Engineering Structures*, Vol. 28, No. 10, pp. 1471-1482.

Oliveira, G., F. Magalhães, A. Cunha, and E. Caetano, 2018a, "Continuous Dynamic Monitoring of an Onshore Wind Turbine", *Engineering Structures*, Vol. 164, pp. 22-39.

Oliveira, G., F. Magalhães, A. Cunha, and E. Caetano, 2018b, "Vibration-based Damage Detection in a Wind Turbine Using 1 Year of Data", *Structural Control and Health Monitoring*, Vol. 25, No. 11, pp. 2238-2251.

Ozbek, M., D.J. Rixen, O. Erne, and G. Sanow, 2010, "Feasibility of Monitoring Large Wind Turbines Using Photogrammetry", *Energy*, Vol. 35, No. 12, pp. 4802-4811.

Pevrot, A.H. and A.M. Goulois, 1979, "Analysis of Cable Structures", *Computers & Structures*, Vol. 10, No. 5, pp. 805–813.

Ren, W.X., I.E. Harik, G.E. Blandford, M. Lenett, and A.T. Baseheart, 2004, "Roebling Suspension Bridge. Ii: Ambient Testing and Live-Load Response", *Journal of Bridge Engineering,* Vol. 9, No. 2, pp. 119-126.

Ren, W.X., X.L. Peng, and Y.Q. Lin, 2005, "Experimental and Analytical Studies on Dynamic Characteristics of a Large Span Cable-Stayed Bridge", *Engineering Structures*, Vol. 27, No. 4, pp. 535-548.

Russell, J.C. and T.J. Lardner, 1998, "Experimental Determination of Frequencies and Tension for Elastic Cables", *Journal of Engineering Mechanics*, Vol. 124, No. 10, pp. 1067-1072.

SAP2000 v22, Computers and Structures Inc. (CSI), Berkeley, USA, 2021.

Schroeder, K., W. Ecke, J. Apitz, E. Lembke, and G. Lenschow, 2006, "A Fibre Bragg Grating Sensor System Monitors Operational Load in a Wind Turbine Rotor Blade", *Measurement Science and Technology*, Vol. 17, No. 5, pp. 1167-1181.

Siringoringo, D.M. and Y. Fujino, 2008, "System Identification of Suspension Bridge from Ambient Vibration Response", *Engineering Structures,* Vol. 30, No. 2, pp. 462-477.

Siringoringo, D.M., Y. Fujino, M. Suzuki, and V. Mehta, 2022, "Implementation of Wireless Sensor Network for Continuous Seismic Monitoring of Isolated Cable-Stayed Bridge", *Journal of Bridge Engineering*, Vol. 27, No. 4, pp. 402-421.

Soyoz, S., S. Hanbay, B. Bagirgan, and O. Ergun, 2021, "Long-term Vibration-based Monitoring and Seismic Performance Assessment of a Wind Turbine", *Journal of Civil Structural Health Monitoring,* Vol. 11, pp. 117-128.

Sun, J.B., Z.Z. Zhao, and H.H. Zhao, 2011, "Measuring Methods of Cable Tension in Cable-stayed Bridges", *Advanced Materials Research*, Vol. 295, pp. 1230-1235.

Sun, Z., Z. Zou, and Y. Zhang, 2017, "Utilization of Structural Health Monitoring in Long-span Bridges: Case Studies", *Structural Control and Health Monitoring*, Vol. 24, No. 10, pp. 1979-1991.

Taha, M. R., A. Noureldin, J.L. Lucero, and T.J. Baca, 2006, "Wavelet Transform for Structural Health Monitoring: A Compendium of Uses and Features", *Structural Health Monitoring*, Vol. 5, No. 3, pp. 267-295.

Tian, Y., C. Zhang, S. Jiang, J. Zhang, and W. Duan, 2021, "Noncontact Cable Force Estimation with Unmanned Aerial Vehicle and Computer Vision", *Computer-Aided Civil and Infrastructure Engineering*, Vol. 36, No. 1, pp. 73-88.

Turkish Electricity Transmission Company, https://www.teias.gov.tr/, accessed on June 11, 2023

Van der Auweraer, H. and B. Peeters, 2003, "International Research Projects on Structural Health Monitoring: An Overview", *Structural Health Monitoring*, Vol. 2, No.4, pp. 341-358.

Wang D., J. Liu, D. Zhou, and S. Huang, 1999, "Using Pvdf Piezoelectric Film Sensors for in Situ Measurement of Stayed-Cable Tension of Cable-Stayed Bridges", *Smart Materials Structure,* Vol. 8, No. 5, pp. 554-567.

Wilson, J. C. and W. Gravelle, 1991, "Modelling of a Cable-stayed Bridge for Dynamic Analysis", *Earthquake Engineering & Structural Dynamics*, Vol. 20, No. 8, pp. 707-721.

Xu, Y., J. Brownjohn, and D. Kong, 2018, "A Non-contact Vision-based System for Multipoint Displacement Monitoring in a Cable-stayed Footbridge", *Structural Control and Health Monitoring*, Vol. 25, No. 5, pp. 2155-2172.

Xu, Y.L., J.M. Ko, and W.S. Zhang, 1997, "Vibration Studies of Tsing Ma Suspension Bridge", *Journal of Bridge Engineering*, Vol. 2, No. 4, pp. 149-156.

Yan, B., D. Li, W. Chen, L. Deng, and X. Jiang, 2021, "Mode Shape–Aided Cable Force Determination Using Digital Image Correlation", *Structural Health Monitoring*, Vol. 20, No. 5, pp. 2430-2445.

Yan, B., W. Chen, J. Yu, and X. Jiang, 2019, "Mode Shape-Aided Tension Force Estimation of Cable with Arbitrary Boundary Conditions", *Journal of Sound and Vibration*, Vol. 440, pp. 315-331.

Yang, Y., S. Li, S. Nagarajaiah, H. Li, and P. Zhou, 2016, "Real-Time Output-Only Identification of Time-Varying Cable Tension from Accelerations via Complexity Pursuit", *Journal of Structural Engineering*, Vol. 142, No. 1, pp. 4015-4028.

Yu, Y., C. Zhang, X. Zhu, W.H. Kang, X. Mao, and B. Uy, 2014, "Design and Experimental Investigations of a Vibration-based Wireless Measurement System for Bridge Cable Tension Monitoring", *Advances in Structural Engineering*, Vol. 17, No. 11, pp. 1657-1668.

Zarbaf, S.E.H.A.M., M. Norouzi, R.J. Allemang, V.J. Hunt, A. Helmicki, and C. Venkatesh, 2018, "Ironton-Russell Bridge: Application of Vibration-based Cable Tension Estimation", *Journal of Structural Engineering*, Vol. 144, No. 6, pp. 4018-4030.

Zhang, L., G. Qiu, and Z. Chen, 2021, "Structural Health Monitoring Methods of Cables in Cable-Stayed Bridge: A Review", *Measurement*, Vol. 168, pp 108-134.

Zhang, L., Q. Gao, and H.W. Zhang, 2013, "An Efficient Algorithm for Mechanical Analysis of Bimodular Truss and Tensegrity Structures", *International Journal of Mechanical Sciences*, Vol. 70, pp. 57-68.

Zhao, G., J. Li, M. Zhang, and Y. Yi, 2022, "Experimental Study on the Bearing Capacity and Fatigue Life of Lightning Rod Structure Joints in High-Voltage Substation Structures", *Thin-Walled Structures*, Vol. 175, pp. 109-128.

Zheng, R., L. Liu, X. Zhao, Z. Chen, C. Zhang, and X. Hua, 2018, "Investigation of Measurability and Reliability of Adhesive-bonded Built-in Fiber Bragg Grating Sensors on Steel Wire for Bridge Cable Force Monitoring", *Measurement*, Vol. 129, pp. 349-357.

Zui, H., T. Shinke, and Y. Namita, 1996, "Practical Formulas for Estimation of Cable Tension by Vibration Method", *Journal of Structural Engineering*, Vol. 122, No. 6, pp. 651-656.

APPENDIX A: Experimental Studies

Considering the challenges that may be encountered in the field, two laboratory and two field tests were conducted. First, the accuracy of the vision-based monitoring system was measured by placing three different accelerometers on the three-story model in the Bogazici University Structure Laboratory in North Campus. This experiment was conducted at the pixel scale instead of the subpixel scale. The displacement of the structure by applying a force was measured on a pixel scale with DSLR. The edge points of each floor were followed in the vision-based monitoring system. Additionally, the acceleration response of each floor was obtained from the placed accelerometers. For each floor, the natural frequencies of the model were compared in the frequency domain. Additionally, the mode shapes obtained by both methods using FDD were compared. A white surface was placed on the back side to create contrast with the measured object.

As a result of this experiment, it was determined that the movement in every structure would not be as measurable and would be at lower levels. Pixels were repositioned using a quadratic polynomial function both to measure movement at the subpixel scale and to prevent geometric distortion caused by deformation and displacement. Following this experiment, a cable experiment was conducted in the Bogazici University Structure Laboratory to estimate the cable tension using taut string theory and to verify the estimation of cable tensions by using the dynamic properties of the cable in the vibration method. The response of the cable under different cable tensions was measured with an accelerometer and DSLR. Instead of controlling the displacement in the time domain with applying scale factor and calibration processes, the FFT of both displacement and acceleration responses was taken and the natural frequencies were compared in the frequency domain.

As a result of this experiment, it had been shown that displacement response could be obtained with sufficient accuracy by using DSLR from a sufficiently long distance

and cable tensions could be obtained by using the dynamic response the characteristic features of the cable. Since both experiments were carried out in the laboratory, the effect of environmental conditions was eliminated. The light intensity between the recorded object and the background could be adjusted as desired. For this reason, field measurements were carried out on the wind turbine located at Boğaziçi University Sarıtepe Campus.

As a result of this experiment, since the turbine was in the active phase, its dynamic properties could be determined in only a single direction. Additionally, since a single camera was used and the movement of the structure was at lower levels, video was recorded only from the top part of the turbine. For this reason, the natural frequencies of the wind turbine had been determined, but no information about the mode shapes had been obtained. Additionally, this experiment was chosen because the wind turbine and pylon of the bridge had similar structural features. Then, a lightning rod experiment was carried out to prove that efficient results can be obtained in cloudier and windier environmental conditions and in a shorter measurement time. In this field experiment, the contrast between the measured object and the background is at lower levels because of environmental conditions.

In this field experiment, three measurements were taken from different distances. The displacement response of the vision-based monitoring system were compared with 6 different accelerometers placed on the lightning rod. In the first of the video recordings, natural frequencies and mode shapes comparison was carried out using the displacement at the top two sensor levels and the acceleration data obtained from the top two accelerometers. In the second video recording, natural frequencies and mode shapes were compared using displacement at the top four sensor levels and acceleration data from the top four accelerometers from a greater distance. In the last video recording, the displacement at the top five sensor levels was found and the same operations were carried out. As a result of this field experiment, the tradeoff between measurement distance and resolution was demonstrated.

From all these laboratory and field test results, the method to be used for the measurement on the bridge was developed. The effect of measurement distance and weather conditions was investigated.

A.1. Shaking Table Test

A study was conducted to measure non-contact vision-based structural displacement at multiple points using a single camera. A method based on two advanced template matching techniques was used. These are the UCC and the orientation code matching (OCM). This study investigated the performance of the vision-based monitoring system in both the time and frequency domain by calculating the displacement of a three-story frame structure at each floor via the shaking table. Structural high-contrast targets such as bolts and nuts on the surface of the structure and low-contrast natural targets were tracked with a camera. The use of artificial targets gave slightly more consistent results than natural targets using lower contrasts. In addition, displacements at all floors by a single camera and displacements measured by high-performance laser displacement sensors were compared in the time domain. In addition, the modal features obtained from the image sensors and the modal features obtained from the reference accelerometers were also compared in the frequency domain. Consistent results were obtained in both comparisons. The performance of the vision-based monitoring system was investigated under environmental problems such as dim light and background image disturbance. Compared to accelerometers, vision-based monitoring system gave more economical and convenient results. With a single camera, displacement at different points of the structure could be measured remotely. While mode shapes could only be obtained from the points where the sensors were placed in accelerometers, mode shapes could be revealed by obtaining displacements at different points depending on the camera resolution in vision-based monitoring systems. In this respect, high-resolution image sensors could be a low-cost, easy-to-implement, more flexible and high-performance alternative to conventional accelerometers. However, there was a tradeoff between resolution and field of view in the case of simultaneous measurements from different points of the measured structure. Using a high-resolution camera or

using several cameras recording in sync could solve this problem (Feng & Feng, 2016).

In another study, the reliability of the vision-based monitoring system was tested with the help of image processing technique to calculate the tension in suspension cables under traffic loads. Before using the created method in cable measurements, an experimental model with three modes was created. Thus, the displacement response of the artificial target in each mode was measured and the validity of the method used was compared. To measure the dynamic character of the model, accelerometer sensors were placed in the mass on each floor. In addition, laser triangulation meters were placed to measure the displacement in the center of the camera image to coincide with the points where the distorted image was large in the measurement taken by using the vision-based monitoring system. Thus, image-based measurement in both time domain and frequency domain was compared with actual measurement values. Percent error, RMSE, and system error, which was the RMSE divided by the maximum displacement, were used to verify the accuracy and precision of the estimated displacement values obtained by vision-based monitoring system. When all three equations were examined, it showed that the dynamic response measurement system using image-processing proposed in the study was applicable for monitoring cables. Thus, the dynamic properties of cables could be estimated economically and efficiently. Since the installation and maintenance costs of accelerometer sensors were high, SHM could only be performed on certain cables. Multiple cables could be tracked using a single measurement using vision-based SHM methods. However, when using the vision-based dynamic measurement system, rainy days, foggy weather conditions and nighttime conditions would cause the images to spread and deteriorate, which would make this method difficult to use (Kim et al., 2013).

In another study, multi-point displacement responses of structures were measured using DIP techniques and a shake table test was performed to validate the algorithm. DIC, one of the DIP techniques, was applied in this algorithm. By comparing the image transformation function (ITF) with the undeformed and deformed images, the movements, and errors between these two images were corrected. Thus, it was aimed to

increase the resolution of displacement responses. The shake table test was conducted on a 2-story steel frame. It was aimed to validate the multi-point displacement response measurement algorithm using DIP. Table motion measured by DAQ and displacement responses estimated by DIP were compared. Percent error, RMSE and system error were compared. The percent error was less than 1%, the RMSE was less than 0.5 mm, and the system error was less than 2% against both displacement responses. In addition, the movement of the target in the frame system and LVDT values were compared. The movement of the temporary support frame securing the LVDT had also been calibrated considering the movement and the errors had been shown to be negligible. Subsequently, the displacement responses obtained were transferred to the frequency domain and the PSD was obtained. The accuracy of natural frequencies was less than 0.1%. Thus, it had been shown that the applied DIP algorithm was a more useful method in finding the natural frequency (Kim & Kim, 2011).

In a different study, an vision-based system for measuring the displacement of bridges in real time using DIP technique was investigated. Shaking table test was performed in the laboratory to verify the algorithm used and to investigate its reliability. The obtained data gave sufficient results not only in the time-consuming analysis but also in the frequency domain. It included the actual displacement, the projection of the captured image by defining the target, and the number of pixels moved. From these data, the trigonometric transformation matrix was calculated with the help of image processing technique. There was less than 3% error between the dynamic displacement obtained with this method used and conventional LVDT sensors. Sufficient dynamic resolution had also been obtained in frequency values. This technique was very cost-effective and easy to apply (Lee & Shinozuka, 2006a).

Based on these studies, an experiment was conducted on a 3-story model at Boğaziçi University North Campus Structure Laboratory. This model used was a model with story drift prevented in one direction. Thus, it was adjusted so that the torsional mode did not appear in the movement. The DSLR was 8 meters away from the model when recording. It was recorded at 60 FPS. In order to check the accuracy

of the data, accelerometer sensors were placed on each story in the direction of the movement. The FFT values of the pixel scale data and the acceleration values were found and compared in the frequency domain. The experimental setup during the measurements of the model is shown in Figure A.1.



Figure A.1. Experiment setup for the vision-based analysis.

During the experiment, force was applied to the model 7 times. The acceleration response of each story is shown separately. The data from the accelerometers were taken at 200 Hz. After these 7 forces applied, the data obtained from the accelerometers are shown in Figure A.2.

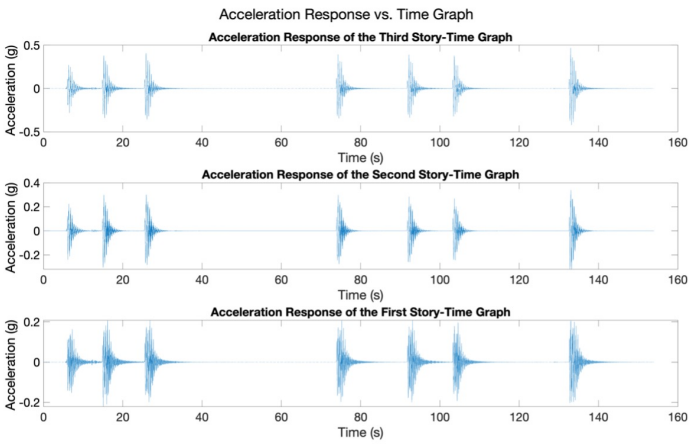


Figure A.2. Acceleration response of each story vs. time graph of model experiment from accelerometer.

The acceleration response values obtained after the applied force were analyzed separately. The numbering used during the analysis and which regions were analyzed are shown in Figure A.3.

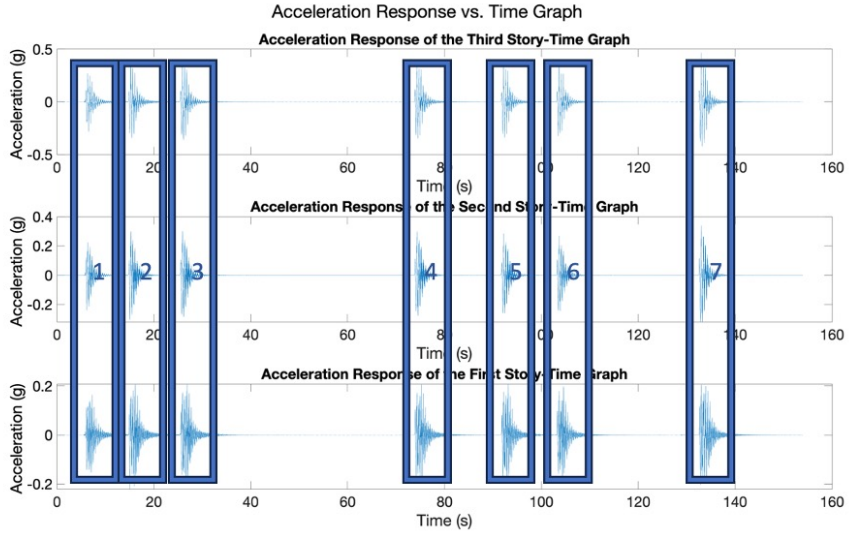


Figure A.3. Data set for each applied force.

To calculate mode shapes from time and acceleration responses, FDD was used. FDD is a non-parametric modal description technique defined using only the output. While applying the identification algorithm, the PSD matrix is first estimated. Using the Welch method, the FFT number was determined as 4096. The PSD matrix was estimated using a 50% overlapping. Then, G_{yy}, which is the estimated version of the output PSD, is calculated by taking the Singular Value Decomposition (SVD) of the PSD matrix. The formula is shown as

$$G_{yy}(w_j) = U_j S_j U_j^H, \tag{A.1}$$

where U_j is orthonormal matrix that means $U_j U_j^H$ is equal to 1. S_j is the diagonal matrix with the scalar singular values. In this way, the spectral matrix is decomposed into auto spectral density functions as many as the number of natural frequencies selected, each being a system with a single-DOF. By plotting the initial singular values, modal frequencies can be determined simply using peak picking. Thus, mode shapes are determined using the first singular vectors at the determined frequencies (Brincker et al., 2001). It was created with functions developed in MATLAB.

As an example, and since they gave similar results in all of them, the acceleration responses in the first section were examined. The Power Spectral Densities of these responses given for each story were calculated. Each story response using accelerometers and analyzes of the first section for all stories are shown in Figure A.4, Figure A.5, and Figure A.6. The table with the results for each section is summarized in Table A.1.

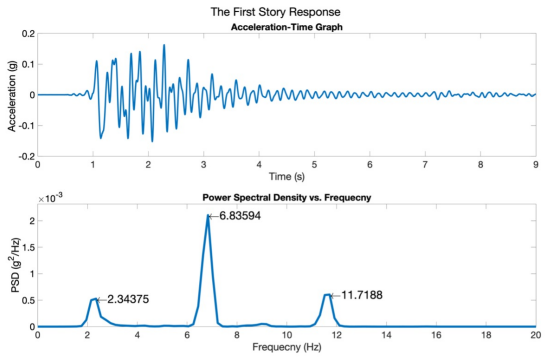


Figure A.4. The first story response and PSD.

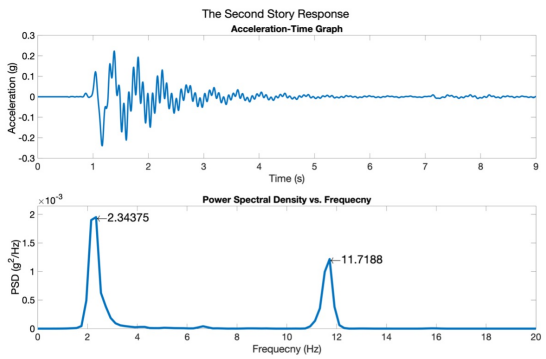


Figure A.5. The second story response and PSD.

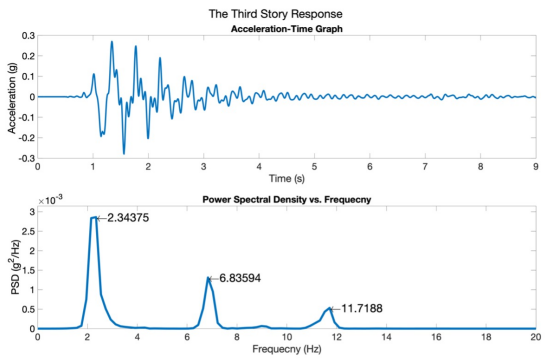


Figure A.6. The third story response and PSD.

Table A.1. Frequency response of each story and section by accelerometer.

	The First Story			The Second Story			The Third Story		
	f1	f2	f3	f1	f2	f3	f1	f2	f3
Section-1	2.34	6.84	11.72	2.34	-	11.72	2.34	6.84	11.72
Section-2	2.25	6.93	11.62	2.25	-	11.62	2.25	6.93	11.62
Section-3	2.25	6.93	11.62	2.25	-	11.62	2.25	6.93	11.62
Section-4	2.34	6.64	11.72	2.34		11.72	2.34	7.03	11.72
Section-5	2.34	6.64	11.72	2.34	-	11.72	2.34	7.03	11.72
Section-6	2.34	6.64	11.72	2.34	-	11.72	2.34	7.03	11.72
Section-7	2.34	6.64	11.72	2.34	-	11.72	2.34	7.03	11.72

FDD was used while mode shapes were found. The SVD graph found when using FDD is shown in Figure A.7.

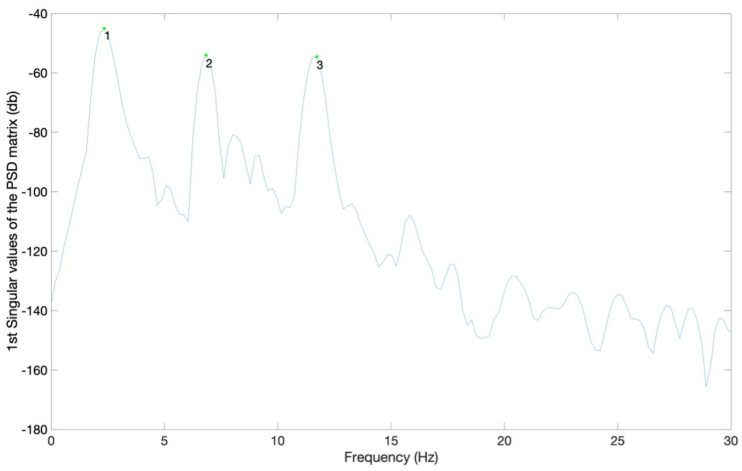


Figure A.7. SVD of experimental model using vision-based system.

The corresponding mode shapes obtained from the acceleration responses of the first section are given in Figure A.8.

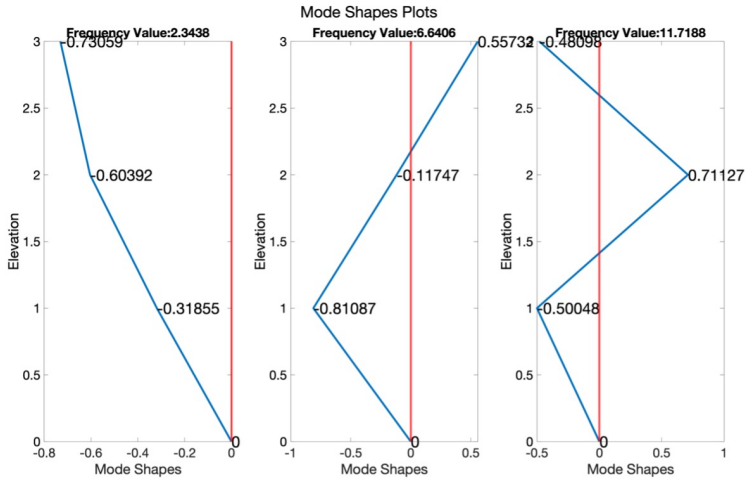


Figure A.8. Mode shapes of model experiment using accelerometer.

After these 7 forces applied, the data obtained from the DSLR camera are shown in Figure A.9. The displacement response of each story is shown separately. The data from the camera were taken at 60 Hz.

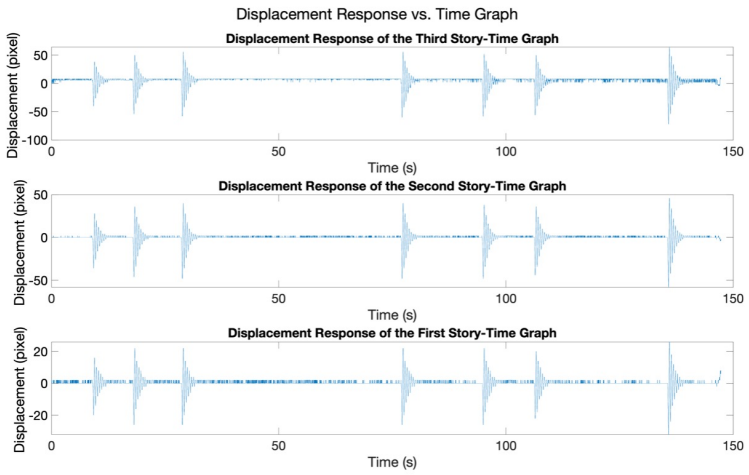


Figure A.9. Displacement response of each story vs. time graph of model experiment from vision-based system.

The displacement response values obtained after the applied force were analyzed separately. The numbering used during the analysis and which regions were analyzed are shown in Figure A.10.

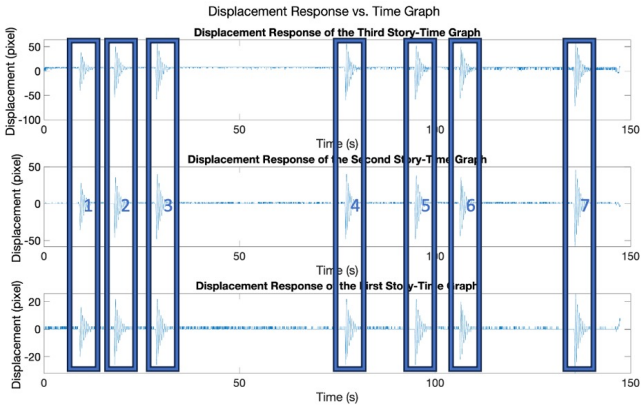


Figure A.10. Data set for each applied force.

As an example, and since they gave similar results in all of them, the displacement responses in the first section were examined. The PSDs of these responses given for each story were calculated. Each story response using vision-based system and analyzes of the first section for all stories are shown in Figure A.11, Figure A.12, and Figure A.13. The table with the results for each section is summarized in Table A.2.

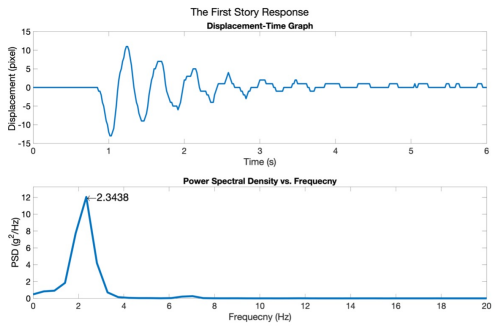


Figure A.11. The first story response and PSD.

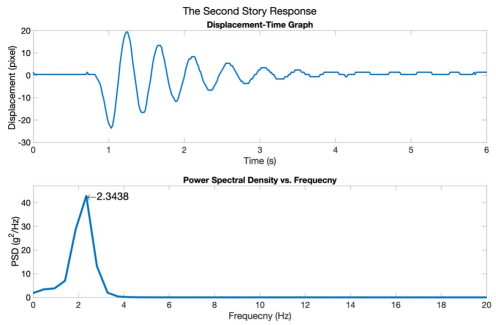


Figure A.12. The second story response and PSD.

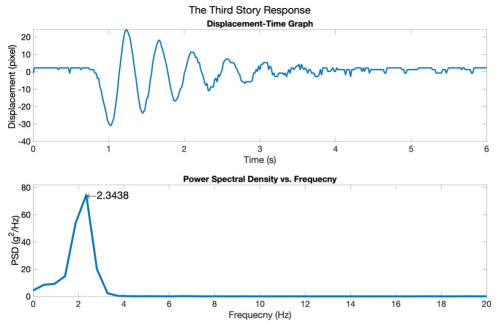


Figure A.13. The third story response and PSD.

Table A.2. Frequency response of each story for each section using vision-based system.

	The First Story			The Second Story			The Third Story		
	f1	f2	f3	f1	f2	f3	f1	f2	f3
Section-1	2.34	6.56	-	2.34	-	-	2.34	-	-
Section-2	2.25	6.56	-	2.34	-	-	2.34	-	-
Section-3	2.25	6.56	-	2.34	-	-	2.34	-	-
Section-4	2.34	-	-	2.34	-	-	2.34	-	-
Section-5	2.34	6.56	-	2.34	-	-	2.34	-	-
Section-6	2.34	-	-	2.34	-	-	2.34	-	-
Section-7	2.34	6.56	-	2.34	-	-	2.34	-	-

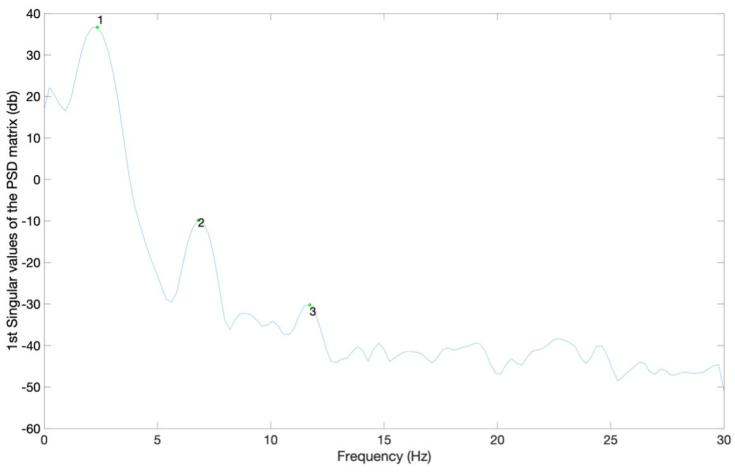


Figure A.14. SVD of experimental model using vision-based system.

FDD was used while mode shapes were found. The SVD graph found when using FDD is shown in Figure A.14. The corresponding mode shapes obtained from the displacement responses of the first section using vision-based system are given in Figure A.15.

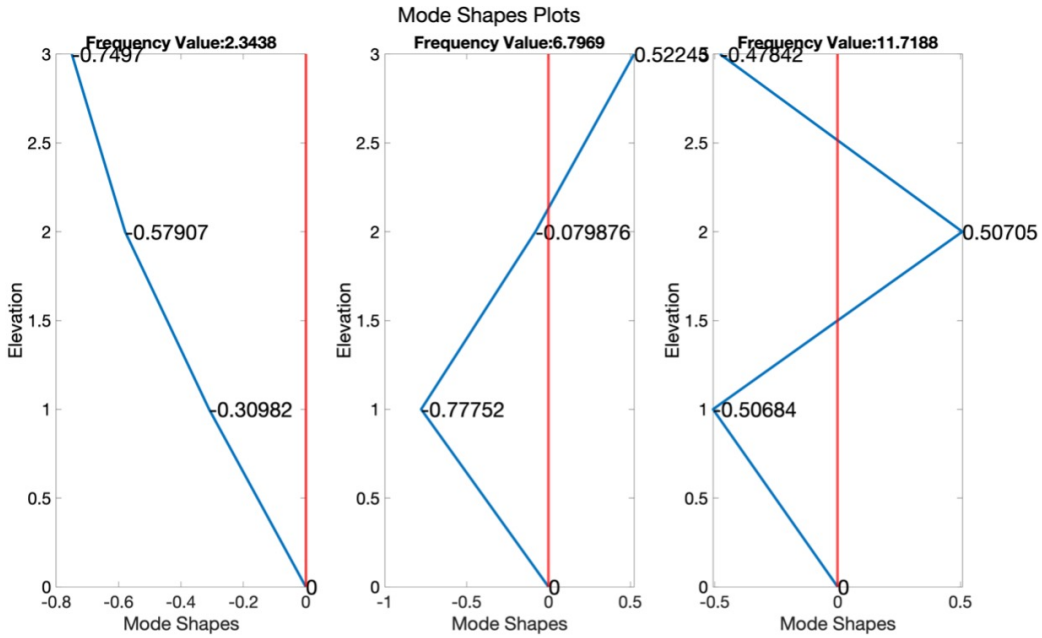


Figure A.15. Mode shapes of model experiment using vision-based system.

When both analyzes were compared, when the responses on the story were analyzed separately, all three frequency values of the model could be obtained from the response of each story in the results obtained from the accelerometers. However, when the displacement response of each floor was analyzed in the vision-based system, only the first natural frequency could be obtained. However, as a result of the FDD analysis, when the SVD values were compared, all three natural frequencies were almost the same. In addition, when the mode shapes obtained as a result of the FDD analysis were compared, the mode shapes were almost the same in the first and second mode, and there were small differences in the third mode shape. The figure with which this comparison is made is shown in Figure A.16.

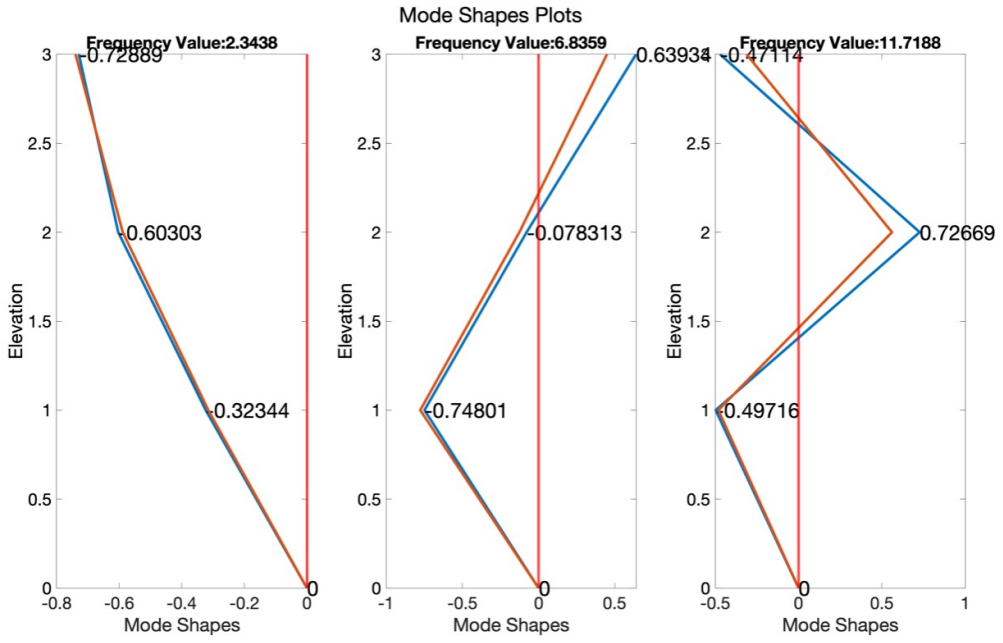


Figure A.16. Comparison of mode shapes of model experiment using accelerometers and vision-based monitoring system.

Improvements in the software used and the hardware system where the video recording was taken may provide closer results (Feng & Feng, 2016). In addition, reducing the distance from which the video recording was taken, recording in high resolution and frequency could improve the analysis results. Using 3 different cameras working in sync was another method that could improve the analysis results (Kim et al., 2013).

A.2. Cable Experiment

With the rapid development of construction techniques and the economy, bridges have become a frequent structure of modern transportation around the world. Many bridges in use are exposed to large traffic loads and complex environmental factors. Therefore, it is vital to monitor bridges with SHM systems. In bridges where cables are used as primary load bearing systems, cables play a vital role in the structural condition of the bridge. Due to environmental factors and traffic usage, it is necessary

to constantly monitor the tensions in the cables (Du et al., 2020). In this type of bridges, dead load (the bridge's self-weight) and live load (traffic loads in use) are directly transferred to the tower by cables. Vibration and fatigue caused by these loads and environmental factors caused by galvanic corrosion may cause deterioration in cables and decrease in load capacity. Therefore, whether the cable tensions are in the reasonable range will affect the overall condition of the structure. Since cables are flexible elements that can withstand tension and have different tensile properties, they are characterized by small stresses and large displacements. Under different conditions, the mechanical properties of suspension cables will directly affect the results of cable tensions. Therefore, it is necessary to examine the static and dynamic behavior of the cable (Zhang et al., 2013). In the static analysis, the static linearity of the cable with both ends fixed under gravity forces was investigated in the first studies. As a result, it was obtained that it was a catenary similar to a parabola (Fallis, 1997). Based on this theory, three assumptions were based. These are; a) flexible member is ideal. b) The deformation of the external force satisfies Hooke's law. c) The cross section does not change under force. Different curves were obtained according to various hypotheses. However, it had been obtained that the curve closest to the reality is catenary (Pevrot & Goulois, 1979; Fleming, 1979). However, cable members under static force were practically not ideal. The self-weight of the cable made the relationship between the deformation in the beam direction and the internal stress less than the actual cable stiffness non-linear. Therefore, in order to simplify this nonlinear calculation, the equivalent elastic modulus was used for the calculation of cable sag. The equivalent elastic modulus could transform the cable curve under the sagging effect into a non-linear elastic straight bar (Freire et al., 2006). In dynamic analysis, the vibration frequency method was widely used in engineering because of its accuracy, simplicity, and convenience (Benedettini & Gentile, 2011). By using the relationship between cable tension and frequency, cable tensions could be obtained directly or indirectly. The free vibration differential equation of the fixed cable was obtained from the flat taut string theory in which both cable sag and bending stiffness were neglected (Zui et al., 1996). The simplified version of the vibration equation is given in the methodology.

The study of Sun et al. (2011) showed that the error between the cable tension obtained from the frequency and the tension value obtained from the Finite Element Model (FEM) was less than 6%. Static methods were load cell method, hydraulic jack method, and EM sensor method. In the load cell method, a load cell was attached to the end of the cable to control the cable tension permanently. This method gave more accurate results than other methods. However, since it was very costly to add this load cell during the maintenance phase of bridges, it was mainly added during construction (Wang et al., 1999). In the hydraulic jack method, the pressure on a hydraulic jack placed at the end of a cable was measured to obtain the cable tension. The hydraulic jack method was more cost effective than the load cell method. However, it had lower accuracy than the load cell method and required sufficient working space to be placed in the first step. This made the method disadvantageous (Casas, 1994). In the EM sensor method, the cable tension was estimated by measuring the velocity of the waves produced by the EM induction. However, only the cable tensions exposed to air could be estimated. The tension of grout-filled cables could not be measured (Duan et al., 2011). Since dynamic methods were faster and more economical than static methods, dynamic methods were generally used in cable measurement. Data obtained from low-frequency accelerometers were used to determine the cable tension. However, since the length of the structure and the cables in the bridges were long, the longer cables through which the data was transferred to the recorder prevents reliable data. In addition, the installation of the system required a large amount of manpower and time, as all sensors and data acquisition device must be interconnected. In addition, separate accelerometers must be placed to monitor all cables in bridges, and since the lifetime of accelerometers is five years, periodic maintenance was required. This made this method costly. Therefore, different methods were needed to obtain the dynamic properties and the cable tension without connecting the sensors to the cables. For this purpose, laser Doppler effect method, GPS method and vision-based monitoring system are used. Although the laser Doppler effect method had high accuracy, it is not used frequently because it requires as many sensors as cables (Nassif et al., 2005; Chen & Petro, 2005). In GPS method, the low error and sampling rate in the signals was not applicable in determining the dynamic properties of cables under traffic loads

(Kaloop, 2012). In contrast, cable dynamic properties obtained with accelerometers could be obtained using vision-based monitoring systems. This system could also reach inaccessible cables and determine dynamic properties. It was also a longer lasting and cost-effective monitoring system (Lee & Shinozuka, 2006b; Ji & Chang, 2008).

A cable experiment was conducted in the laboratory to evaluate the accuracy of the method. In this experiment, the accuracy of the formula was checked by determining the dynamic properties of the cable under different forces. The system setup during the experiment is shown in Figure A.17.

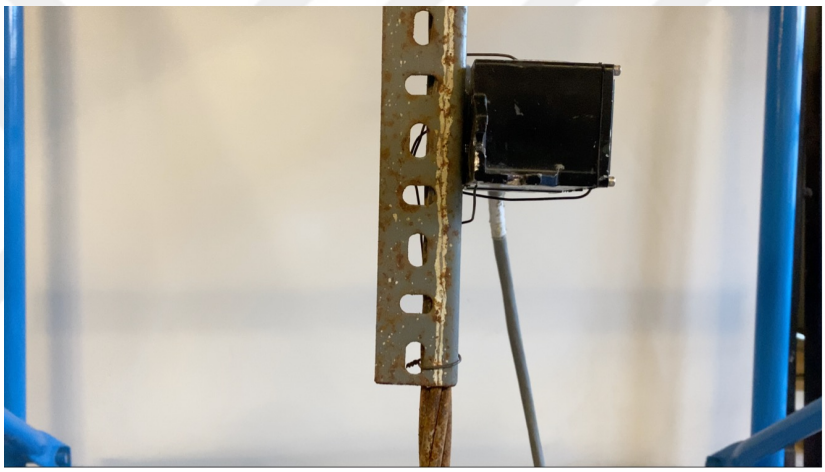


Figure A.17. Experiment setup for the cable.

During the experiment, a cable previously used in the laboratory was held at a certain force on both sides with the help of a hydraulic jack. The accelerometer was placed near the midpoint of the cable. The purpose of this experiment was to determine the dynamic properties of the cable using vision-based monitoring system. For this reason, the acceleration data obtained from the accelerometer and the displacement value in pixel scale obtained from the vision-based monitoring system were compared in the frequency domain. Since a fixed length measurement was taken using the same cable, the values of m and l in the vibration formula in Zui et al. (1996) were constant. For this reason, in this experiment, the relationship between natural frequency and cable tension was investigated under different forces.

In the first case, the cable tension was set to 1.32 tons, or 12.94 kN. In this case, force was applied to the cable six times. The acceleration data obtained from the accelerometers as a result of these applied forces are shown in Figure A.18.

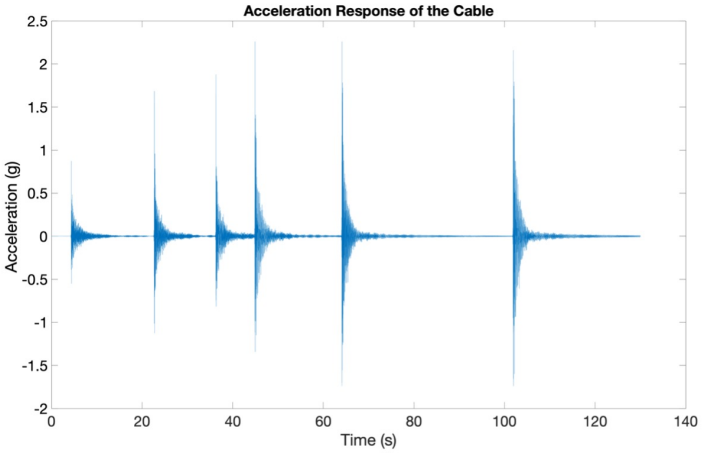


Figure A.18. Acceleration response of the cable for the first case.

Each acceleration response of these applied forces was examined separately. The sections separated during this analysis and their numbering are shown in Figure A.19.

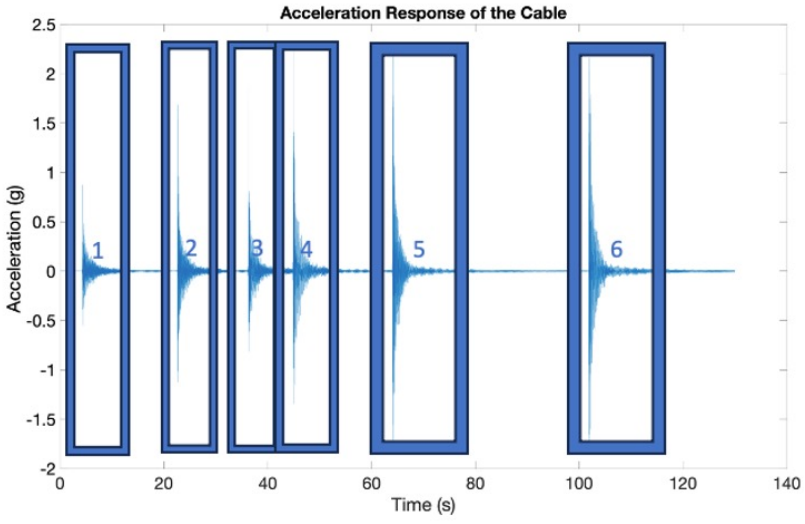


Figure A.19. Data set for each applied force for the first case.

Since they give similar results, only the acceleration data in the first data set are shown in Figure A.20.

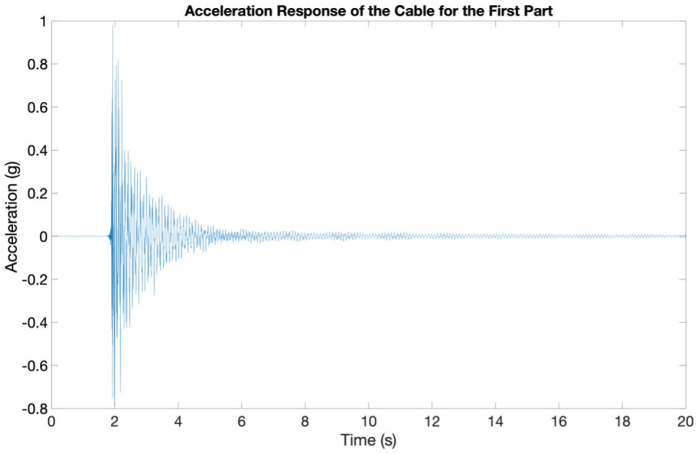


Figure A.20. Acceleration response of the first part for the first case.

The PSD values of the data in this range were found in the frequency domain. These values are shown in Figure A.21. Since the acceleration records were taken at 200 Hz, the peaks in the frequency domain were found up to 100 Hz.

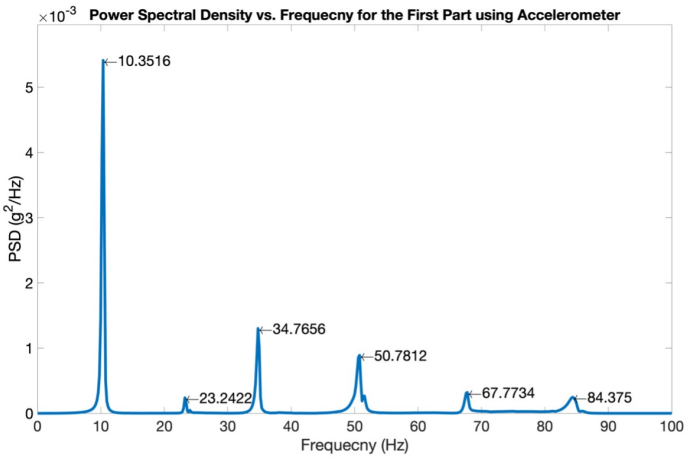


Figure A.21. PSD of the cable for the first case.

Simultaneous video recording was taken with accelerometers to compare the dynamic properties obtained. This video recording was analyzed by vision-based analysis. The displacement response in pixel scale is shown in Figure A.22.

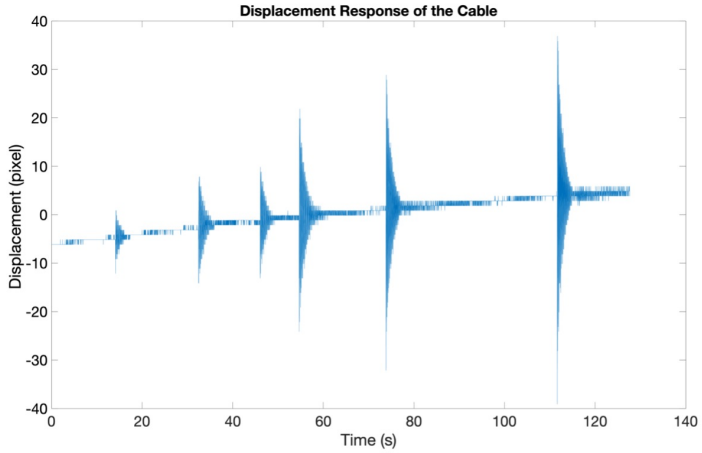


Figure A.22. Displacement response of the cable for the first case.

Each displacement response in pixel scale of these applied forces was examined separately. The sections separated during this analysis and their numbering are shown in Figure A.23.

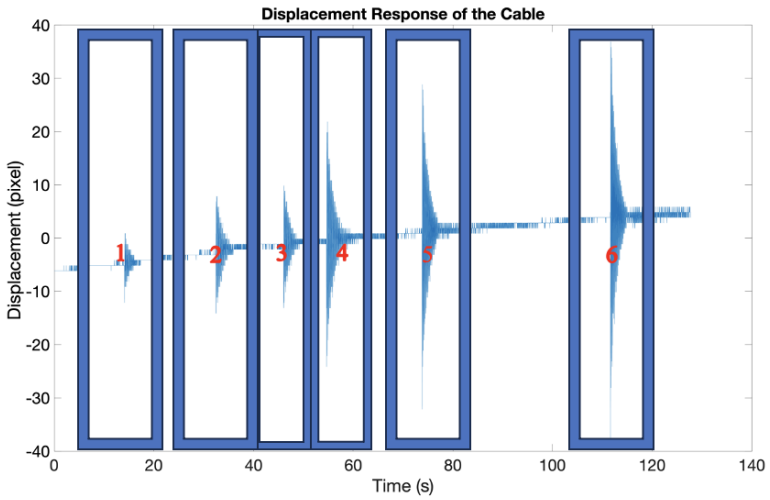


Figure A.23. Data set for each applied force for the first case using vision-based monitoring.

Since they gave similar results, only the displacement data of the first data set in pixel scale are shown in Figure A.24.

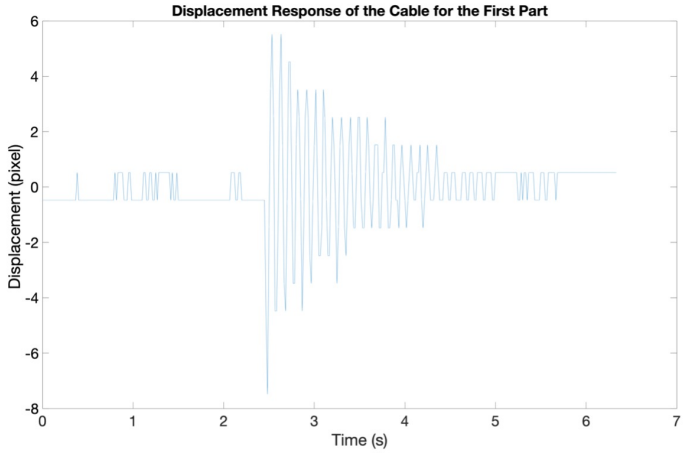


Figure A.24. Displacement response of the first part for the first case.

The PSD values of the data in this range were found in the frequency domain. These values are shown in Figure A.25. Since the video recording was taken at 60 FPS, the peaks in the frequency domain were found up to 30 Hz.

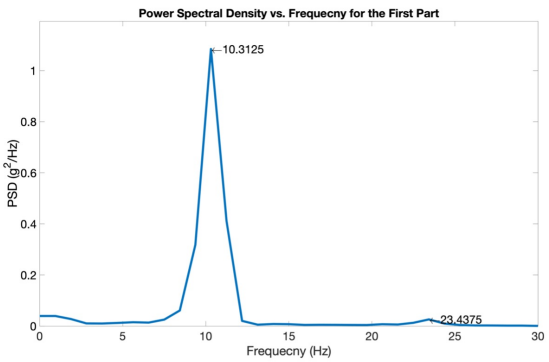


Figure A.25. PSD of the cable for the first case.

According to the formula used to calculate the cable tension, the $f_n/\ n$ ratio is expected to be constant. However, it was given that these ratios were not constant in the results obtained. Nevertheless, the same results in vibration-based analysis from accelerometers and vision-based analysis showed the accuracy of the method used. The peaks for each section and the tensions obtained from these peaks is shown in Table A.3.

Table A.3. Summary of the each section for the first case.

Applied Force=12.94 kN							Experiment-1							
	f						L	Mat.	Tension (kN)					
	1	2	3	4	5	6	(m)	Prop.						
Kinem.	10.4	23.2	34.8	50.8	67.8	84.4	4.2	1.43	10.83	13.66	13.59	16.3	18.58	20
	10.4	23.4	35.0	50.9	67.7	84.5	4.2	1.43	10.96	13.78	13.76	16.36	18.57	20.06
	10.4	23.3	35.1	51.0	67.9	84.5	4.2	1.43	10.85	13.68	13.82	16.43	18.64	20.05
	10.4	23.3	35.1	51.1	68.1	85.4	4.2	1.43	10.98	13.69	13.86	16.51	18.76	20.47
	10.4	23.4	35.2	51.2	68.2	85.4	4.2	1.43	10.97	13.79	13.92	16.6	18.82	20.5
	10.4	23.5	35.2	51.3	68.3	86.3	4.2	1.43	10.96	13.95	13.95	16.64	18.87	20.92
Vision-based Monit.	10.3	23.4	-	-	-	-	4.2	1.43	10.75	13.89	-	-	-	-
	10.4	23.3	-	-	-	-	4.2	1.43	10.97	13.76	-	-	-	-
	10.4	23.3	-	-	-	-	4.2	1.43	11.02	13.76	-	-	-	-
	10.5	23.4	-	-	-	-	4.2	1.43	11.09	13.89	-	-	-	-
	10.4	23.4	-	-	-	-	4.2	1.43	10.9	13.8	-	-	-	-
	10.4	23.5	-	-	-	-	4.2	1.43	10.93	13.92	-	-	-	-

Then, the cable tension was increased to investigate the reason for the $f_n/\ n$ ratio not being constant. The hydraulic jack was set at 2.97 tons, ie 29.13 kN. For this case, force was applied to the cable five times. The acceleration data obtained from the accelerometers as a result of these applied forces are shown in Figure A.26.

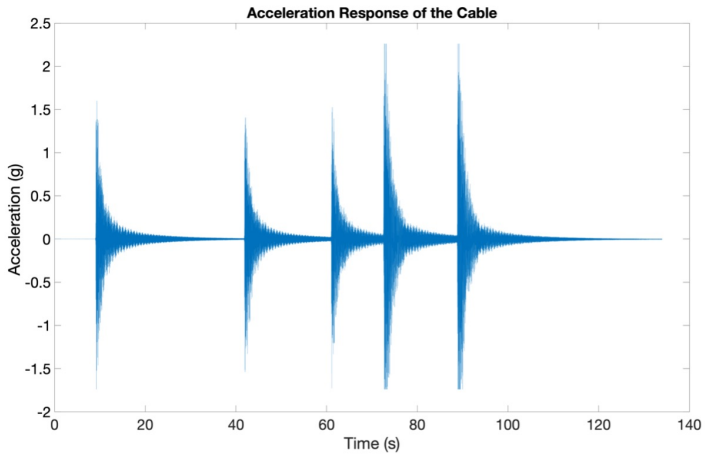


Figure A.26. Acceleration response of the cable for the second case.

Each acceleration response of these applied forces was examined separately. The sections separated during this analysis and their numbering are shown in Figure A.27.

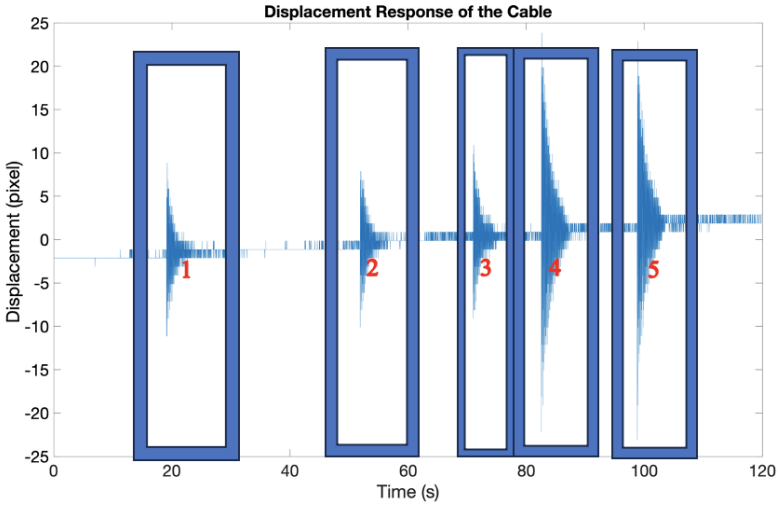


Figure A.27. Data set for each applied force for the second case.

Since they gave similar results, only the acceleration data in the first data set are shown in Figure A.28.

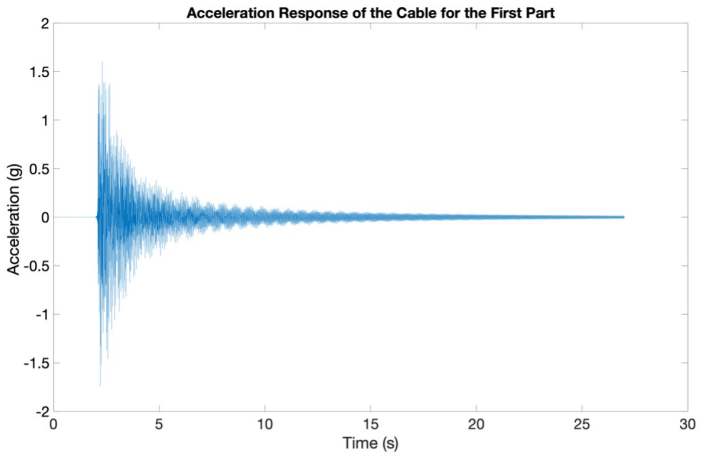


Figure A.28. Acceleration response of the first part of the cable for the second case.

The PSD values of the data in this range were found in the frequency domain. These values are shown in Figure A.29.

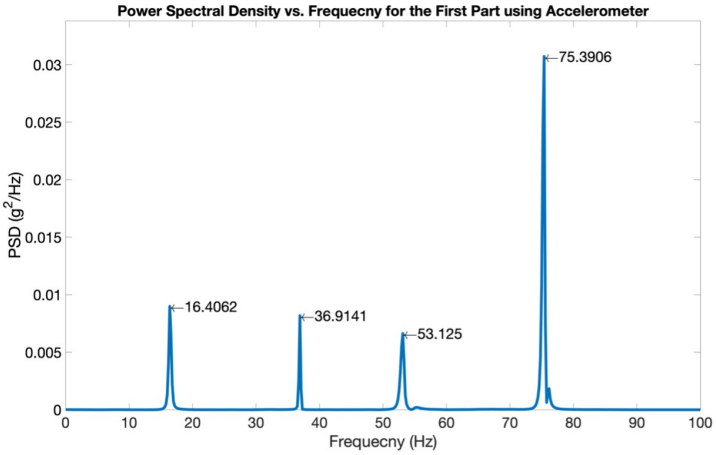


Figure A.29. PSD of the cable for the second case.

Simultaneous video recording was taken with accelerometers to compare the dynamic properties obtained. This video recording was analyzed by vision-based analysis. The displacement response in pixel scale is shown in Figure A.30.

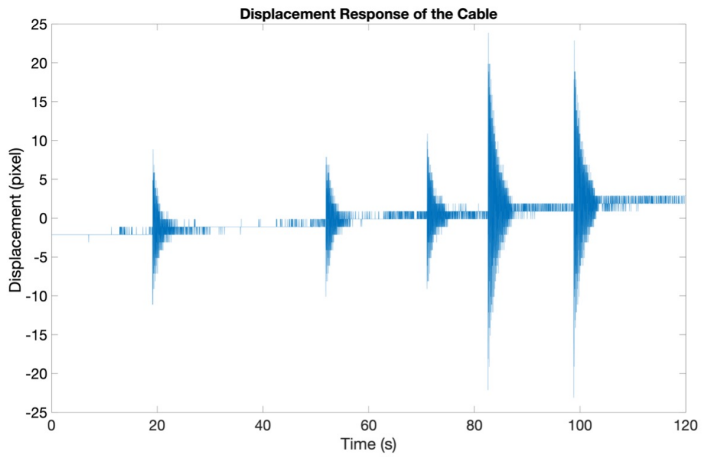


Figure A.30. Displacement response of the cable for the second case.

Each displacement response in pixel scale of these applied forces was examined separately. The sections separated during this analysis and their numbering are shown in Figure A.31.

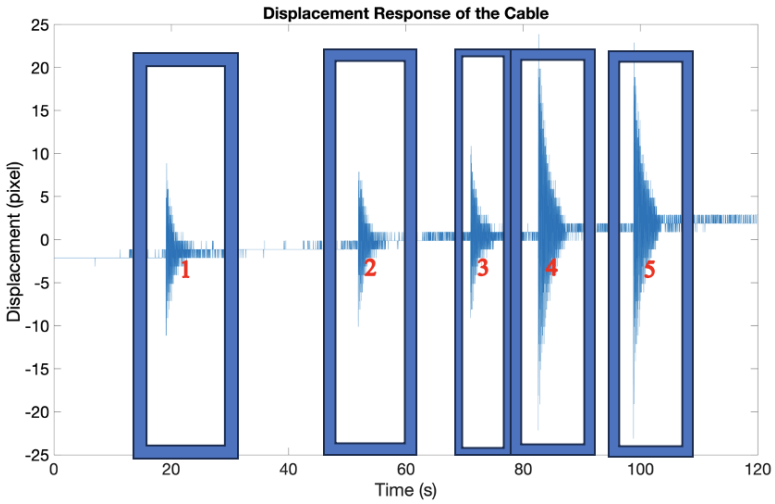


Figure A.31. Data set for each applied force for the second case using vision-based processing.

Since they gave similar results, only the displacement data of the first data set in pixel scale are shown in Figure A.32.

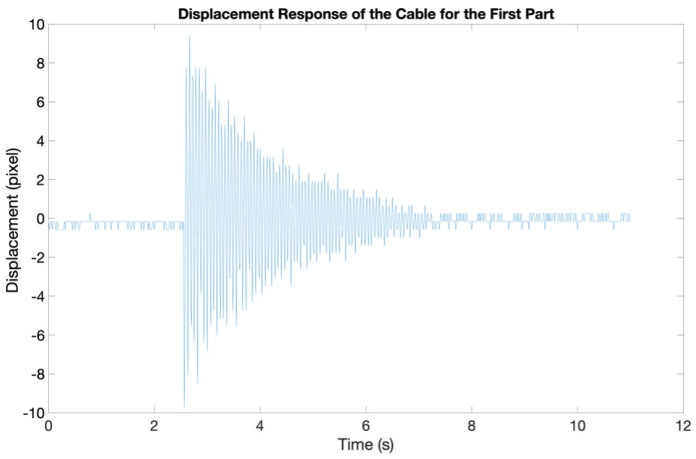


Figure A.32. Displacement response of the first part of the cable for the second case.

The PSD values of the data in this range were found in the frequency domain. These values are shown in Figure A.33. Since the video recording was taken at 60 FPS, the peaks in the frequency domain were found up to 30 Hz.

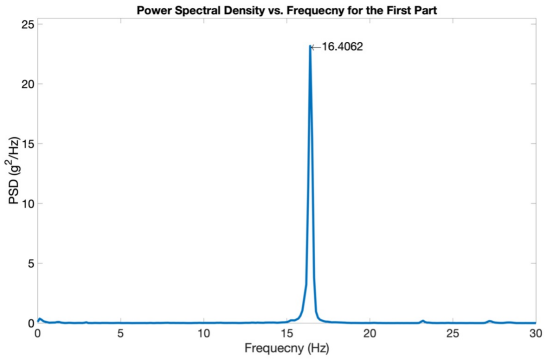


Figure A.33. PSD of the cable for the second case.

The table with the peaks for each section and the tensions obtained from these peaks is shown in Table A.4. As a result of this analysis, $f_n/\ n$ ratio was not the same for the peaks. However, the results in this analysis as in the first analysis showed that vibration-based analysis using accelerometers and vision-based analysis gave almost the same results.

Table A.4. Summary of the each section for the second case.

Applied Force=29.13 kN					**Experiment 2**					
	f				**L**	**Material**	**Tension (kN)**			
	1	**2**	**3**	**4**	**(m)**	**Property**				
Kinem.	16.4	36.9	53.1	75.4	4.2	1.43	27.23	34.45	31.72	35.93
	16.4	36.9	52.9	75.2	4.2	1.43	27.18	34.34	31.39	35.79
	16.4	36.9	53.1	75.4	4.2	1.43	27.17	34.39	31.65	35.9
	16.4	36.9	53.0	75.4	4.2	1.43	27.19	34.41	31.61	35.92
	16.4	36.9	53.1	75.4	4.2	1.43	27.34	34.46	31.73	35.93
Vision-based Monit.	16.4	-	-	-	4.2	1.43	27.23	-	-	-
	16.4	-	-	-	4.2	1.43	27.3	-	-	-
	16.4	-	-	-	4.2	1.43	27.3	-	-	-
	16.4	-	-	-	4.2	1.43	27.23	-	-	-
	16.5	-	-	-	4.2	1.43	27.38	-	-	-

Finally, the hydraulic jack was set at 4.96 tons, ie 48.64 kN. For this case, force was applied to the cable four times. The acceleration data obtained from the accelerometers as a result of these applied forces are shown in Figure A.34.

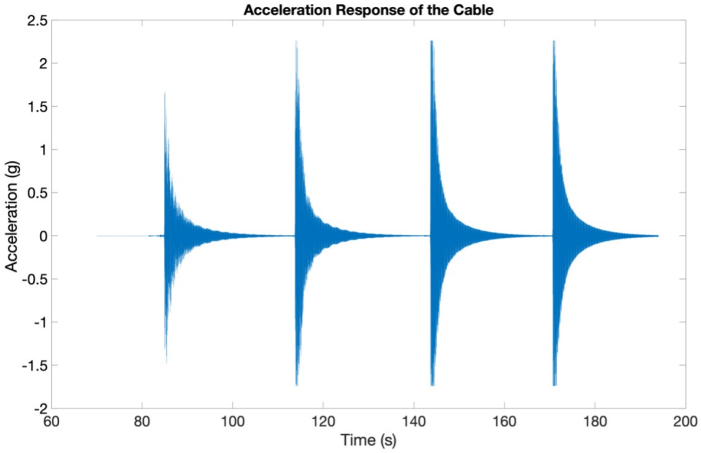


Figure A.34. Acceleration response of the cable for the third case.

Each acceleration response of these applied forces was examined separately. The sections separated during this analysis and their numbering are shown in Figure A.35.

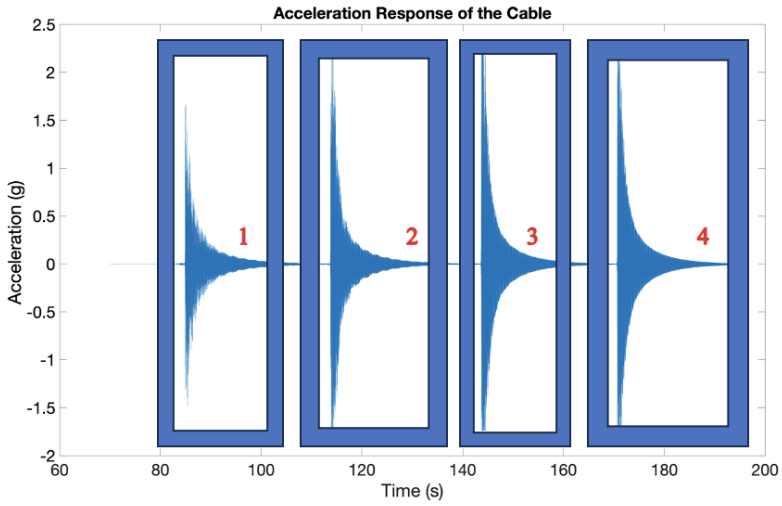


Figure A.35. Data set for each applied force for the third case.

Since they gave similar results, only the acceleration data in the first data set are shown in Figure A.36.

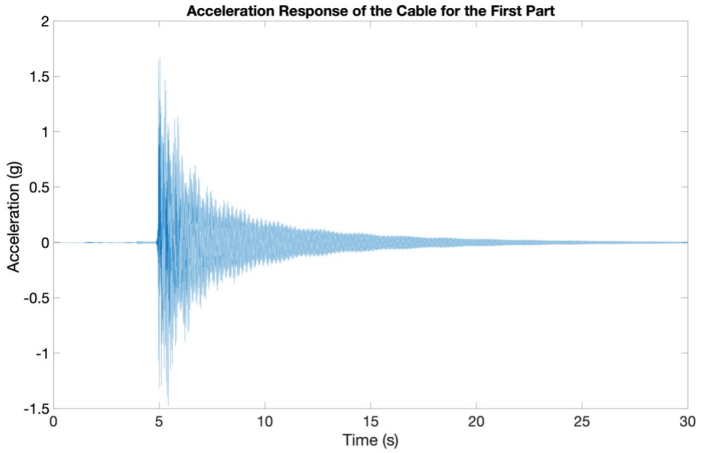


Figure A.36. Acceleration response of the first part for the third case.

The PSD values of the data in this range were found in the frequency domain. These values are shown in Figure A.37.

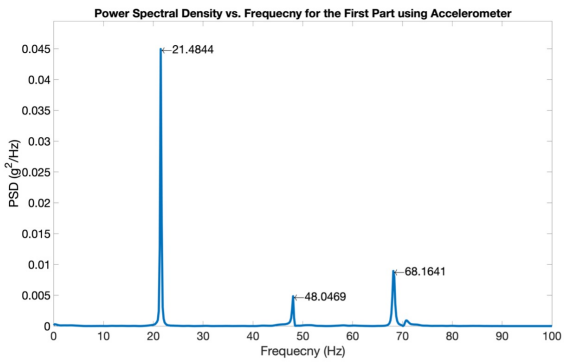


Figure A.37. PSD of the cable for the third case.

Simultaneous video recording was taken with accelerometers to compare the dynamic properties obtained. This video recording was analyzed by vision-based analysis. The displacement response in pixel scale is shown in Figure A.38.

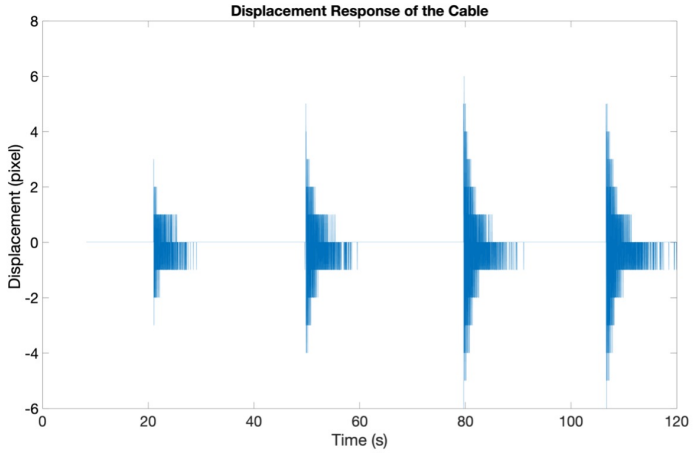


Figure A.38. Displacement response of the cable for the third case.

Each displacement response in pixel scale of these applied forces was examined separately. The sections separated during this analysis and their numbering are shown in Figure A.39.

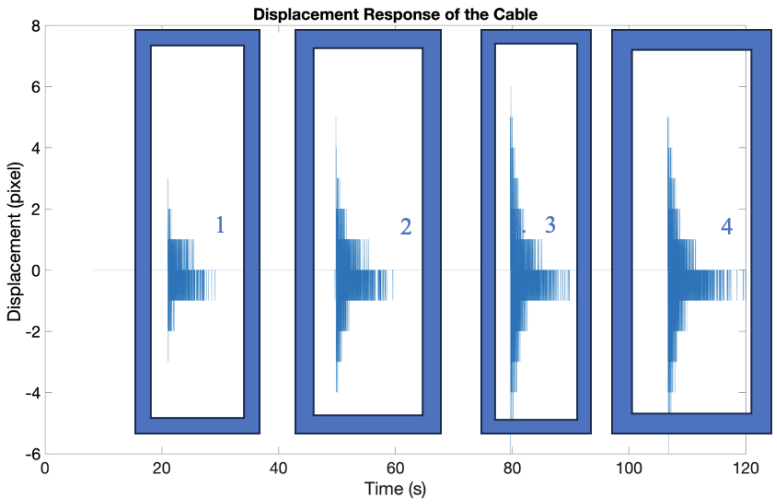


Figure A.39. Data set for each applied force for the first case using vision-based monitoring.

Since they gave similar results, only the displacement data of the first data set in pixel scale are shown in Figure A.40.

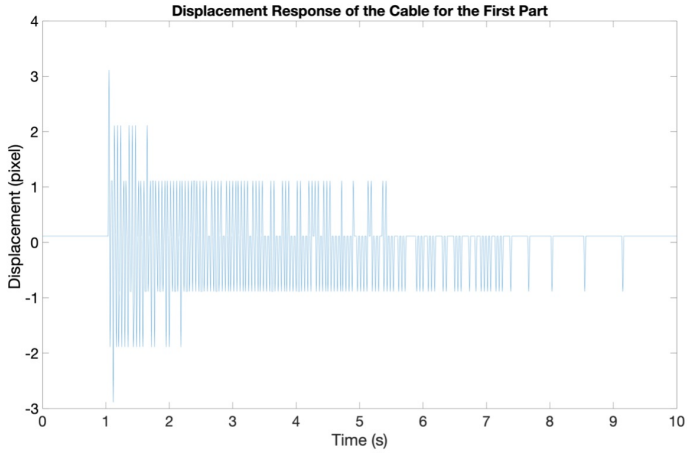


Figure A.40. Displacement response of the first part for the third case.

The PSD values of the data in this range were found in the frequency domain. These values are shown in Figure A.41. Since the video recording was taken at 60 FPS, the peaks in the frequency domain were found up to 30 Hz.

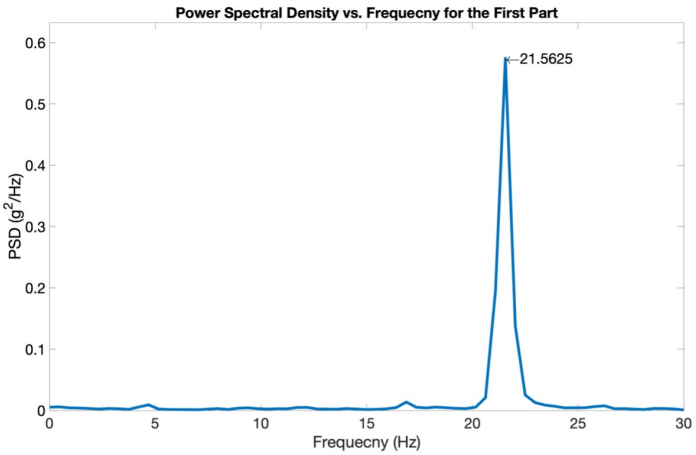


Figure A.41. PSD of the cable for the third case.

The table with the peaks for each section and the tensions obtained from these peaks is shown in Table A.5. As a result of this analysis, $f_n/\ n$ ratio was not the same for the peaks. However, the results in this analysis as in the first analysis showed that traditional accelerometers and vision-based analysis gave almost the same results.

Table A.5. Summary of the each section for the third case.

Applied Force=48.64 kN				**Experiment 3**				
	f			**L**	**Material**	**Tension (kN)**		
	1	**2**	**3**	**(m)**	**Property**			
Kinem.	21.5	48.1	68.2	4.2	1.43	46.64	58.38	52.21
	21.5	-	68.0	4.2	1.43	46.64	-	51.88
	21.5	-	68.2	4.2	1.43	46.73	-	52.25
	21.5	48.1	68.3	4.2	1.43	46.73	58.4	52.35
Vision-based Monit.	21.6	-	-	4.2	1.43	47.01	-	-
	21.6	-	-	4.2	1.43	46.95	-	-
	21.6	-	-	4.2	1.43	46.98	-	-
	21.6	-	-	4.2	1.43	47.03	-	-

As a result of all three experiments, it was seen that the vision-based monitoring system gave almost the same results as the traditional accelerometers. However, there could be several reasons why the $f_n/\ n$ ratio was inconsistent. The fact that this ratio did not give consistent results despite the change in tension might indicated that there was a situation where it was related to the m or l value in the formula. For this reason, changing the cable used or changing the length of the cable fixed from both sides could provide consistent results at $f_n/\ n$ ratio.

A.3. Vision-based Analysis of Wind Turbine

Wind is a type of renewable energy production that has become widespread in Turkey and around the world in recent years. Currently, most countries are investing in installing modern wind turbines on onshore and offshore (Oliveira et al., 2018a). Some of the electricity use of most countries is met by these wind turbines. For example, in Turkey, the share of wind energy in the total installed power capacity was given as 11 % in December 2022. The share of the daily consumption change during the year varies between 8 and 25 % related with the change in energy production according to Turkish Electricity Transmission Company (https://www.teias.gov.tr/).

Investments have been made in wind turbines to increase the capacity with a life expectancy of at least 20 years. The fact that some of them are close to completing their expected life period, their share in electricity production, and the increase in the size of their structural elements for harvesting more energy necessitate monitoring systems for early damage detection. Of the reasons, the last one is important for reliability because generally increased dimensions lead to higher loads and more flexible structures. It makes the structure prone to degradation and resonance problem (Oliveira et al., 2018a). In the Hu et al. (2015)'s study, the phenomenon of resonance was detailly examined. The explanation of this kind of phenomenon was based on the theory of the Sommerfeld effect. A significant resonance occured when the fundamental frequency of the tower matched the harmonic frequency induced by the rotation of the three blades. The rotational speed of the rotor increased as the energy source increased until it approached the fundamental frequency of the tower. Afterwards, the rotor speed remained the same as the energy source increased further. With this extra input energy, the vibration amplitude of the tower increased significantly. The input energy caused the vibration amplitude of the tower to increase until the rotation speed of the rotor jumps to a higher value and the resonance value was exceeded. The Sommerfeld effect showed that the wind tower caused the vibration amplitude of the tower to always remain in a resonant state. In other words, this caused a sudden jump of the tower frequency and rotor speed to a higher value, as well as a sudden decrease in the fundamental vibration amplitude (Hu et al., 2015). Thanks to the vibration-based monitoring systems, the dynamic properties of the structure (period, mode shape, and damping ratio) could be determined to design, maintain, and manage the wind turbine systems and to avoid this effect. It could also be used as an early warning system for damage to the foundation and blades. Thus, abnormal changes in these dynamic parameters could be used to determine what could be causing the damage. Abnormal decreases in natural frequency could be considered as the presence of damage since damage in structures was normally associated with a decrease in stiffness. Considering the natural frequency calculation, it was assumed that the mass change could be neglected, which was perfectly acceptable in wind turbines. In this context, the change in natural frequency could be used as the first indicator for damage detection. It was

necessary to examine the natural frequency behavior of vibration modes across different scenarios and to eliminate the natural frequency variation under different operating regimes. This was an expected result because some effects such as rotor rotation and change in blade pitch angle affect the natural period. For instance, Hu et al. (2015) stated that the maximum rotation speed of rotor blades was provided by automatically changing the direction of nacelle according to the wind direction under operational conditions. Therefore, a multivariate linear regression model was created that reflects the operating conditions of the structure under different regimes. Estimated variables consist of:

- Outdoor temperature
- Wind Speed
- Rotor Speed
- Blades pitch angle

Thus, by eliminating operational and environmental factors, the change in natural period could be used as a clearer indicator of damage (Oliveira et al., 2018b).

Dynamic measurements were required to determine dynamic properties, especially natural frequency of the tower. For dynamic measurements carried out in wind turbines in the last 30 years, accelerometers and/or strain gauges placed inside the tower were used. However, during these measurements, lightning and electromagnetic fields could cause data corruption. In addition, in these installations, a cable and data transfer device must be installed for power supply and data transfer. This showed the difficulties in establishing the system. For large commercial turbines, these setups and sensor calibrations were time consuming and expensive (Hu et al., 2015).

Satellite GPS was used to examine quasi-static and dynamic deformations for large slender structures. In this study, deformation measurements made with GPS in previous studies were summarized and it was shown that GPS results could be verified with accelerometer data. Problems such as Karman vortex vibrations, earthquake-

induced oscillations, and quasi-static deformations of most slender structures were investigated. In recent years, GPS had been used for anti-seismic design based on displacement deformation. The dynamic properties of the structure could be determined using GPS (Nickitopoulou et al., 2006).

In the following years, fiber optic strain gauges had been used instead of accelerometers and conventional strain gauges. It was used to monitor the structural health and to generate a real-time strain profile of 4.5 MW wind turbines in the wind park in Wilhelmshaven, Germany. As an advantage, optical sensors were not sensitive to electromagnetic fields or lightning. On the other hand, additional feasibility studies were required for the efficient and economical use of this measurement system. Necessary error compensation methods for these systems, which were sensitive to humidity and temperature changes, were being observed (Schroeder et al., 2006).

In recent years, the feasibility of applying photogrammetry to large wind turbines and the accuracy of the results with the latest technology software and hardware had been investigated (Ozbek et al., 2010). As a result of the research, the accuracy of measurements for model validation and SHM of wind turbines with this method was compared. After the accuracy of the measurement estimation, it had been discussed whether it could be used to determine the modal behavior of wind turbines or not. While photogrammetry was widely used to measure coordinates and displacements of objects under ambient or forced vibration, its use was limited. For instance, measurements were usually made in laboratories or in environments where environmental factors could be controlled. These measurements were used in static or dynamic deformation measurements of the structures and modal analysis and system identification of these. When measuring fast-moving objects, the shutter time, which was the time that light enters through the shutter creates the image, must be small enough to limit the blur caused by the motion of the object during image formation. However, the small shutter time made proper lighting more important. A stronger light intensity was required to provide sufficient contrast. In this study, some signs were placed on the object to be tracked. The camera system created a deformation vector by following the

movement of these signs. Thus, camera calibration was one of the most important factors that directly affect the accuracy of the deformation vector. In order to make this placed sign appear more clearly, an LED-based flash system was used. This created a contrast with the background material. Experiments were carried out at night to obtain a higher contrast, as there would be less reflection during the day. In addition to these problems, the number of pixels per displayed area was another criterion during measurement, since the number of pixels (resolution) was limited. To increase measurement accuracy, the camera was mounted on a tripod one-third of the tower height. While such an approach increased the accuracy in photogrammetric measurements, it increased the difficulty of measurement in larger turbines (Ozbek et al., 2010).

Ozbek et al. (2010)'s study had clearly shown that markers used as displacement sensors in photogrammetry could be easily placed on an existing turbine. Traditional methods did not require extra cable installation used for data transfer and power supply inside the turbine. Therefore, compared to the traditional sensors mentioned above (accelerometers, piezoelectric or fiber optic strain gauges), the marker installation could be completed in a very short time and was very cost effective. In fact, the use of special paints during the production of wind turbine parts in the factory could replace these markings. This further reduced costs. If the installation was not to be used as a continuous monitoring system, all turbines in the wind farm could be observed using a single system. In addition, any technical problem could be easily detected and repaired as all measuring systems were located on the ground. Although the image processing software, hardware and modal analysis techniques used during monitoring were not specifically designed for wind turbines, the accuracy achieved as a result of the feasibility study was very high. This accuracy could be further increased by using more specialized hardware and data processing. Developments in recent years have produced more sensitive and higher resolution cameras. Therefore, it had revealed that photogrammetry was a more specialized and cost-effective technique for health monitoring and dynamic characterization of wind turbines.

In order to test the reliability of the method to be used in the bridge based on this study, a video recording was taken to perform vision-based analysis at a 900-kW onshore wind turbine at Saritepe Campus of Bogazici University, Kilyos, Istanbul. The photograph taken during video recording is shown in Figure A.42. The dynamic properties obtained by using vision-based analysis were compared with the values in the article published by Soyoz et al. (2020). In this study, long-term vibration-based monitoring of the mentioned wind turbine was carried out. Turbine, 12 different accelerometers located at 4 different levels of the tower were continuously examined. The sensors were located in the Northeast (NE) direction (defined as Direction-1), which is the dominant wind direction in this region, and vertical direction (defined as Direction-2) of it. Modal properties such as frequency, mode shapes and damping ratios were obtained using the EFDD method. As a result of the analysis of long-term data, environmental/operational changes on modal parameters were determined and these effects were eliminated by performing multiple regression analysis. Then, the FEM developed using these modal features had been updated. Afterwards, seismic fragility curves of the structure were obtained under different wind levels and different scenarios were examined.



Figure A.42. The photograph taken during video recording.

The method mentioned in the methodology was used. In order to reduce the computational load and not to calculate subpixels for each pixel in each frame, only a certain region had been determined as ROI window. The ROI window is shown in Figure A.43.



Figure A.43. Region of interest for top displacement.

The contrast between the color difference on the sides of the tower and the sky had been used. By using the intensity difference between the light reflected from the edge of the material and the sky, displacement measurement was made at the subpixel level. While calculating the FFT, the amplitude value of the displacement graph does not change the frequency value in the frequency domain. For this reason, the camera calibration and transformation to the mm level were not used in the displacement vector. The displacement was shown at the pixel level. These steps were required to find the top displacement value at the metric level. The displacement-time graph in pixels is shown in Figure A.44. Since DSLR is used for video recording, only 10 minutes of video could be recorded.

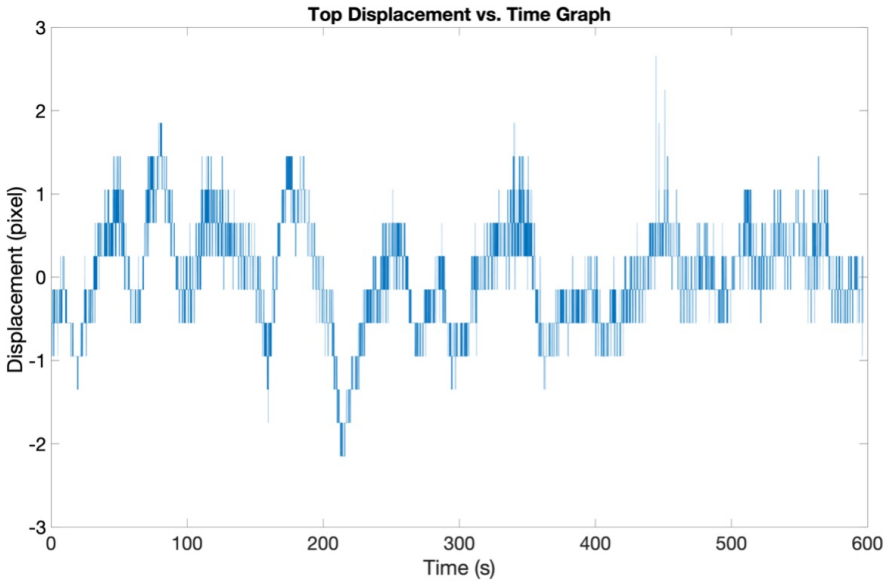


Figure A.44. Top displacement vs. time graph.

As a result of the analysis, it had been shown that the first mode frequency was not affected by environmental/operational conditions, and these conditions influence the second and third mode frequencies. Mode frequencies in which environmental/operational effects were removed are given in Table A.6 (Soyoz et al., 2020).

Table A.6. The mode frequency means when effects are removed (Soyoz et al., 2020).

	Direction 1	**Direction 2**
1st Mode (Hz)	0.47	0.46
2nd Mode (Hz)	3.3	3.3
3rd Mode (Hz)	9.29	9.36

The natural frequency graph of the structure obtained using the top displacement data is given in Figure A.45. As a result of this analysis, only the first mode frequency was observed as 0.45 Hz. The recording was taken in Direction-2. The results are satisfactory in terms of the accuracy of the method. When only 10 minutes of video recording could be taken at 60 FPS, the number of FFT could not be increased during the analysis. The number of FFT defines the number of partitions used to divide the

received data into equal strips or partitions. So, bin is an example of a spectrum.

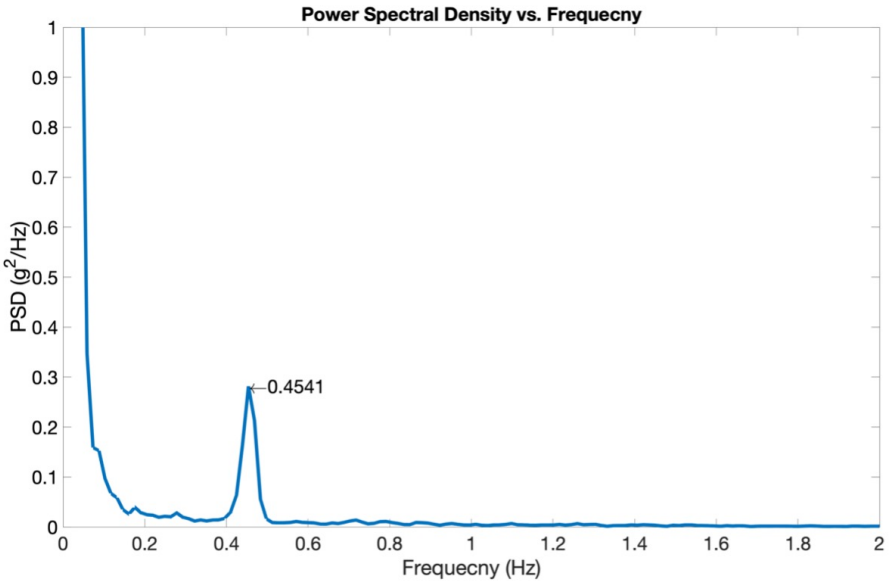


Figure A.45. PSDs for operating wind turbine.

Recording longer video could reveal other modes as well. In addition, using a camera with higher resolution, using a camera to measure from different points of the tower at the same time, and using a camera with a higher FPS could also improve the result of the analysis. Thus, the second and third mode frequencies could also be obtained.

A.4. Lightning Rod Measurement

Since substations and natural gas utilities are critical points for the receipt, conversion, and distribution of energy, it is vital to ensure that they operate safely. During the working period of these points, problems and fires caused by a common natural disaster such as lightning seriously endanger the equipment and distribution at this point. In order to prevent damage caused by lightning, many lightning rods were placed at the points where these facilities were located. In some facilities, frame-lightning rod structure was used. Lightning rods were slender structures as they were generally thin and long structures with heights ranging from 10 m to 30 m. For this reason, they were

very sensitive structures against wind loads (Zhao et al., 2022). In recent years, there had been accidents in which lightning rod destruction caused by wind-induced vibration had occurred. Therefore, in such structures, SHM techniques, FEM analyzes, and wind tunnel tests (WTTs) obtained as a result of these analyzes were critical for the vibration analysis of the structure (Gomez-Cabrera & Escamilla-Ambrosio, 2022). These analyzes allowed to accurately calculate the bearing performance of the structure and then take the necessary maintenance measures to increase the reliability of the structure. During these analyses, SHM, WTTs and their accompanying FEM simulations were costly for analysis and require large amounts of data to be recorded and stored. In recent years, with the development of sensor technologies, wireless sensor networks had been used frequently in online monitoring of structures in large-scale structures and laboratory experiments (Amezquita-Sanchez & Valtierra-Rodriguez, 2018).

However, these traditional methods have some disadvantages. As the configuration of the structure becomes more complex, it was necessary to increase the number of test equipment and sensors. This made the monitoring of the structure more costly and time-consuming. Recent developments in hardware and software used for vision-based monitoring system implementation offered a new method to overcome these drawbacks. With these methods, it had been shown that the response of the structure could be measured, and its dynamic properties could be calculated (Choi & Han, 2018).

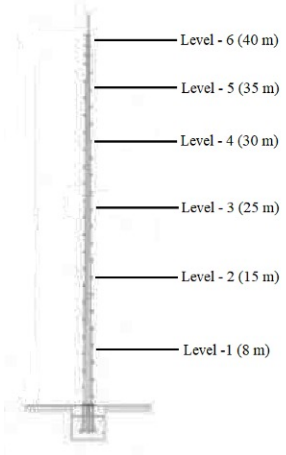


Figure A.46. Sensor layouts for the lightning rod.

In order to test the applicability of the method and to analyze in real life structures, a video recording was taken from the lightning rod to be measured using accelerometers. Details on which levels of accelerometers are present are shown in Figure A.46. The lowest diameter of the measured lightning rod was 78 cm, and the highest diameter was 15 cm. The cross-section was hexadecagon.

The values of the acceleration data obtained from the accelerometers at each level are shown in Figure A.47. The received data was taken at 200 Hz. The length of the data was 33 minutes.

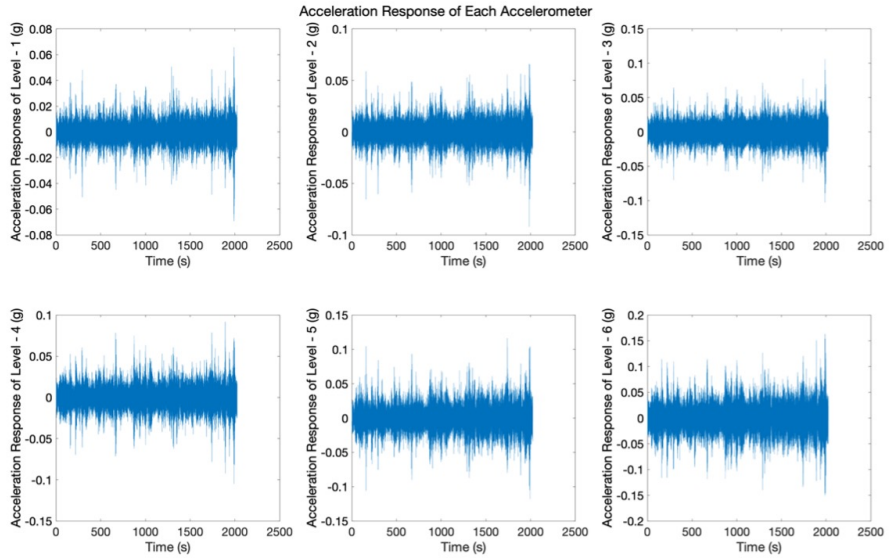


Figure A.47. Acceleration response of each level.

PSD values were calculated by taking the FFT of the data from each level. The values corresponding to the natural frequency of the structure in the obtained data are shown in Figure A.48. These values were compared in the frequency domain with the results obtained from the vision-based monitoring system. While the natural frequencies of the structure were obtained at each level in acceleration measurements, fewer natural frequencies were obtained in the vision-based monitoring system.

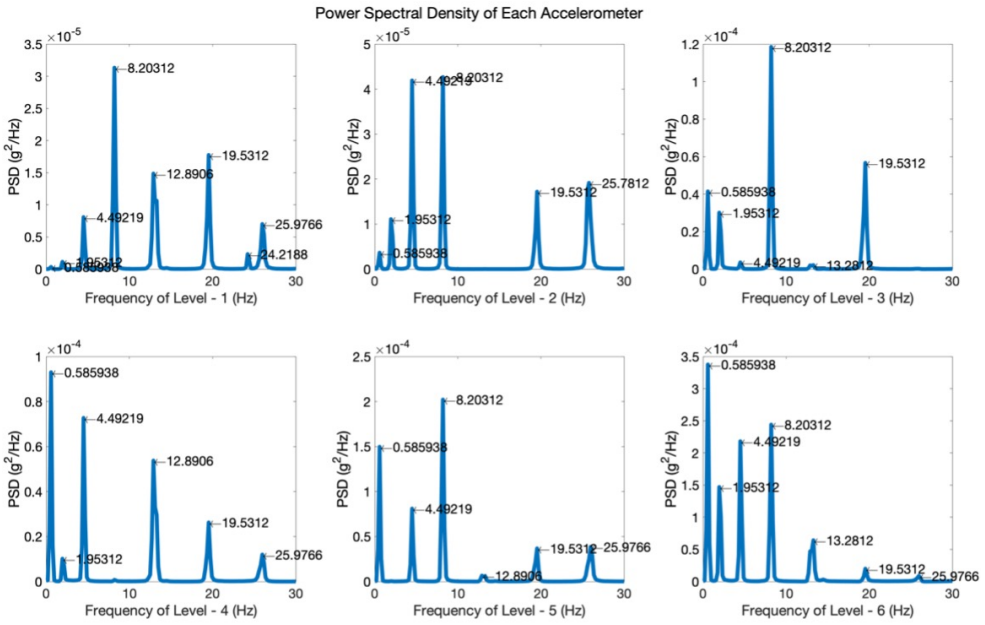


Figure A.48. PSD values for each level.

In addition, FDD was used while mode shapes were found. The SVD graph found when using FDD is shown in Figure A.49.

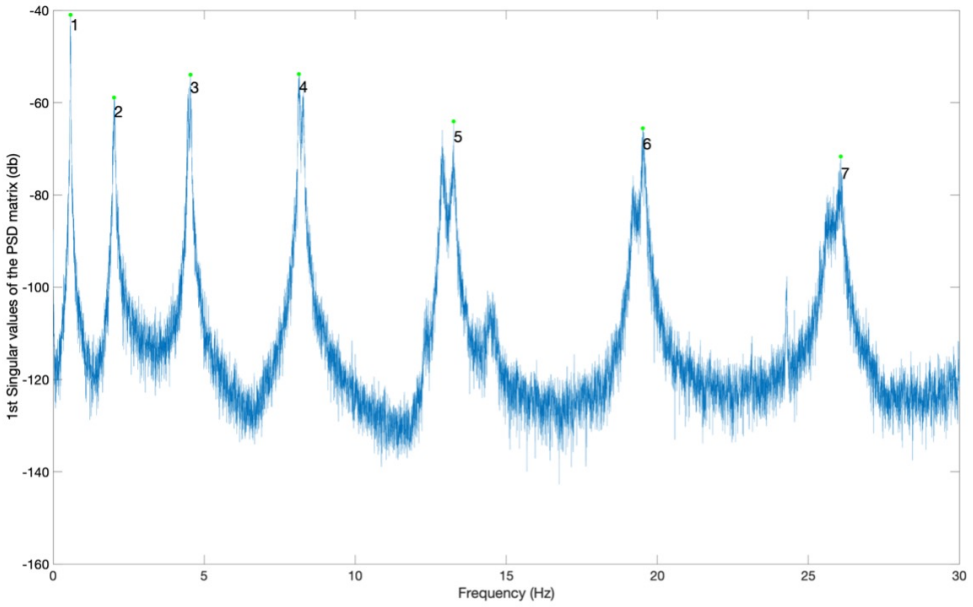


Figure A.49. SVD values of the structure using accelerometer.

The corresponding mode shapes obtained from the acceleration responses of the structure are given in Figure A.50.

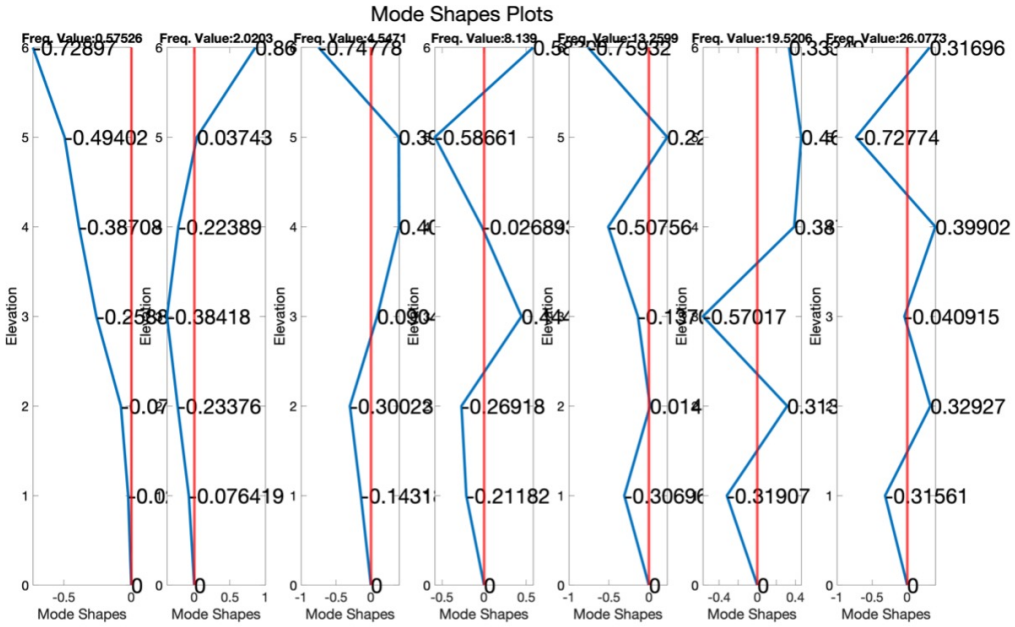


Figure A.50. Mode shapes of lightning rod using accelerometer.

Video recordings were taken from different distances. 3 video recordings were taken. The length of the videos varies between 100 and 140 seconds. Since the records were taken on a windy winter day, the weather conditions were not suitable for long recordings. Since the sensor locations were known from the video recording, the displacement values at the level of the sensors were calculated. Since the dynamic properties of the structure would be compared in the frequency domain, camera calibration and scale factor had not been calculated. The displacement value was given in pixels. Video recordings were taken at 60 fps.

In the first video recording, the displacement value of the fifth and sixth level accelerometers was calculated. The first frame of the captured video recording and ROI windows is shown in Figure A.51.



Figure A.51. ROIs for top two sensor levels.

The displacement responses and PSD values found by taking FFT of the fifth and sixth level in the first video are shown in Figure A.52.

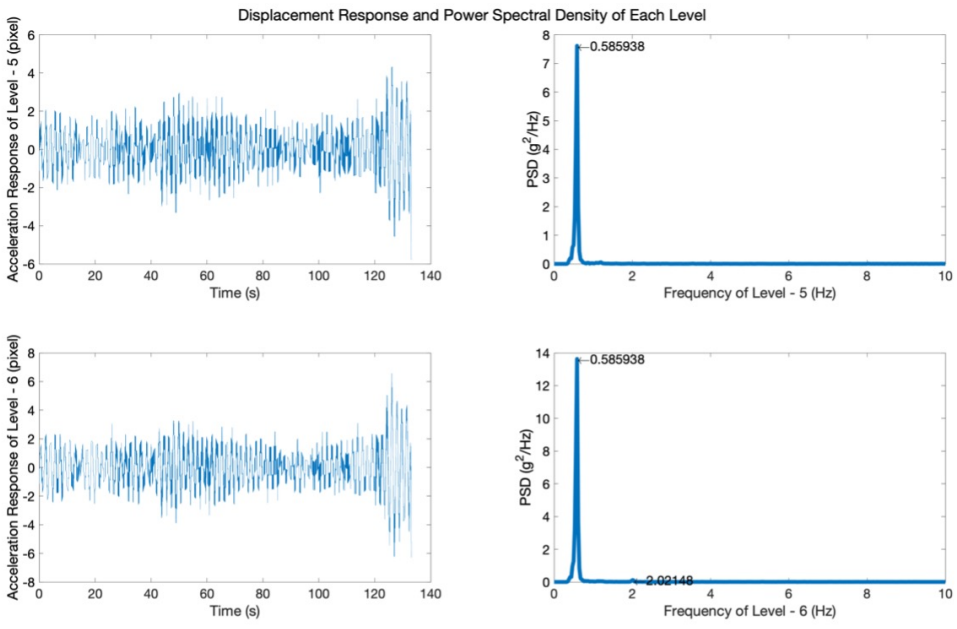


Figure A.52. Displacement response and PSD for top two sensor levels.

SVD values were obtained using FDD from the displacement responses. The values in SVD were determined by using the natural frequencies of the structure obtained from the accelerometers. The values selected in the SVD values are shown in Figure A.53.

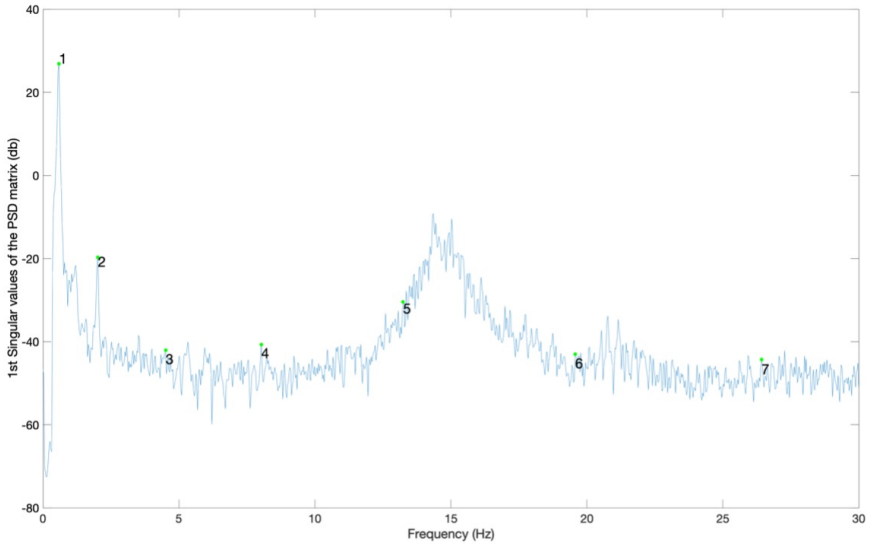


Figure A.53. SVD values used in obtaining mode shapes from displacement response for top two sensor levels.

The mode shapes obtained using the displacement response at the top 2 sensor levels are shown in Figure A.54.

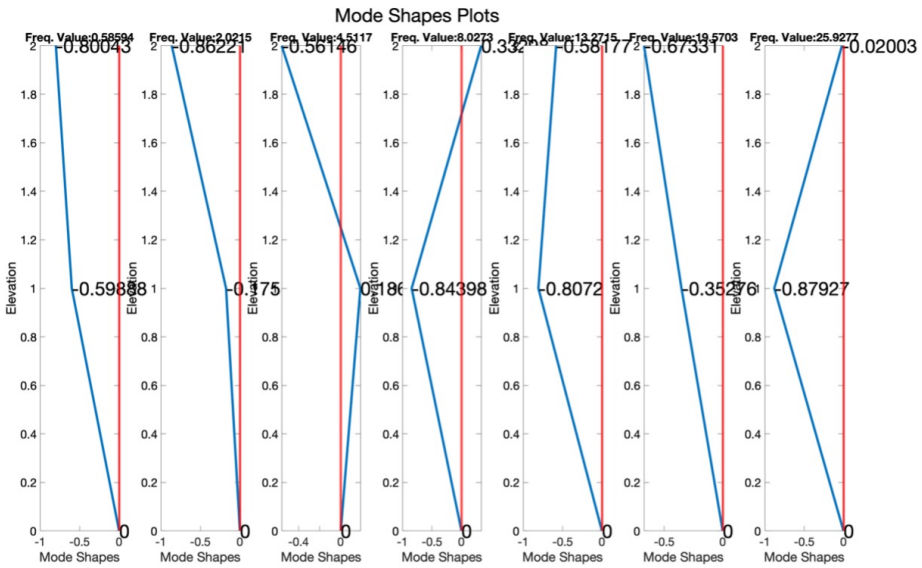


Figure A.54. Mode shapes obtained from displacement response for top two sensor levels.

The comparison of the mode shapes obtained with the acceleration response obtained from the accelerometers and the mode shapes obtained from the same level displacement response obtained from the DSLR is shown in Figure A.55.

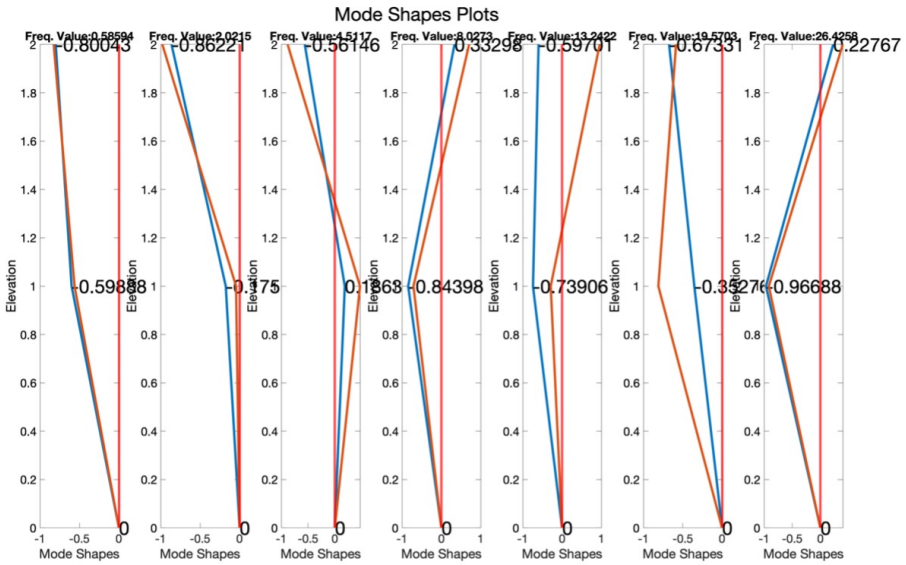


Figure A.55. Comparison of mode shapes from acceleration and displacement response for top two sensor levels.

In the second video recording, the displacement value of the third, fourth, fifth, and sixth level accelerometers was calculated. The first frame of the captured video recording and ROI windows is shown in Figure A.56.

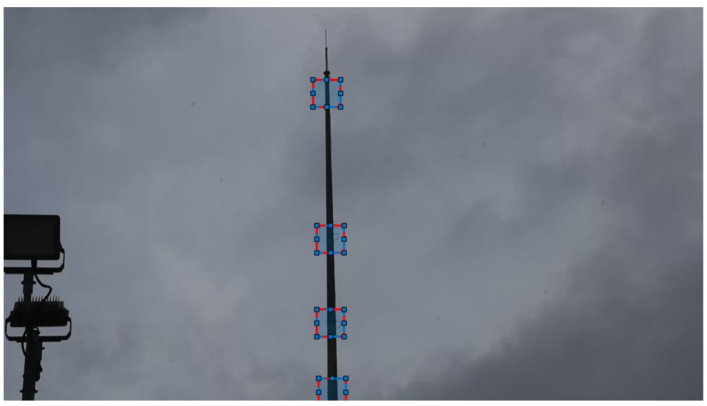


Figure A.56. ROIs for top four sensor levels.

The displacement responses and PSD values found by taking FFT of the third, fourth, fifth, and sixth level in the second video are shown in Figure A.57.

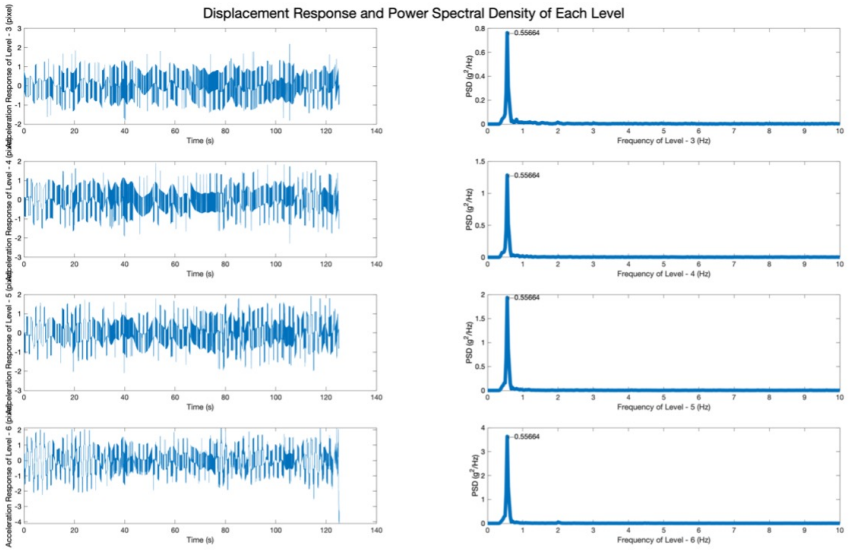


Figure A.57. Displacement response and PSD for top four sensor levels.

SVD values were obtained using FDD from the displacement responses. The values in SVD were determined by using the natural frequencies of the structure obtained from the accelerometers. The values selected in the SVD values are shown in Figure A.58.

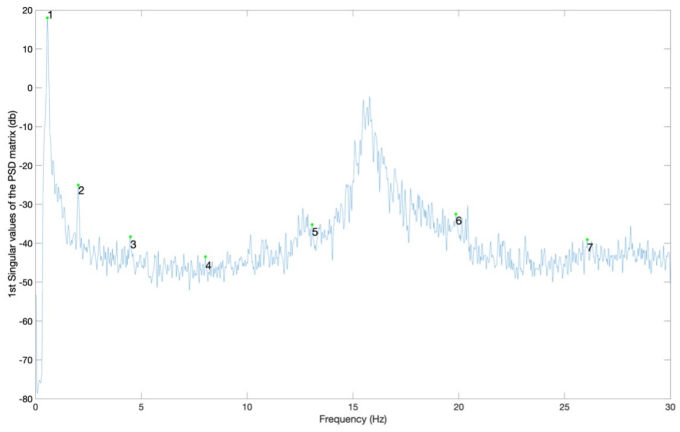


Figure A.58. SVD values used in obtaining mode shapes from displacement response for top four sensor levels.

The mode shapes obtained using the displacement response at the top 4 sensor levels are shown in Figure A.59.

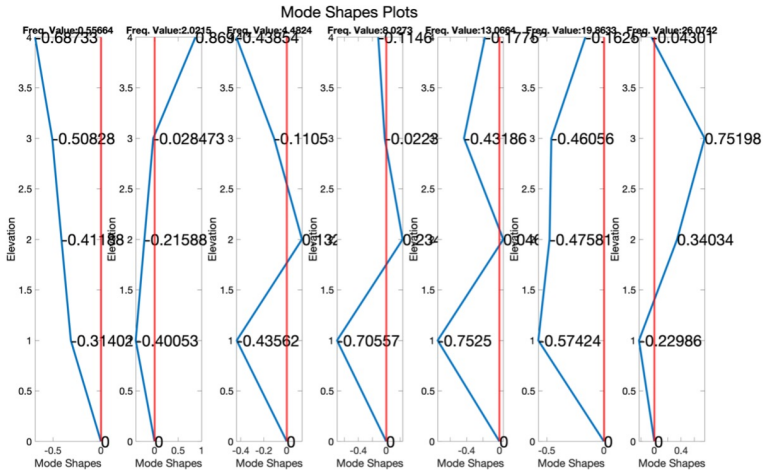


Figure A.59. Mode shapes obtained from displacement response for top four sensor levels.

The comparison of the mode shapes obtained with the acceleration response obtained from the accelerometers and the mode shapes obtained from the same level displacement response obtained from the DSLR is shown in Figure A.60.

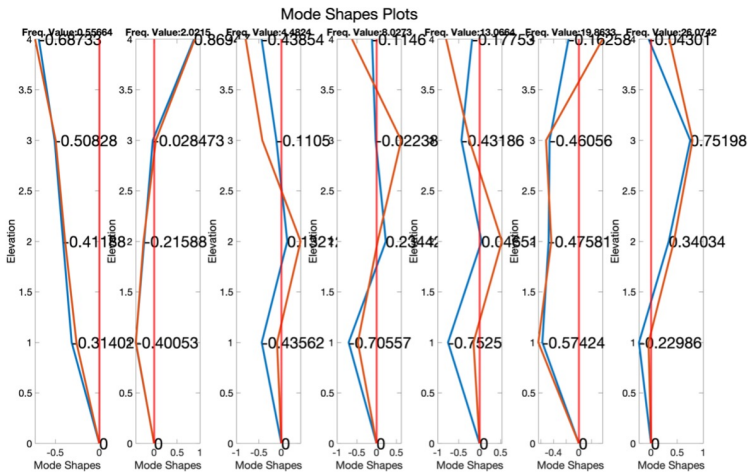


Figure A.60. Comparison of mode shapes from acceleration and displacement response for top four sensor levels.

In the third video recorded, the displacement value of the second, third, fourth, fifth, and sixth level accelerometers was calculated. The first frame of the captured video recording and ROI windows is shown in Figure A.61.

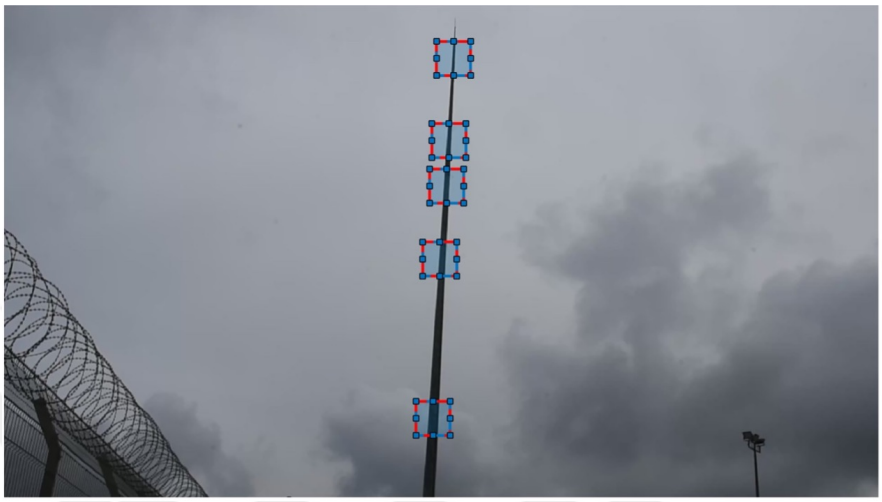


Figure A.61. ROIs for top five sensor levels.

The displacement responses and PSD values found by taking FFT of the second, third, fourth, fifth, and sixth level in the third video are shown in Figure A.62.

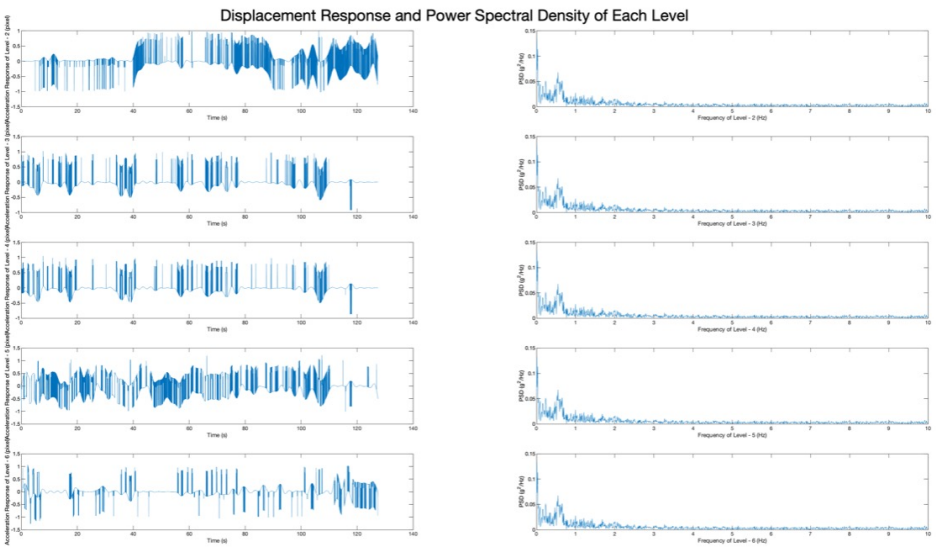


Figure A.62. Displacement response and PSD for top five sensor levels.

SVD values were obtained using FDD from the displacement responses. The values in SVD were determined by using the natural frequencies of the structure obtained from the accelerometers. The values selected in the SVD values are shown in Figure A.63.

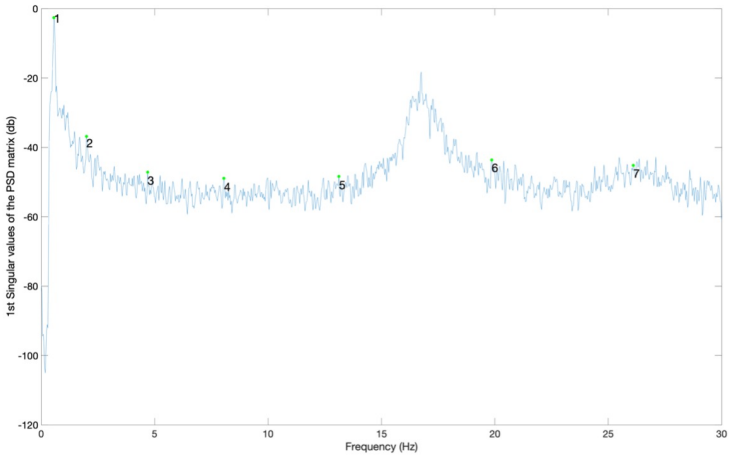


Figure A.63. SVD values used in obtaining mode shapes from displacement response for top five sensor levels.

The mode shapes obtained using the displacement response at the top 5 sensor levels are shown in Figure A.64.

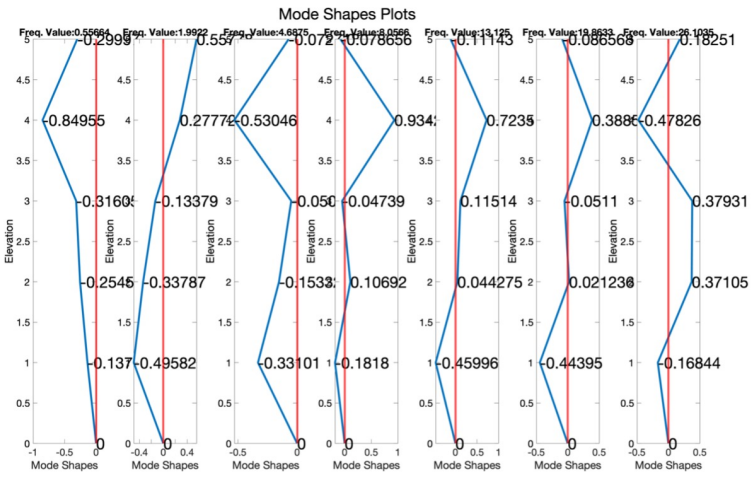


Figure A.64. Mode shapes obtained from displacement response for top five sensor levels.

The comparison of the mode shapes obtained with the acceleration response obtained from the accelerometers and the mode shapes obtained from the same level displacement response obtained from the DSLR is shown in Figure A.65.

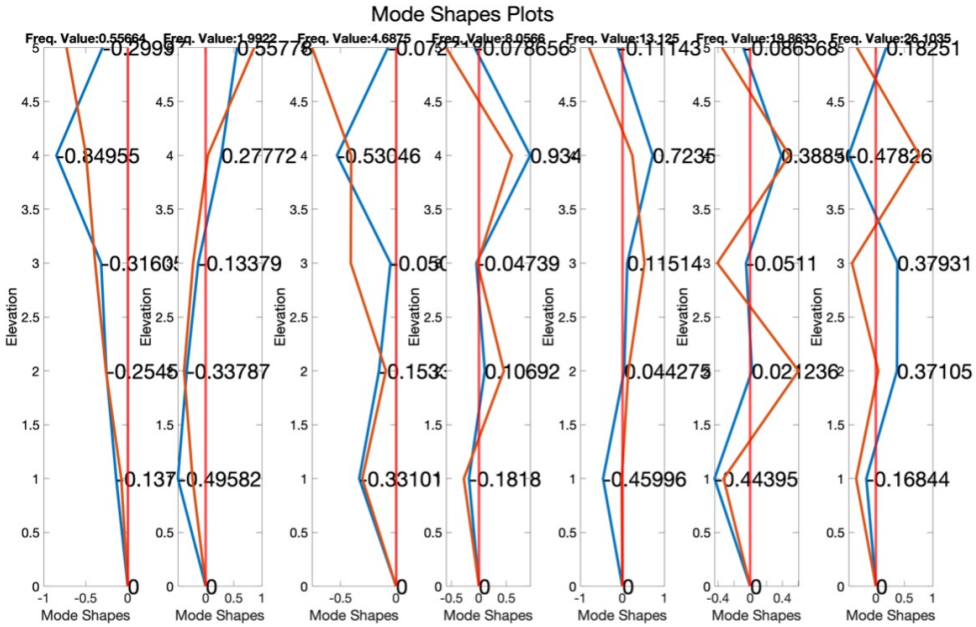


Figure A.65. Comparison of mode shapes from acceleration and displacement response for top four sensor levels.

When all three video recordings were examined, it was determined that the natural frequencies of the structure, which were obtained from the displacement responses measured from the top 2 sensor levels, were more prominent. When the displacement responses taken from farther away and obtained from more sensor levels were analyzed, serious distortions were observed in both the natural frequency and the mode shapes. However, even from a total of 6 minutes of video recording, the dynamic features of the structure could be found up to a certain point. Increasing the length of the video recording and using a higher resolution camera from a farther distance could help solve these problems. In addition, using multiple cameras in sync with each other measuring different levels could also help solve these problems.